

# University of St Andrews

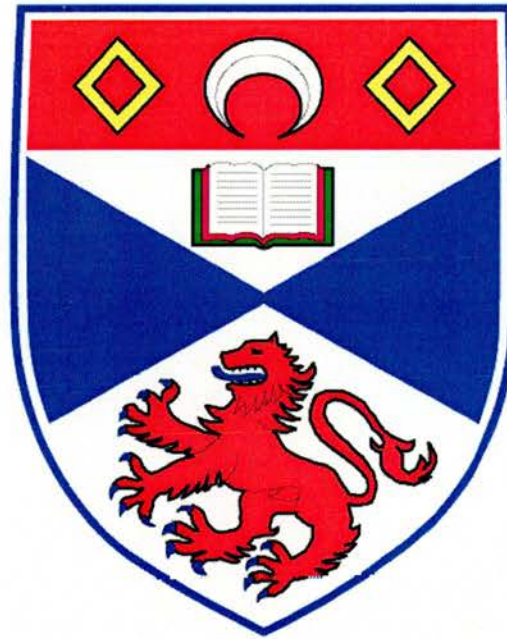


Full metadata for this thesis is available in  
St Andrews Research Repository  
at:

<http://research-repository.st-andrews.ac.uk/>

This thesis is protected by original copyright

# **Rapid techniques for ultrashort optical pulse characterisation**



**Thesis presented for the degree of Doctor of Philosophy to the  
University of St. Andrews**

**By**

**Iain Gavin Cormack MSc**

**The J. F. Allen Physics Research Laboratories  
School of Physics and Astronomy  
University of St. Andrews  
North Haugh  
St Andrews  
Fife, KY16 9SS  
Scotland**

**October 2001**



Th 0992

### **Declaration**

I, Iain Gavin Cormack, hereby certify that this thesis, which is approximately 46000 words in length, has been written by me, that it is the record of work carried out by me and that it has not been submitted in any previous application for a higher degree

Date 16-10-01                      Signature of candidate

I was admitted as a research student and a candidate for the degree of Doctor of Philosophy in October, 1998; the higher study for which this is a record was carried out in the University of St Andrews between 1998 and 2001

Date 16-10-01                      Signature of candidate

I hereby certify that the candidate has fulfilled the conditions of the Resolution and Regulations appropriate for the degree of Doctor of Philosophy in the University of St Andrews and that the candidate is qualified to submit this thesis in application for that degree.

Date 16-10-01                      Signature of supervisor

### **Copyright**

In submitting this thesis to the University of St Andrews I wish access to it to be subject to the following conditions:

For a period of 2 year from the date of submission, the thesis shall be withheld from use.

I understand, however, that the title and abstract of the thesis will be published during this period of restricted access; and that after the expiry of this period the thesis will be made available for use in accordance with the regulations of the University Library for the time being in force, subject to any copyright in the work not being affected thereby, and a copy of the work may be made and supplied to any *bona fide* library or research worker.

Date 16-10-01                      Signature of candidate

**To  
Mam  
&  
Dad**

## **Abstract**

In this thesis several rapidly updating pulse characterisation schemes have been developed to enable the full characterisation of ultrashort laser pulses. These techniques have been based upon the measurement of a sonogram of an optical pulse.

The first ever technique capable of single-shot and video-rate acquisition of a sonogram is demonstrated. The design and implementation of this technique is detailed. Results are compared with externally acquired experimental data to show excellent agreement.

Two separate characterisation systems are reported which utilise two-photon detectors to provide extremely sensitive and accurate measurements of sonogram traces. These two systems differ in the way they spectrally filter a pulse. One system, capable of an update rate of 0.5Hz, uses a grating-lens-mirror arrangement so that a rapidly scanning slit, placed in the Fourier plane can be used to pass selectively a narrow band of frequencies. The other technique, with a higher repetition rate of 1.5 Hz, uses a rapidly scanning Fabry-Perot filter to provide the filtering action. Detailed experimental results have been obtained from these systems. By using the sonograms trace marginals and other experimentally acquired data it is shown that the retrieved results from both of these systems give excellent comparison.

A dispersion characterisation technique using Fourier transform white light interferometry is described which provides dispersion characteristics of optical components including those used in the sonogram characterisation optical arrangements. Results from this technique are compared with theoretically predicted results and show excellent agreement. The sensitivity of this technique has also been demonstrated by measuring the small amount of dispersion that occurs from the reflection from a silver mirror.

The first practical demonstration of dispersion-propagation time-resolved optical gating (DP-TROG) is demonstrated. The use of the trace marginals is shown to provide self-calibration, making DP-TROG a very attractive and simple alternative to other pulse characterisation techniques.

## **Preface**

In Chapter 1, an introduction to the field of ultrafast laser physics is given. Some applications that utilise the unique properties that ultrashort laser pulses possess are discussed. The propagation of such ultrashort pulses through an optical medium is then outlined with descriptions of both linear and nonlinear dispersive effects. Methodologies enabling these dispersive effects to be compensated are then analysed. Finally, the principle of modelocking of a laser is outlined to show how ultrashort pulses are generated. The two separate Ti:sapphire laser systems that were used throughout this project are then described in some detail.

In Chapter 2 there is a review of techniques employed to characterise ultrashort laser pulses. Temporal pulse measurement techniques such as SHG and TPA autocorrelation are discussed initially. This is followed by a description of the various techniques capable of determining comprehensively the intensity and phase of the spectral and temporal components of ultrashort pulses. These techniques are divided into two separate categories, those that operate in the time-frequency domain and those that rely on interferometry. Time-frequency domain methodologies such as frequency-resolved optical gating (FROG) and sonograms are discussed in detail, together with the various geometries that have been devised to obtain experimentally time-frequency measurements of an ultrashort pulses. The retrieval algorithms that are required for these time-frequency measurements are also discussed. Interferometric techniques such as SPIDER are then outlined and finally, the advantages and disadvantages of each geometry are discussed.

Chapter 3 includes a discussion of the development of a technique, later used in Chapter 4, that is capable of determining the dispersion characteristics of optical components using white light interferometry. A review of alternative dispersion characterisation techniques is presented. These techniques are capable of measuring the dispersion of either a single optical

component or the overall dispersion within a laser cavity. Using white light interferometry, a simplified and sensitive technique is introduced. Dispersion measurements from a KDP crystal and a silver mirror are reported which demonstrate the overall reliability of the technique. Importantly, a description is given of how this technique was used to explain why a Cr:LiSAF laser was unexpectedly modelocking in the femtosecond temporal regime.

In Chapter 4, two separate rapid characterisation schemes are discussed that measure the sonogram of a pulse to fully characterise ultrashort laser pulses. The systems differ in the way they frequency filter a pulse. The first system uses a grating-lens-mirror arrangement that employs a slit in the Fourier plane to selectively filter the pulse. The dispersion characteristics of this filter are measured using the technique developed in Chapter 3. The second system uses a scanning Fabry-Perot etalon to provide the required filtering. To ensure both systems gave accurate results extensive data analysis was carried out to compare trace marginals and experimentally acquired data with retrieved results.

The investigation of a new geometry capable of acquiring a sonogram without the need of a frequency filter, known as dispersive-propagation time-resolved optical gating (DP-TROG) is described in Chapter 5. An experimental procedure is described that, arguably, provides the first practical technique which allows a DP-TROG trace to be measured accurately. The simplicity and practicality of the new technique is highlighted. An investigation is also carried out to establish the fundamental limitations in measuring extremely short and complex pulse profiles.

In Chapter 6, the first ever technique that is capable of making a single-shot acquisition of a sonogram trace is described. This technique is also shown to obtain a sonogram trace at video-rate acquisition speeds. The design of this highly compact system is explained in detail including the design of the mixing crystal and the new procedures that have been devised to

calibrate the sonogram trace. The results are then compared to complementary experimentally measured results.

# CONTENTS

Declarations	ii
Abstract	iv
Preface	v
Contents	viii
<b>1 Introduction</b>	<b>1</b>
1.1 A solution looking for a problem	1
1.2 Ultrashort Laser Pulses	2
1.3 Applications of ultrashort pulses	3
1.4 Mathematical description of an optical pulse	6
1.5 Pulse propagation within a dielectric medium	7
1.5.1 Linear pulse propagation	8
1.5.1.1 Techniques used to achieve negative GVD	11
1.5.1.2 Linear pulse propagation through an anisotropic medium	15
1.5.2 Nonlinear pulse propagation	17
1.5.2.1 Third-order nonlinear effects	17
Self-induced optical Kerr effect	17
1.6 Generation of ultrashort pulses	20
1.6.1 Modelocking	20
1.6.1.1 Active modelocking	22
1.6.1.2 Passive modelocking	22
1.6.1.3 Self-modelocking	23
1.7 Laser sources	24
1.8 Conclusion	26
1.9 References	27
<b>2 Ultrashort pulse measurement techniques</b>	<b>30</b>
2.1 Introduction	30
2.2 Temporal pulse measurements – SHG autocorrelation	30
2.3 Techniques allowing the full characterisation of an ultrashort pulse	38
2.3.1 Methodologies working in the time-frequency domain	39
2.3.1.1 Frequency Resolved Optical Gating (FROG)	41
Polarisation-gate FROG (PG-FROG)	41
Second-harmonic-generation FROG (SHG-FROG)	43
Self-diffraction FROG (SD-FROG)	45

Transient-gating FROG (TG-FROG)	46
Third-harmonic-generation FROG (THG-FROG)	48
2.3.1.2 Other techniques deriving from FROG	49
GRENOUILLE	49
TADPOLE	51
TREEFROG	53
Cross-FROG (X-FROG)	54
2.3.1.3 The retrieval of FROG traces	55
Principal component generalised projections (PCGP)	58
Checking for systematic errors using the trace marginals	64
2.3.2 Interferometric characterisation techniques	65
2.3.2.1 SPIDER	65
2.3.2.2 Can SPIDER's gobble up FROG's?	68
2.4 Conclusion	69
2.5 References	70
<b>3 Measurement of group velocity dispersion using white light interferometry</b>	<b>75</b>
3.1 Introduction	75
3.2 Dispersion characterisation techniques	76
3.2.1 Interferometric techniques	76
3.2.2 Intracavity-dispersion techniques	78
3.3 Measurement of group velocity dispersion using the Fourier transform white-light interferometry	79
3.3.1 Experimental configuration	81
3.3.2 Dispersion measurements of a KTP crystal	85
3.3.3 Dispersion measurements of a silver coated mirror	89
3.3.4 The mystery of the non-dispersion-compensated modelocked laser	91
3.4 Conclusion	92
3.5 References	93
<b>4 Development towards real-time pulse characterisation using sonograms</b>	<b>94</b>
4.1 Introduction	94
4.2 Using the 'traditional' sonogram optical arrangement	100
4.2.1 Design of the frequency bandpass filter	100
4.2.2 Experimental configuration and procedure	105
4.2.3 Synchronisation and acquisition of the sonogram trace	106
4.2.4 Calibration and filtering of acquired sonogram trace	108

4.2.5	Retrieval of the sonogram trace	109
4.2.6	Results	111
4.3	Fast acquisition of a sonogram using a scanning Fabry-Perot etalon	115
4.3.1	Design of the frequency bandpass filter	115
4.3.2	Design of the delay line	118
4.3.3	Design of the optical setup	119
4.3.4	Acquisition and synchronisation of the frequency filter and delay-line	120
4.3.5	The calibration and retrieval program	123
4.3.6	Results	125
4.4	Conclusion	130
4.5	References	131
<b>5</b>	<b>Dispersive propagation time-resolved optical gating (DP-TROG)</b>	<b>133</b>
5.1	Introduction	133
5.2	Experimental configuration	136
5.3	Calibration, analysis and retrieval of experimental results	140
5.4	Limitations of the DP-TROG technique	146
5.5	Conclusion	153
5.6	References	154
<b>6</b>	<b>Single-shot acquisition of a sonogram trace</b>	<b>155</b>
6.1	Introduction	155
6.2	Design of the mixing crystal	157
6.3	Creating a variable delay	164
6.4	The optical arrangement	165
6.5	Calibration of the sonogram trace	168
6.5.1	Calibration of the time axis	168
6.5.2	Calibration of the frequency axis	171
6.5.3	Normalisation of the sonogram trace due to spatially varying intensity profile	173
6.6	Results	175
6.7	Conclusion and discussion	179
6.8	References	181

<b>7 Conclusions and future work</b>	<b>182</b>
7.1 Summary and Conclusions	182
<b>Publications</b>	<b>187</b>

# CHAPTER 1

## Introduction

---

### 1.1 A solution looking for a problem

When the first laser was built over 40 years ago [1, 2], Charles Townes, one of the co-inventors of the laser would often be teased by colleagues at the Hughes Aircraft Corporation who would say to him "That's a great idea, but it's a solution looking for a problem".



*Figure 1.1 Dr. T H Maiman with the first ruby laser, a solution looking for a problem*

As time passed and research was applied increasingly to the development of laser based technologies, it was soon realised that the unique properties that laser light exhibits could be utilised within an extraordinary range of applications that ranged from reading bar codes in supermarkets to splitting the atom [3, 4]. Under the umbrella that is “laser physics”, there now exist a large number of research avenues, each concerning itself with specific types of lasers and applications. This thesis concerns itself with a branch of laser physics that uses a laser to produce a sequence of ultrashort pulses instead of the usual narrow-band and continuous wave (CW) operation of a laser. These ‘ultrashort laser pulses’ possess many characteristics that are truly unique and have been used, especially over the past decade, to achieve remarkable results in many areas of science and technology.

## 1.2 Ultrashort Laser Pulses

So what exactly is an ultrashort laser pulse? There is no precise definition of what “ultrashort” really means but in the context of this thesis an ultrashort laser pulse is one which has a temporal duration less than a few hundred femtoseconds ( $1\text{fs} \equiv 10^{-15}\text{s}$ ). It is now common for lasers to routinely produce sub-10 fs pulses directly from the oscillator and such durations can thus be easily taken for granted. The true meaning of what a femtosecond really is can often be forgotten as its scale is extremely difficult to comprehend and visualise in every-day life. It is for this reason that many real-life analogies have been made comparing a femtosecond with a whole second. One such analogy is if we take one second to be equivalent to the wealth of Bill Gates (currently around 37 billion dollars), if he were to donate one femtosecond’s worth of his fortune to charity, the lucky recipient would receive 0.0037 cents!!!! Some of the most visually stunning pictures have been created using pulsed laser light.

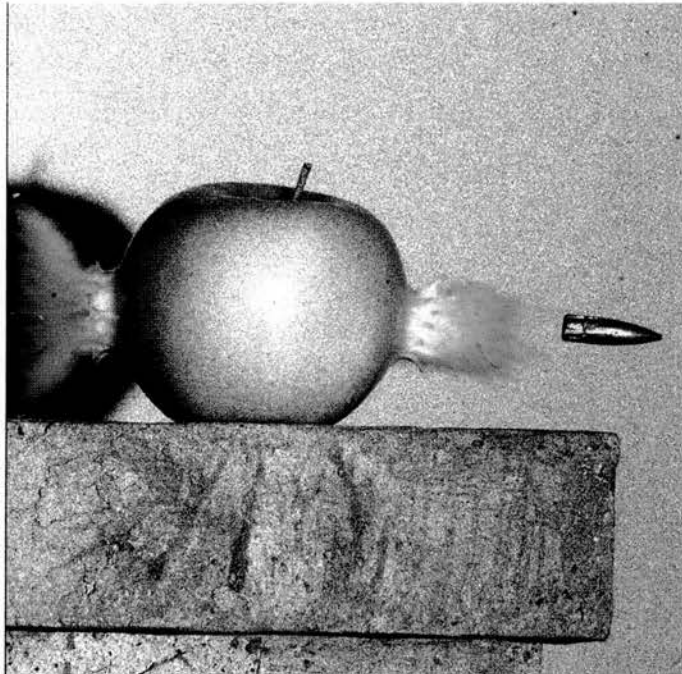


*Figure 1.2 Photograph, using a ‘slow’ 50 picosecond laser pulse to act as a shutter, to view a bullet passing through an apple[5]*

Figure 1.2 shows a photograph of a bullet passing through an apple. To enable the successful capture of such a picture an extremely fast shutter was required. A relatively ‘long’ 50 picosecond pulse ( $1\text{ps} \equiv 10^{-12}\text{s}$ ) was used to take for this picture, that is three orders of

magnitude longer than the pulses being measured in my project. Throughout the work described in this thesis, the lasers used to produce ultrashort pulses had repetition rates around 100MHz. This means a pulse is generated every 10ns which suggests that the peak power of each pulse will be approximately one hundred thousand times larger than the average laser output power. With such tremendous peak powers being available in such a short time-period a vast array of applications has been devised to exploit these unique characteristics.

### **1.3 Applications of ultrashort pulses**

Importantly, many atomic and molecular processes happen within the picosecond and femtosecond regime. To enable scientists to investigate these processes in detail, some faster event is required and ultrashort laser pulses provide the perfect tool to achieve this. In the field of semiconductor spectroscopy, pump-probe experiments have been instrumental in developing theoretical models of semiconductor devices and have thus been partly responsible for the increasing speeds of semiconductor devices. By saturating the conduction band of a semiconductor with an initial strong pump pulse, a weak, time-delayed probe pulse can be used to measure the transmission at various delays with respect to the initial pump pulse. The variation of the transmission with time is directly related to the rate at which the saturation recovers which in turn gives information about the rate at which electrons and holes are scattered from their excited states by non-radiative processes such as phonon emission and electron-electron scattering.

In ultrafast chemistry, ultrashort laser pulses are used to investigate many chemical processes such as bond breakage and formation, ionisation, and molecular collisions, rotation, vibration and fragmentation, all of which occur with characteristic times on a femtosecond scale. By using a similar pump-probe setup, a molecule can be excited into the transition state and be probed to stimulate ionisation, laser-induced fluorescence (LIF) or chemiluminescence, the intensity of which can be used to determine the molecular dynamics. One of the first experiments which utilised this idea was to investigate the vibrational motion of  $I_2$  molecules

[6], and soon after, similar experiments went on to investigate bond breaking in ICN[7], NaI [8] and  $C_2F_4I_2$  [9]. Kent Wilson's group (U.C.S.D) was first to demonstrate that not only the pulse duration and intensity were important to light interaction with molecules but also the chirp on such pulses. It was demonstrated that the precise quantum state of molecules could be selected by using positively and negatively chirped pulses [10]. This was an important observation which demonstrated the usefulness of precise knowledge of the temporal and spectral intensity and phase of an ultrashort pulse.

Ultrashort pulses are currently being used for new imaging techniques that provide advantages over conventional imaging techniques in that they have greater resolution and they allow 3-D and 4-D images to be obtained at deeper penetration depths. Nonlinear microscopy [11] was first demonstrated for bio-medical imaging. This technique measures two-photon fluorescence generated by the sample by a focused femtosecond pulse. As two-photon fluorescence only occurs at the focus of the beam, 3-D cross-sectional images can be achieved. Using a similar technique, semiconductor devices have been imaged by scanning focussed femtosecond pulses across the device and recording the photocurrent caused by two-photon absorption[12]. A technique called fluorescence life-time imaging (FLIM) has shown its potential for real-time medical imaging [13, 14] . Following excitation by an ultrashort laser pulse it has been shown that by measuring the difference between fluorescence lifetimes across a sample, it is possible to discriminate between cancerous and healthy tissue [15]. This technique has then been combined with holographic detection to provide 4-D (x,y,z and t) images of lifetime fluorescence [16].

The high peak powers that are associated with ultrashort laser pulses can be practically used in material processing. Soon after the invention of the laser it became clear that material processing would become an important application for lasers. Whereas CW lasers such as  $CO_2$  lasers are used for cutting materials, pulsed lasers are often used to drill holes in materials. Laser drilling possesses many advantages over conventional mechanical drilling

such as speed, and reliability. Trying to machine sub-100 $\mu\text{m}$  dimensions is extremely difficult whereas with laser drilling it is possible to drill to a resolution of  $\sim 1\mu\text{m}$ . Until recently large pulsed  $\text{CO}_2$  and metal vapour lasers have been used for laser drilling. Such lasers produce pulses with durations of a few tens of nanoseconds ( $10^{-9}\text{s}$ ). By applying such a long pulse onto the surface of a material, a large area surrounding the initial absorption area is affected by conduction of heat. The molten material which occurs from the heat-affected zone is splattered around the surrounding area of the hole causing the edges of the hole to become rough and uneven. When an intense ultrashort pulse is applied to the same surface, the pulse is short enough not to create a heat-affected zone and instead, the majority of the energy of the pulse goes into vaporising the area onto which it is focused. Consequently a much cleaner hole is achieved with no molten material surrounding the hole. These favourable characteristics have been used successfully to create surgical implants [17] and waveguides [18]. By focussing an ultrashort pulse into a transparent material, the internal structure of the material has been shown to change without affecting the surface [19, 20].

By using a technique called chirped pulse amplification (CPA) the energy within a single pulse can be increased so that when focused it can produce an intensity of over  $10^{20}\text{Wcm}^{-2}$ . With peak powers in excess of a petawatt, some of the most extreme conditions in the universe can be created such as the processes within a star as it becomes a supernova [21]. Nuclear fusion has also been achieved in a laser laboratory using such a laser system [3, 4].

The large spectral bandwidth associated with ultrashort pulses (section 1.4) has great implications within the area of metrology [22, 23] where ultrashort pulse have shown to be ideal to relate optical frequencies with conventional reference oscillators [22]. Diddams et al. have recently used a mode-locked femtosecond laser to demonstrate an “optical clock” that is 100 times more accurate than conventional atomic clocks [24].

Although this section has only touched briefly upon the extensive applications that ultrashort laser pulses are currently being used for, it serves to demonstrate how important ultrafast optics has become over recent years. As the number of applications have increased so has the demand for simpler, more robust, faster, and more accurate techniques for the complete measurement of an ultrashort laser pulse. The work carried out in this project has extended the knowledge of ultrashort pulse characterisation to enable overall progress in the area. The remaining part of this chapter describes in formal terms the propagation and generation of ultrashort pulses, knowledge of which is essential for the full understanding of the rest of the thesis material.

#### 1.4 Mathematical description of an optical pulse

Before we are able to discuss what happens when a pulse passes through a material we must first be able to describe the incident pulse in mathematical terms. The most common technique is to use the slowly varying envelope approximation which assumes the pulse envelope varies slowly with respect to the carrier frequency  $\omega_0$ . The time-varying electric field  $E(t)$  can therefore be described as:

$$E(t) = \varepsilon(t) e^{i\phi(t)} e^{-i\omega_0 t} \quad (1.1)$$

where  $\omega_0$  is the carrier frequency,  $\varepsilon(t)$  is the time varying electric field envelope and  $\phi(t)$  is the temporal phase variation across the pulse. The soliton-like pulse shaping in the Ti:Sapphire lasers that have been used throughout the experiments described in this thesis has been shown theoretically to result in a pulse that has a temporal envelope which can generally be represented as a hyperbolic secant function [25] and can be expressed as:

$$\varepsilon(t) = \varepsilon_0 \operatorname{sech} \left( \frac{1.763t}{\Delta\tau_p} \right) \quad (1.2)$$

where  $\varepsilon_0$  is the real electric field amplitude and  $\Delta\tau_p$  is the full width half maximum duration of the pulse.

The spectral field amplitude of a pulse is obtained by Fourier transforming its temporal field amplitude. This means the spectral and temporal components of a pulse are directly dependent upon one another such that if the temporal characteristics (ie. intensity and phase profiles) of the pulse change, so will the spectral characteristics. This dependence upon one another gives way to the bandwidth theorem which states that there is a minimum duration-bandwidth product,

$$\Delta\nu\Delta\tau_{\text{pulse}} \geq C_B \quad (1.3)$$

where  $C_B$  is the value produced when a pulse is “transform limited” ie.  $\phi(t)=0$ . For a  $\text{sech}^2$  pulse profile the value of  $C_B$  is 0.315. When a pulse becomes chirped so that differing frequencies arrive at a fixed reference point at different times, although the spectral intensity remains the same, the pulse duration increases. This has the effect of increasing the value of the duration-bandwidth product.

### 1.5 Pulse propagation within a dielectric medium

The knowledge of how an intense electric field interacts with a dielectric medium is of paramount importance in the generation, measurement and control of ultrashort pulses. In this section there is an outline of the main processes and phenomena that occur when an ultrashort pulse passes through such a medium. It is known that when an electric field is applied to a dielectric material, a polarisation ( $P$ ) is induced

$$P = \varepsilon_0\chi_1E + \varepsilon_0\chi_2E^2 + \varepsilon_0\chi_3E^3 + \dots \quad (1.4)$$

where  $\varepsilon_0$  is the permittivity of free space,  $E$  is the applied electric field and  $\chi_1, \chi_2$  and  $\chi_3$  are the first, second and third order susceptibilities respectively. When dealing with low intensity electric fields, only the linear susceptibility term,  $\chi_1$ , is significant and is responsible for optical effects such as refraction and dispersion. When ultrashort laser pulses are used, the extremely high electric fields associated with their high peak powers mean that

nonlinear effects attributed to higher orders of susceptibility become significant and must also be taken into consideration.

### 1.5.1 Linear pulse propagation

The first-order susceptibility of a material is related to the frequency of the electric field applied upon it [26]

$$\chi_1(\omega) = \frac{Ne^2}{m\epsilon_0 \left[ (\omega_0^2 - \omega^2) + i\omega\gamma \right]} \quad (1.5)$$

where  $\omega$  is the frequency of the applied optical field,  $m$  is the reduced mass of the electron,  $e$  is the charge on the electron,  $N$  is the density of the polarisable atoms in the sample and  $\gamma$  is the damping rate for the electronic vibrational motion. The refractive index  $n$  of the material is related to the susceptibility using equation (1.6)

$$n^2(\omega) - 1 = \chi_1(\omega) \quad (1.6)$$

To calculate the refractive index of a specific material at a specific wavelength Sellmeier's formula is often used

$$n^2(\omega) - 1 = \sum_j \frac{A_j}{\omega_j^2 - \omega^2} \quad (1.7)$$

where  $\omega_j$  is the frequency of the  $j_{\text{th}}$  optical resonance and  $A_j$  is its subsequent strength. Both these constants are specific to the material which the pulse is passing through. Their values can be obtained in many optical reference books. An alternative method to determine the refractive index of a material is to use the Schott coefficients. These coefficients do not consider resonance frequencies but instead originate from the fitting of experimental data of refractive index across a wide range of wavelengths. As the pulse passes through a material of length  $L$ , the phase change on the pulse is given as

$$\phi(\omega) = \frac{\omega}{c} n(\omega) L = \beta(\omega) L \quad (1.8)$$

$\beta(\omega)$  is defined as the propagation constant. To investigate which dispersive effects the first susceptibility term is responsible for, it is useful to expand the propagation constant as a Taylor series

$$\beta(\omega) = \beta_0 + \beta_1(\omega - \omega_0) + \frac{1}{2!}\beta_2(\omega - \omega_0)^2 + \frac{1}{3!}\beta_3(\omega - \omega_0)^3 + \dots \quad (1.9)$$

where  $\beta_1$  is the derivative of  $\beta_0$  with respect to  $\omega$ ,  $\beta_2$  is the derivative of  $\beta_1$  with respect to  $\omega$  and so on. Equation (1.9) is critical to the overall understanding of linear dispersion through a dielectric medium with every term within the equation relating to a different behaviour of a pulse. The first and for the context of his thesis the least important term  $\beta_0$  relates to the phase velocity of the pulse, ie. the velocity at which the central carrier frequency,  $\omega_0$ , propagates

$$\beta_0 = \frac{\omega_0}{v_p} \quad (1.10)$$

The second term,  $\beta_1$ , related to the group velocity of the pulse which is the speed at which the pulse envelope propagates inside a dispersive medium

$$\beta_1 = \frac{d\beta}{d\omega} = \frac{1}{c} \left( n + \omega_0 \frac{dn}{d\omega} \right) = \frac{1}{v_g} \quad (1.11)$$

The third term,  $\beta_2$ , found in equation (1.9) describes modifications to the actual shape of the envelope of the propagating pulse.

$$\beta_2 = \frac{d\beta_1}{d\omega} = \frac{1}{c} \left( 2 \frac{dn}{d\omega} + \omega_0 \frac{d^2n}{d\omega^2} \right) \quad (1.12)$$

This term describes what is known as group velocity dispersion (GVD) or what is commonly referred to as second-order dispersion

$$\beta_2 = \frac{dv_g}{d\omega} \quad (1.13)$$

By definition, in a normally dispersive material, the value of the group velocity dispersion is positive. This means that longer wavelength components of a pulse travel faster than shorter

wavelengths. A transform-limited pulse that passes through a dispersive system that has non-zero GVD will cause the temporal pulse envelope to broaden and the pulse will become frequency-chirped. The fourth term from equation (1.9),  $\beta_3$ , refers to a higher order of GVD and is often referred to as third-order dispersion (TOD)

$$\beta_3 = \frac{d\beta_2}{d\omega} = \frac{1}{c} \left( 3 \frac{d^2 n}{d\omega^2} + \omega_0 \frac{d^3 n}{d\omega^3} \right) \quad (1.14)$$

where TOD can be described as

$$TOD = \frac{d \text{ GVD}}{d\omega} \quad (1.15)$$

Third-order dispersion results in much more complicated distortions of the pulse but can often be discarded because it only becomes important when very short pulses are involved.

A transform-limited pulse that has had an amount of positive GVD applied to it is said to have positive linear frequency chirp. A simple way of expressing this phenomenon mathematically is by writing the instantaneous frequency as a linearly varying function so that the net phase shift can be obtained from:

$$-\frac{d\phi}{dt} = \omega(t) = \omega_0 + 2bt \quad (1.16)$$

where  $b$  is used as a measure of chirp. By applying equation (1.16) onto an optical pulse we can see that

$$E(t) \propto \exp \left[ -i(\omega_0 t + bt^2) \right] \quad (1.17)$$

It is interesting to note that there is a quadratic dependence on the temporal phase when linear chirp is present. Measurements reported throughout this thesis will demonstrate this in practice. Figure 1.3 shows a comparison between (a) a transform-limited  $\text{sech}^2$  pulse and (b) one which has had some inherent positive GVD.

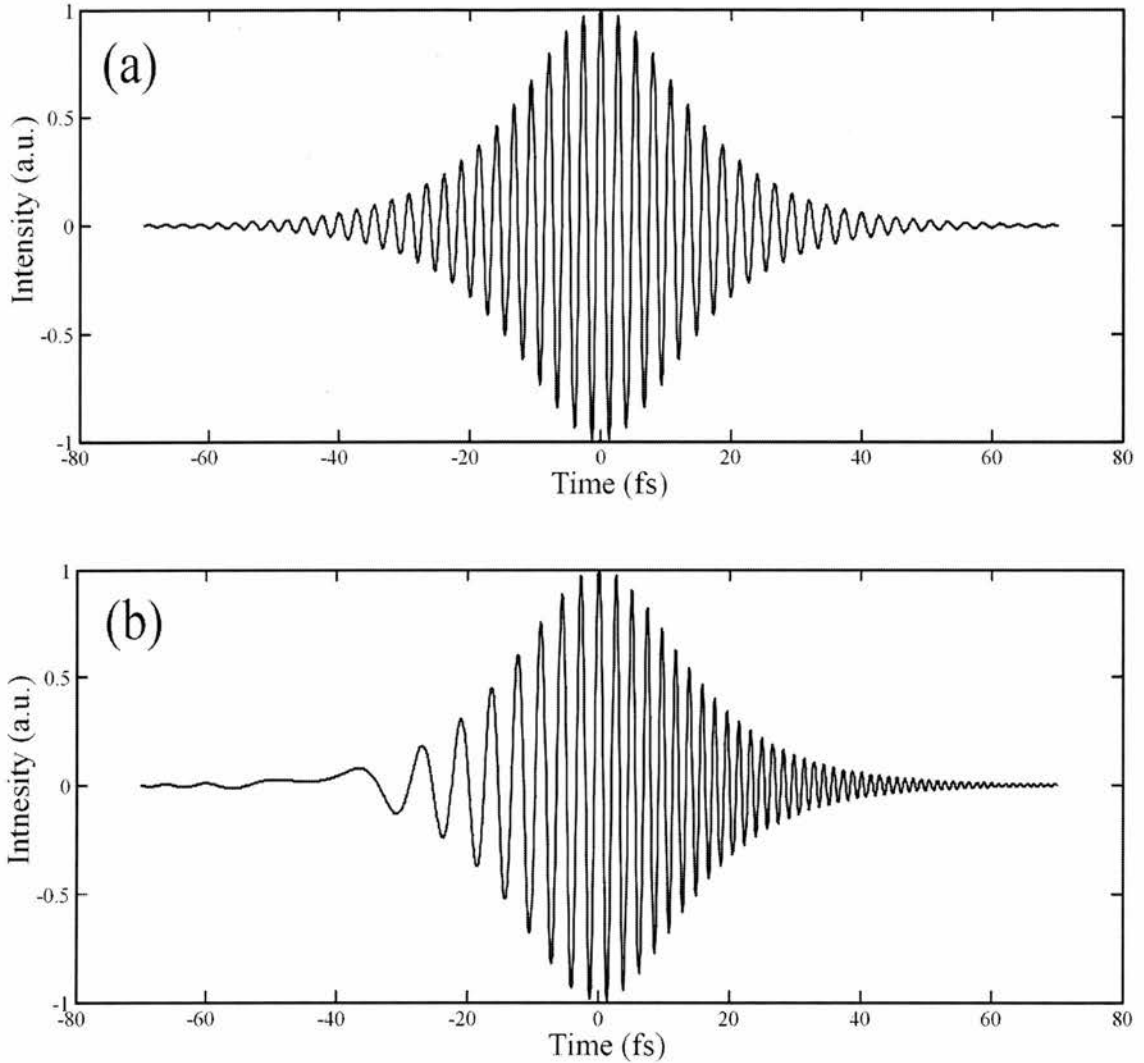


**Figure 1.3** Comparison between the electric field of a 20fs pulse at 800nm that is (a) transform limited and (b) positively chirped

### 1.5.1.1 Techniques used to achieve negative GVD

As a transform-limited pulse passes through a normally dispersive ( $\beta_2 > 0$ ) optical material, it acquires positive linear chirp. This results in the longer wavelength components emerging from the material earlier than the shorter wavelength components and causes the duration of the pulse to increase. For many practical purposes such as pulse generation and shaping it is vital to have control of the pulse chirp, and consequently optical components and systems are needed that have negative GVD and can be used to compensate for positive chirp, allowing shorter wavelengths to ‘catch up’ with the longer wavelength components of the pulse. A number of techniques have been employed to achieve this and they can be divided into two

separate categories of those that use bulk optics and geometry to create a wavelength dependent path length and those that use interference effects.

One of the first ever techniques to introduce negative GVD was by Treacy [27, 28] who used pairs of diffraction gratings to allow shorter wavelengths to travel with a reduced optical path length with respect to longer wavelengths.

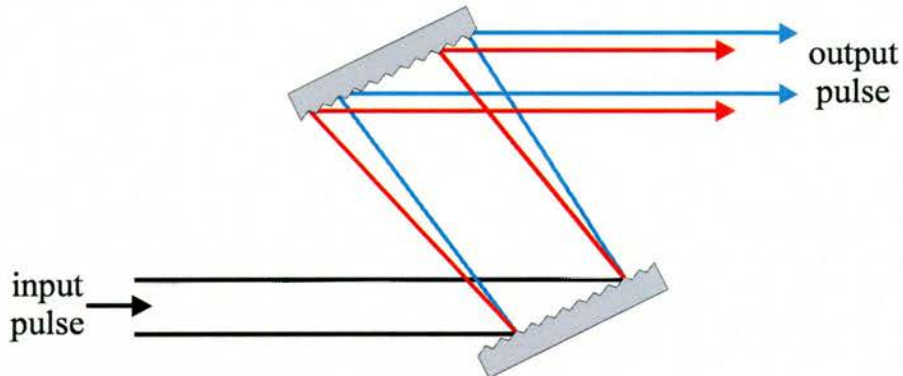


*Figure 1.4 The use of two gratings to produce negative GVD*

The main limitation associated with this technique is the loss that is incurred from both diffraction gratings. An improved technique to provide negative GVD was devised by R.L. Fork et al [29-32] who used a double prism pair arrangement.

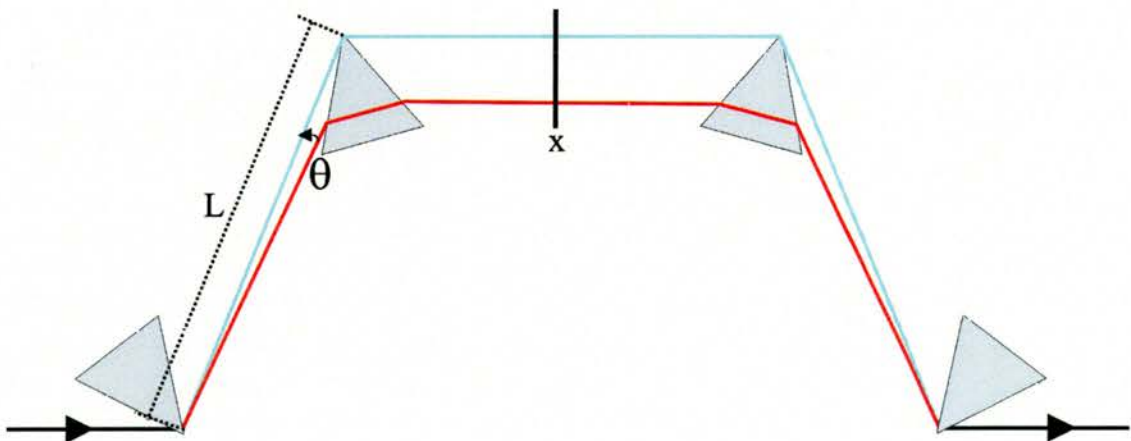


*Figure 1.4 A prism pair arrangement used to produce negative GVD*

The prism arrangement outlined in Figure 1.4 consists of four identical prisms that are cut such that the minimum deviation angle coincides with the Brewster angle, thereby minimising propagation loss through the four prisms. The exit angle from the first prism is dependent

solely upon the wavelength of the incident light. The shorter the wavelength, the more acute the exit angle. This effect allows the shorter wavelength components to pass through less of the second prism and with a shorter optical path length than longer wavelengths negative GVD is achieved. The amount of quadratic phase caused by the prism arrangement can be expressed as [32]

$$\frac{d^2\phi_p}{d\omega^2} = \frac{\lambda_0^3}{2\pi c^2} \left( \frac{d^2P}{d\lambda^2} + L \frac{d^2n_p}{d\lambda^2} \right) \quad (1.18)$$

where  $P$  is the optical path length and derivative  $d^2P/d\lambda^2$  is a function of the propagation angle  $\theta$ , the refractive index of the prism material  $n_p$  and the prism apex separation  $L$ :

$$\frac{d^2P}{d\lambda^2} = 4L \sin\theta \left[ \frac{d^2n}{d\lambda^2} + \left( 2n_p - \frac{1}{n^3} \right) \left( \frac{dn}{d\lambda} \right)^2 \right] - 8L \cos\theta \left( \frac{dn}{d\lambda} \right)^2 \quad (1.19)$$

By varying the prism separation and insertion, the amount of positive or negative dispersion added to the pulse varies. This ability combined with its low loss has made the technique ideal for controlling dispersion within a laser cavity. Using such a setup within a Ti:Sapphire laser has been shown to produce pulses as short as 11 fs [33]. Recently, a more general expression which calculated the second and third-order dispersion through a prism pair has been devised [34]. This expression enables the use of differing prisms within the optical setup. The prism arrangement within Figure 1.4 is symmetric between the two prism pairs and allows in practice the double-pass use of a single prism pair with a mirror being placed at position X. Although the higher order dispersion introduced by the prisms can be calculated, the task of removing higher order dispersion is very difficult and is one of the main difficulties in trying to gain ever shorter pulses. Recent efforts such as those by Xu et al [35] have used a spatial light modulator within a similar prism arrangement to try and compensate for higher orders of dispersion and have successfully achieved pulse compression down to 6 fs. The general issue of pulse compression helps highlight one of the important driving forces behind the need for full ultrashort pulse characterisation. If accurate knowledge of the phase is known, the task of compensating it is made that much easier.

Some of the shortest pulses ever created have been obtained using lasers containing carefully engineered intra-cavity dispersion mirrors [36, 37]. It was first realised in 1986 that negative GVD could be achieved when a laser was tuned so that its centre wavelength was longer than that of the mirror centre wavelength. This forced the longer wavelength of the laser pulse to penetrate deeper into the Bragg stack thus causing it to have a longer optical delay than shorter wavelengths [38]. The disadvantage of this technique was that there was little control over the amount of negative dispersion obtained and that the longer wavelength experienced a lower reflectivity. Some of these problems were overcome in 1994 when chirped multilayer dielectric coatings were devised [39]. By varying the thickness of the high-low refractive index stack found within a Bragg mirror stack it was found that a wide frequency bandwidth could be reflected by the same amount while still forcing larger wavelengths to be reflected more deeply within the multilayer structure. Although only small amounts of negative dispersion are obtained from these structures, by using multiple reflections from these chirped mirrors within a laser cavity the amount of positive dispersion caused by the gain medium can be compensated for in a precise fashion. Consequently, chirped mirrors have become popular in the creation of prismless, dispersion-compensated Ti:Sapphire laser oscillators. Over recent years much progress has been made in increasing the bandwidth of chirped mirrors. One major obstacle to increasing the bandwidth is caused by interference between light reflected off the mirror/air interface and the light reflected from the Bragg stacks. This results in an undesirable modulation in the group delay dispersion (GDD). The use of a so-called double-chirped mirror technique (DCM) [40-42] has served to reduce this modulation. Recently, modulation has been reduced even further by using novel designs such as a tilted-front interference chirped mirror [43] and applying the Bragg stack onto the back of the mirror substrate so that there is no mirror/air interface [44]. Another interferometric technique is to use the frequency-dependent phase property of a Fabry-Perot filter [45]. This has been achieved by using a Gires-Tournois (GTI) mirror [46, 47]. A GTI mirror has an etalon fabricated within the Bragg stack that has a thickness of  $\lambda/2$ . Compared to chirped mirrors, a

far larger amount of negative GVD is produced and a consequently a single GTI mirror is capable of compensating the positive dispersion within a laser cavity.

### 1.5.1.2 Linear pulse propagation through an anisotropic medium

When dealing with the linear propagation of light through a dielectric medium, the electric displacement vector  $D$  is introduced. This term includes both the vacuum electric field term as well as the response of the medium

$$\bar{D} = \epsilon_0 \bar{E} + \bar{P} \quad (1.20)$$

By substituting equation (1.4) into equation (1.20) we get

$$\bar{D} = \epsilon_0 \epsilon \bar{E} \quad (1.21)$$

where  $\epsilon$  is the relative permittivity  $(1 + \chi)$ . Equation (1.21) cannot however be used if the induced medium polarisation is not parallel to the electric field which is exactly what happens within an anisotropic medium. Instead we need to write down each component of the electric displacement vector to produce the dielectric tensor.

$$\frac{1}{\epsilon_0} \begin{pmatrix} D_x \\ D_y \\ D_z \end{pmatrix} = \begin{pmatrix} \epsilon_x & \epsilon_{xy} & \epsilon_{xz} \\ \epsilon_{yx} & \epsilon_y & \epsilon_{yz} \\ \epsilon_{zx} & \epsilon_{zy} & \epsilon_z \end{pmatrix} \begin{pmatrix} E_x \\ E_y \\ E_z \end{pmatrix} \quad (1.22)$$

By choosing a particular set of axes (known as the “principal axis”), a large number of terms in equation (1.22) can be eliminated.

$$\frac{1}{\epsilon_0} \begin{pmatrix} D_x \\ D_y \\ D_z \end{pmatrix} = \begin{pmatrix} \epsilon_x & 0 & 0 \\ 0 & \epsilon_y & 0 \\ 0 & 0 & \epsilon_z \end{pmatrix} \begin{pmatrix} E_x \\ E_y \\ E_z \end{pmatrix} \quad (1.23)$$

To help visualise the change in refractive index with orientation the use of the optical indicatrix can be used. From the Fresnel equation it can be shown that the dependence of the relative permittivity upon propagation direction and polarisation can be given as [48]

$$\frac{x^2}{\epsilon_x} + \frac{y^2}{\epsilon_y} + \frac{z^2}{\epsilon_z} = 1 \quad (1.24)$$

Using the principal dielectric axis of a uniaxial crystal ( $\epsilon_x = \epsilon_y \neq \epsilon_z$ ) and knowing that  $n_k^2 = \epsilon_k$ , the following expression for the index ellipsoid can be produced

$$\frac{x^2}{n_o^2} + \frac{y^2}{n_o^2} + \frac{z^2}{n_e^2} = 1 \quad (1.25)$$

where  $n_o$  and  $n_e$  are the refractive indices of the ordinary and extraordinary ray respectively. Equation (1.25) can now be used to calculate and visualise the refractive index experienced by an electric field at a given angle to the axis

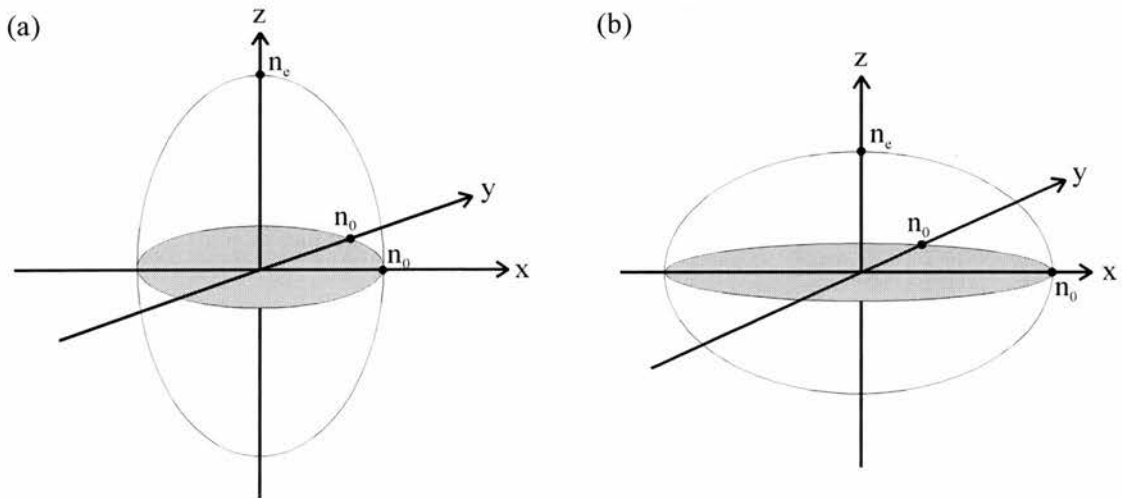


**Figure 1.5** The use of the optical indicatrix to show the index ellipsoid of (a) a positive uniaxial crystal and (b) a negative uniaxial crystal

Figure 1.5 helps demonstrate how a uniaxial crystal can be described in two ways, a positive uniaxial crystal ( $n_e > n_o$ ) and negative uniaxial ( $n_e < n_o$ ). Birefringent media like this play a vital role in optics, enabling devices such electro-optic, magneto-optic and acousto-optic modulators to operate. In the context of this thesis, a birefringent material allows two differing wavelengths to travel through a material with the same phase velocity (phasematching). This enables the interaction of both electric fields over a much longer distance enabling non-linear effects such as frequency doubling and frequency mixing that form the basis of a number of ultrafast laser systems.

## 1.5.2 Nonlinear pulse propagation

When dealing with ultrashort laser pulses and their associated high peak powers the second and third orders of susceptibility that are contained within equation (1.4) must be considered. Second-order nonlinear effects only occur within non-centrosymmetric materials ( $d_{ijk} \neq 0$ ) and are responsible for nonlinear effects such as frequency mixing. The polarisation change caused within the material is proportional to the square of the field applied to it. Third-order nonlinear effects occur within all optical materials (including centrosymmetric materials with  $d_{ijk} = 0$ ). Since some third-order non-linear effects are crucial to the understanding of how ultrafast lasers operate they will be discussed in greater detail within this chapter. For a more detailed description of second-order effects such as sum frequency mixing the reader is referred to Chapter 6.

### 1.5.2.1 Third-order nonlinear effects

Third-order nonlinear effects can occur in any optical material. This is unlike second-order non-linear effects for which only non-centrosymmetric materials (ie. low symmetry crystals) can be used. For all centrosymmetric media (where  $d_{ijk} = 0$ ),  $\chi_3$  is the first non-linear term. It is responsible for a number of important phenomena including third harmonic generation ( $\omega + \omega + \omega \rightarrow 3\omega$ ), Raman scattering and the optically induced Kerr effect. The optical Kerr effect is vital for ultrashort pulse generation and will now be described in more detail.

#### Self-induced optical Kerr effect

If we consider an isotropic medium ( $\chi_2 = \chi_4 = 0$ ) with a significantly large  $\chi_3$  we can use equation (1.4) to say

$$D = \varepsilon_0 \chi_1 E + \varepsilon_0 \chi_3 E^3 \quad (1.26)$$

Equation (1.26) can be rearranged to give

$$D = \varepsilon_0 \varepsilon E \quad (1.27)$$

where  $\varepsilon$  is the total dielectric constant is given as

$$\varepsilon = \varepsilon_L + \chi_3 E^2 \quad (1.28)$$

where

$$\varepsilon_L = 1 + \chi_1 \quad (1.29)$$

Equation (1.28) can now be put into terms of irradiance:

$$n = \sqrt{\varepsilon} = n_0 + n_{2I} I \quad (1.30)$$

where the Kerr coefficient  $n_{2I}$  is given as

$$n_{2I} = \frac{6\chi_3}{8\varepsilon_0 c n_0} \quad (1.31)$$

Equations (1.30) shows that if there is a sufficiently strong irradiance within any medium the refractive index will change. Two important effects arise that are associated to ultrashort pulse generation. These two effects are known as self-focussing [49] and self-phase modulation (SPM) [50].

To consider self focussing we need to consider a pulse with a Gaussian-like spatial profile that is passing through a medium where the term  $n_2 I$  is significant. By assuming that the wavefront is initially plane with the Gaussian intensity profile, Figure 1.6 demonstrates what happens as the pulse propagates into the medium

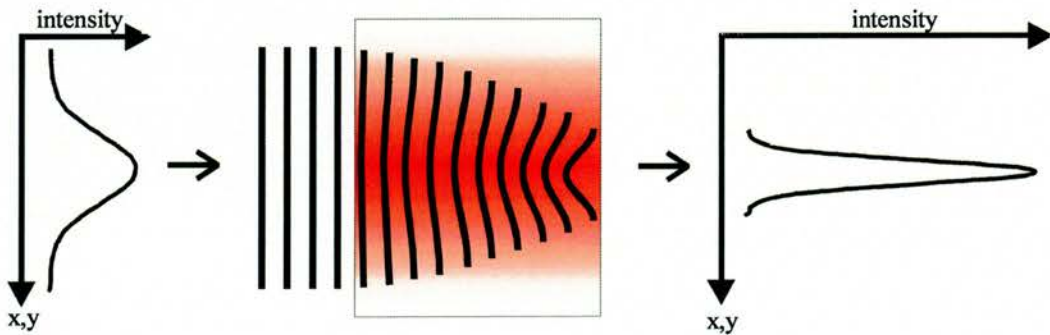


Figure 1.6 Graphical representation of self focusing

If we assume  $n_2$  is positive then the phase velocity ( $v = c/n$ ) is reduced as the intensity increases. Consequently the outer wavefronts of the pulse have higher speeds compared to those nearer the centre and more intense part of the pulse. This has the effect of creating a ‘virtual lens’ within the optical material causing the beam to be focused. As well as having important consequences for ultrashort pulse generation [51-53], self-focusing is also responsible for beam break-up in high power lasers as well as optically induced damage caused by the laser beam focussing within the optical material and resulting in the formation of damage tracks.

Self-phase modulation (SPM) is the second important result of the self-induced optical Kerr effect. If it is assumed that the refractive index change caused by the optical Kerr effect is instantaneous then we can say that as a pulse propagates through a media, different parts of the pulse will experience a different refractive index. This effect causes a phase shift within the pulse

$$\Delta\phi(t) = \frac{2\pi L n_2 I(t)}{\lambda} \quad (1.32)$$

where  $L$  is the material length and  $I(t)$  is the intensity profile of the pulse. The phase shift causes an instantaneous increase in frequency that can be represented as

$$\Delta\omega = -\frac{d(\Delta\phi(t))}{dt} = -\frac{2\pi L n_2}{\lambda} \left( \frac{dI(t)}{dt} \right) \quad (1.33)$$

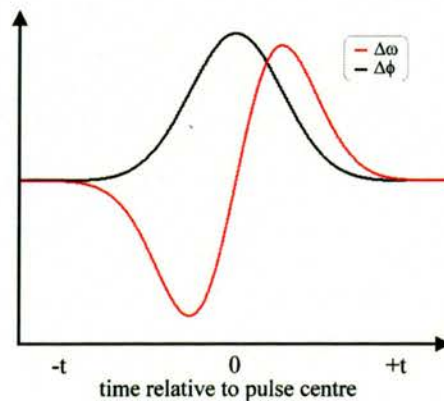


**Figure 1.7** The phase shift (black) and instantaneous frequency shift (red) of a pulse caused by self phase modulation

From looking at the instantaneous frequency shift,  $\Delta\omega$ , in Figure 1.7 it is possible to see a positive linear ramp through the centre region of the pulse. It is this positive linear chirp region that is responsible for SPM being often approximated as another form of linear dispersion that can be compensated for using the techniques described in section 1.5.1.1. Self-phase modulation is a very useful phenomenon in enabling the generation of ultrashort pulses as it broadens the spectral bandwidth so that shorter pulses can be sustained within the laser cavity (see Equation (1.3)).

## **1.6 Generation of ultrashort pulses**

Techniques to force a laser oscillator to produce a periodic sequence of pulses rather than a continuous waveform have existed for a long time. Methods such as gain switching [54], cavity-dumping [55] and Q-switching [56] have all successfully been used to produce short pulsed lasers. To produce the shortest possible pulse (ie. ultrashort pulses), a technique called modelocking is used. It should be noted that this thesis details techniques that are capable of characterising these pulses and does not largely concern itself with how such pulses are created. Consequently only a brief overview of ultrashort pulse generation is presented. For a more detailed description of ultrashort pulse lasers, the reader is referred to the following references [57-59]

### **1.6.1 Modelocking**

Modelocking has become the most common and efficient way of producing ultrashort laser pulses. Normally when a laser oscillates within a cavity the axial modes exhibit random phase between one another to give a noise-like output. When a laser becomes modelocked all the axial modes that exist within a laser cavity become in phase with one another.

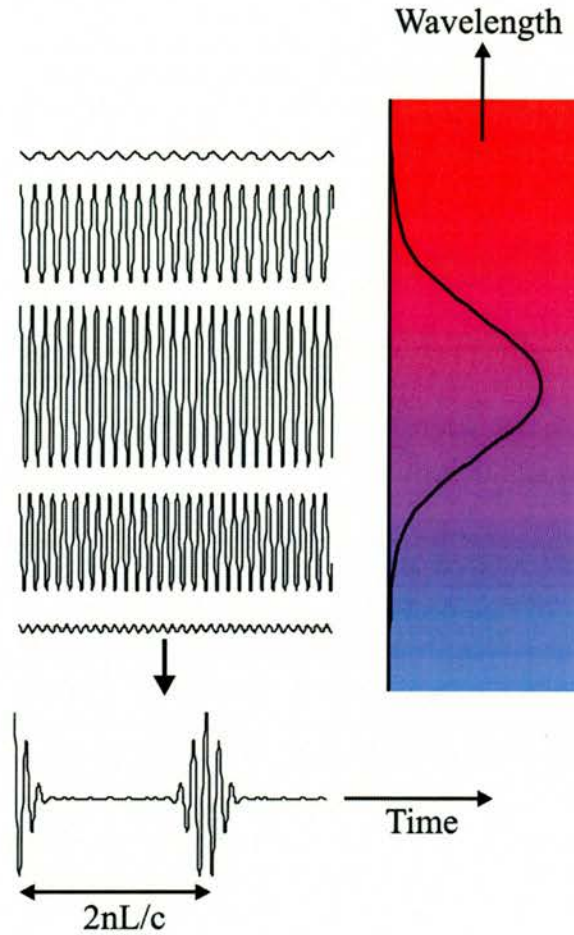


**Figure 1.8** Illustration how five axial modes within a gain medium that are in phase with one another can interfere to form a pulsed output [60]

Figure 1.8 demonstrates how when 5 axial modes are in phase with one another within a laser cavity, the interference between the modes produces a pulsed output, the separation of which is determined by the round trip cavity time

$$\Delta t_{sep} = \frac{2nL}{c} \quad (1.34)$$

where  $n$  is the average refractive index and  $L$  is the length of the cavity. The greater number of modes that oscillate within a cavity, the shorter the pulse duration becomes. Consequently to obtain the shortest possible pulse the gain bandwidth of laser medium must be large. In ‘normal’ operation, a laser will operate to produce a CW output. A laser needs to be ‘encouraged’ to operate in a modelocked fashion and this is achieved by applying some kind of amplitude or phase modulation within the cavity. The modulation can either be introduced

to the laser actively by an external source, so called ‘active modelocking’, or introduced passively. ‘passive modelocking.

### **1.6.1.1 Active modelocking**

In active modelocking, amplitude or phase modulation is used to generate ultrashort pulses. The frequency of the modulation is set to exactly match a multiple of the round-trip frequency of the laser (Equation (1.34)). By using this exact modulation frequency a pulse is able to make a round trip of the cavity so that it returns to the modulating component when the gain or transmission of the device is at its maximum. This ensures that only multiples of this mode are capable of propagation within the cavity, hence modelocked operation is achieved. An alternative description can be made in the frequency domain where the applied modulation will cause the axial modes to have sidebands. By having the modulation match the round-trip frequency of the laser, the side bands of each mode will coincide with other adjacent modes enabling power to be transferred from one mode to another. Various techniques have been used to achieve active modelocking including gain modulation [61], synchronous pumping [62] or the use of optical switches such as acousto-optic [63] or electro-optic [64] modulators that are placed within the cavity itself.

### **1.6.1.2 Passive modelocking**

Whereas active modelocking relies on an external modulation source, passive modelocking utilises nonlinear effects to cause the output of the laser to modulate itself. Using the analogy of a ‘switch’ that is controlled by the laser, passive modelocking is able to self-adjust its modulation for small variations of the laser, thus providing a more stable method of modelocking that is also able to produce shorter pulses than actively modelocked lasers. The first example of a passively modelocked laser used an organic dye as a saturable absorber [65]. A saturable absorber is optically lossy at low incident light intensities but becomes transparent at high intensities. One of the characteristics of an organic dye is its broad-

bandwidth which makes it ideal for supporting ultrashort pulses. Passive modelocking relies on modelocked oscillation to build up from noise. This is achieved from a noise spike in the cavity that is large enough to begin to saturate the absorber. The noise spike will experience less cavity loss than other smaller oscillations and will consequently begin to grow at the expense of all other oscillations within the cavity. As the oscillation grows, its leading edge will erode due to the saturation of the absorber dye solution and its trailing edge will be eroded by gain saturation within the gain medium. This erosion helps reduce the overall pulse duration until its bandwidth equals the gain bandwidth of the gain medium.

Many improvements of modelocking techniques were developed such as regenerative [66], coupled-cavity [67-69] and colliding-pulse [70, 71] modelocking. Further improvement was made when organic dyes started being replaced by new solid-state materials such as Ti:Sapphire ( $\text{Ti:Al}_2\text{O}_3$ ). These materials possessed much larger gain bandwidths than organic dyes, opening the possibility of reducing pulse durations even further. The real break-through came in 1990 when a technique known as self-modelocking was discovered [51, 53].

### **1.6.1.3 Self-Modelocking**

Self-modelocking, often referred to as Kerr-lens modelocking (KLM), uses a couple of third-order nonlinear effects described in section 1.5.2.1, specifically self-phase modulation and self-focussing. It was discovered that, when a large noise spike was introduced into a laser cavity during normal CW operation, a high enough intensity existed to cause self-focussing within the gain medium (Ti:Sapphire). When the laser cavity was correctly adjusted the focusing effect resulted in the noise spike experiencing lower loss than that of CW operation because of its different mode size. By adding apertures into the cavity it was therefore possible to force the laser to favour pulsed operation rather than CW operation. Two different types of apertures exist – soft and hard. Hard apertures consist of physically placing actual apertures within the cavity, usually at each end of the cavity. A soft aperture carefully aligns

the pump source so that there is greater overlap during pulsed operation rather than in CW operation. This leads to a larger gain for pulsed operation thus causing the laser to remain stably modelocked. Self-phase modulation also occurs within the gain medium, helping to broaden the pulse so that shorter pulse durations are possible. Since Ti:Sapphire has an extremely large gain bandwidth, SPM is able to broaden the pulse enormously, thereby, in theory enabling pulses as short as 3 fs to be produced. Of course to obtain such a short pulse experimentally is extremely difficult because the intracavity dispersion must be controlled precisely. Using carefully engineered double chirped intracavity mirrors, sub 5fs pulsed have recently been generated directly from a Ti:sapphire oscillator [37]. In Ti:Sapphire lasers a prism-pair arrangement is most commonly used within the laser cavity to provide the negative dispersion that compensates for the positive dispersion created by material dispersion and self-phase modulation.

## 1.7 Laser sources

Two separate Ti:sapphire lasers were used during the course of this thesis. Both lasers used a Spectra Physics 5W Millennia (diode pumped Nd:VO<sub>4</sub> frequency-doubled CW laser at 532nm) as the pump source.

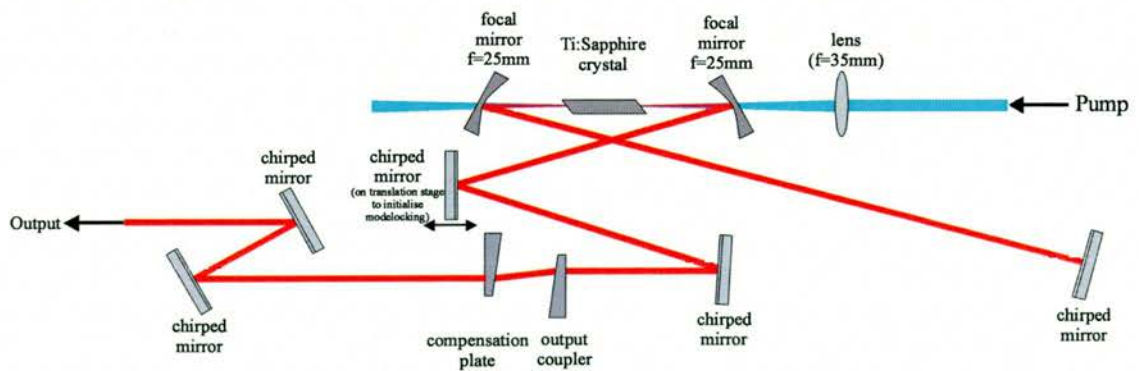


**Figure 1.9** Optical layout of the 'Stingl' Ti:Sapphire laser

Figure 1.9 shows the optical arrangement of the Stingl Ti:Sapphire laser which was used in the majority of the work carried out within this thesis [72]. The use of chirped mirrors enabled the cavity design to be very straightforward. The chirped mirrors had been designed

to produce enough negative dispersion to compensate for the positive dispersion created within the Ti:Sapphire crystal. By translating one of the chirped mirrors, a noise spike was introduced into the cavity that was large enough to initialise modelocking. This laser had an average output power of  $\sim 250\text{mW}$  and had a repetition rate of  $\sim 80\text{MHz}$ . Two extra-cavity chirped mirrors were used to compensate for the positive dispersion put onto the pulse by the output coupler and compensation plates. It was possible to vary the chirp on the pulse by using multiple reflections off these two mirrors. The use of chirped mirrors limited the tunability of this laser and always operated at a centre wavelength of  $790\text{nm}$ , producing pulses with durations of  $\sim 30\text{fs}$ .

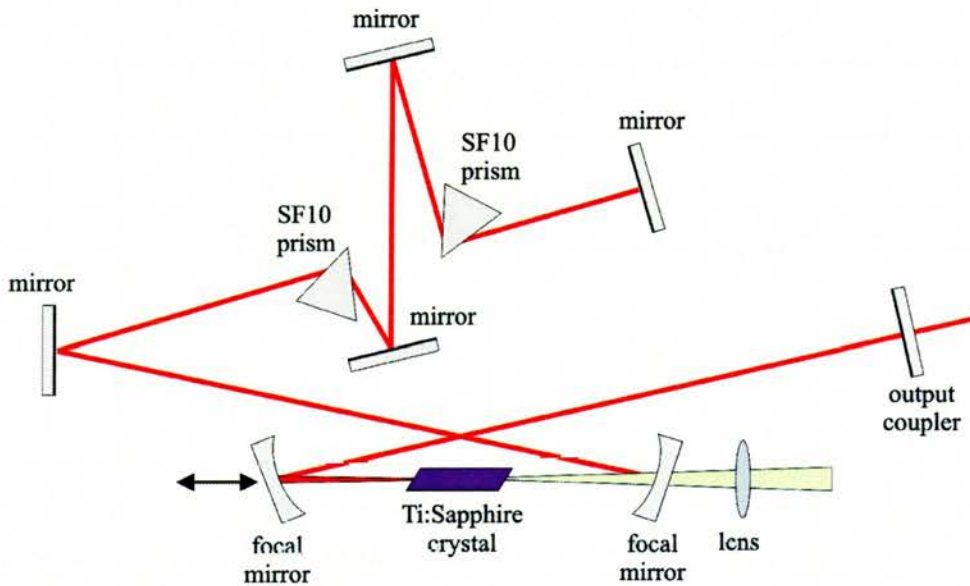


**Figure 10** The optical arrangement of a Ti:sapphire laser with intra-cavity prisms to compensate for positive dispersion

The second laser, shown in Figure 1.10, was used throughout Chapter 6. The intra-cavity negative dispersion was obtained using a prism pair arrangement. By varying the prism insertion, the positive dispersion created within the Ti:Sapphire crystal was compensated. The laser could be tuned to operate at different wavelengths by either varying the alignment of the cavity or by placing a slit after the prism arrangement. The laser normally operated at a centre wavelength  $\sim 815\text{nm}$  to produce  $50\text{fs}$ , transform limited pulses. Its repetition rate was around  $\sim 80\text{MHz}$  and had an average output power of  $\sim 800\text{mW}$ .

## **1.8 Conclusion**

Within this chapter I have given an introduction to the applications, behaviour and production of ultrashort laser pulses all of which are vital for the full understanding of this thesis material. One vital area has yet to be discussed and involves the techniques used to measure ultrashort pulses. Since the majority of the material within this thesis concerns itself with pulse characterisation, chapter 2 goes on to describe in detail the many techniques that have been used characterise ultrashort pulses.

## 1.9 References

- [1] A. Schawlow and C. Townes, "Infrared and Optical Masers," *Physical Review*, vol. 112, pp. 1940, 1958.
- [2] T. Maiman, *Nature*, vol. 187, pp. 493, 1960.
- [3] T. E. Cowan, A. W. Hunt, T. W. Phillips, S. C. Wilks, M. D. Perry, C. Brown, W. Fountain, S. Hatchett, J. Johnson, M. H. Key, T. Parnell, D. M. Pennington, R. A. Snavely, and Y. Takahashi, "Photonuclear fission from high energy electrons from ultraintense laser-solid interactions," *Physical Review Letters*, vol. 84, pp. 903-906, 2000.
- [4] K. W. D. Ledingham, I. Spencer, T. McCanny, R. P. Singhal, M. I. K. Santala, E. Clark, I. Watts, F. N. Beg, M. Zepf, K. Krushelnick, M. Tatarakis, A. E. Dangor, P. A. Norreys, R. Allott, D. Neely, R. J. Clark, A. C. Machacek, J. S. Wark, A. J. Cresswell, D. C. W. Sanderson, and J. Magill, "Photonuclear physics when a multiterawatt laser pulse interacts with solid targets," *Physical Review Letters*, vol. 84, pp. 899-902, 2000.
- [5] [http://www.af.mil/news/Jan1998/n19980114\\_980049.html](http://www.af.mil/news/Jan1998/n19980114_980049.html).
- [6] M. Gruebele, G. Roberts, M. Dantus, R. M. Bowman, and A. H. Zewail, "Femtosecond Temporal Spectroscopy and Direct Inversion to the Potential - Application to Iodine," *Chemical Physics Letters*, vol. 166, pp. 459-469, 1990.
- [7] M. Dantus, R. M. Bowman, and A. H. Zewail, "Femtosecond Laser Observations of Molecular Vibration and Rotation," *Nature*, vol. 343, pp. 737-739, 1990.
- [8] T. S. Rose, M. J. Rosker, and A. H. Zewail, "Femtosecond Real-Time Probing of Reactions .4. The Reactions of Alkali-Halides," *Journal of Chemical Physics*, vol. 91, pp. 7415-7436, 1989.
- [9] L. R. Khundkar and A. H. Zewail, "Picosecond Photofragment Spectroscopy .4. Dynamics of Consecutive Bond Breakage in the Reaction  $C_2F_4I_2 \rightarrow C_2F_4 + 2I$ ," *Journal of Chemical Physics*, vol. 92, pp. 231-242, 1990.
- [10] B. Kohler, V. V. Yakovlev, J. W. Che, J. L. Krause, M. Messina, K. R. Wilson, N. Schwentner, R. M. Whitnell, and Y. J. Yan, "Quantum Control of Wave-Packet Evolution with Tailored Femtosecond Pulses," *Physical Review Letters*, vol. 74, pp. 3360-3363, 1995.
- [11] W. Denk, J. H. Strickler, and W. W. Webb, "2-Photon Laser Scanning Fluorescence Microscopy," *Science*, vol. 248, pp. 73-76, 1990.
- [12] C. Xu and W. Denk, "Two-photon optical beam induced current imaging through the backside of integrated circuits," *Applied Physics Letters*, vol. 71, pp. 2578-2580, 1997.
- [13] R. Cubeddu, F. Docchio, W. Q. Liu, R. Ramponi, and P. Taroni, "Time-Resolved Fluorescence Spectroscopy with Programmable Gating," *Journal of Photochemistry and Photobiology B-Biology*, vol. 3, pp. 129-131, 1989.
- [14] R. Cubeddu, R. Ramponi, W. Q. Liu, and F. Docchio, "Time-Gated Fluorescence Spectroscopy of the Tumor Localizing Fraction of Hpd in the Presence of Cationic Surfactant," *Photochemistry and Photobiology*, vol. 50, pp. 157-163, 1989.
- [15] R. Jones, K. Dowling, M. J. Cole, D. Parsons-Karavassilis, M. J. Lever, P. M. W. French, J. D. Hares, and A. K. L. Dymoke-Bradshaw, "Fluorescence lifetime imaging using a diode-pumped all-solid-state laser system," *Electronics Letters*, vol. 35, pp. 256-258, 1999.
- [16] K. Dowling, M. J. Dayel, S. C. W. Hyde, J. C. Dainty, P. M. W. French, P. Vourdas, M. J. Lever, A. K. L. Dymoke-Bradshaw, J. D. Hares, and P. A. Kellett, "Whole-field fluorescence lifetime imaging with picosecond resolution using ultrafast 10-kHz solid-state amplifier technology," *IEEE Journal of Selected Topics in Quantum Electronics*, vol. 4, pp. 370-375, 1998.
- [17] S. Nolte, C. Momma, G. Kamlage, B. Chichikov, A. Tunnerman, F. Von Alvensleben, and H. Welling, presented at Conference on Electro Optics and Lasers (CLEO 1998), San Francisco, 1998.
- [18] C. B. Schaffer, A. Brodeur, J. F. Garcia, and E. Mazur, "Micromachining bulk glass by use of femtosecond laser pulses with nanojoule energy," *Optics Letters*, vol. 26, pp. 93-95, 2001.
- [19] J. Kruger and W. Kautek, "Femtosecond-pulse visible laser processing of transparent materials," *Applied Surface Science*, vol. 96-8, pp. 430-438, 1996.
- [20] J. Kruger and W. Kautek, "Femtosecond pulse visible laser processing of fibre composite materials," *Applied Surface Science*, vol. 106, pp. 383-389, 1996.
- [21] J. Kane, D. Arnett, B. A. Remington, S. G. Glendinning, G. Bazan, R. P. Drake, and B. A. Fryxell, "Supernova experiments on the Nova laser," *Astrophysical Journal Supplement Series*, vol. 127, pp. 365-369, 2000.

- [22] R. Holzwarth, T. Udem, T. W. Hansch, J. C. Knight, W. J. Wadsworth, and P. S. J. Russell, "Optical frequency synthesizer for precision spectroscopy," *Physical Review Letters*, vol. 85, pp. 2264-2267, 2000.
- [23] T. W. Hansch, *Optics Communications*, vol. 13, pp. 68, 1975.
- [24] S. A. Diddams, T. Udem, J. C. Bergquist, E. A. Curtis, R. E. Drullinger, L. Hollberg, W. M. Itano, W. D. Lee, C. W. Oates, K. R. Vogel, and D. J. Wineland, "An optical clock based on a single trapped Hg-199(+) ion," *Science*, vol. 293, pp. 825-828, 2001.
- [25] H. A. Haus, J. G. Fujimoto, and E. P. Ippen, "Structures for Additive Pulse Mode-Locking," *Journal of the Optical Society of America B-Optical Physics*, vol. 8, pp. 2068-2076, 1991.
- [26] I. Walmsley, L. Waxer, and C. Dorrer, "The role of dispersion in ultrafast optics," *Review of Scientific Instruments*, vol. 72, pp. 1-29, 2001.
- [27] E. Treacy, "Pulse compression with diffraction gratings," *IEEE Journal of Quantum Electronics*, vol. 5, pp. 454-458, 1969.
- [28] E. Treacy, "Compression of picosecond light pulses," *Phys Letters*, vol. 28a, pp. 34-35, 1968.
- [29] R. L. Fork, O. E. Martinez, and J. P. Gordon, "Negative Dispersion Using Pairs of Prisms," *Optics Letters*, vol. 9, pp. 150-152, 1984.
- [30] J. P. Gordon, R. L. Fork, and O. E. Martinez, "Negative Dispersion from Prisms," *Journal of the Optical Society of America B-Optical Physics*, vol. 1, pp. 437-437, 1984.
- [31] O. E. Martinez, J. P. Gordon, and R. L. Fork, "Negative Group-Velocity Dispersion Using Refraction," *Journal of the Optical Society of America a-Optics Image Science and Vision*, vol. 1, pp. 1003-1006, 1984.
- [32] R. L. Fork, C. H. B. Cruz, P. C. Becker, and C. V. Shank, "Compression of Optical Pulses to 6 Femtoseconds by Using Cubic Phase Compensation," *Optics Letters*, vol. 12, pp. 483-485, 1987.
- [33] P. F. Curley, C. Spielmann, T. Brabec, F. Krausz, E. Wintner, and A. J. Schmidt, "Operation of a Femtosecond Ti-Sapphire Solitary Laser in the Vicinity of Zero Group-Delay Dispersion," *Optics Letters*, vol. 18, pp. 54-56, 1993.
- [34] R. E. Sherriff, "Analytic expressions for group-delay dispersion and cubic dispersion in arbitrary prism sequences," *Journal of the Optical Society of America B-Optical Physics*, vol. 15, pp. 1224-1230, 1998.
- [35] L. Xu, N. Nakagawa, R. Morita, H. Shigekawa, and M. Yamashita, "Programmable chirp compensation for 6-fs pulse generation with a prism-pair-formed pulse shaper," *IEEE Journal of Quantum Electronics*, vol. 36, pp. 893-899, 2000.
- [36] A. Baltuska, Z. Y. Wei, M. S. Pshenichnikov, and D. A. Wiersma, "Optical pulse compression to 5 fs at a 1-MHz repetition rate," *Optics Letters*, vol. 22, pp. 102-104, 1997.
- [37] R. Ell, U. Morgner, F. X. Kartner, J. G. Fujimoto, E. P. Ippen, V. Scheuer, G. Angelow, T. Tschudi, M. J. Lederer, A. Boiko, and B. Luther-Davies, "Generation of 5-fs pulses and octave-spanning spectra directly from a Ti : sapphire laser," *Optics Letters*, vol. 26, pp. 373-375, 2001.
- [38] M. Yamashita, M. Ishikawa, K. Torizuka, and T. Sato, "Femtosecond-Pulse Laser Chirp Compensated by Cavity-Mirror Dispersion," *Optics Letters*, vol. 11, pp. 504-506, 1986.
- [39] R. Szipocs, K. Ferencz, C. Spielmann, and F. Krausz, "Chirped Multilayer Coatings for Broad-Band Dispersion Control in Femtosecond Lasers," *Optics Letters*, vol. 19, pp. 201-203, 1994.
- [40] F. X. Kartner, N. Matuschek, T. Schibli, U. Keller, H. A. Haus, C. Heine, R. Morf, V. Scheuer, M. Tilsch, and T. Tschudi, "Design and fabrication of double-chirped mirrors," *Optics Letters*, vol. 22, pp. 831-833, 1997.
- [41] N. Matuschek, F. X. Kartner, and U. Keller, "Analytical design of double-chirped mirrors with custom-tailored dispersion characteristics," *IEEE Journal of Quantum Electronics*, vol. 35, pp. 129-137, 1999.
- [42] R. Paschotta, G. J. Spuhler, D. H. Sutter, N. Matuschek, U. Keller, M. Moser, R. Hovel, V. Scheuer, G. Angelow, and T. Tschudi, "Double-chirped semiconductor mirror for dispersion compensation in femtosecond lasers," *Applied Physics Letters*, vol. 75, pp. 2166-2168, 1999.
- [43] G. Tempea and F. Krausz, "Dispersion management over one octave with tilted-front-interference chirped mirrors," presented at The Twelfth International Conference on Ultrafast Phenomena, Charleston, South Carolina, 2000.
- [44] N. Gallmann, N. Matuschek, D. H. Sutter, G. Steinmeyer, U. Keller, V. Scheuer, G. Angelow, and T. Tschudi, "Smooth dispersion compensation over one octave: novel chirped mirrors with suppressed dispersion oscillations," presented at The Twelfth International Conference on Ultrafast Phenomena, Charleston, South Carolina, 2000.

- [45] A. Yariv, in *Optical Electronics*, 4th edition ed, 1998, pp. 117.
- [46] R. Szipocs, A. Kohazi-Kis, S. Lako, P. Apai, A. P. Kovacs, G. DeBell, L. Mott, A. W. Louderback, A. V. Tikhonravov, and M. K. Trubetskov, "Negative dispersion mirrors for dispersion control in femtosecond lasers: chirped dielectric mirrors and multi-cavity Gires-Tournois interferometers," *Applied Physics B-Lasers and Optics*, vol. 70, pp. S51-S57, 2000.
- [47] B. Golubovic, R. R. Austin, M. K. Steiner-Shepard, M. K. Reed, S. A. Diddams, D. J. Jones, and A. G. Van Engen, "Double Gires-Tournois interferometer negative-dispersion mirrors for use in tunable mode-locked lasers," *Optics Letters*, vol. 25, pp. 275-277, 2000.
- [48] A. Yariv, "The index ellipsoid," in *Quantum Electronics*, r. edition, Ed.: Willey, 1988, pp. 90.
- [49] A. Siegman, "Whole beam self-focusing," in *Lasers: University Science Books*, 1986, pp. 380.
- [50] A. Siegman, "Self-Phase modulation," in *Lasers: University Science Books*, 1986, pp. 382.
- [51] D. E. Spence, P. N. Kean, and W. Sibbett, "60-Fsec Pulse Generation from a Self-Mode-Locked Ti-Sapphire Laser," *Optics Letters*, vol. 16, pp. 42-44, 1991.
- [52] D. E. Spence, J. M. Evans, W. E. Sleat, and W. Sibbett, "Regeneratively Initiated Self-Mode-Locked Ti-Sapphire Laser," *Optics Letters*, vol. 16, pp. 1762-1764, 1991.
- [53] D. E. Spence and W. Sibbett, "Femtosecond Pulse Generation by a Dispersion-Compensated, Coupled-Cavity, Mode-Locked Ti-Sapphire Laser," *Journal of the Optical Society of America B-Optical Physics*, vol. 8, pp. 2053-2069, 1991.
- [54] A. Siegman, "Gain switching," in *Lasers: University Science books*, 1986, pp. 966.
- [55] A. Siegman, "Repetitive Cavity Dumping," in *Lasers: University Science Books*, 1986, pp. 977.
- [56] A. Siegman, "Laser Q-switching," in *Lasers: University Science books*, 1986, pp. 1004-1040.
- [57] D. T. Reid, "Ultrashort Pulses," in *The Handbook of Laser Technology and Applications*: Institute of Physics Publishing, 2001.
- [58] W. Sibbett, D. T. Reid, and M. Ebrahimzadeh, "Versatile femtosecond laser sources for time-resolved studies: configurations and characterizations," *Philosophical Transactions of the Royal Society of London Series a-Mathematical Physical and Engineering Sciences*, vol. 356, pp. 283-296, 1998.
- [59] A. Siegman, *Lasers: University Science publishing*, 1986.
- [60] D. T. Reid, "Few cycle EM pulses," *Contemporary Physics*, vol. 40, pp. 193-204, 1999.
- [61] L. Glasser, *Electronics Letters*, vol. 14, pp. 725, 1978.
- [62] C. Spielmann, F. Krausz, T. Brabec, E. Wintner, and A. J. Schmidt, "Femtosecond Pulse Generation from a Synchronously Pumped Ti- Sapphire Laser," *Optics Letters*, vol. 16, pp. 1180-1182, 1991.
- [63] A. Yariv, "Bragg diffraction of light by acoustic waves," in *Quantum Electronics: Wiley*, 1988, pp. 327.
- [64] S. Smith, "Amplitude modulation," in *Optoelectronic devices: Prentice Hall*, 1995, pp. 234.
- [65] R. L. Fork, B. I. Greene, and C. V. Shank, *Applied Physics Letters*, vol. 38, pp. 671, 1981.
- [66] G. Huggett, *Applied Physics Letters*, vol. 13, pp. 186, 1968.
- [67] L. F. Mollenauer and R. H. Stolen, "The Soliton Laser," *Journal of the Optical Society of America B-Optical Physics*, vol. 1, pp. 444-445, 1984.
- [68] K. J. Blow and D. Wood, "Mode-Locked Lasers with Nonlinear External Cavities," *Journal of the Optical Society of America B-Optical Physics*, vol. 5, pp. 629-632, 1988.
- [69] E. P. Ippen, H. A. Haus, and L. Y. Liu, "Additive Pulse Mode-Locking," *Journal of the Optical Society of America B-Optical Physics*, vol. 6, pp. 1736-1745, 1989.
- [70] R. L. Fork, B. I. Greene, and C. V. Shank, "Generation of Optical Pulses Shorter Than 0.1 Psec by Colliding Pulse Mode-Locking," *Applied Physics Letters*, vol. 38, pp. 671-672, 1981.
- [71] R. L. Fork, B. I. Greene, and C. V. Shank, "Generation of Optical Pulses Shorter Than 0.1 Psec by Colliding Pulse Mode-Locking," *IEEE Journal of Quantum Electronics*, vol. 17, pp. 52, 1981.
- [72] Femtolasers, *Floragasse7, A-1040 Vienna*.

# CHAPTER 2

## Ultrashort pulse measurement techniques

---

### 2.1 Introduction

Chapter 1 gave an introduction to a number of key aspects related to the creation and physical characteristics of an ultrashort pulse. Contained within this chapter is a description of the non-trivial task of measuring these pulses. So how exactly do we manage to measure the fastest ever man made event? Ideally we would like to characterise pulses in both frequency and time. A frequency measurement is perhaps the simplest of all pulse characterisation techniques as it just involves passing pulses through a spectrometer and recording the resulting spectrum. The temporal measurement of pulses is more demanding. To be measured, an event in time normally must be compared with something shorter. In the case of ultrashort laser pulses this is not possible because there is no faster event to compare it with. If this were not a difficult enough problem to solve, we would also ideally like to know the chirp of the pulse, ie to have knowledge of the arrival time of each spectral component of the pulse. Many techniques have been devised over the past two decades that are able to characterise ultrashort pulses. It is beyond the scope of this chapter to describe all of these techniques, and instead, only the most common techniques will be described.

### 2.2 Temporal pulse measurements – SHG autocorrelation

One of the first ever techniques used to measure the temporal features of ultrashort pulses is a second-harmonic generation (SHG) autocorrelation[1-3]. The technique is still commonly used in ultrafast science laboratories due to its simplicity and fast update rate.

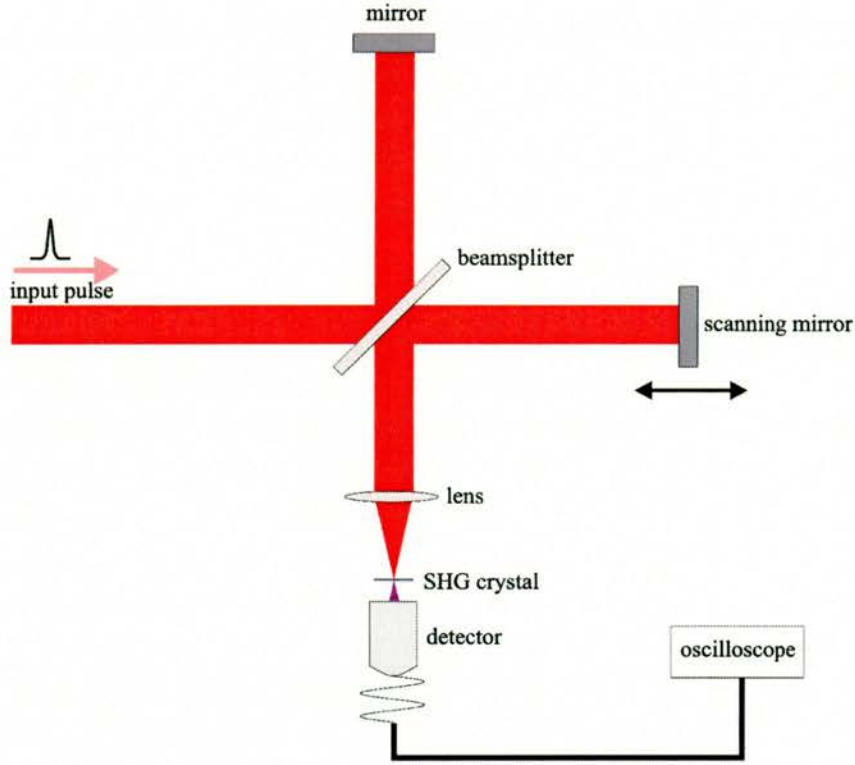


**Figure 2.1** Optical arrangement of a SHG autocorrelator

The optical setup is based on a Michelson interferometer. The pulse is initially split into two copies, each travelling down a separate arm. By varying the relative delay between the two sub-components pulses by moving one arm back and forth, they exit the interferometer with a fixed delay,  $\tau$ , and are spatially overlapped with one another within the second harmonic crystal. The net field in the crystal resulting from the two overlapping pulses is:

$$E(t) + E(t - \tau) \quad (2.1)$$

where  $\tau$  is the delay of the second pulse with respect to the first. The signal within the SHG crystal can be described by:

$$G(\tau) = \int_{-\infty}^{\infty} \left| [E(t) + E(t - \tau)] \right|^2 dt \quad (2.2)$$

where  $E(t)$  is defined as:

$$E(t) = \varepsilon(t) e^{i\phi(t)} e^{i\omega_0 t} \quad (2.3)$$

where  $\varepsilon(t)$  represents the real electric field amplitude of the pulse and  $\phi(t)$  its phase at frequency  $\omega_0$ . The frequency doubled signal from the SHG crystal has a quadratic response

to intensity. By detecting this frequency doubled signal using a photomultiplier tube, a temporal measurement is transformed into a spatial (or delay) measurement. For ultrashort pulses the thickness of the doubling crystal must be chosen carefully to ensure, firstly, that there is an adequate phase-matching bandwidth and, secondly, that group velocity mismatch (GVM) [4] is kept to a minimum, otherwise distortion of the pulse will occur [5]. The signal measured by the detector is the interferometric autocorrelation of the pulse and is mathematically described in normalised form as:

$$g_2(\tau) = \frac{\int_{-\infty}^{\infty} |E(t) + E(t+\tau)|^2 dt}{2 \int_{-\infty}^{\infty} |E(t)|^4 dt} \quad (2.4)$$

The maximum and minimum value of each fringe half-period, for a transform-limited pulse, corresponds to a change of delay of  $\Delta\tau = \pm\pi/\omega$ . By plotting an array of these minimum and maximum values, two envelope functions can be created, one for the upper bounds of the fringes,  $g_u$ , and one for the lower bounds of the fringes,  $g_l$ :

$$g_u(\tau) = \frac{\int_{-\infty}^{\infty} |\varepsilon(t) + \varepsilon(t-\tau)|^4 dt}{2 \int_{-\infty}^{\infty} \varepsilon^4(t) dt} \quad (2.5)$$

$$g_l(\tau) = \frac{\int_{-\infty}^{\infty} |\varepsilon(t) - \varepsilon(t-\tau)|^4 dt}{2 \int_{-\infty}^{\infty} \varepsilon^4(t) dt} \quad (2.6)$$

Provided the pulses are near transform limited, the interferometric autocorrelation trace is self-calibrating because the time period between each fringe is known (2.67fs per fringe at 800nm). From Equations (2.5) and (2.6) it is observed that the overall maximum and minimum values are when the delay is zero ( $\tau=0$ ) so that equation (2.4) becomes

$$g_2(\tau) = \frac{\int |2E(t)|^4 dt}{2 \int |E(t)|^4 dt} = \frac{16}{2} = 8 \quad (2.7)$$

and when  $\tau \rightarrow \pm\infty$

$$g_2(\tau) = \frac{\int |E(t)|^4 dt + \int |E(t)|^4 dt}{2 \int |E(t)|^4 dt} = 1 \quad (2.8)$$

From equations (2.7) and (2.8) we can see that an interferometric autocorrelation has a contrast ratio of 8:1.

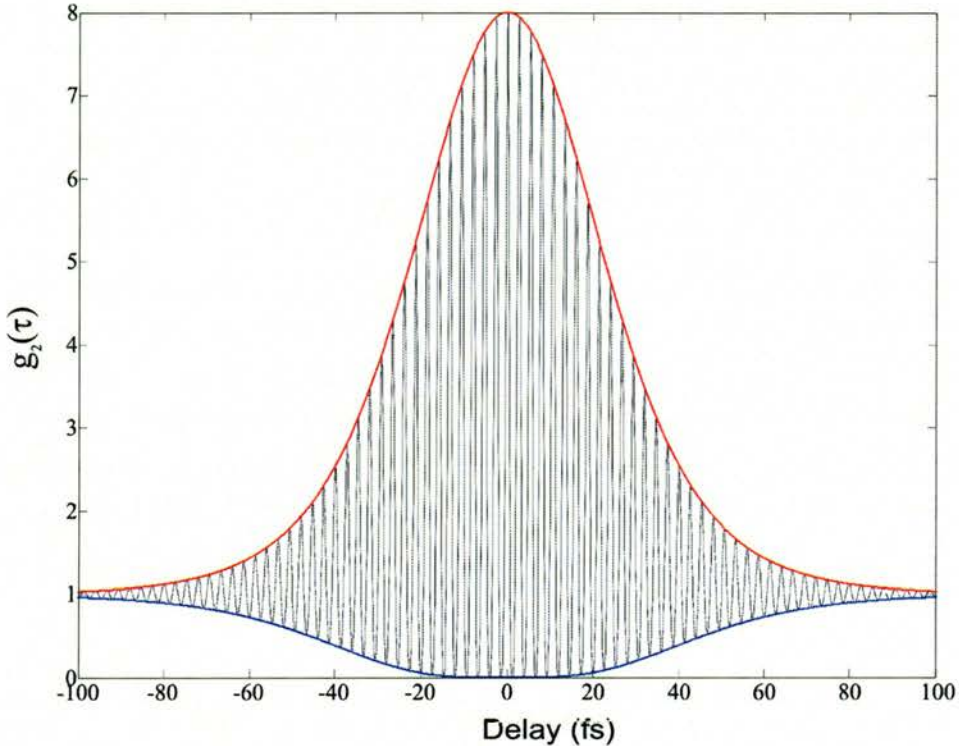


**Figure 2.2** An interferometric autocorrelation trace of a 30fs  $\text{sech}^2$  pulse that is centred at 800nm, where  $G_I$  is the solid black line,  $G_{\mu}$  is the solid red line and  $G_{\beta}$  is the solid blue line[6]

For chirped pulses, the upper and lower envelopes of the interferometric trace will become distorted as the two electric fields will only interfere perfectly when they are exactly overlapped in time ( $\tau=0$ ). Consequently, an interferometric autocorrelation does hold some phase information and attempts have been made to extract phase information from the trace [7]. This technique was found to be difficult and prone to experimental errors and consequently is not often used. More recently, using a technique called PICASO [8] greater success has been achieved into retrieving phase information from these traces. Due to the envelope distortion it is not advisable to infer direct pulse duration values from an interferometric autocorrelation trace.

The interferometric (or fringe resolved) signal can only be experimentally acquired if the entire detection system has a fast enough time response so that the detection signal rise time is faster than the time for the delay to scan through one fringe. If the time response is slower than this, the intensity autocorrelation is recorded. The intensity autocorrelation is a time averaged autocorrelation trace resulting in all of the phase information being removed. The intensity autocorrelation trace can be described as:

$$G_2(\tau) = 1 + \frac{2 \int_{-\infty}^{\infty} I(t)I(t-\tau) dt}{\int_{-\infty}^{\infty} I(t)^2 dt} \quad (2.9)$$

When  $\tau=0$  and  $\pm\infty$  equation (2.9) produces values of 3 and 1 respectively, hence for an intensity autocorrelation a contrast ratio of 3:1 is found

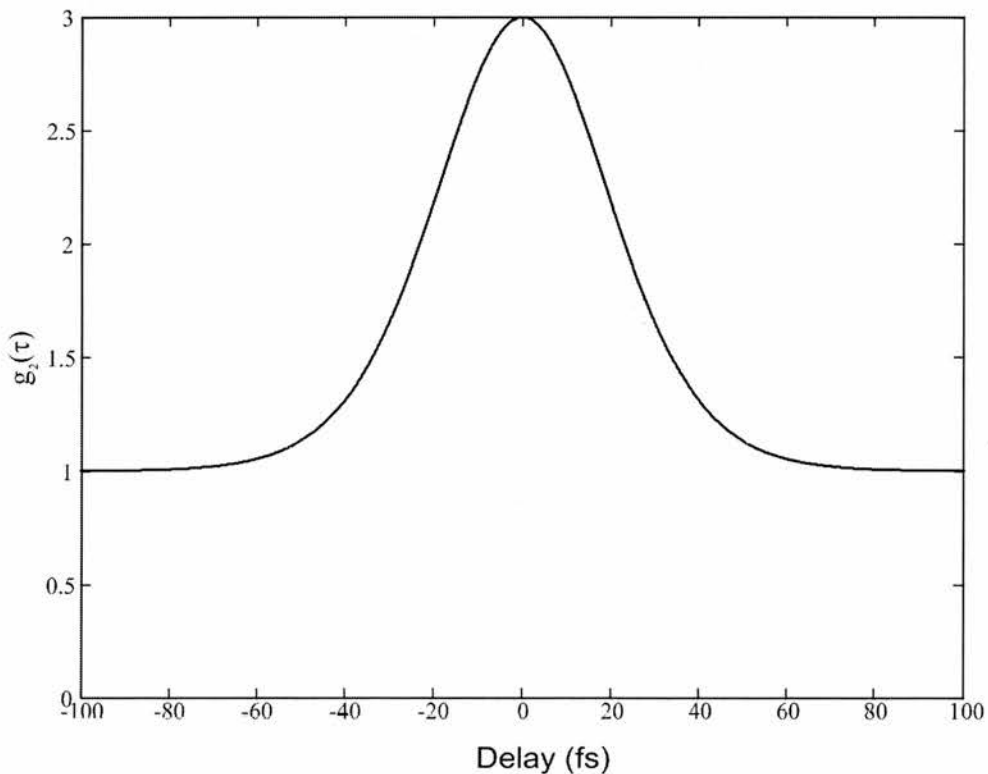


**Figure 2.3** An intensity autocorrelation trace of a 30fs  $\text{sech}^2$  pulse that is centred at 800nm

As the intensity autocorrelation contains no phase information, unlike an interferometric autocorrelation trace, it does not get distorted by the presence of frequency-chirp on the pulse. This makes intensity autocorrelation the preferred technique for pulse duration measurements.

To calculate the pulse duration from the pulse autocorrelation one has to assume a shape for the pulse. The full-width-half-maximum (FWHM) of the pulse autocorrelation is equal to the actual pulse duration multiplied by a conversion factor that depends on the assumed pulse shape and the type of autocorrelation that is used. The FWHM of an autocorrelation trace,  $\Delta t$ , is related to the pulse duration,  $\Delta\tau_p$  by the following expression:

$$\Delta\tau_p = \frac{\Delta t}{k} \quad (2.10)$$

Table 2.1 outlines the values of the conversion factor  $k$  for pulses with a Gaussian ( $e^{-t^2}$ ) and  $\text{sech}^2(t)$  intensity profiles along with their respective pulse duration bandwidth product,  $\Delta\nu\Delta\tau_p$ , of the transform-limited pulse shape.

Pulse profile	Conversion factor $k$		$\Delta\nu\Delta\tau_p$
	<i>Intensity</i>	<i>Interferometric</i>	
Gaussian	1.414	1.697	0.441
$\text{sech}^2$	1.543	1.897	0.315

**Table 2.1** Interferometric and intensity autocorrelation conversion factors with the pulse duration bandwidth product of the transform limited pulse profile

Although intensity autocorrelations do not contain any phase information, researchers have devised extensions of the autocorrelation techniques to extract complete phase information [8-11]. One of the most successful of these techniques is PICASO (Phase and Intensity from Cross correlation And Spectrum Only) [8]. PICASO uses an unbalanced Michelson interferometer to measure the cross correlation between the original pulse and a replica which has passed through a linear element with known dispersive properties. This measurement when combined with the experimentally-measured pulse spectrum, allows the determination of the phase of the pulse. Although the technique works adequately, the retrieval algorithm used to obtain the pulse information is slow and prone to undetectable experimental errors. Consequently the methods described later in this chapter are preferable for complete pulse

characterisation. Third-order autocorrelations[12-15] have also recently been used to try and improve the PICASO characterisation technique [13].

Recent developments have helped to reduce the complexity and expense of typical autocorrelators by using semiconductor devices such as a photodiode or LED [16-20]. If the energy bandgap of the semiconductor is given as  $E_g$ , then under normal circumstances, where photon energies are greater than  $E_g$ , linear absorption occurs producing a linear response with respect to input power. It has, however, been discovered that at sufficiently high intensities where the photon energies are less than  $E_g$  but greater than  $E_g/2$ , a quite efficient two-photon absorption process occurs. Here the current produced from the device has a quadratic response to input intensity. By selecting the correct semiconductor device for a specific wavelength, the two-photon quadratic response is equivalent to the conventional combination of a SHG crystal and a photomultiplier tube. This cheaper method is also ideal for use with ultrashort pulses due to its large bandwidth. This large bandwidth is due to the two-photon process being able to detect photon energies ranging from  $\frac{1}{2}E_g$  to  $E_g$ . Other advantages are that two-photon detection is polarisation insensitive and phasematching is not required. Figure 2.4 shows a low dispersion two-photon autocorrelator designed as part of this research project that is capable of measuring sub 10-fs pulse durations.

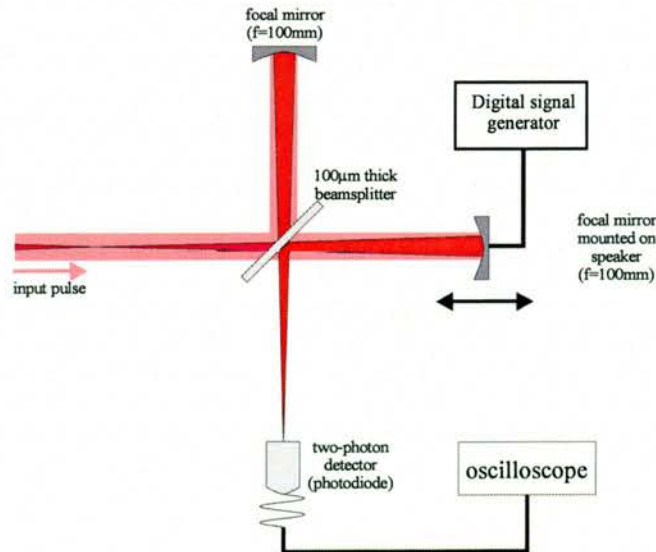


**Figure 2.4** The optical arrangement for the two-photon, low dispersion, autocorrelator

Various semiconductor materials have been used to measure the autocorrelations of ultrashort pulses and table 2.2 summarises some published two-photon absorption autocorrelation results [18].

Device	Measured wavelength ( $\mu\text{m}$ )	Pulse duration measured	Reference
GaN	0.415 – 0.630	80 – 285 fs	[20]
SiC photodiode	0.500 – 0.600	15fs	[17]
ZnSe array	0.8	85 fs	[16]
AlGaAs LED	0.8	90 fs	[19]
SiC photodiode	0.420 – 0.760	90 fs	[21]
GaAs p-i-n waveguide	1.5	150fs	[22]
AlGaAs waveguide	0.8	17.7fs	[23]
ZnSe photoconductive switch	0.8	120 fs	[24]
GaAs, GaP photodiodes	0.8	6 fs, 100 fs	[25, 26]
InGaAs photodiode	2.5 , 3.45	90 fs	[27]
Si photodiode	1.5	1.6 ps	[28]
AlGaAs LED	0.8	90 fs	[19]
InGaAs waveguide	1.55	>50 ps	[29]
GaAs / AlGaAs Quantum well	10.6	3 ps	[30]
GaAs / AlGaAs waveguide	1.06, 1.3	>13 ps	[31]
CsI, CuI photocathode	0.213 – 0.532	>10 ps	[32]
GaAs substrate	0.93	>2.1 ps	[33]
GaAs / AlGaAs waveguide	1.06	88 ps	[34]
Si, GaAsP photodiode	1.06	30 ps	[35]
CdS photocell	1.91		

**Table 2.2** Some published two-photon absorption autocorrelation measurements outlining the device used and pulse measured

Some of the published work outlined in Table 2.2 relied on specially fabricated device that are not readily available. Consequently, table 2.3 lists commercial products than can bought ‘off the shelf’ [18]

Device	Product	Wavelength range (nm)
Si photodiode	FND100 (EG&G)	1100 – 2100
GaAsP photodiode	G1115 (Hamamatsu)	700 - 1400
GaAsP photodiode	G1116 (Hamamatsu)	700 - 1400
AlGaAs LED	564-015 (RS Components)	660 - 1320
InGaAs	G3476-10 (Hamamatsu)	1800 - 3600
GaAs LED	195-344 (RS Components)	950 - 1900
GaAs edge-emitting LED	S86018E	950 – 1900
InGaAsP laser diode	NLK1301CCA (NEL)	1300 – 2600

*Table 2.3 Table of commercially available two-photon detectors*

### 2.3 Techniques allowing the full characterisation of an ultrashort pulse

Surprisingly, before the early 1990's, there was no easy technique that allowed the phase and intensity of a pulse to be measured, and it was only when Trebino's group, in 1993, came up with a technique called Frequency Resolved Optical Gating (FROG) that phase could be successfully measured[36-38] . The years that followed this discovery resulted in a vast array of alternative techniques being devised, some of which are variations of FROG, and some of which rely on totally different processes. All these techniques have various distinctive advantages and disadvantages and have led to much heated debate within the ultrafast community, over which technique is ultimately the best. In fact the truth is that it is not possible to say which single technique is best, because a method that is well-suited for a particular pulse duration and wavelength may not be the best for different pulse parameters. In this section I shall discuss the many various techniques that provide full characterisation, outlining their relative advantages and disadvantages.

So, what exactly does the full characterisation of an ultrashort pulse really mean? Until recently (and for the purposes of the majority of this section), the definition of 'full characterisation' shall refer to techniques that can determine the intensity and phase of the spectral and temporal components of an ultrashort pulse without the need to assume the

temporal pulse shape (as is the case for an autocorrelation measurements). These techniques assume that the phase across the spatial profile of the pulse is constant and are in essence used to perform spatially integrated measurements. Although this type of spatial integration is fair in the majority of applications it is not of course true. Due to nonlinear optical processes and frequency-dependent mode sizes (FDMS's) [39], which can lead to laterally changing spectral content of the beam, spatial distortion is known to occur in some complex broadband amplifier chains and in sub-10 fs Ti:sapphire lasers[40]. With the emergence of techniques that offer spatially resolved amplitude and phase characterisations [41] there is now strong debate among the scientific community over whether the term “full characterisation” should be used exclusively to describe these techniques.

There are two main categories of characterisation techniques that allow determination of the intensity and phase of a pulse. Firstly there are those that work in the time-frequency domain and, secondly, there are the alternatives that rely on interferometry. I shall describe these two approaches in turn, starting with methodologies that work in the time-frequency domain.

### 2.3.1 Methodologies working in the time-frequency domain

Simple techniques such as measuring the pulse spectrum or autocorrelation are constrained in either the frequency or time domain respectively. It is, however, possible to make measurements in both regimes at the same time and this measurement-space is referred to as the time-frequency domain. Millions of musicians around the world are familiar with this approach, the reason being that a musical score is an excellent example of a signal expressed in the time-frequency domain (Figure 2.5).

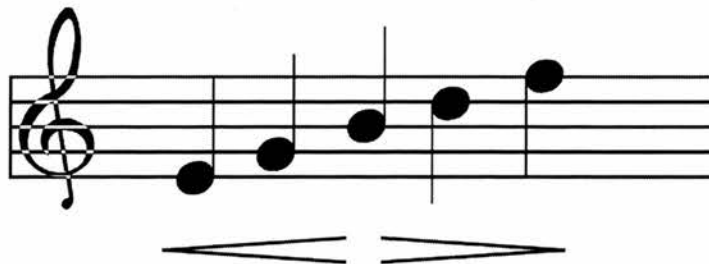


*Figure 2.5 A musical score, an example of working in the time-frequency regime*

The frequency (or wavelength) being played depends on the position of the note within the y-axis. The time at which the note is played is dependent upon the position of the note within the x-axis. Also, how loud this note is played (or intensity) is dependent upon whether the score indicates for example fortissimo (loud, or high intensity) or pianissimo (soft, or low intensity).

A musical score is an example of a spectrogram, and an analogous optical spectrogram can be written as:

$$SP(\omega, \tau) = \left| \int_{-\infty}^{\infty} E(t) G(t - \tau) \exp(-i\omega t) dt \right|^2 \quad (2.11)$$

where  $G(t - \tau)$  is the varying delay gate function so that the spectrogram is simply a set of spectra of gated sections of  $E(t)$  as the delay,  $\tau$ , is varied. Spectrograms are very intuitive to consider because they allow a quick visual determination of which frequencies arrive earliest. An alternative to the optical spectrogram exists so that instead of first gating in time (as in a spectrogram), the frequency is gated first. This is called a sonogram [42-44]:

$$SN(t, \Omega) = \left| \int_{-\infty}^{\infty} E(\omega) G(\omega - \Omega) \exp(-i\omega t) d\omega \right|^2 \quad (2.12)$$

Here,  $G(\omega - \Omega)$  is the varying frequency gate so that a sonogram records the group delay of each frequency component using the frequency filter  $G(\omega)$  followed by a time-resolved measurement of its intensity. This technique is described in much more detail within Chapters 4 and 5.

All measurement techniques that work within the time-frequency domain strive to measure either the spectrogram or sonogram of the pulse. The following few sections describe how this can be done experimentally along with the processes used to extract (or retrieve) pulse information from the spectrogram or sonogram. Much of this thesis describes time-frequency techniques, and consequently a detailed introduction is provided here.

### 2.3.1.1 Frequency Resolved Optical Gating (FROG)

Until as late as 1993, the problem of how to determine the phase of a pulse had yet to be tackled satisfactorily or reliably. It was only when, in 1993 that Trebino and co-workers developed a technique called Frequency Resolved Optical Gating (FROG) [36-38, 45] that the possibility of phase measurement was realised. FROG is a technique that makes it possible to record experimentally the pulse spectrogram. It does this by spectrally resolving the signal beam produced by any second-harmonic or frequency-mixing autocorrelation measurement. As there are several beam geometries capable of performing autocorrelation measurements, there are consequently many different FROG varieties, each of which has its own distinct advantages and disadvantages. All of these techniques allow the experimental determination of the pulse spectrogram.

### Polarisation-gate FROG (PG-FROG)

Polarisation-gate FROG relies on the optical Kerr effect, a third-order susceptibility (see Chapter 1). The intensity of a pulse is split into two equal parts. The first part, called 'the probe' passes through a polariser, while the second, called the 'gate' is sent through a half wave-plate to provide a  $\pm 45$  degree linear polarisation with respect to that of the probe. The two beams are then spatially recombined with one another within a material that has a very fast third-order susceptibility such as fused silica. The probe then passes through a polariser or analyser which is oriented so that it prevents transmission of the probe (ie crossed with respect to the first polariser). Under normal circumstances no light will pass through the analyser but as the gate is scanned in delay and the probe and gate overlap temporally (as well as spatially), the intensity of the gate pulse can be sufficient within the fused silica to induce a birefringence thereby allowing some of the probe intensity to be transmitted through the analyser to be detected. As the gate is scanned in delay a measurement of transmitted intensity versus delay can be recorded to yield an autocorrelation. By inserting a spectrometer after the polariser, the light passed through the analyser can be spectrally resolved with respect to

delay and thus the PG-FROG trace can be generated. Figure 2.6 shows the schematic of the PG-FROG setup.

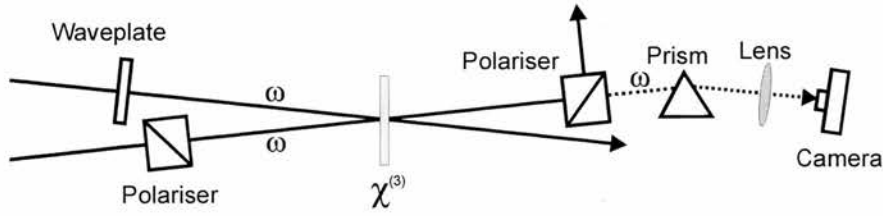


**Figure 2.6** Schematic representation of the PG FROG optical setup

The PG-FROG trace can be described mathematically by the following expression:

$$I_{FROG}^{PG}(\omega, \tau) = \left| \int_{-\infty}^{\infty} E(t) |E(t - \tau)|^2 \exp(-i\omega t) dt \right|^2 \quad (2.13)$$

PG-FROG offers many advantages, the first of which is that traces generated using PG-FROG are very intuitive and accurately reflect the pulse frequency versus time. This, as will be evident later, is not always the case with FROG traces. There are also no ambiguities in the trace such that a PG-FROG trace yields a complete pulse characterisation and, because it uses third order nonlinearities, no phase matching is required making the optical setup and alignment relatively simple.

Disadvantages with this technique include the need for very high quality and thus expensive polarisers. Even using high quality polarisers, a PG-FROG trace will suffer some polariser-leakage background noise[46]. The need for polarisers also means that the pulse must travel through a substantial amount of glass before it is measured. For longer pulses this is not a problem, but as the pulse duration is reduced material dispersion in the polarisers causes the pulse to distort dramatically. Although this effect can be taken into account it is not ideal and other FROG techniques are better suited for characterising ultrashort femtosecond pulses. The shortest ever pulse measured using PG-FROG was 30fs [47] and this used a thin-film polariser to avoid these effects of material dispersion. Another consequence of having to pass

through a large amount of glass in the polarisers is that it makes PG-FROG not suitable for measurement of ultra violet pulses.

### Second-harmonic-generation FROG (SHG-FROG)

SHG-FROG[36, 38, 48-51], as the name suggests uses the same autocorrelation geometry described earlier (section 2.2) for a SHG-autocorrelator. The identical optical arrangement can be used as in the SHG autocorrelator except that instead of using a photomultiplier to detect the frequency-doubled light, a spectrometer in conjunction with a CCD array is used to spectrally resolve the frequency-doubled light at various time-delay positions.

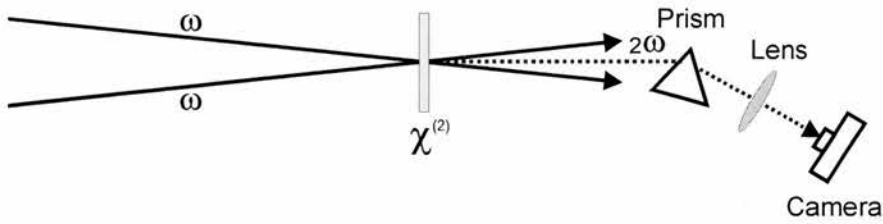


**Figure 2.7** Schematic representation of the SHG-FROG optical setup

The SHG-FROG trace can be described mathematically by the following expression:

$$I_{FROG}^{SHG}(\omega, \tau) = \left| \int_{-\infty}^{\infty} E(t) E(t - \tau) \exp(-i\omega t) dt \right|^2 \quad (2.14)$$

which illustrates (see equation (2.11)) that in SHG-FROG the gating pulse is identical to the probe pulse.

There are many advantages associated with SHG-FROG that make it the most commonly used FROG technique. The main advantage is that, with the exception of methods using cascaded second-order nonlinearities [52], SHG-FROG is the only FROG technique that relies on second-order nonlinearities, making SHG-FROG very sensitive. Also, SHG-FROG unlike PG-FROG introduces very little material dispersion, especially since material dispersion after the doubling crystal does not affect the measurement because the spectral rather than temporal characteristics are recorded. This characteristic makes SHG-FROG ideal

for the measurement of very short pulses where material dispersion needs to be kept to a minimum. One criterion that must be seriously considered when contemplating measuring ultrashort pulses with SHG-FROG is to ensure that the SHG crystal will have sufficient bandwidth to allow frequency doubling of the entire bandwidth of the pulse. This problem is caused by phase mismatch within the crystal and is described more detail in section 6.2. This phase shift is reduced by minimizing the interaction length (ie. reduce crystal thickness). The SHG crystal bandwidth is inversely proportional to the crystal thickness, thus the shorter the measured pulse, the thinner the SHG crystal must be so that the measurement of sub 10 fs pulses typically requires a  $\sim 10 \mu\text{m}$  thick SHG crystal [53]. The use of such a thin crystal reduces the peak conversion that could be achieved with longer crystals and thus the sensitivity is drastically reduced. When the crystal is too thick, the spectrum recorded at each delay position will become narrower than it should be, resulting in the FROG trace becoming distorted. There are simple techniques described later in chapter this (section 2.3.1.3) that ensure systematic errors such as these are detected.

Recently, progress has been made to develop a technique that addresses the SHG crystal bandwidth problem [54]. The technique uses a thick SHG crystal which, in a normal SHG-FROG setup there would be insufficient bandwidth to successfully record an SHG-FROG trace (a 1mm thick BBO crystal is used to measure 70fs). However O'Shea et al point out that *only the phase-matching bandwidth integrated over the measurement period need exceed the pulse bandwidth*. This statement is actually saying that in a multishot measurement, only a fraction of the pulse spectrum needs to be phase matched in one shot, as long as the remaining portion of the pulse spectrum achieves phase-matching on other shots during the measurement. Phase matching across all parts of the pulse spectrum is achieved by angling the crystal such that by angle-dithering the crystal the effective phase-matching bandwidth is increased. An advantage of this technique is that the crystal can be thicker so that the SHG efficiency is greatly enhanced and this yields a significantly greater signal strength.

The requirement for phase matching has already been discussed but there are other disadvantages associated with SHG-FROG. Unlike PG-FROG, SHG-FROG has a number of ambiguities, the main one being in the direction of time. The pulse,  $E(t)$ , and its time reversed phase-conjugate replica  $E^*(-t)$ , both yield the same SHG-FROG trace. This has the effect of making the SHG-FROG trace symmetrical with respect to delay and thus making it very unintuitive to look at. As a consequence of this, the sign of chirp on the pulse cannot be determined.

### Self-diffraction FROG (SD-FROG)

SD-FROG was the first ever demonstration of frequency resolved optical gating [38]. The technique used is similar to PG-FROG in that it uses the optical Kerr effect to provide the process of optical gating. In SD-FROG no polarisers are used so that the two beams interacting within the third-order nonlinear medium have the same polarisation. This has the effect of generating a sinusoidal intensity pattern that constitutes a grating within the material. By spectrally resolving one of these diffracted beams, a SD-trace can be produced.

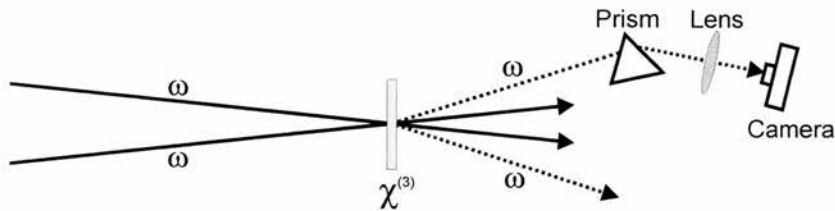


**Figure 2.8** Schematic representation of the SD-FROG optical setup

The SD-FROG trace can be described mathematically by the following expression:

$$I_{FROG}^{SD}(\omega, \tau) = \left| \int_{-\infty}^{\infty} E(t)^2 E(t - \tau)^* \exp(-i\omega t) dt \right|^2 \quad (2.15)$$

The absence of polarisers has enabled SD-FROG to measure deep UV pulses successfully in a single shot regime [55]. SD-FROG is, unfortunately, very susceptible to phase mismatch and

as phase mismatch is highly dependent upon frequency and because ultrashort pulses have a wide frequency bandwidth, SD-FROG is not suited for pulses that have durations below 100fs.

### Transient-gating FROG (TG-FROG)

TG-FROG [56] is a more recent FROG based geometry with which the advantages associated with PG-FROG and SG-FROG can be maintained while eliminating their respective disadvantages. TG-FROG uses a three-beam geometry shown below in Figure 2.9

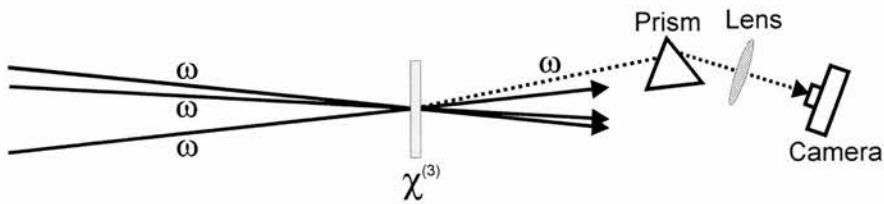


*Figure 2.9 Schematic representation of the TG-FROG optical setup*

Two beams are used to create the refractive index grating (as in SD-FROG) by being overlapped temporally and spatially within the nonlinear medium. The third beam is scanned temporally while passing through the refractive index grating created by the other two beams. The diffracted fourth output beam is detected and spectrally resolved to produce the TG-FROG trace. Figure 2.10 shows the most common optical arrangement used for this technique, known as the BOXCARS arrangement.

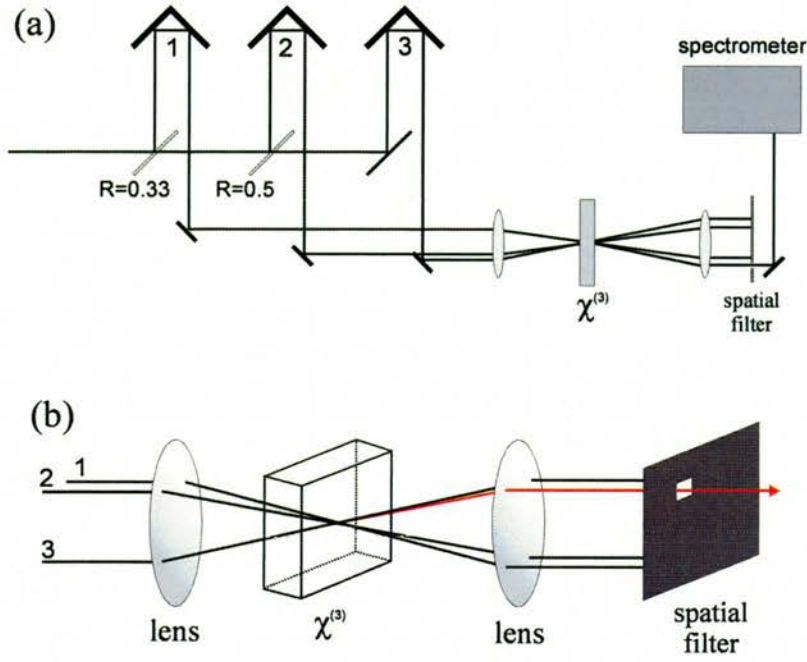


**Figure 2.10** (a) the BOXCARS arrangement for TG-FROG with (b) 3-D interpretation of the beam geometries

The mathematical expression describing TG-FROG is dependent upon which one of the three beams is varied in time. When pulse 2 (in Figure 2.10) is delayed relative to pulses 1 and 3 the expression is given as:

$$E_{sig}^{TG1}(t, \tau) = E_1(t) E_2^*(t - \tau) E_3(t) \quad (2.16)$$

As it is known that all three pulses are identical (ie  $E_1 = E_2 = E_3$ ), the expression can be reduced to give:

$$E_{sig}^{TG1}(t, \tau) = E(t)^2 E^*(t - \tau) \quad (2.17)$$

Equation (2.17) is exactly the same as the SD-FROG signal electric field and consequently results in the identical trace. If pulse 1 or pulse 3 (in figure 2.10) is used as the temporally varying pulse the signal electric field becomes identical to that of PG-FROG (with a reversed sign of delay):

$$E_{sig}^{TG2} = E(t) |E(t + \tau)|^2 \quad (2.18)$$

So, in essence, TG-FROG can produce what is equivalent to a PG-FROG trace but with the advantage of not requiring any polarisers. This allows TG-FROG to be used to measure much

shorter pulses and pulses that have wavelengths in the deep-UV. TG-FROG, unlike PG-FROG, yields a background free signal, making it a much more sensitive technique. Unlike SD-FROG, TG-FROG is phase matched so that long interaction lengths can be used, resulting in enhanced signal strengths, this therefore helps TG-FROG to also be more sensitive than SD-FROG.

### Third-harmonic-generation FROG (THG-FROG)

In THG FROG, yet another third-order nonlinearity process has been used successfully to obtain a FROG trace [57]. Usually third harmonic generation is an extremely weak process but it is found that by spatially overlapping the pulses at an air-dielectric interface, the normally weak THG process becomes much stronger; this is known as surface third-harmonic generation (STHG) [58].

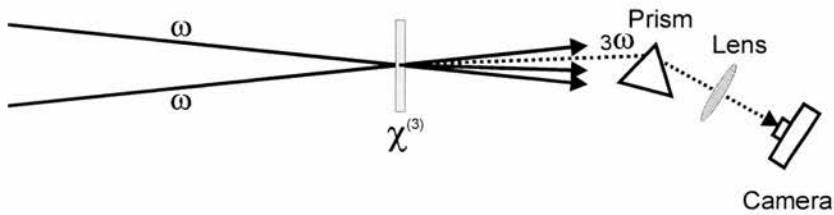


**Figure 2.11** Schematic representation of the THG-FROG optical setup

The THG-FROG trace can be described mathematically by the following expression:

$$I_{FROG}^{THG}(\omega, \tau) = \left| \int_{-\infty}^{\infty} E(t)^2 E(t - \tau) \exp(-i\omega t) dt \right|^2 \quad (2.19)$$

THG-FROG is by far the most sensitive of the third-order FROG techniques and along with SHG-FROG is the only FROG technique capable of characterising pulses directly from an oscillator (ie. unamplified pulses). An advantage of THG-FROG is that because the interaction is localised at the surface of a material, the conversion bandwidth is very large, making it viable for measurement of very short pulses. THG-FROG traces are not as intuitive as other third-order techniques although they do have slight asymmetry that can distinguish between whether the pulse has negative or positive chirp.

### 2.3.1.2 Other techniques deriving from FROG

Described in section 2.3.1.1 are the ‘normal’ FROG geometries that exist and have been demonstrated experimentally. There are also a subset of characterisation techniques that, although based on the FROG technique, vary slightly in operation, making it either simpler to measure a FROG trace or making it possible to measure pulses that would otherwise be thought impossible with more traditional techniques. In this section some of these techniques will be highlighted.

#### GRENOUILLE

Researchers involved with pulse characterisation schemes seem to have an unofficial competition to see who can come up with the most intriguing acronyms for new characterisation techniques. This is certainly the case for GRENOUILLE (the French word for frog) which is an acronym for GRating-Eliminated No-nonsense Observation of Ultrafast Incident Laser Light E-fields !!!!!. Yes, it is a daft name, however the technique that it describes a quite logical extension to FROG.

GRENOUILLE is a new SHG-FROG optical arrangement that provides a much-simplified way of obtaining a trace. The optical arrangement (Figure 2.12) consists of only 6 optical elements, three cylindrical lenses, a Fresnel biprism, a SHG crystal and a CCD camera.

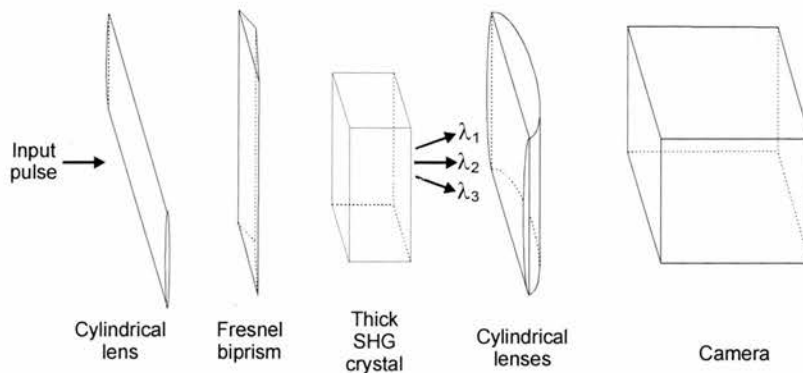


**Figure 2.12** The GRENOUILLE optical arrangement consisting of a few cylindrical lenses, CCD camera, fresnel biprism and a thick SHG crystal

The first thing to notice in the optical arrangement is that there is no scanning delay line or spectrometer. The delay line has been replaced by a Fresnel biprism. This simple optical component separates the beam into two separate beams and recombines them at an angle within the crystal, resulting in the delay of the pulse being mapped horizontally across the crystal. This in turn can then be imaged across the horizontal axis of the camera. The frequency-resolving component is in fact the SHG crystal. Phase-mismatch (section 6.2) is normally a problem as it restricts the frequency bandwidth of the crystal thus requiring thin crystals for the measurement of ultrashort pulses. In GRENOUILLE, this is an advantage, because the crystal acts as a wavelength filter so that the wavelength achieving the phase-matching criteria varies linearly with crystal incidence angle. By focussing in the vertical plane, a large divergence is achieved, so that when a couple of Fourier-transforming lenses are aligned with the SHG crystal being placed within the Fourier plane, a map of wavelength can be imaged in the vertical plane of the CCD camera.

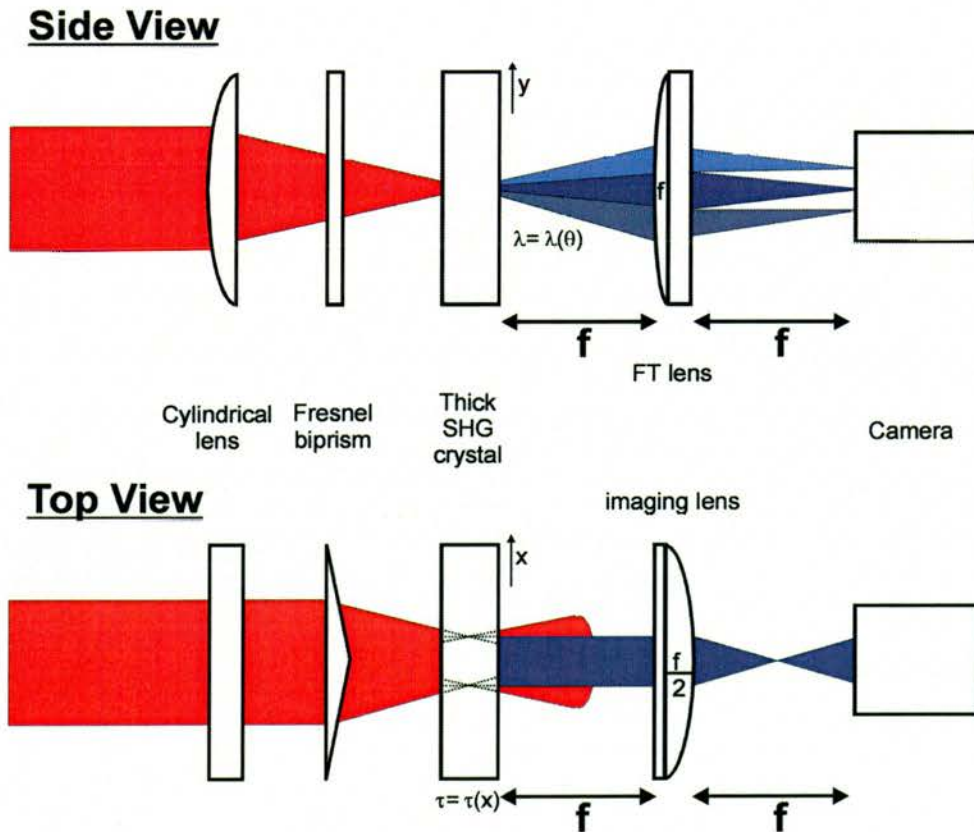


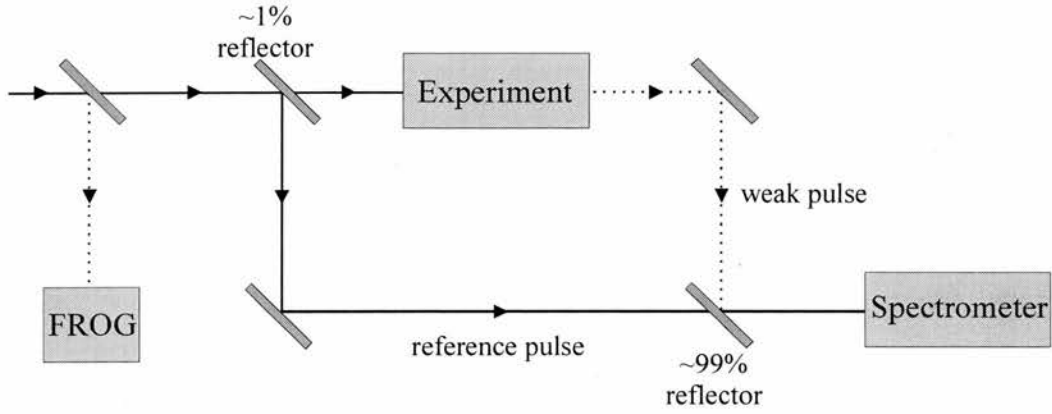
Figure 2.13 The side and top geometries of the GRENOUILLE optical arrangement

Figure 2.13 helps clarify how the frequency (side view) and temporal (top view) components are resolved. A  $f/2$  cylindrical lens is used in the horizontal axis so that any fundamental light could be filtered out at the line focus using a vertical slit.

Obviously the main advantage of GRENOUILLE is its simplicity because the ease of alignment makes the technique extremely attractive. Also, the use of a thick SHG crystal dramatically increases the output signal power and makes GRENOUILLE an extremely sensitive technique. Although measurement of 100fs pulses has been demonstrated, the measurement of shorter pulses would need to consider carefully the thickness of the crystal. If the crystal was too thick then group velocity dispersion would start distorting the pulse being measured and this is obviously undesirable. Other disadvantages include the limited flexibility of the GRENOUILLE setup. The delay across the crystal is solely dependent upon the Fresnel biprism such that, if the pulse was to dramatically change in duration or chirp, there will either be insufficient or too large delay so that resolving the pulse on the CCD camera would become a challenge. To solve the problem, the Fresnel Biprism would need to be replaced and the calibration would need to be repeated.

## TADPOLE

TADPOLE (Temporal Analysis by Dispersing a Pair Of Light E-fields) is a pulse characterisation technique capable of measuring pulses with tiny energies (zeptojoules ( $10^{-21}$ -J)) [59]. The technique relies on the assumption that a pulse with a small intensity will have originated from a more intense source. Using FROG, the more intense pulses can be fully characterised and used as a reference pulse for spectral interferometry [60]. Spectral interferometry consists of measuring the spectrum of the sum of a reference pulse and an unknown pulse. By fully characterising the reference pulse (using FROG) there is sufficient information to determine the unknown pulse.



**Figure 2.14** Optical arrangement TADPOLE, used for the measurement of extremely weak ultrafast pulses

TADPOLE is also an excellent method for the measurement of pulses that have complex shapes. To measure such pulses using traditional FROG techniques requires long traces and thus takes time for the pulse information to be retrieved. The use of TADPOLE applies only to the characterisation of a simple smooth pulse and a single spectra. A restriction to this technique is that the reference pulse must have a broader spectrum that is centred at the same wavelength as the measured pulse.

There is a further derivative of TADPOLE called POLIWOG (POLARISED Light Interference versus Wavelength of Only a Glint) [61] that is also able to time resolve the polarisation state of very weak ultrashort pulses.

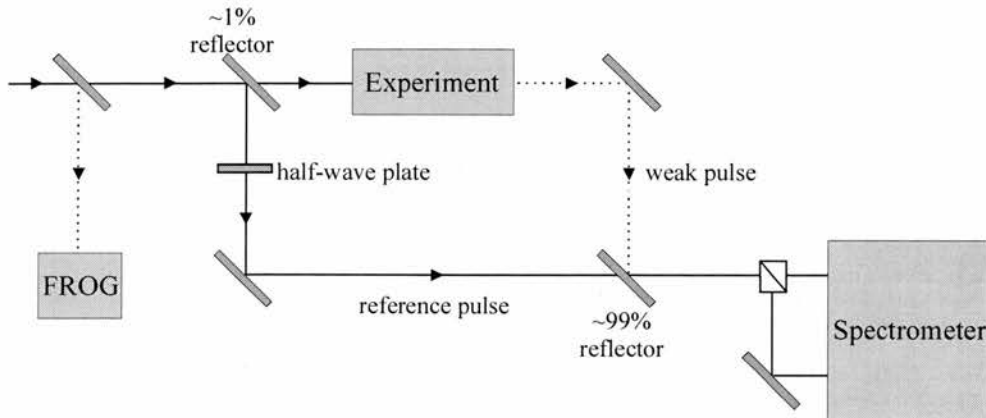


**Figure 2.15** Optical arrangement POLIWOG

The reference pulse is linearly polarised at  $45^\circ$  so it has equal x and y components. Once recombined with weak pulse, these are passed through a polariser cube so that the horizontal and vertical polarisation states are separated. The spectra of both beams are then measured and have the form:

$$I_{SI}^i(\omega) = I_{sig}^i(\omega) + I_{ref}^i(\omega) + 2\sqrt{I_{sig}^i(\omega)}\sqrt{I_{ref}^i(\omega)}\cos[\phi_{sig}^i(\omega) - \phi_{ref}^i(\omega) - \omega\tau] \quad (2.20)$$

where  $I_{sig}^i(\omega)$  and  $I_{ref}^i(\omega)$  are the spectra and  $\phi_{sig}^i(\omega)$  and  $\phi_{ref}^i(\omega)$  are the phases of the signal and the reference pulses respectively. Since both the amplitude and phase of the reference pulse are known, by using one of several fringe inversion routines, the signal pulse information for both polarisation states can be gained [62].

## TREEFROG

TREEFROG[63] (Twin Recovery of Electric-field Envelopes by use of FROG) is a technique capable of simultaneously measuring two separate pulses that have different phase but identical spectra. All previously mentioned FROG techniques use the pulse to gate itself so that the autocorrelation is frequency resolved. TREEFROG uses a different pulse as the gate function so that the cross-correlation and not the autocorrelation is frequency resolved. The SHG version of TREEFROG can be described mathematically as:

$$I_{TREEFROG}(\omega, \tau) = \left| \int_{-\infty}^{\infty} E_p(t) E_g(t - \tau) \exp(-i\omega t) dt \right|^2 \quad (2.21)$$

where  $E_p$  and  $E_g$  are the two separate pulses that are to be measured (called probe and gate).

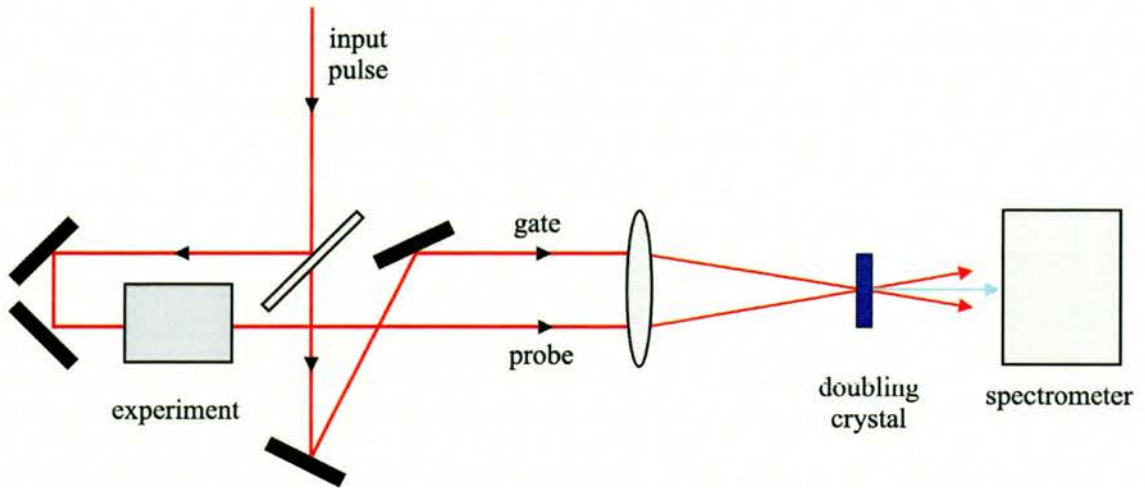


**Figure 2.16** Optical arrangement of TREEFROG

At first, the problem of obtaining the characteristics of both pulses, without initial knowledge of either pulse seems insurmountable. This problem was already solved within the area of image science where a technique was available which allowed one to extract the image and an unknown blurring function from a blurred image. This method is known as two-dimensional blind deconvolution [64] and is described in more detail in section 2.3.1.3. Using this technique, TREEFROG can successfully characterise both the gate and probe pulse.

### **Cross-FROG (X-FROG)**

X-FROG[65] is closely related to TREEFROG so that instead of using the same pulse as the gate function (as in FROG), two separate pulses are used as the gate and probe. The difference between the two techniques is that X-FROG can use two pulses that have differing phase AND spectra. Using sum-frequency mixing [63] or difference-frequency mixing [66] of the two pulses, the resulting cross-correlation is spectrally resolved to yield the X-FROG trace.

X-FROG was first developed to be an alternative to TADPOLE to avoid the need for spectral interferometry. It used to be the case that both techniques required a fully characterised reference pulse for the unknown pulse to be successfully retrieved. By using an algorithm

similar to that used in TREEFROG, it has recently been demonstrated that X-FROG does not need any prior knowledge of either of the pulses for both to be successfully retrieved [67]. In this demonstration, a  $4\mu\text{m}$  mid-IR pulse from an Optical Parametric Oscillator (OPO) was characterised by mixing with the  $770\text{nm}$  OPO pump pulses.

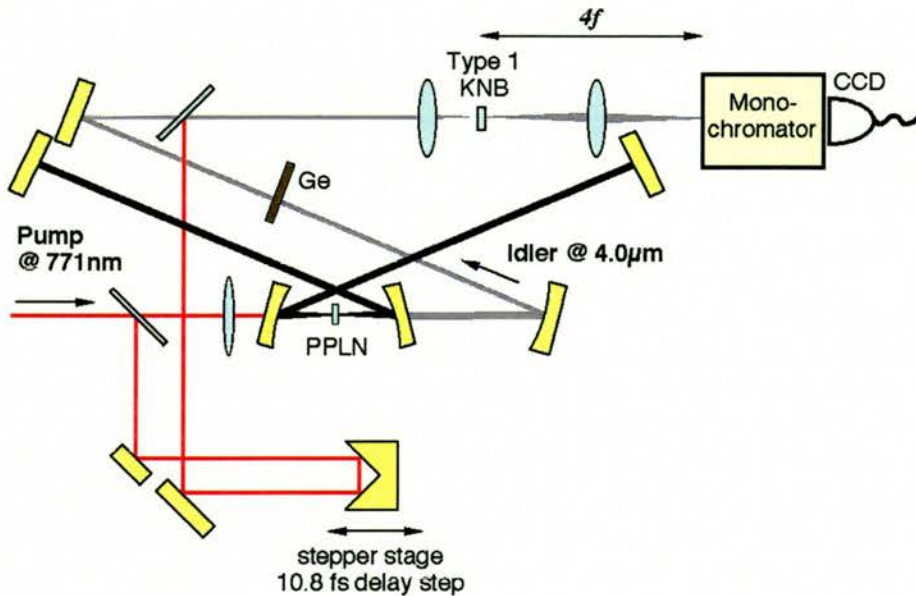


*Figure 2.17 The optical setup used to characterise two unknown pulses using XFROG [67]*

The fundamental advantage of X-FROG is its capability to fully characterise weak ultrashort pulses in the mid-IR [67] and deep UV [66] spectral regions.

### 2.3.1.3 The retrieval of FROG traces

So far we have discussed the various techniques that are capable of experimentally acquiring a time-frequency trace of a pulse (or pulses). Although some of these traces are fairly intuitive and one can approximate the chirp of a pulse, there is a need to utilise the trace to obtain an accurate characterisation of the pulse. At first, the problem of extracting data from a FROG trace seems to be intractable and, although the first time-frequency measurement was taken in 1971 by Treacy [44] it wasn't until 1993 when Trebino's group successfully devised a technique capable extracting pulse information from a spectrogram [36-38, 45] that time-frequency characterisation techniques became established, and the rest as they say is history.

Many retrieval algorithms have been developed to extract the pulse characteristics of a spectrogram or sonogram [36, 37, 68-73]. Over recent years, one specific technique has become the standard algorithm due to its fast computation speed and robustness and this technique is referred to as Principal Component Generalised Projections (PCGP) [71, 72, 74]. PCGP will be the technique used throughout this thesis and so a detailed description of the technique is necessary.

The overall aim of the retrieval algorithm is to find the form of the complex function  $E(t)$  or more generally  $E_{sig}(t, \tau)$ . The term  $E_{sig}(t, \tau)$  is the complex amplitude of the signal field and must satisfy two separate equations, or constraints, for it to be correct. The first constraint is that the Fourier transform of  $E_{sig}(t, \tau)$  must have an intensity equal to the experimentally measured trace which is given (for FROG) as:

$$I_{FROG}(\omega, \tau) = \left| \int_{-\infty}^{\infty} E_{sig}(t, \tau) \exp(-i\omega t) dt \right|^2 \quad (2.22)$$

Equation (2.22) is known as the intensity constraint. The other constraint is the mathematical form of the signal field produced when two identical pulses are combined within a nonlinear material. This is known as the physical constraint and can be described in a more generalised form of:

$$E_{sig}(t, \tau) = E(t) \Gamma[E(t - \tau)] \quad (2.23)$$

where  $E(t)$  is the probe and  $\Gamma[E(t - \tau)]$  is the gate function. The gate function is dependent upon the type of FROG geometry that was used. Table 2.4 summarises the mathematical expression for the signal field for a number of FROG geometries.

Version of FROG	$E_{sig}(t, \tau)$
PG FROG or TG FROG	$E(t) E(t-\tau) ^2$
SD-FROG or TG FROG	$E(t)^2 E^*(t-\tau)$
SHG FROG	$E(t)E(t-\tau)$
THG FROG	$E(t)^2 E(t-\tau)$

**Table 2.4** The mathematical form of the signal field  $E_{sig}(t, \tau)$  for various FROG geometries

The measured FROG trace  $I_{FROG}(\omega, \tau)$  is of course a real quantity meaning that there is no phase information present. The aim of the algorithm is therefore to determine this phase by minimising the difference between the measured FROG trace and the FROG trace calculated from the current pulse  $E(t)$ . By combining equations (2.22) and (2.23) we get the following expression that needs to be solved

$$\sqrt{I_{FROG}(\omega, \tau)} = \int_{-\infty}^{\infty} E(t) \Gamma[E(t-\tau)] \exp(-i\omega t) dt \quad (2.24)$$

All spectrogram/sonogram retrieval algorithms use the same general technique, shown in Figure 2.18

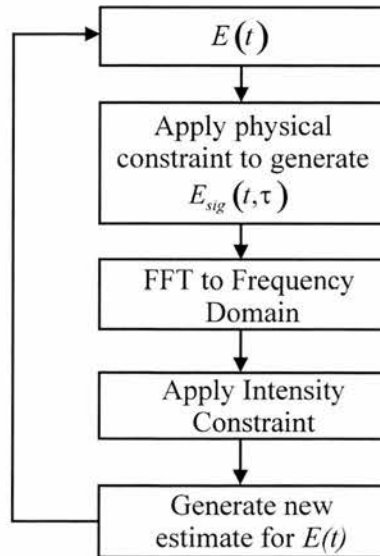


**Figure 2.18** The generalised technique for retrieval algorithms

An iterative process is carried out so that after each iteration there is an improved match between the measured and calculated FROG trace. After an initial guess of  $E(t)$  is made, the guess value of  $E_{sig}(t, \tau)$  is calculated. By taking the Fourier transform the calculated FROG trace is obtained ie.  $\sqrt{I_{calc}(\omega, \tau)}\phi_{calc}(\omega, \tau)$ . The square root of the measured FROG trace ( $\sqrt{I_{FROG}(\omega, \tau)}$ ) is then substituted for the calculated intensity. The whole procedure is now reversed so that a new value of  $E(t)$  is calculated from  $\sqrt{I_{FROG}(\omega, \tau)}\phi_{calc}(\omega, \tau)$ . It is this final minimisation procedure for determining a value of  $E(t)$  for which  $E_{sig}(t, \tau)$  is closest to  $\sqrt{I_{FROG}(\omega, \tau)}\phi_{calc}(\omega, \tau)$  that differs between the various algorithms and this is where the technique of PCGP comes into its own.

### Principal component generalised projections (PCGP)

All previous retrieval algorithms before PCGP were developed to assume that the gate was related to the probe pulse. PCGP [71, 72, 74] does not assume this and instead, as with TREEFROG, assumes that the gate is entirely independent of the probe. This is referred to as a blind-deconvolution algorithm [63] so that  $I_{FROG}(\omega, \tau)$ , known as the blind-FROG trace becomes:

$$I_{FROG}(\omega, \tau) = \left| \int_{-\infty}^{\infty} E(t)G(t-\tau)\exp(-i\omega t) dt \right|^2 \quad (2.25)$$

where  $G(t-\tau)$  is the gate function and  $E(t)$  is the probe. By having two unknowns (the gate and probe) initial thoughts would suggest that it would be harder to retrieve than only having a single unknown as is the case when you assume the gate and probe are identical. This is in fact not true and instead makes thing more straight forward.

At any time interval  $\tau$ , the blind-FROG trace is the intensity spectrum of the product of the gate and probe and the trace is obtained when the whole gate is scanned in time across the

gate  $E(t)$ . By sampling the intensity spectrum at differing values of  $t$  with a constant spacing of  $\Delta t$ , a vector representation of the gate and the probe can be obtained:

$$E_{Probe} = \left[ E\left(-\frac{N}{2}\Delta t\right), E\left(-\left(\frac{N}{2}-1\right)\Delta t\right), E\left(-\left(\frac{N}{2}-2\right)\Delta t\right), \dots, E\left(\left(\frac{N}{2}-1\right)\Delta t\right) \right] \quad (2.26)$$

$$E_{Gate} = \left[ G\left(-\frac{N}{2}\Delta t\right), G\left(-\left(\frac{N}{2}-1\right)\Delta t\right), G\left(-\left(\frac{N}{2}-2\right)\Delta t\right), \dots, G\left(\left(\frac{N}{2}-1\right)\Delta t\right) \right] \quad (2.27)$$

where  $N$  is the length of the vector. To simply things somewhat Equations (2.26) and (2.27) can be reduced to the following

$$E_{Probe} = [E_1, E_2, E_3, \dots, E_N] \quad (2.28)$$

$$E_{Gate} = [G_1, G_2, G_3, \dots, G_N] \quad (2.29)$$

A matrix, referred to as the outer product form can now be created which consists of all conceivable products of the gate and probe:

$$O = \begin{bmatrix} E_1G_1 & E_1G_2 & E_1G_3 & E_1G_4 & \cdots & E_1G_N \\ E_2G_1 & E_2G_2 & E_2G_3 & E_2G_4 & \cdots & E_2G_N \\ E_3G_1 & E_3G_2 & E_3G_3 & E_3G_4 & \cdots & E_3G_N \\ E_4G_1 & E_4G_2 & E_4G_3 & E_4G_4 & \cdots & E_4G_N \\ \vdots & \vdots & \vdots & \vdots & \cdots & \vdots \\ E_NG_1 & E_NG_2 & E_NG_3 & E_NG_4 & \cdots & E_NG_N \end{bmatrix} \quad (2.30)$$

As all the products of the gate and probe are held within the matrix, the time domain FROG trace can be formed by simple matrix manipulation. This process can then be reversed to get back to the outer product form. By shifting each row along in incremental steps, a new matrix is formed where columns are made up from gate and probe products that have equal temporal delay:

$$\begin{bmatrix} E_1 G_1 & E_1 G_2 & E_1 G_3 & \cdots & E_1 G_{N-2} & E_1 G_{N-1} & E_1 G_N \\ E_2 G_2 & E_2 G_3 & E_2 G_4 & \cdots & E_2 G_{N-1} & E_2 G_N & E_2 G_1 \\ E_3 G_3 & E_3 G_4 & E_3 G_5 & \cdots & E_3 G_N & E_3 G_1 & E_3 G_2 \\ E_4 G_4 & E_4 G_5 & E_4 G_6 & \cdots & E_4 G_1 & E_4 G_2 & E_4 G_3 \\ \vdots & \vdots & \vdots & \vdots & \vdots & \vdots & \vdots \\ E_N G_N & E_N G_{N+1} & E_N G_{N+2} & \cdots & E_N G_{N-3} & E_N G_{N-2} & E_N G_{N-1} \end{bmatrix} \quad (2.31)$$

$$\tau = 0 \quad \tau = -\Delta t \quad \tau = -2\Delta t \quad \cdots \quad \tau = 3\Delta t \quad \tau = 2\Delta t \quad \tau = \Delta t$$

By permutating the columns so that  $\tau$  increments from negative to positive, the matrix becomes in essence  $E_{sig}(t, \tau)$ . Taking the magnitude of the Fourier transform of this matrix yields the FROG trace. Figure 2.19 helps outline graphically the procedure for getting from the initial guess of  $E(t)$  to the production of the FROG trace

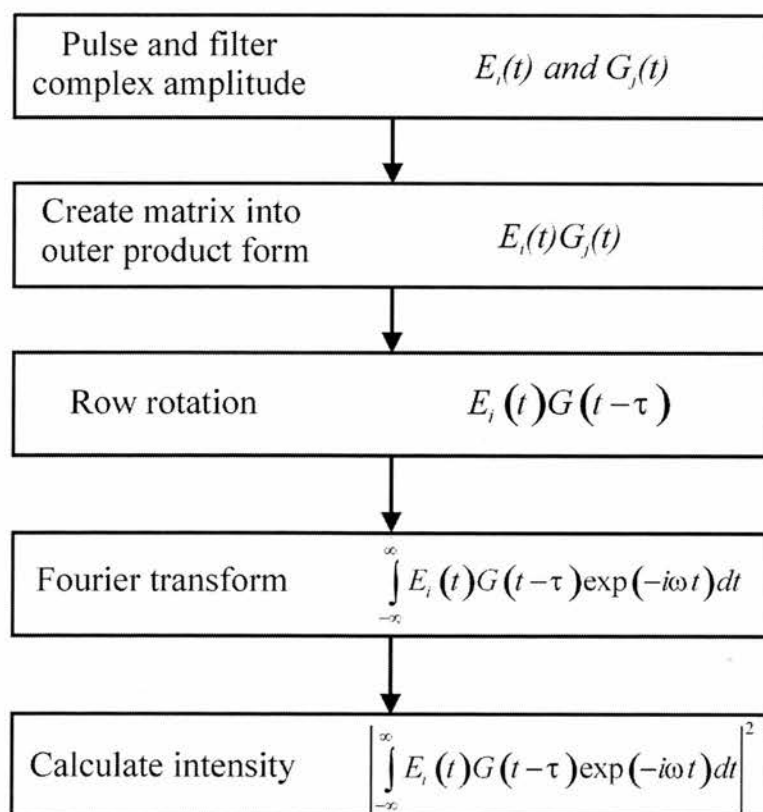


Figure 2.19 Procedure for generating FROG trace using the PCGP

The magnitude of the generated FROG trace can now be replaced with that of the square root of the magnitude of the experimentally acquired FROG trace. The procedure in Figure 2.19 is then reversed so that using an inverse Fourier transform a time-domain spectrogram is created; the row rotation is then applied to get back to the outer product. Values of the gate and probe now need to be extracted from this matrix. This can be achieved very elegantly by using a singular value decomposition (SVD). Even though many routines already exist in software libraries to carry out SVD, the procedure is very computationally intensive and time consuming. A less time consuming technique is to reduce the SVD step to a low-overhead and fast matrix-vector multiples [71, 72, 75] whereby the next guess for the pulse is gained from multiplying the previous guess pulse by the outer product matrix and its transpose so that:

$$E_{new} = E_{old}OO' \quad (2.32)$$

$$G_{new} = G_{old}OO' \quad (2.33)$$

where  $E_{old}$  and  $G_{old}$  are the previous guesses of the probe and gate respectively and  $O'$  is the transpose of the outer product form matrix  $O$ . The new values of the gate and probe are then used to create a new outer product matrix and the whole iteration is repeated over and over again until the experimental trace matches well with the computed trace. For a technique such as FROG where it is known that both the  $G(t)$  and  $E(t)$  are identical an extra constraint can be applied to guess pulses. The full retrieval procedure is represented in Figure 2.20.

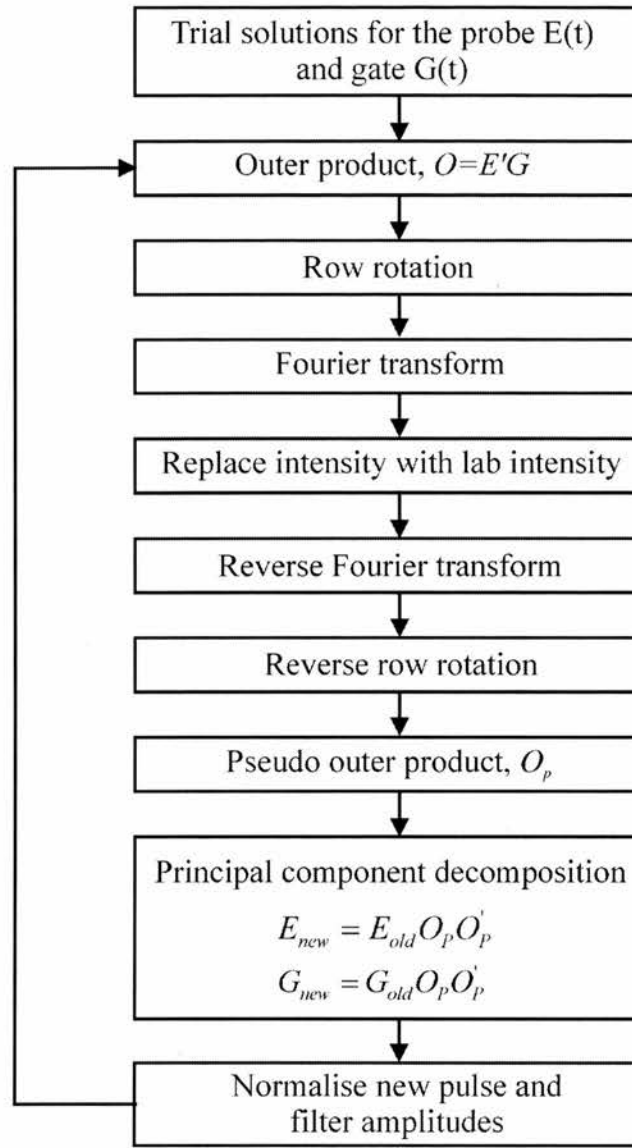


**Figure 2.20** Schematic representation of the steps involved within the PCGP retrieval algorithm

To determine how accurately the experimentally measured FROG trace compares with the computed trace, the 'G-error' can be calculated. The G-error is the rms difference between the experimentally measured trace  $I_{FROG}(\omega_i, \tau_j)$  and the computed trace  $I_{FROG}^{(k)}(\omega_i, \tau_j)$  where  $k$  indicates the most recent iteration:

$$G = \sqrt{\frac{1}{N^2} \sum_{i,j=1}^N |I_{FROG}(\omega_i, \tau_j) - I_{FROG}^{(k)}(\omega_i, \tau_j)|^2} \quad (2.34)$$

Typical values of the G-error vary from <1% for PG-FROG to <0.5% for SHG-FROG due to the technique having very little background noise.

The PCGP algorithm is inherently a blind-FROG algorithm [74] and consequently tries to find the probe and gate independently without any prior assumptions between them. This can cause trouble when trying to retrieve a FROG trace given that a slight change of width in the probe can be compensated by a small change in width of the gate without much change seen in the G-error. As a consequence it is wise to give the algorithm a bit of help by adding some spectral constraint on either the probe or gate. The spectral constraint can be added just before the principal component decomposition is carried out on the outer-product matrix. At this point, the columns are arranged so that one element of the gate is multiplied by the probe field. The Fourier transform of each column is then carried out and its magnitude is replaced by the square root of the measured pulse spectra. Care must be taken to keep the area of the intensities equal to ensure the gate field is preserved. The columns are then reverse Fourier transformed to get back to the outer-product form.

There is an alternative to the spectral constraint however which utilises the fact that the gate is made up from the probe by the function  $\Gamma$ . Its inverse,  $\Gamma^{-1}$ , will therefore produce the probe from the gate. Instead of obtaining the outer product form by taking the outer product of the probe,  $E_{probe}$ , and the gate,  $E_{gate}$ , we can take the sum of the outer products of  $E_{probe} E_{gate}$  and  $\Gamma^{-1}(E_{probe}) \Gamma^{-1}(E_{gate})$  to give:

$$O^{ij} = probe^i gate^j + \Gamma^{-1}(gate)^i \Gamma^{-1}(probe)^j \quad (2.35)$$

In terms of SHG-FROG, the above equation can be further simplified by the fact that the gate is identical to the probe, so that the outer product can become:

$$O^{ij} = probe^i gate^j + gate^i probe^j \quad (2.36)$$

In this section I have described the general technique used to retrieve pulse information a spectrogram. The same approach can be applied to a sonogram and more detail of this will be presented in Chapters 4 and 5

### Checking for systematic errors using the trace marginals

One of the most useful and important aspects of time-frequency characterisation techniques is the over determination of the pulse. A time-frequency trace is made up from a  $N \times N$  array of points, which are then used to determine a  $N$  number of intensity and phase points (total of  $2N$  points). This over determination enables the marginals of the trace to be used as a check to see if any systematic errors have crept into the experimental acquisition [49, 73, 76-78]. The delay marginal of a FROG trace is its integral along the frequency axis:

$$M_{\tau}(\tau) = \int_{-\infty}^{\infty} d\omega I_{FROG}(\omega, \tau) \quad (2.37)$$

When using SHG-FROG the delay marginal has the form:

$$M_{\tau}^{SHG}(\tau) = \int_{-\infty}^{\infty} dt I(t) I(t-\tau) \quad (2.38)$$

which is the standard second-order intensity autocorrelation of the pulse. This can be simply measured experimentally and compared with the SHG-FROG delay marginal. If the two traces disagree then it is implied that there is some systematic error within the trace. Similarly the frequency marginal of a FROG trace is its integral along the delay axis:

$$M_{\omega}(\omega) = \int_{-\infty}^{\infty} d\tau I_{FROG}(\omega, \tau) \quad (2.39)$$

and when using SHG-FROG the frequency marginal has the form:

$$M_{\omega}^{SHG}(\omega) = 2I(\omega) * I(\omega) \quad (2.40)$$

which is simply the autoconvolution of the experimentally measured spectrum of the pulse. Again, if there is disagreement between the two traces, there must be systematic error within the trace. Although only the marginals of an SHG-FROG trace are discussed here, the same approach can be used with all time-frequency measurements, with different techniques having differing mathematical forms describing the trace marginals [73, 78].

### 2.3.2 Interferometric characterisation techniques [79, 80]

Interferometric characterisation techniques until recently have been overshadowed by time-frequency techniques. There are, however, two main advantages that are associated with interferometric techniques. Firstly only a 1-D array needs to be recorded instead of a 2-D array that is associated with time-frequency measurements. Secondly, pulse information can be extracted using a much less computationally intensive direct data inversion algorithm rather than an iterative retrieval algorithm. Diels demonstrated an interferometric technique that uses an ultrafast diode and a Schottky nonlinear mixer to record the beat noted between pairs of spectral components of the input pulse [81]. Another similar technique known as Direct Optical Spectral Phase Measurement (DOSPM) uses a nonlinear crystal as a time gate to record interference beats [82]. When compared to characterisation techniques such as FROG, these techniques are experimentally difficult requiring either a fast detector or a fast nonlinear time gate and have subsequently not been widely used. All this changed in 1998, when Walmsley and co-workers, devised a practical interferometric technique called Spectral Phase Interferometry for Direct Electric-field Reconstruction (SPIDER) [83, 84]. SPIDER is currently the main alternative to FROG for the full characterisation of an ultrashort pulse and is therefore discussed here in some detail.

#### 2.3.2.1 SPIDER

Spider uses spectral shearing interferometry to retrieve the spectral phase of the incident pulse. This is achieved by measuring the interference pattern between two pulses separated in time that are identical in every respect except for their centre frequency (ie two pulses which are spectrally sheared). The resultant spectrum of these two pulses is in the form of an interferogram, described mathematically as:

$$S(\omega) = I(\omega + \Omega) + I(\omega) + 2\sqrt{I(\omega + \Omega)I(\omega)} \cos\{\phi(\omega + \Omega) - \phi(\omega) + \omega\tau\} \quad (2.41)$$

where  $I(\omega)$  is the pulse spectrum,  $\Omega$  is the difference between the central frequencies of the two pulses (spectral shear),  $\phi(\omega)$  is the spectral phase of the pulse and  $\tau$  is the time delay between the pulses.

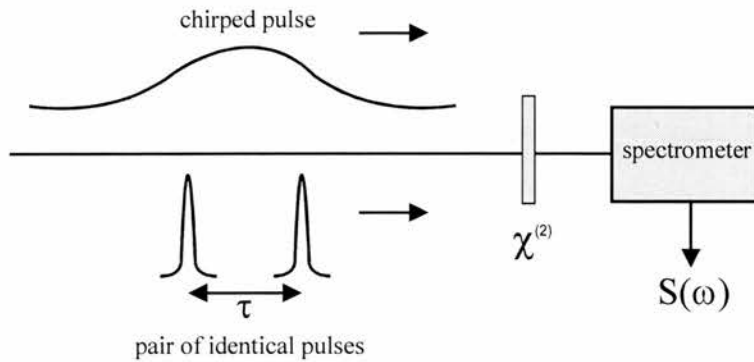


**Figure 2.21** The experimental setup used in SPIDER

The spectral shearing of the pulse is achieved experimentally by combining two properly conditioned beams within a nonlinear crystal such that the resulting sum or difference signal comprises a spectrally sheared pulse pair. The first beam consists of a pair of identical pulses, separated by a known time delay of  $\tau$ . The second beam consists of a highly chirped pulse. The amount of chirp added to this pulse is dependent upon two conditions. First, to ensure the pair of pulses in the first beam successfully interacts with the chirped pulse, the duration of the chirped pulse must be much longer than  $\tau$ . Secondly, the chirp must be large enough to ensure that when the two beams mix each of the paired pulses mix with a different frequency in the chirped pulse. This has the result that each pulse emerging from the mixing crystal has a different centre frequency (ie. spectrally sheared). By measuring the spectrum from the output of the nonlinear crystal, the SPIDER interferogram is recorded. To ensure the sampling rate is above the Nyquist limit ( $> 2$  points per fringe) the value of  $\tau$  must be carefully chosen. Also, the amount of spectral shearing must also be carefully controlled to ensure the Whittaker-Shannon sampling theorem [85] is satisfied. If the shearing is too small or too large, the phase measurement will become incorrect.

To retrieve the phase information the interferogram is Fourier transformed into the time domain. A DC component and two AC sidebands will be present. The DC components correspond to the constant terms in equation (2.41). The two AC side bands are inverted replicas of one another, both of which correspond to the cosine term in equation (2.41) so only the positive AC term is required. By filtering out the other two components and reverse Fourier transforming, the phase profile of the remaining trace is that of the contents of the cosine term in equation (2.41). The linear phase term,  $\omega\tau$ , can be removed by subtracting from the trace a previously measured calibration interferogram that has no spectral shearing, achieved by simply blocking the chirped pulse. What is left is known as the phase difference:

$$\theta(\omega) = \phi(\omega) - \phi(\omega - \Omega) \quad (2.42)$$

By using concatenation [84], the sampled spectrum phase at intervals  $\Omega$  across the pulse spectrum can be calculated. To gain temporal information from SPIDER, it used to be the case that an experimental measurement of the spectrum was required, which when combined with the spectral phase yields the temporal profile of the pulse. Improvements to the initial SPIDER technique have provided ways of retrieving both spectral phase AND spectral amplitude from the same interferometric trace so that an experimentally measured spectrum is not required [86]

The fact that there is no need for a computationally intensive iterative retrieval algorithm makes SPIDER ideal for a real-time characterisation technique. This potential was realised by Shuman et al. who characterised the output of a 1kHz regeneratively amplified laser system at repetition rate of 20 Hz [87]. Due to the reconstruction of the phase being insensitive to phase-matching bandwidth of the nonlinear crystal, SPIDER is also ideally suited for ultrashort pulses and has been used to measure some of the shortest ever pulses created [88-90]. SPIDER has also been demonstrated in a single shot geometry [91] and then used to characterise a chirped pulse amplification system [92]. As discussed at the start of this section, the term ‘full characterisation’ has been defined to not include spatial measurements,

but SPIDER has been used successfully to measure the phase variation across the spatial profile of an ultrashort pulse [41].

### 2.3.2.2 Can SPIDER's gobble up FROG's?

So, with SPIDER having so many advantages the obvious question to ask is, "If SPIDER is such a good technique, why keep using techniques such as FROG and sonograms?". The answer to this controversial question is that although SPIDER is an excellent technique there are a few fundamental disadvantages associated with it. The main disadvantage of SPIDER is its lack of any major error checking ability. In time-frequency characterisation techniques, marginals may be utilised to ensure no systematic errors have crept into the measurement. In SPIDER, because only a 1-D plot is measured, there is as yet no method to check for systematic errors as thoroughly as time-frequency techniques allow. Consequently, the SPIDER measurements are solely dependent upon the calibration of the whole optical setup, which can be prone to errors. The influence of this calibration has been investigated by Dorrer et al. [93] who suggest a few techniques for improving the calibration of a SPIDER setup. Another consequence of acquiring less data points is that it makes SPIDER more susceptible to noise. Anderson et al carried out theoretical calculations on how noise can effect phase measurements [94]. It was found that by adding 10% additive noise the pulse shape could only be recovered to an accuracy of 1.5%. This could be improved by averaging a number of the noisy interferograms together, at the expense of slower update rates.

The second fundamental disadvantage is the flexibility of SPIDER. Both the Nyquist limit and the Whittaker-Shannon sampling theorem need to be considered and altered for different pulses. This poses two problems. Firstly, to initially design the SPIDER optical arrangement, knowledge of the pulse to be measured must be known. This can only be done using techniques such as FROG that do not have such critical optical constraints to enable it to characterise a pulse. Secondly, if the duration or phase of the measured pulse varies while measuring with SPIDER, the delay within the pulse pair,  $\tau$ , will need to be altered along with

the amount of spectral sheering being produced, and consequently the whole optical setup will require re-calibration. A comparison between SPIDER and SHG-FROG has been carried to see which technique is best suited for the measurement of sub 10fs pulses [40]. It is concluded that there is no overall winner and that both methods have yet to be fully utilised and both should allow for the accurate characterisation of pulses into the single-cycle regime.

## **2.4 Conclusion**

Within this chapter I have described a vast range of ultrashort pulse characterisation techniques. SHG-FROG and SPIDER are now the most commonly used techniques but still possess their individual disadvantages. The following chapters mainly concentrate upon the development of 'real-time' pulse characterisation systems based on the measurement of a sonogram (section 2.3.1). As will be discussed, the measurement of a sonogram has many advantages over more commonly used techniques but has not been considered for a viable real-time system due to requirement of a near dispersionless frequency filter. This need enabled me to develop a procedure capable of accurately determining the dispersion characteristics of an optical arrangement. Chapter 3 describes the development of this technique.

## 2.5 References

- [1] J. Armstrong, *Applied Physics Letters*, vol. 10, pp. 16, 1967.
- [2] M. Maier, W. Kaiser, and J. Giordmaine, *Physics Review Letters*, vol. 17, pp. 1275, 1966.
- [3] H. Weber, *Journal of Applied Physics*, vol. 38, pp. 2231, 1967.
- [4] R. Miller, *Physics Letters*, vol. 26-A, pp. 177, 1968.
- [5] A. M. Weiner, "Effect of Group-Velocity Mismatch On the Measurement of Ultrashort Optical Pulses Via 2nd Harmonic-Generation," *IEEE Journal of Quantum Electronics*, vol. 19, pp. 1276-1283, 1983.
- [6] J.-M. Hopkins, "Compact, Low-threshold Femtosecond Lasers," in *PhD Thesis*, 1999.
- [7] J. C. M. Diels, J. J. Fontaine, I. C. McMichael, and F. Simoni, "Control and Measurement of Ultrashort Pulse Shapes (in Amplitude and Phase) With Femtosecond Accuracy," *Applied Optics*, vol. 24, pp. 1270-1282, 1985.
- [8] J. W. Nicholson, J. Jasapara, W. Rudolph, F. G. Omenetto, and A. J. Taylor, "Full-field characterization of femtosecond pulses by spectrum and cross-correlation measurements," *Optics Letters*, vol. 24, pp. 1774-1776, 1999.
- [9] J. Peatross and A. Rundquist, "Temporal decorrelation of short laser pulses," *Journal of the Optical Society of America B-Optical Physics*, vol. 15, pp. 216-222, 1998.
- [10] A. Baltuska, A. Pugzlys, M. Pshenichnikov, and D. Wiersma, presented at Conference on Lasers and Electro-Optics (CLEO), 1999.
- [11] T. Yau, Y. Jau, C. Lee, and J. Wang, presented at Conference on Lasers and Electro-Optics (CLEO), 1999.
- [12] S. Marzenell, P. Mahnke, and R. Beigang, "Unbalanced multiphoton interferometric autocorrelation techniques for fs pulse measurements in the near it," presented at The Twelfth International Conference on Ultrafast Phenomena, Charleston, South Carolina, USA, 2000.
- [13] J. W. Nicholson, M. Mero, J. Jasapara, and W. Rudolph, "Unbalanced third-order correlations for full characterization of femtosecond pulses," *Optics Letters*, vol. 25, pp. 1801-1803, 2000.
- [14] P. Langlois and E. P. Ippen, "Measurement of pulse asymmetry by three-photon-absorption autocorrelation in a GaAsP photodiode," *Optics Letters*, vol. 24, pp. 1868-1870, 1999.
- [15] H. Schulz, H. Schuler, T. Engers, and D. Vonderlinde, "Measurement of Intense Ultraviolet Subpicosecond Pulses Using Degenerate 4-Wave Mixing," *IEEE Journal of Quantum Electronics*, vol. 25, pp. 2580-2585, 1989.
- [16] A. Gutierrez, P. Dorn, J. Zeller, D. King, L. F. Lester, W. Rudolph, and M. Sheik-Bahae, "Autocorrelation measurement of femtosecond laser pulses by use of a ZnSe two-photon detector array," *Optics Letters*, vol. 24, pp. 1175-1177, 1999.
- [17] S. Lochbrunner, P. Huppmann, and E. Riedle, "Crosscorrelation measurements of ultrashort visible pulses: comparison between nonlinear crystals and SiC photodiodes," *Optics Communications*, vol. 184, pp. 321-328, 2000.
- [18] D. T. Reid, W. Sibbett, J. M. Dudley, L. P. Barry, B. Thomsen, and J. D. Harvey, "Commercial semiconductor devices for two photon absorption autocorrelation of ultrashort light pulses," *Applied Optics*, vol. 37, pp. 8142-8144, 1998.
- [19] D. T. Reid, M. Padgett, C. McGowan, W. E. Sleat, and W. Sibbett, "Light-emitting diodes as measurement devices for femtosecond laser pulses," *Optics Letters*, vol. 22, pp. 233-235, 1997.
- [20] P. Loza-Alvarez, W. Sibbett, and D. T. Reid, "Autocorrelation of femtosecond pulses from 415-630nm using GaN laser diode," *Electronics Letters*, vol. 36, pp. 631-633, 2000.
- [21] T. Feurer, A. Glass, and R. Sauerbrey, "Two-photon photoconductivity in SiC photodiodes and its application to autocorrelation measurements of femtosecond optical pulses," *Applied Physics B-Lasers and Optics*, vol. 65, pp. 295-297, 1997.
- [22] Z. Zheng, A. M. Weiner, J. H. Marsh, and M. M. Karkhanehchi, "Ultrafast optical thresholding based on two-photon absorption GaAs waveguide photodetectors," *IEEE Photonics Technology Letters*, vol. 9, pp. 493-495, 1997.
- [23] M. M. Karkhanehchi, C. J. Hamilton, and J. H. Marsh, "Autocorrelation measurements of modelocked Nd:YLF laser pulses using two-photon absorption waveguide autocorrelator," *IEEE Photonics Technology Letters*, vol. 9, pp. 645-647, 1997.
- [24] W. Rudolph, M. SheikBahae, A. Bernstein, and L. F. Lester, "Femtosecond autocorrelation measurements based on two-photon photoconductivity in ZnSe," *Optics Letters*, vol. 22, pp. 313-315, 1997.

- [25] A. Baltuska, Z. Wei, M. S. Pshenichnikov, D. A. Wiersma, and R. Szipocs, "All-solid-state cavity-dumped sub-5-fs laser," *Applied Physics B-Lasers and Optics*, vol. 65, pp. 175-188, 1997.
- [26] J. K. Ranka, A. L. Gaeta, A. Baltuska, M. S. Pshenichnikov, and D. A. Wiersma, "Autocorrelation measurement of 6-fs pulses based on the two-photon-induced photocurrent in a GaAsP photodiode," *Optics Letters*, vol. 22, pp. 1344-1346, 1997.
- [27] D. T. Reid, C. McGowan, M. Ebrahimzadeh, and W. Sibbett, "Characterization and modeling of a noncollinearly phase-matched femtosecond optical parametric oscillator based on KTA and operating to beyond 4  $\mu\text{m}$ ," *IEEE Journal of Quantum Electronics*, vol. 33, pp. 1-9, 1997.
- [28] L. P. Barry, P. G. Bollond, J. M. Dudley, J. D. Harvey, and R. Leonhardt, "Autocorrelation of ultrashort pulses at 1.5  $\mu\text{m}$  based on nonlinear response of silicon photodiodes," *Electronics Letters*, vol. 32, pp. 1922-1923, 1996.
- [29] H. K. Tsang, L. Y. Chan, J. B. D. Soole, H. P. Leblanc, M. A. Koza, and R. Bhat, "High-Sensitivity Autocorrelation Using 2-Photon Absorption in InGaAsP Wave-Guides," *Electronics Letters*, vol. 31, pp. 1773-1775, 1995.
- [30] A. Zavriyev, E. Dupont, P. B. Corkum, H. C. Liu, and Z. Biglov, "Direct Autocorrelation Measurements of Midinfrared Picosecond Pulses by Quantum-Well Devices," *Optics Letters*, vol. 20, pp. 1886-1888, 1995.
- [31] F. R. Laughton, J. H. Marsh, D. A. Barrow, and E. L. Portnoi, "The 2-Photon Absorption Semiconductor Wave-Guide Autocorrelator," *IEEE Journal of Quantum Electronics*, vol. 30, pp. 838-845, 1994.
- [32] Y. Takagi, "Simple Autocorrelator for Ultraviolet Pulse-Width Measurements Based on the Nonlinear Photoelectric Effect," *Applied Optics*, vol. 33, pp. 6328-6332, 1994.
- [33] N. D. Whitbread, J. A. R. Williams, J. S. Roberts, I. Bennion, and P. N. Robson, "Optical Autocorrelator That Uses a Surface-Emitting 2nd-Harmonic Generator on (211)B GaAs," *Optics Letters*, vol. 19, pp. 2089-2091, 1994.
- [34] F. R. Laughton, J. H. Marsh, and A. H. Kean, "Very Sensitive 2-Photon Absorption GaAs/AlGaAs Wave-Guide Detector for an Autocorrelator," *Electronics Letters*, vol. 28, pp. 1663-1665, 1992.
- [35] Y. Takagi, T. Kobayashi, K. Yoshihara, and S. Imamura, "Multiple-Shot and Single-Shot Autocorrelator Based on 2-Photon Conductivity in Semiconductors," *Optics Letters*, vol. 17, pp. 658-660, 1992.
- [36] R. Trebino and D. J. Kane, "Using Phase Retrieval to Measure the Intensity and Phase of Ultrashort Pulses - Frequency-Resolved Optical Gating," *Journal of the Optical Society of America a-Optics Image Science and Vision*, vol. 10, pp. 1101-1111, 1993.
- [37] D. J. Kane and R. Trebino, "Single-Shot Measurement of the Intensity and Phase of an Arbitrary Ultrashort Pulse By Using Frequency-Resolved Optical Gating," *Optics Letters*, vol. 18, pp. 823-825, 1993.
- [38] D. J. Kane and R. Trebino, "Characterization of Arbitrary Femtosecond Pulses Using Frequency-Resolved Optical Gating," *IEEE Journal of Quantum Electronics*, vol. 29, pp. 571-579, 1993.
- [39] S. T. Cundiff, W. H. Knox, E. P. Ippen, and H. A. Haus, "Frequency-dependent mode size in broadband Kerr-lens mode locking," *Optics Letters*, vol. 21, pp. 662-664, 1996.
- [40] L. Gallmann, D. H. Sutter, N. Matuschek, G. Steinmeyer, and U. Keller, "Techniques for the characterization of sub-10-fs optical pulses: a comparison," *Applied Physics B-Lasers and Optics*, vol. 70, pp. S67-S75, 2000.
- [41] L. Gallmann, G. Steinmeyer, D. H. Sutter, T. Rupp, C. Iaconis, I. A. Walmsley, and U. Keller, "Spatially resolved amplitude and phase characterization of femtosecond optical pulses," *Optics Letters*, vol. 26, pp. 96-98, 2001.
- [42] E. P. Ippen, "Dynamic Spectroscopy and sub picosecond pulse compression," *Applied Physics Letters*, vol. 27, pp. 488-190, 1975.
- [43] J. L. A. Chilla and O. E. Martinez, "Direct Determination of the Amplitude and the Phase of Femtosecond Light-Pulses," *Optics Letters*, vol. 16, pp. 39-41, 1991.
- [44] E. Treacy, "Measurement and Interpretation of Dynamic Spectrograms of Picosecond Light Pulses," *Journal of Applied Physics*, vol. 42, pp. 3848, 1971.
- [45] R. Trebino, K. W. DeLong, D. N. Fittinghoff, J. N. Sweetser, M. A. Krumbugel, B. A. Richman, and D. J. Kane, "Measuring ultrashort laser pulses in the time-frequency domain using frequency-resolved optical gating," *Review of Scientific Instruments*, vol. 68, pp. 3277-3295, 1997.

- [46] D. N. Fittinghoff, K. W. DeLong, R. Trebino, and C. L. Ladera, "Noise Sensitivity in Frequency-Resolved Optical-Gating Measurements of Ultrashort Pulses," *Journal of the Optical Society of America B-Optical Physics*, vol. 12, pp. 1955-1967, 1995.
- [47] K. W. DeLong, C. L. Ladera, R. Trebino, B. Kohler, and K. R. Wilson, "Ultrashort-Pulse Measurement Using Noninstantaneous Nonlinearities - Raman Effects in Frequency-Resolved Optical Gating," *Optics Letters*, vol. 20, pp. 486-488, 1995.
- [48] K. W. DeLong, R. Trebino, J. Hunter, and W. E. White, "Frequency-Resolved Optical Gating With the Use of 2nd-Harmonic Generation," *Journal of the Optical Society of America B-Optical Physics*, vol. 11, pp. 2206-2215, 1994.
- [49] G. Taft, A. Rundquist, M. M. Murnane, I. P. Christov, H. C. Kapteyn, K. W. DeLong, D. N. Fittinghoff, M. A. Krumbugel, J. N. Sweetser, and R. Trebino, "Measurement of 10-fs laser pulses," *IEEE Journal of Selected Topics in Quantum Electronics*, vol. 2, pp. 575-585, 1996.
- [50] G. Taft, "Ultrashort optical waveform measurements using frequency resolved optical gating," *Optics Letters*, vol. 20, pp. 743-745, 1995.
- [51] Z. E. Penman, T. Schittkowski, W. Sleat, D. T. Reid, and W. Sibbett, "Experimental comparison of conventional pulse characterisation techniques and second-harmonic-generation frequency-resolved optical gating," *Optics Communications*, vol. 155, pp. 297-300, 1998.
- [52] A. Kwok, L. Jusinski, M. A. Krumbugel, J. N. Sweetser, D. N. Fittinghoff, and R. Trebino, "Frequency-resolved optical gating using cascaded second-order nonlinearities," *IEEE Journal of Selected Topics in Quantum Electronics*, vol. 4, pp. 271-277, 1998.
- [53] A. Baltuska, M. S. Pshenichnikov, and D. A. Wiersma, "Second-harmonic generation frequency-resolved optical gating in the single-cycle regime," *IEEE Journal of Quantum Electronics*, vol. 35, pp. 459-478, 1999.
- [54] P. O'Shea, M. Kimmel, X. Gu, and R. Trebino, "Increased-bandwidth in ultrashort-pulse measurement using an angle-dithered nonlinear-optical crystal," *Optics Express*, vol. 7, pp. 342-349, 2000.
- [55] T. S. Clement, A. J. Taylor, and D. J. Kane, "Single-Shot Measurement of the Amplitude and Phase of Ultrashort Laser-Pulses in the Violet," *Optics Letters*, vol. 20, pp. 70-72, 1995.
- [56] J. N. Sweetser, D. N. Fittinghoff, and R. Trebino, "Transient-grating frequency-resolved optical gating," *Optics Letters*, vol. 22, pp. 519-521, 1997.
- [57] T. Tsang, M. A. Krumbugel, K. W. DeLong, D. N. Fittinghoff, and R. Trebino, "Frequency-resolved optical-gating measurements of ultrashort pulses using surface third-harmonic generation," *Optics Letters*, vol. 21, pp. 1381-1383, 1996.
- [58] T. Y. F. Tsang, "Optical 3rd-Harmonic Generation At Interfaces," *Physical Review a*, vol. 52, pp. 4116-4125, 1995.
- [59] D. N. Fittinghoff, J. L. Bowie, J. N. Sweetser, R. T. Jennings, M. A. Krumbugel, K. W. DeLong, R. Trebino, and I. A. Walmsley, "Measurement of the intensity and phase of ultraweak, ultrashort laser pulses," *Optics Letters*, vol. 21, pp. 884-886, 1996.
- [60] J. Piasecki, B. Colombeau, M. Vampouille, C. Froehly, and J. Arnaud, "Nouvelle methode de mesure de la reponse impulsionnelle des fibres optiques," *Applied Optics*, vol. 19, pp. 3749, 1980.
- [61] W. J. Walecki, D. N. Fittinghoff, A. L. Smirl, and R. Trebino, "Characterization of the polarization state of weak ultrashort coherent signals by dual-channel spectral interferometry," *Optics Letters*, vol. 22, pp. 81-83, 1997.
- [62] L. Lepetit, G. Cheriaux, and M. Joffre, "Linear techniques of phase measurement by femtosecond spectral interferometry for applications in spectroscopy," *Journal of the Optical Society of America B-Optical Physics*, vol. 12, pp. 2467-2474, 1995.
- [63] K. W. DeLong, R. Trebino, and W. E. White, "Simultaneous recovery of two ultrashort laser pulses from a single spectrogram," *Journal of the Optical Society of America B-Optical Physics*, vol. 12, pp. 2463-2466, 1995.
- [64] B. C. McCallum and J. M. Rodenburg, "Simultaneous Reconstruction of Object and Aperture Functions From Multiple Far-Field Intensity Measurements," *Journal of the Optical Society of America a-Optics Image Science and Vision*, vol. 10, pp. 231-239, 1993.
- [65] S. Linden, H. Giessen, and J. Kuhl, "XFROG - A new method for amplitude and phase characterization of weak ultrashort pulses," *Physica Status Solidi B-Basic Research*, vol. 206, pp. 119-124, 1998.
- [66] S. Linden, J. Kuhl, and H. Giessen, "Amplitude and phase characterization of weak blue ultrashort pulses by downconversion," *Optics Letters*, vol. 24, pp. 569-571, 1999.

- [67] D. T. Reid, P. Loza-Alvarez, C. T. A. Brown, T. Beddard, and W. Sibbett, "Amplitude and phase measurement of mid-infrared femtosecond pulses by using cross-correlation frequency-resolved optical gating," *Optics Letters*, vol. 25, pp. 1478-1480, 2000.
- [68] K. W. DeLong, D. N. Fittinghoff, R. Trebino, B. Kohler, and K. Wilson, "Pulse Retrieval in Frequency-Resolved Optical Gating Based On the Method of Generalized Projections," *Optics Letters*, vol. 19, pp. 2152-2154, 1994.
- [69] K. W. DeLong and R. Trebino, "Improved Ultrashort Pulse-Retrieval Algorithm For Frequency-Resolved Optical Gating," *Journal of the Optical Society of America a-Optics Image Science and Vision*, vol. 11, pp. 2429-2437, 1994.
- [70] J. Paye, M. Ramaswamy, J. G. Fujimoto, and E. P. Ippen, "Measurement of the Amplitude and Phase of Ultrashort Light- Pulses From Spectrally Resolved Autocorrelation," *Optics Letters*, vol. 18, pp. 1946-1948, 1993.
- [71] D. J. Kane, "Real-time measurement of ultrashort laser pulses using principal component generalized projections," *IEEE Journal of Selected Topics in Quantum Electronics*, vol. 4, pp. 278-284, 1998.
- [72] D. J. Kane, "Recent progress toward real-time measurement of ultrashort laser pulses," *IEEE Journal of Quantum Electronics*, vol. 35, pp. 421-431, 1999.
- [73] D. T. Reid, "Algorithm for complete and rapid retrieval of ultrashort pulse amplitude and phase from a sonogram," *IEEE Journal of Quantum Electronics*, vol. 35, pp. 1584-1589, 1999.
- [74] D. J. Kane, G. Rodriguez, A. J. Taylor, and T. S. Clement, "Simultaneous measurement of two ultrashort laser pulses from a single spectrogram in a single shot," *Journal of the Optical Society of America B-Optical Physics*, vol. 14, pp. 935-943, 1997.
- [75] H. Anton, *Elementary Linear Algebra*, 2nd ed: Wiley, 1977.
- [76] R. Altes, "Detection, estimation, and classification with spectrograms," *J. Acoust. Soc. Am.*, vol. 67, pp. 1232-1246, 1980.
- [77] K. W. DeLong, D. N. Fittinghoff, and R. Trebino, "Practical issues in ultrashort-laser-pulse measurement using frequency-resolved optical gating," *IEEE Journal of Quantum Electronics*, vol. 32, pp. 1253-1264, 1996.
- [78] K. W. DeLong, R. Trebino, and D. J. Kane, "Comparison of Ultrashort-Pulse Frequency-Resolved-Optical- Gating Traces For 3 Common Beam Geometries," *Journal of the Optical Society of America B-Optical Physics*, vol. 11, pp. 1595-1608, 1994.
- [79] I. A. Walmsley and V. Wong, "Characterization of the electric field of ultrashort optical pulses," *Journal of the Optical Society of America B-Optical Physics*, vol. 13, pp. 2453-2463, 1996.
- [80] C. Iaconis, V. Wong, and I. A. Walmsley, "Direct interferometric techniques for characterizing ultrashort optical pulses," *IEEE Journal of Selected Topics in Quantum Electronics*, vol. 4, pp. 285-294, 1998.
- [81] S. Prein, S. Diddams, and J. C. Diels, "Complete characterization of femtosecond pulses using an all- electronic detector," *Optics Communications*, vol. 123, pp. 567-573, 1996.
- [82] K. C. Chu, J. P. Heritage, R. S. Grant, K. X. Liu, A. Dienes, W. E. White, and A. Sullivan, "Direct Measurement of the Spectral Phase of Femtosecond Pulses," *Optics Letters*, vol. 20, pp. 904-906, 1995.
- [83] C. Iaconis and I. A. Walmsley, "Spectral phase interferometry for direct electric-field reconstruction of ultrashort optical pulses," *Optics Letters*, vol. 23, pp. 792-794, 1998.
- [84] C. Iaconis and I. A. Walmsley, "Self-referencing spectral interferometry for measuring ultrashort optical pulses," *IEEE Journal of Quantum Electronics*, vol. 35, pp. 501-509, 1999.
- [85] J. Goodman, *Introduction to Fourier Optics*. New York: McGraw-Hill, 1988.
- [86] C. Dorrer, "Implementation of spectral phase interferometry for direct electric-field reconstruction with a simultaneously recorded reference interferogram," *Optics Letters*, vol. 24, pp. 1532-1534, 1999.
- [87] T. M. Shuman, M. E. Anderson, J. Bromage, C. Iaconis, L. Waxer, and I. A. Walmsley, "Real-time SPIDER: ultrashort pulse characterization at 20 Hz," *Optics Express*, vol. 5, pp. 134-143, 1999.
- [88] L. Gallmann, D. H. Sutter, N. Matuschek, G. Steinmeyer, U. Keller, C. Iaconis, and I. A. Walmsley, "Characterization of sub-6-fs optical pulses with spectral phase interferometry for direct electric-field reconstruction," *Optics Letters*, vol. 24, pp. 1314-1316, 1999.
- [89] D. H. Sutter, L. Gallmann, N. Matuschek, F. Morier-Genoud, V. Scheuer, G. Angelow, T. Tschudi, G. Steinmeyer, and U. Keller, "Sub-6-fs pulses from a SESAM-assisted Kerr-lens

- modelocked Ti : sapphire laser: at the frontiers of ultrashort pulse generation," *Applied Physics B-Lasers and Optics*, vol. 70, pp. S5-S12, 2000.
- [90] G. Cheriaux, O. Albert, V. Wanman, J. P. Chambaret, C. Felix, and G. Mourou, "Temporal control of amplified femtosecond pulses with a deformable mirror in a stretcher," *Optics Letters*, vol. 26, pp. 169-171, 2001.
- [91] C. Dorrer, B. de Beauvoir, C. Le Blanc, S. Ranc, J. P. Rousseau, P. Rousseau, and J. P. Chambaret, "Single-shot real-time characterization of chirped-pulse amplification systems by spectral phase interferometry for direct electric-field reconstruction," *Optics Letters*, vol. 24, pp. 1644-1646, 1999.
- [92] C. Dorrer, B. de Beauvoir, C. Le Blanc, J. P. Roussaeu, R. Ranc, P. Rousseau, J. P. Chambaret, and F. Salin, "Characterization of chirped-pulse amplification systems with spectral phase interferometry for direct electric-field reconstruction," *Applied Physics B-Lasers and Optics*, vol. 70, pp. S77-S84, 2000.
- [93] C. Dorrer, "Influence of the calibration of the detector on spectral interferometry," *Journal of the Optical Society of America B-Optical Physics*, vol. 16, pp. 1160-1168, 1999.
- [94] M. E. Anderson, L. E. E. de Araujo, E. M. Kosik, and I. A. Walmsley, "The effects of noise on ultrashort-optical-pulse measurement using SPIDER," *Applied Physics B-Lasers and Optics*, vol. 70, pp. S85-S93, 2000.

## CHAPTER 3

# Measurement of group velocity dispersion using white light interferometry

---

### 3.1 Introduction

A vital part of the work carried out within Chapter 4 was the development of a scanning frequency filter which is a key component of the sonogram acquisition setup. The main criterion for this filter design was the need for it to be near-dispersionless across the bandwidth of the pulse spectrum. This chapter contains an initial overview of techniques that have been used to measure the dispersion of bulk optics followed by a description of a simplified procedure which was developed to allow the dispersion of bulk optical systems and components to be measured simply and accurately. This procedure was then used successfully in the work described in chapter 4 to characterise the dispersion of a frequency filter.

Careful control and knowledge of GVD is essential when dealing with generation and characterisation of ultrashort laser pulses. As mentioned in Chapter 1, ultrashort laser pulses have a characteristically large frequency bandwidth and to create the shortest possible pulse its frequency components must arrive simultaneously (ie. transform limited). When ultrashort pulses are generated each passes through various optical components inside and outside the cavity such as lenses, polarisers, waveplates, mirrors and crystals which all possess differing amounts of GVD. To compensate for this GVD, detailed dispersion characteristics are required for each optical component. Also, and more relevant in the context of this thesis, when measuring ultrashort pulses, great care must be taken to ensure that any GVD in the optical characterisation arrangement does not alter the measured pulse while it is being measured because this would result in errors in the pulse measurement.

## 3.2 Dispersion characterisation techniques

The techniques that are used to determine the dispersion characteristics of optical components can be divided into two separate categories. Firstly there are interferometric techniques which are able to determine the dispersion of a single optical component and, secondly, there are techniques that can determine the overall dispersion within a laser cavity. Both of these techniques will be discussed within this section.

### 3.2.1 Interferometric techniques

Some of the earliest work carried out to calculate the dispersion of the optics used in ultrafast lasers employed white light interferometry [1]. The simplest approach, often referred to as the Fringe Contour Shift (FCS) technique, was initially used to calculate the dispersion of single mode fibre [2] and was later used to measure the group delay of optical components [1].

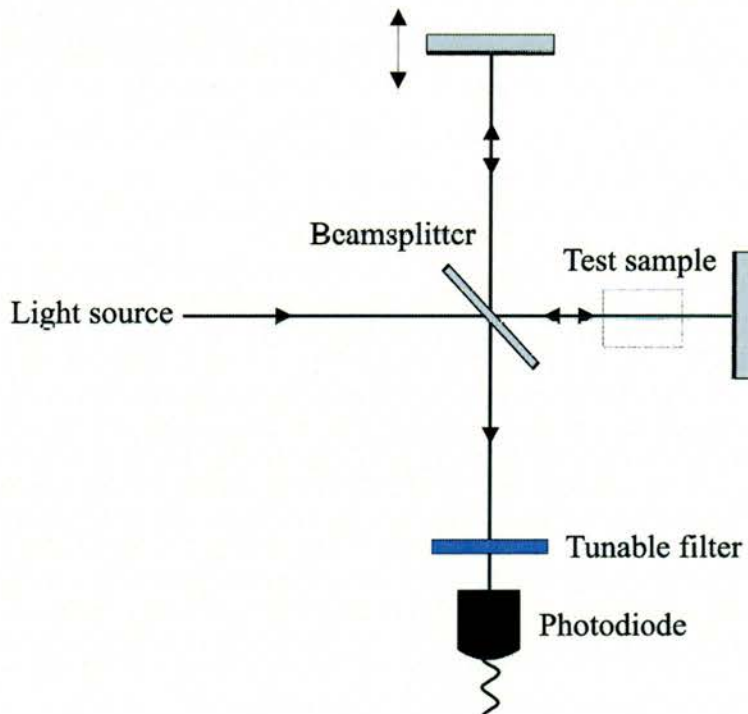


**Figure 3.1** Experimental arrangement used in the Fringe Contour Shift (FCS) technique

The FCS technique, shown in Figure 3.1, uses a collimated white light source that is passed through a Michelson interferometer. The output of the interferometer is detected using a photomultiplier tube and a lock-in amplifier, in front of which a tunable filter is placed. One

arm of the interferometer is scanned with high precision to produce an interferogram for a specific filter centre wavelength. Many interferograms are then recorded at differing filter positions. In a carefully balanced interferometer in which both arms possess equal amounts of dispersion, the centroid of each interferogram will have an identical temporal response. If, however, a dispersive element is added to one of the interferometric arms, the dispersion in each of the arms will become unbalanced making the centroid of each interferogram shift temporally. Measuring this shift across a range of filter positions allows the relative dispersion of the dispersive element to be measured. Tateda et al used a similar approach to measure the dispersion of a single-mode fibre but replaced the white light source and the frequency filter with a number of lasers, each operating at a distinct wavelength [2].

Although the FCS technique is relatively simple, its sensitivity is solely dependent upon the accurate location of the interferogram centroid. This also means that the measured light must have a finite spectral bandwidth to form a wave packet. To avoid this problem an alternative technique was devised called Phase-locked interferometry (PLI) [3, 4]. With PLI a monochromator is placed at the output of the Michelson interferometer to allow a narrow bandwidth of light to pass onto the photomultiplier tube. A fringe near the peak fringe visibility is then locked onto and used in an active feedback loop to make slight adjustments to the optical path length of one of the interferometric arms. If the interferometric arms are unbalanced, as the output wavelength of the monochromator is scanned, the optical path difference will change. To compensate, the active loop is utilised and automatically adjusts to keep the optical path difference the same. By recording the movement of the interferometric arm with respect to the scanning of the monochromator, the dispersion characteristics of the optical component are measured.

Both techniques described so far (FCS and PLI) require the filtering of the white light. Also, both techniques are known to give misleading results if the sample being measured is absorptive or if it has sharply varying spectral features [5, 6]. An interferometric technique

that does not have these disadvantages is the Fourier-Transform Correlation technique [6] and is the basis behind the simplified experimental technique described later in Section 3.3.

### 3.2.2 Intracavity-dispersion techniques

The dispersion within a laser cavity can critically determine the duration of the pulse that can be generated from it. A number of techniques have therefore been developed that allow the sum total of the dispersion within a cavity to be calculated. Two main techniques exist, one that is able to calculate the dispersion when the laser is not operational [7] and one that calculates the dispersion while the laser is modelocked [8]. These techniques, as discussed later, produced some unexpected results.

Naganuma et al [7] devised a technique very similar to the optical setup shown in Figure 3.1 but instead of a white light source the laser cavity was used as the light source into the Michelson interferometer. By pumping the gain medium just below threshold, the light emitted from the cavity consisted of periodic noise spikes that were separated by the round-trip time of the laser cavity. Each successive spike had a different temporal shape caused by the extra dispersion added to it after passing through the cavity for one additional transit. By allowing the arms of the Michelson interferometer to be separated so that the delay was equivalent to a whole number of round trips, it was possible to measure the interferogram between a spike and the same spike after it had circulated the cavity a set number of times. The spectral phase difference could then be measured to calculate the overall dispersion of the cavity.

A technique devised by Knox [8], enables the accurate dispersion measurement of a laser cavity while it is modelocked by measuring its repetition rate. The repetition rate of a laser is dependent upon the overall round-trip time of the cavity at a specific mean wavelength of the pulse. The optical path length of the cavity and hence the repetition rate will change if the

mean wavelength of the pulse changes. By tuning the laser across a range of wavelengths, while it is still modelocked, the change in repetition rate can be measured and thus the dispersion characteristics of the laser cavity can be deduced. Before this technique was devised it had been assumed that the dispersion characteristics of the cavity would change dramatically when the laser changed from CW to modelocked operation. This assumption was shown to be incorrect because the dispersion calculated within a modelocked cavity was very close to that of the sum of all the dispersive elements within the cavity [8]. This result showed it was only necessary to measure the dispersion of separate optical components within the cavity to be able to determine the dispersion within the whole cavity. A technique, outlined in Section 3.3, allows this to be carried out simply and accurately using white light interferometry.

### 3.3 Measurement of group velocity dispersion using the Fourier transform white-light interferometry

The majority of the techniques described in section 3.2 used to measure the dispersion of optical components rely on a Michelson interferometer. When white light is incident on the interferometer and the end mirror of one of the arms is scanned about zero path difference, an interferogram is formed [5, 6]. If a sample of unknown dispersion is included in the static arm while the scanned (reference) arm is kept empty, the interferogram signal,  $I(\tau)$ , measured by a photodiode at the interferometer output port is the intensity of the total field resulting from combining the field from the time-delayed reference arm,  $E_r(t-\tau)$ , with the field returned from the sample arm,  $E_s(t)$ :

$$I_1(\tau) = \int_{-\infty}^{\infty} |E_r(t-\tau) + E_s(t)|^2 dt \quad (3.1)$$

When the sample arm is lossless, the returned field differs from the reference field only by a frequency-dependent phase factor  $\phi_s$ , so that

$$e_s(\omega) = e_r(\omega) \exp[i\phi_s(\omega)] \quad (3.2)$$

where  $e_s(\omega)$  and  $e_r(\omega)$  are the Fourier transforms of  $E_s(t)$  and  $E_r(t)$  respectively.

Equation (3.1) can be expanded as

$$I_1(\tau) = \int_{-\infty}^{\infty} 2I(t)dt + \int_{-\infty}^{\infty} [E(t)E^*(t-\tau) + E^*(t)E(t-\tau)]dt \quad (3.3)$$

Combining equations (3.2) and (3.3) gives

$$I_1(\tau) = 2 \int_{-\infty}^{\infty} I_r(t)dt + FT^{-1}\{i(\omega)\exp[i\phi_s(\omega) + \pi]\} + FT^{-1}\{i(-\omega)\exp[-i\phi_s(-\omega) - \pi]\} \quad (3.4)$$

where the inverse Fourier-transform operation is denoted by  $FT^{-1}$  and the power spectrum of the light from the reference and sample arm is given as

$$i(\omega) = |e_r(\omega)|^2 = |e_s(\omega)|^2 \quad (3.5)$$

It is evident from Equation (3.4) that Fourier transforming the interferogram will result in a DC component and two conjugate terms at positive and negative frequency whose intensity is the power spectrum of the light source  $i(\omega)$  and whose phase,  $\phi_s(\omega) + \pi$ , is due to the sample dispersion. The dispersion of an unknown sample can therefore be found from two interferograms - a bias signal measured with an empty sample arm and a measurement signal recorded with the sample in place. Fourier transforming both interferograms and subtracting the phase of the bias spectrum from that of the measurement spectrum gives the double-pass sample phase dispersion,  $\phi_s(\omega)$ . If the sample is lossy then the ratio of the measurement and bias intensity spectra gives the *single-pass* frequency-dependent intensity loss factor. When the sample is lossless the power spectra calculated from the bias and measurement interferograms should be identical and this provides a useful check for the presence of systematic error in the data. The group delay,  $\tau(\omega)$ , can be expressed as a function of frequency,  $\omega$ , and optical phase,  $\phi$ :

$$\tau(\omega) = \frac{d\phi}{d\omega} \quad (3.6)$$

Once the sample phase dispersion,  $\phi_s(\omega)$  has been determined, Equation (3.6) can then be used to calculate the wavelength-dependent group delay of the sample.

### 3.3.1 Experimental configuration

The optical setup used to measure the group delay (Figure 3.2) comprised two parts. The principal part, used to measure the white light interferograms, consisted of a Michelson interferometer in which identical end mirrors were used in both the delay and sample arms to ensure that they contributed identical amounts of dispersion.

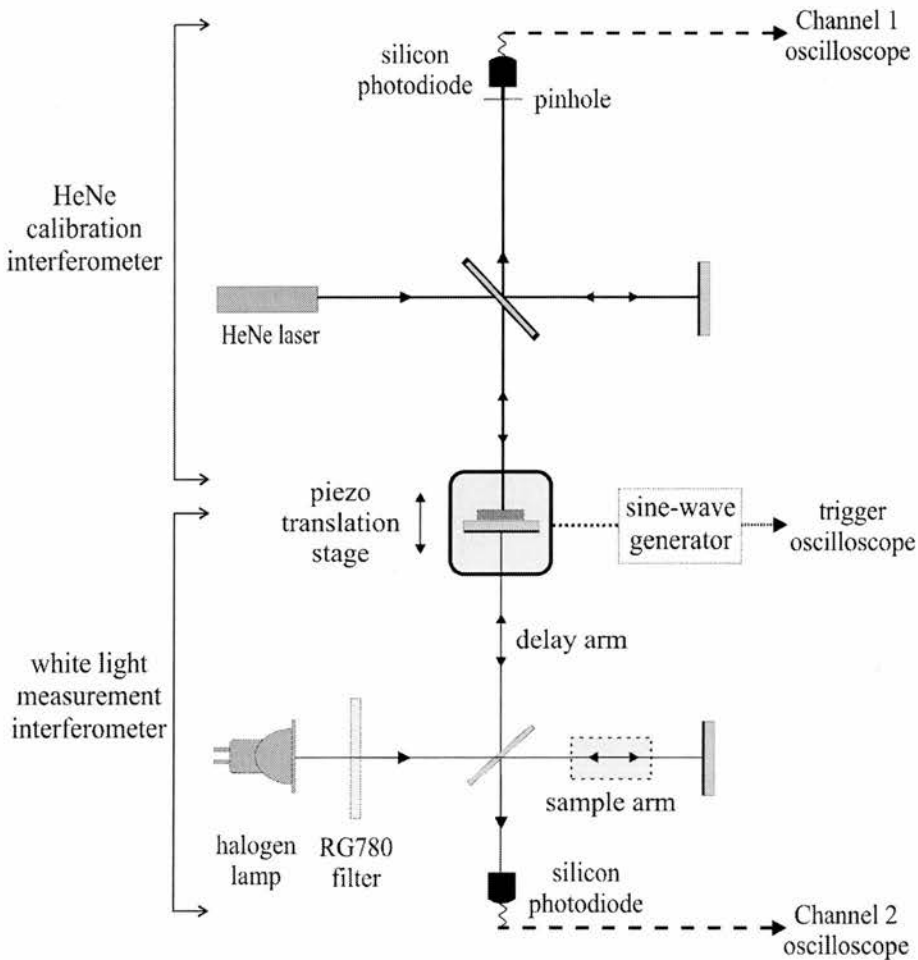


**Figure 3.2** The optical arrangement used to accurately measure the interferograms

The interferometer used a 1mm thick broadband near-infrared beamsplitter ( $R=50\pm 6\%$  from 530-1070nm) which allowed dispersion measurements around 800nm. Another beamsplitter could be substituted to allow measurements in the visible. The scanning of the delay arm end mirror was achieved using a piezo translation stage (Spindler & Hoyer, PX5-400) and a sine-wave generator was used to drive it at a frequency of  $\sim 15\text{Hz}$ , allowing a maximum travel of  $400\mu\text{m}$  to be achieved. It should be mentioned that the piezo stage could easily have been

replaced with a modified loudspeaker to provide a cheaper alternative. The only criterion the scan element must meet is that the travel produced by it must be large enough to allow the whole interferogram to be measured. The piezo translator was sufficient to allow measurement of a glass substrate with a thickness of  $\sim 5\text{mm}$  and a loudspeaker-based design would enable measurements of samples several times longer. A standard halogen lamp of the kind found in low-voltage domestic lighting was used as the white light source. An infrared pass (RG 780) filter was included in front of the halogen lamp to confirm that the apparatus calibration was correct by checking that the calculated power spectrum of the lamp did not contain wavelengths shorter than the filter cut-off.

Exact calibration of the time-axis of the measured interferogram is vital if group delay is to be calculated accurately. The second part of the optical setup dealt with this problem. By attaching an aluminium mirror to the back surface of the delay arm mirror, a second interferometer was configured as shown in Figure 3.2. By aligning a 633nm HeNe laser beam through both arms of this interferometer a simultaneous fringe pattern was recorded at the output using another silicon photodiode. The wavelength of the HeNe laser is known precisely and therefore accurate calibration of the delay arm was possible simply by counting fringes (1 fringe=2.11 fs).

To provide an accurate calibration, both the interferogram and the HeNe fringes were recorded simultaneously using a two-channel digitising oscilloscope (Tektronix TDS3032) capable of sampling 10000 data points per channel. The timebase of the oscilloscope was optimised to spread the interferogram across the whole trace, while ensuring the interferogram intensity was zero at the trace edges. The information from the oscilloscope was then transferred via the oscilloscope RS232 interface to a computer where the scientific programming language MATLAB was used to analyse the data. The MATLAB code counted the number of HeNe fringes observed over the recorded region, enabling a time-scale to be created across the sampled scanning range. These data were then used to interpolate the

interferogram onto a linear  $2^n$  array that had a constant sampling period,  $dt$ . This acquisition and calibration procedure was repeated twice, once with the empty sample arm to give the bias signal, and again in the unbalanced state with the sample in place.

The MATLAB code in Figure 3.3 takes the Fourier transform of the two calibrated interferograms (*sample.dat* and *bias.dat*). The imaginary part of each Fourier transform ( $p$  and  $p0$ ) relates to the spectral phase where as the real part relates only to the spectral amplitude. The dispersion characteristics of the test sample are obtained by subtracting the two spectral phase terms with one another. Using equation (3.6), the group velocity of the sample is then determined. The power spectra from both interferograms were also plotted and compared with one another. This provided a useful test to ensure that the data were not corrupted. This is because if the test sample was lossless both spectra should be identical, it is only the spectral phase that should change.

```



```

**Figure 3.3** MATLAB code used to calculate the dispersion characteristics from the two experimentally acquired interferograms

### 3.3.2 Dispersion measurements of a KTP crystal

The dispersion characteristics of a 1.2mm thick potassium titanyl phosphate (KTP) crystal were investigated to provide an example of a typical transmission measurement. KTP is a birefringent (positive biaxial) crystal so in addition to the optical arrangement in Figure 3.3, a polariser cube was placed in front of the measurement photodiode to ensure that the recorded results were for one optical axis only. Results presented within this section apply only to the z-axis, but it should be noted that other orientations of the crystal could have been readily investigated.

To ensure the correct interferogram was recorded it was important that only light that had passed through the crystal was allowed to travel through the sample arm, and this was achieved by masking the area around the crystal with a card. Pre-alignment of the interferometer using a HeNe laser meant that finding the white-light interferogram only required translation of one of the interferometer end mirrors.

For ease of calibration both the sample and bias interferograms were recorded using the same timebase on the digitising oscilloscope. The interferogram with the sample present (the 'sample' condition) will always be wider in time than the one obtained when the sample arm is empty (the 'bias' condition). It was therefore convenient to record the sample interferogram first to ensure the timescale was sufficient. Once recorded, the oscilloscope settings did not require changing for the bias measurement.

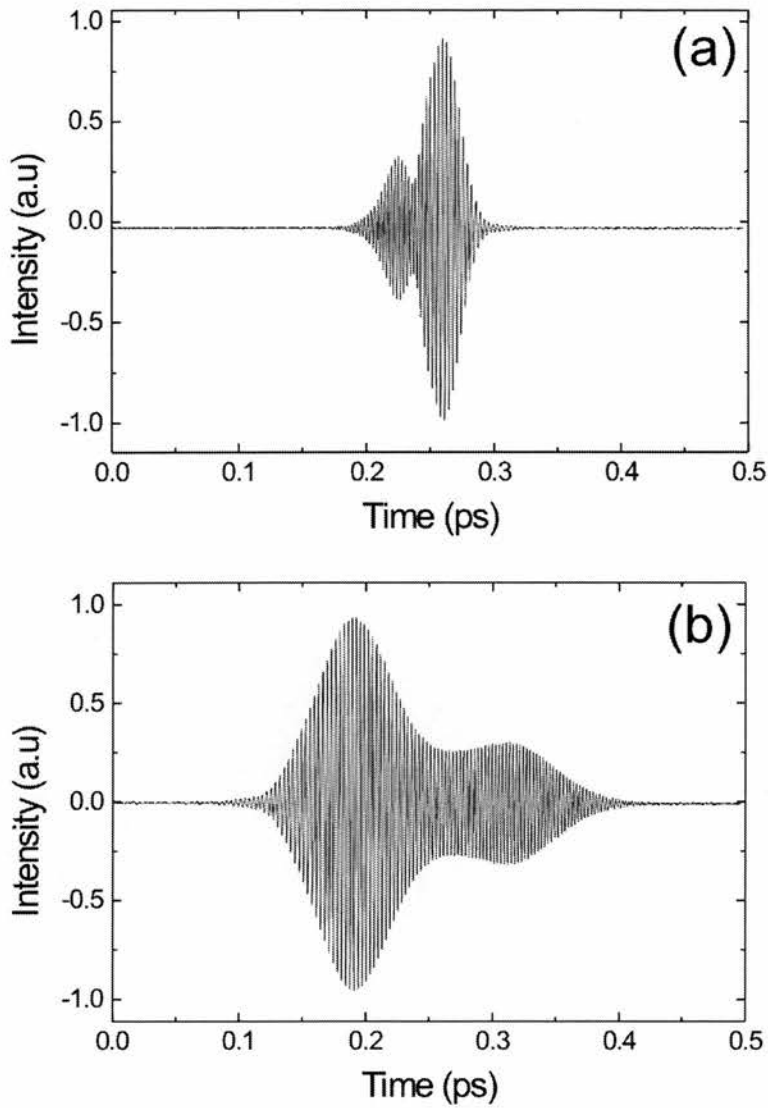


**Figure 3.4** The bias (a) and sample (b) interferograms from the interferometer

Figure 3.4 shows the two interferogram traces acquired when the KDP crystal was in and out of the interferometer optical setup. The interferogram clearly broadens as a dispersive element is added into one of the interferometric arms. Figure 3.5 compares the power spectrum obtained from each of the interferograms.

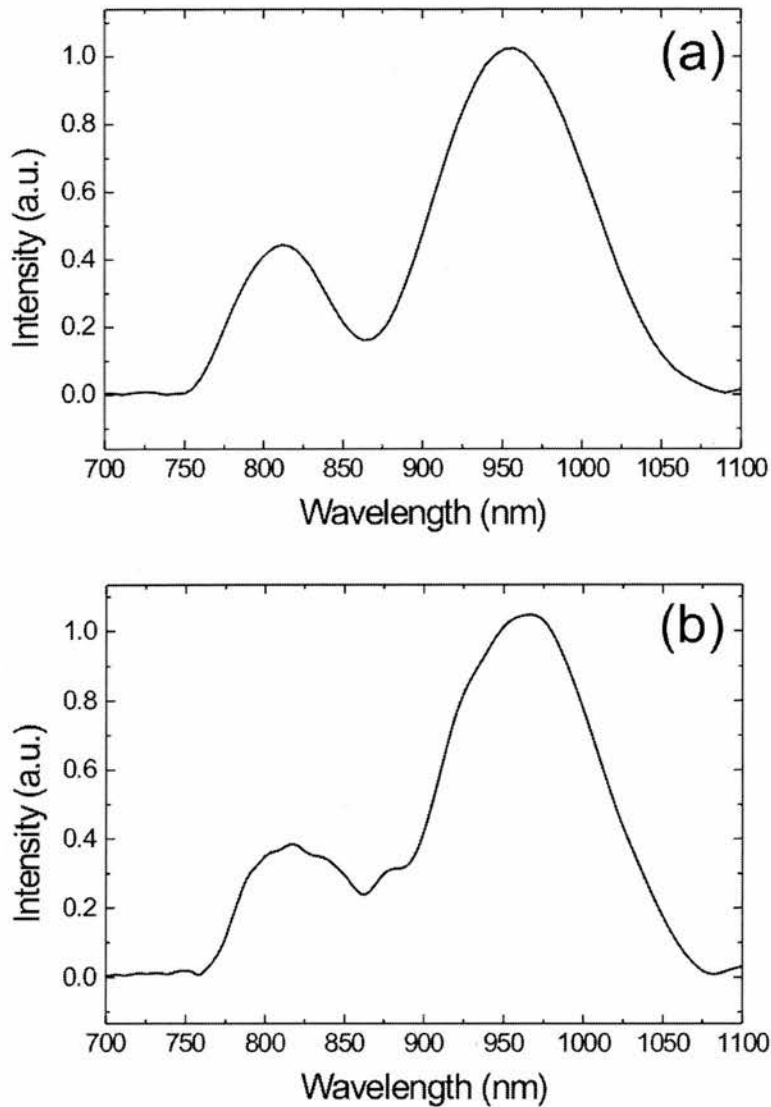


**Figure 3.5** The power spectrum from (a) the bias interferometer and (b) the sample interferometer

As expected, the two power spectra show a spectrum with a minimum wavelength of around 750nm that corresponds to the cut off wavelength of the RG780 filter. It is easy to see that the two spectra compare extremely well with one another and this confirms two things. Firstly, it shows that the experimental data acquired were taken correctly and that no fringe information from the interferograms was lost during the acquisition stage. Secondly, it shows that the KTP crystal had uniform transmission across the measured range of wavelengths.

The experimentally obtained group velocity dispersion measurements are shown in Figure 3.6. These results were compared with those predicted theoretically for a flux grown KTP crystal using a Sellmeier equation for the crystal z-axis refractive index [9]

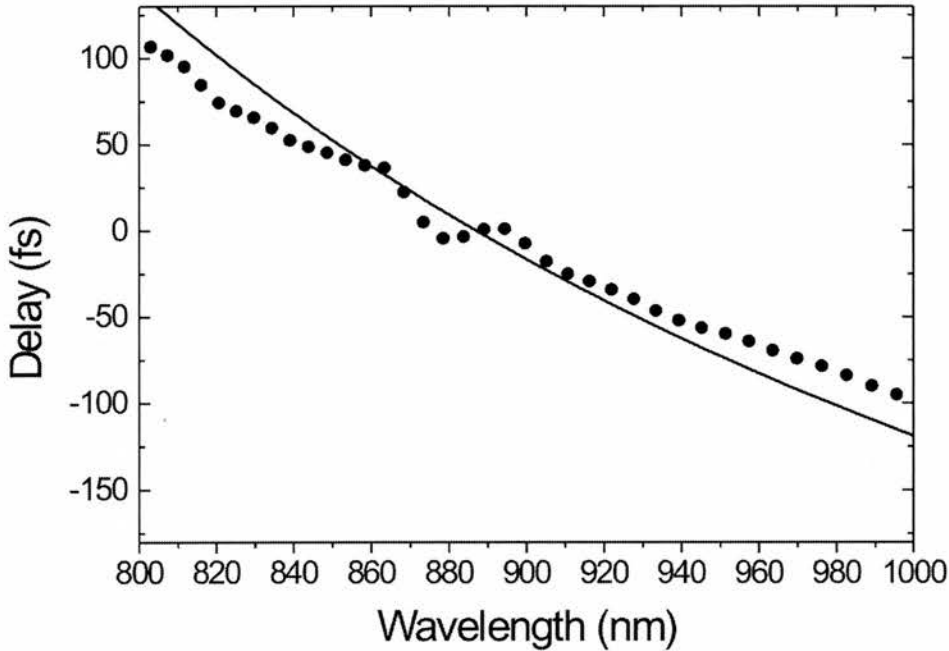


**Figure 3.6** The group velocity dispersion measured experimentally (symbols) and that inferred from KTP Sellmeier data (solid line)

The close agreement between the experimental and theoretical data demonstrates the effectiveness of this technique. It should be emphasized that although the length of the crystal was 1.2mm, a double-pass optical layout exists such that the effective dispersion length seen by the white light is twice the crystal length (ie. 2.4mm).

### 3.3.3 Dispersion measurements of a silver coated mirror

To demonstrate the sensitivity of this method, the reflectivity dispersion of a silver coated mirror (New Focus, 5103) was analysed. The measurement was made by placing a silver mirror at a fold within the sample arm and at  $45^\circ$  incidence to the incident light. The sample arm end mirror was unchanged and identical to the reference arm end mirror. A HeNe laser was initially used to align the sample arm. The bias and sample interferograms were measured in exactly the same way as in section 3.3.2. Again, a double-pass optical setup was in place so that the measured dispersion was in fact from two reflections of the silver mirror.

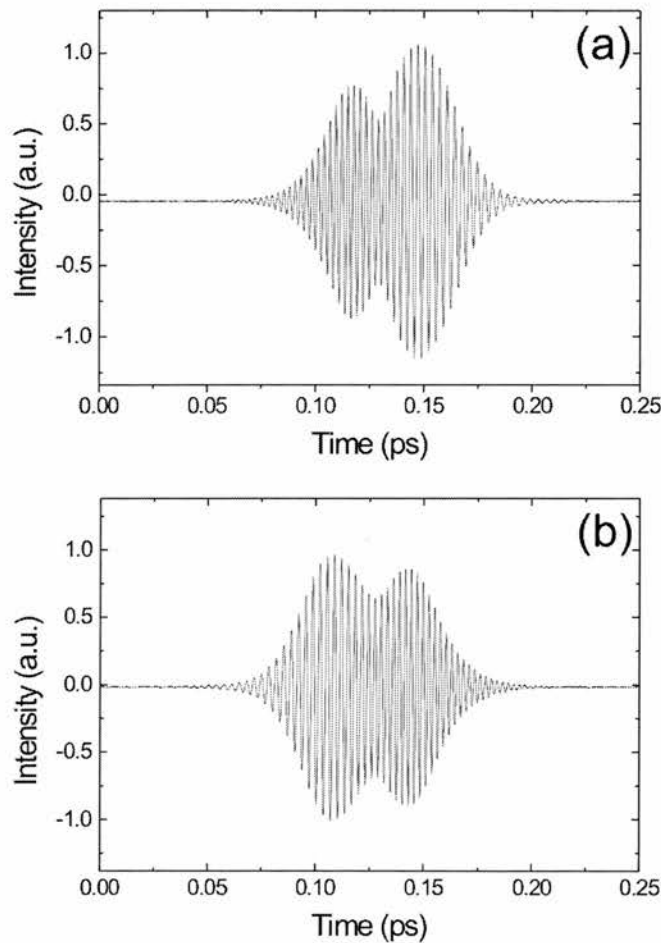


**Figure 3.7** The interferograms obtained while measuring the reflectivity dispersion of a silver mirror from the (a) bias interferometer and (b) the sample interferometer

Both the bias and sample interferograms show very similar temporal durations. This gives an initial indication that only minimal dispersion was added by the reflection from the silver

mirror. Again, to ensure that the two interferograms were recorded correctly, the power spectra obtained from each interferogram were compared with one another.

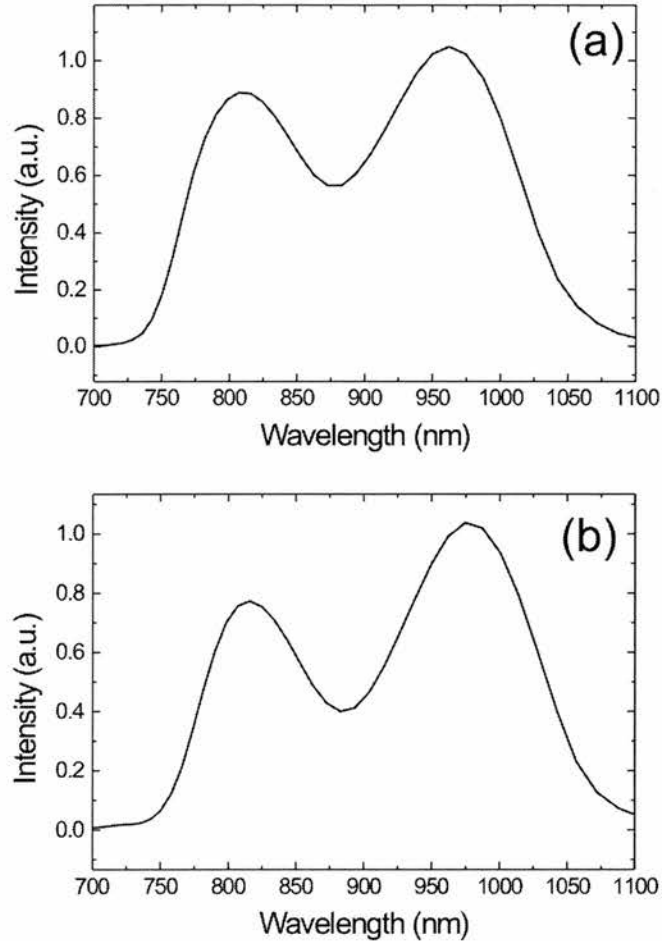


**Figure 3.8** The power spectrum obtained while measuring the reflectivity dispersion of a silver mirror from the (a) bias interferometer and (b) the sample interferometer

Again the two power spectra are similar showing that all data were acquired correctly as well as showing that the silver mirror had broad and uniform transmission at the measured wavelengths. The dispersion results outlined in Figure 3.9 show the dispersion characteristics for a single reflection from a silver mirror. This is important to highlight because the initial, calculated result is of a double-pass arrangement and must consequently be halved to obtain a value for a single reflection.

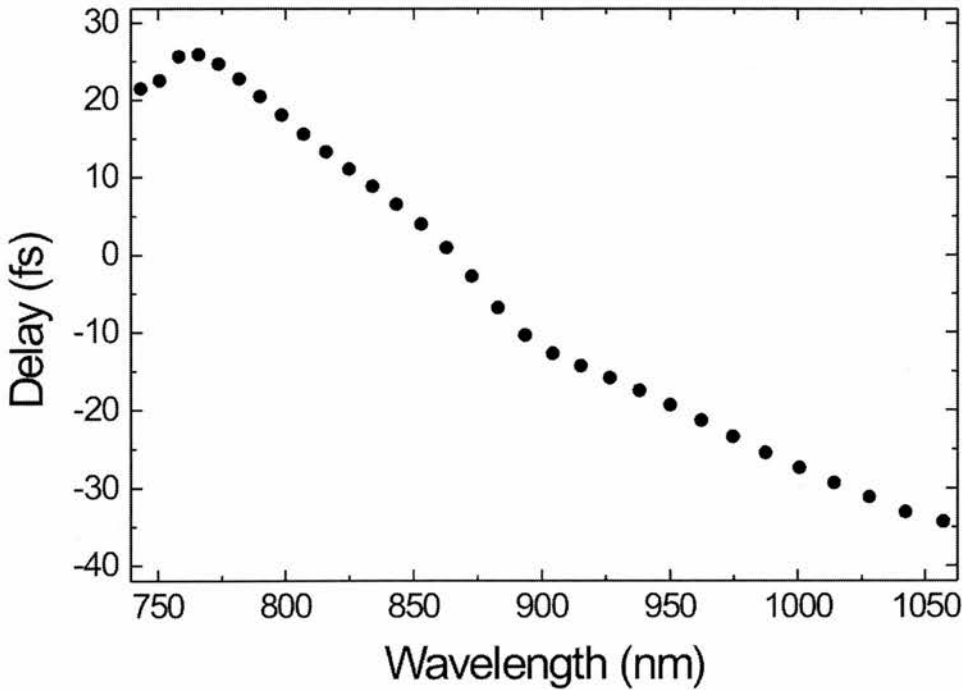


*Figure 3.9* The group velocity dispersion inferred for a single reflection from a silver mirror

Although the measured dispersion from the silver mirror is small, the data obtained is extremely smooth. This demonstrates the high degree of accuracy provided by this dispersion measurement technique.

### 3.3.4 The mystery of the non-dispersion-compensated modelocked laser

Soon after the dispersion characterisation technique was devised, it was used to help explain why a colleague's laser, which contained no apparent dispersion compensation element, was modelocking in a femtosecond pulse regime. During the initial alignment of a compact Cr:LiSAF laser it was noticed that the laser could be successfully modelocked to give transform-limited pulses of 136fs [10]. This was highly unusual because there was no obvious source of negative GVD that was required for modelocked operation within the femtosecond regime. After substituting optical components within the laser cavity it was concluded that the source of negative dispersion could only have originated from the cavity mirrors. This was

very surprising given that the mirrors (Quality Thin Films (QTF), Tampa, FL, USA) were designed only to be standard high reflectors. The dispersion characteristics of these mirrors were therefore investigated in some detail. Figure 3.10 outlines the results obtained using the same technique described in section 3.3.3.

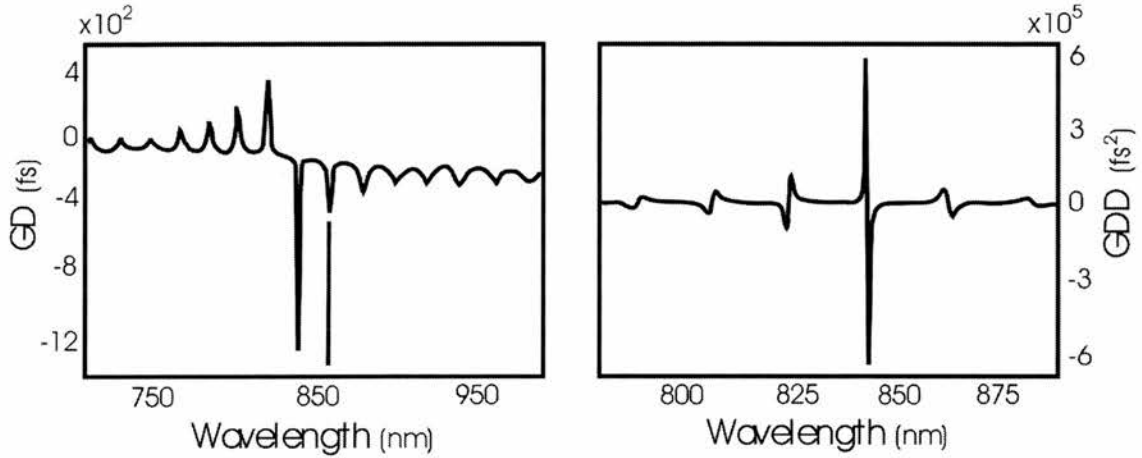


**Figure 3.10** Dispersion characteristics obtained from the Cr:LiSAF laser's QTF mirrors

The dispersion characteristics from the QTF mirrors, although surprising, explained why the laser modelocked successfully. The dielectric mirror coating shows periodic drops in dispersion. One of these periodic drops corresponds coincidentally to the Cr:LiSAF lasing wavelength of 859nm. The dispersion at this wavelength is similar to that of a GTI mirror that has already been shown to provide enough negative GVD to compensate for positive intra-cavity dispersion [11, 12].

### 3.4 Conclusion

In this chapter I have described a number of techniques that have been used to measure the dispersion characteristics of optical components and systems. I have then described a relatively simple but powerful technique capable of accurately measuring the dispersion of optical components. The accuracy and sensitivity of the technique was demonstrated by measuring the dispersion of a KDP crystal and a silver mirror. In the next chapter this technique will be utilised to provide dispersion characteristics of a frequency filter which is required for successful sonogram pulse retrieval.

### 3.5 References

- [1] W. H. Knox, N. M. Pearson, K. D. Li, and C. A. Hirlimann, "Interferometric Measurements of Femtosecond Group Delay in Optical-Components," *Optics Letters*, vol. 13, pp. 574-576, 1988.
- [2] M. Tateda, N. Shibata, and S. Seikai, "Interferometric Method for Chromatic Dispersion Measurement in a Single-Mode Optical Fiber," *Ieee Journal of Quantum Electronics*, vol. 17, pp. 404-407, 1981.
- [3] M. Beck and I. A. Walmsley, "Measurement of Group Delay with High Temporal and Spectral Resolution," *Optics Letters*, vol. 15, pp. 492-494, 1990.
- [4] M. Beck, I. A. Walmsley, and J. D. Kafka, "Group Delay Measurements of Optical-Components near 800 Nm," *Ieee Journal of Quantum Electronics*, vol. 27, pp. 2074-2081, 1991.
- [5] W. H. Knox, "Dispersion Measurements For Femtosecond-Pulse Generation and Applications," *Applied Physics B-Lasers and Optics*, vol. 58, pp. 225-235, 1994.
- [6] K. Naganuma, K. Mogi, and H. Yamada, "Group-Delay Measurement Using the Fourier-Transform of an Interferometric Cross-Correlation Generated By White-Light," *Optics Letters*, vol. 15, pp. 393-395, 1990.
- [7] K. Naganuma and Y. Sakai, "Interferometric Measurement of Wavelength Dispersion on Femtosecond Laser Cavities," *Optics Letters*, vol. 19, pp. 487-489, 1994.
- [8] W. H. Knox, "Insitu Measurement of Complete Intracavity Dispersion in an Operating Ti - Sapphire Femtosecond Laser," *Optics Letters*, vol. 17, pp. 514-516, 1992.
- [9] T. Fan, C. Huang, B. Hu, R. Eckardt, Y. Fan, R. Byer, and R. Feigelson, "Second harmonic-generation and accurate index of refraction measurements in flux-grown KTiOPO<sub>4</sub>," *Applied Optics*, vol. 26, pp. 2390-2394, 1987.
- [10] B. Agate, A. Kemp, J.-M. Hopkins, D. Burns, U. Keller, and W. Sibbett, "Highly-compact femtosecond Cr:LiSAF Lasers," presented at Conference on Lasers and Electro Optics, Baltimore, 2001.
- [11] R. Szipocs, A. Kohazi-Kis, S. Lako, P. Apai, A. P. Kovacs, G. DeBell, L. Mott, A. W. Louderback, A. V. Tikhonravov, and M. K. Trubetskov, "Negative dispersion mirrors for dispersion control in femtosecond lasers: chirped dielectric mirrors and multi-cavity Gires-Tournois interferometers," *Applied Physics B-Lasers and Optics*, vol. 70, pp. S51-S57, 2000.
- [12] B. Golubovic, R. R. Austin, M. K. Steiner-Shepard, M. K. Reed, S. A. Diddams, D. J. Jones, and A. G. Van Engen, "Double Gires-Tournois interferometer negative-dispersion mirrors for use in tunable mode-locked lasers," *Optics Letters*, vol. 25, pp. 275-277, 2000.

# CHAPTER 4

## Developments towards real-time pulse characterisation using sonograms

---

### 4.1 Introduction

The past decade has seen tremendous developments in ultrafast laser science. The improved availability of stable and reliable commercial systems has allowed ultrafast lasers to become more widespread in industry and the life sciences, enabling the unique properties that their output pulses exhibit to be utilised for many diverse purposes. As applications have increased over recent years, so has the demand for techniques that are able to fully characterise a pulse in amplitude and phase, thus enabling the exact tailoring of pulses for specific experiments. Such a capability is becoming vital in an ever-increasing number of studies such as coherent control experiments where it has been shown that not only the pulse duration but also its phase (or chirp) can affect the interaction [1]. Conventional rapidly-updating pulse measurements such as those provided by scanning autocorrelators [2] and spectrometers are versatile and convenient but fail to give complete and ambiguous pulse information. Ideally the experimentalist would have access to a real-time technique that would be capable of updating while tailoring of the pulse was being carried out. This would allow greater control and knowledge of the pulse prior to the experiment and would eliminate uncertainties arising from laser fluctuations in the time between the pulse measurement and the actual experiment.

The two most successful techniques that have been demonstrated to provide real-time pulse characterisation are SHG-FROG [3-5] and SPIDER [6-8]. A SHG-FROG system has been shown to acquire and retrieve a spectrogram at a frequency of 2.3 Hz [9]. The SPIDER

technique, already described in detail in chapter 2, requires only the acquisition of a one-dimensional (1-D) array as opposed to SHG-FROG in which a much larger two-dimensional (2-D) array is required. The computationally intensive retrieval algorithm needed in SHG-FROG is not required with SPIDER which instead uses a direct, non-iterative inversion routine. As a consequence, rapid, real-time (20Hz) pulse characterisation from the output of a regeneratively amplified laser has been achieved using SPIDER [10].

One of the fundamental advantages of time-frequency techniques like SHG-FROG is their powerful ability to verify calibration and check for any systematic errors that may have been introduced during the acquisition and retrieval stages by using the properties of the temporal and spectral marginals of the trace [11]. An alternative technique that possesses certain advantages over SHG-FROG yet which still retains the same error checking ability of marginals is based on measuring the sonogram of the pulse:

$$I_{sonogram}(t, \Omega) = \left| \int_{-\infty}^{\infty} E(\omega) G(\omega - \Omega) e^{+i\omega t} d\omega \right|^2 \quad (4.1)$$

A sonogram records the group delay of each frequency component using a frequency-filter  $G(\Omega)$  followed by a time-resolved measurement of its intensity[12]. A Michelson or Mach-Zehnder interferometer with a spectral bandpass filter placed within one of its arms can be used to experimentally measure a sonogram. By taking many cross-correlations at various filter centre frequencies, the sonogram can be constructed. The main difference between the FROG and sonogram techniques is that whereas FROG initially gates in the time-domain and then, using a spectrometer to measure the mixing signal from a nonlinear crystal, gates in the frequency-domain (Figure 4.1a), the sonogram reverses the orders of the gating processes. This difference allows the nonlinear crystal and the photomultiplier tube from the FROG apparatus to be replaced with a much simpler two-photon absorption (TPA) detector [13, 14] (Figure 4.1b).

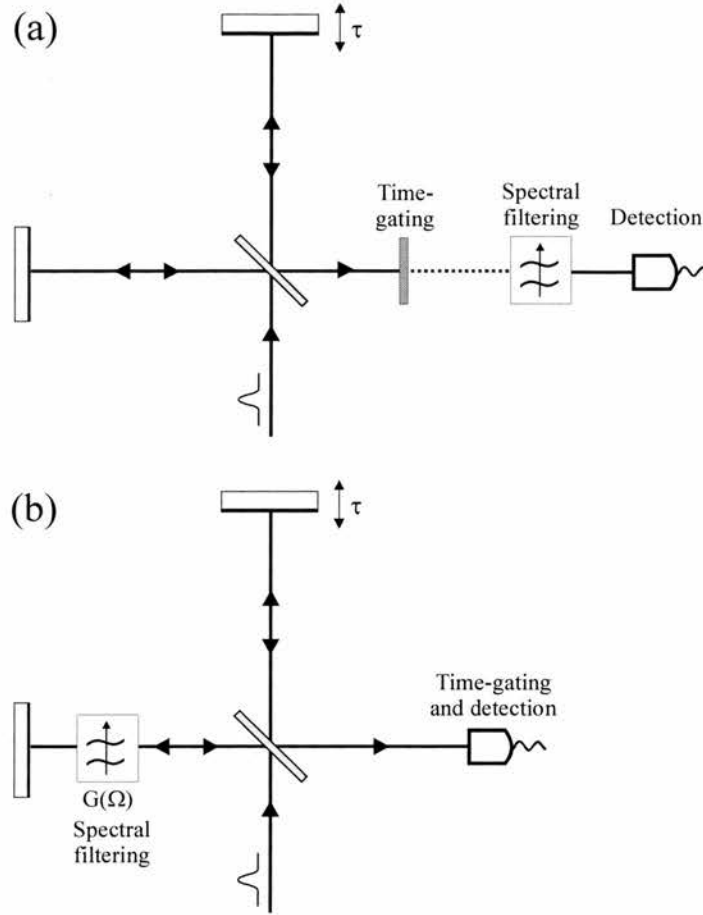


**Figure 4.1** Schematic of how a FROG trace (a) and a sonogram trace (b) are acquired

TPA detectors have an inherently broad detection bandwidth, making them ideally suited to measurement of ultrashort pulses; they are also highly sensitive, polarisation insensitive, cheap and readily available. The use of TPA detectors within a typical autocorrelation setup is now commonplace and they have been used to measure very short pulses without the restrictions of limited phase-matching bandwidth associated with conventional frequency mixing crystals [15]. Pulses with energies as little as 12 pJ have been characterised using TPA-sonograms [16], helping underline the high sensitivity that can be achieved by combining TPA and sonogram techniques. The sonogram trace is much more intuitive than that of a SHG-FROG and allows, unlike SHG-FROG, the direct determination of the sign of the chirp. Figure 4.2 helps demonstrate this by comparing SHG-FROG and sonogram traces with various pulses; it shows how negative and positive chirp skews the sonogram trace

anticlockwise and clockwise respectively whereas the SHG-FROG traces remain symmetric along the delay axis.

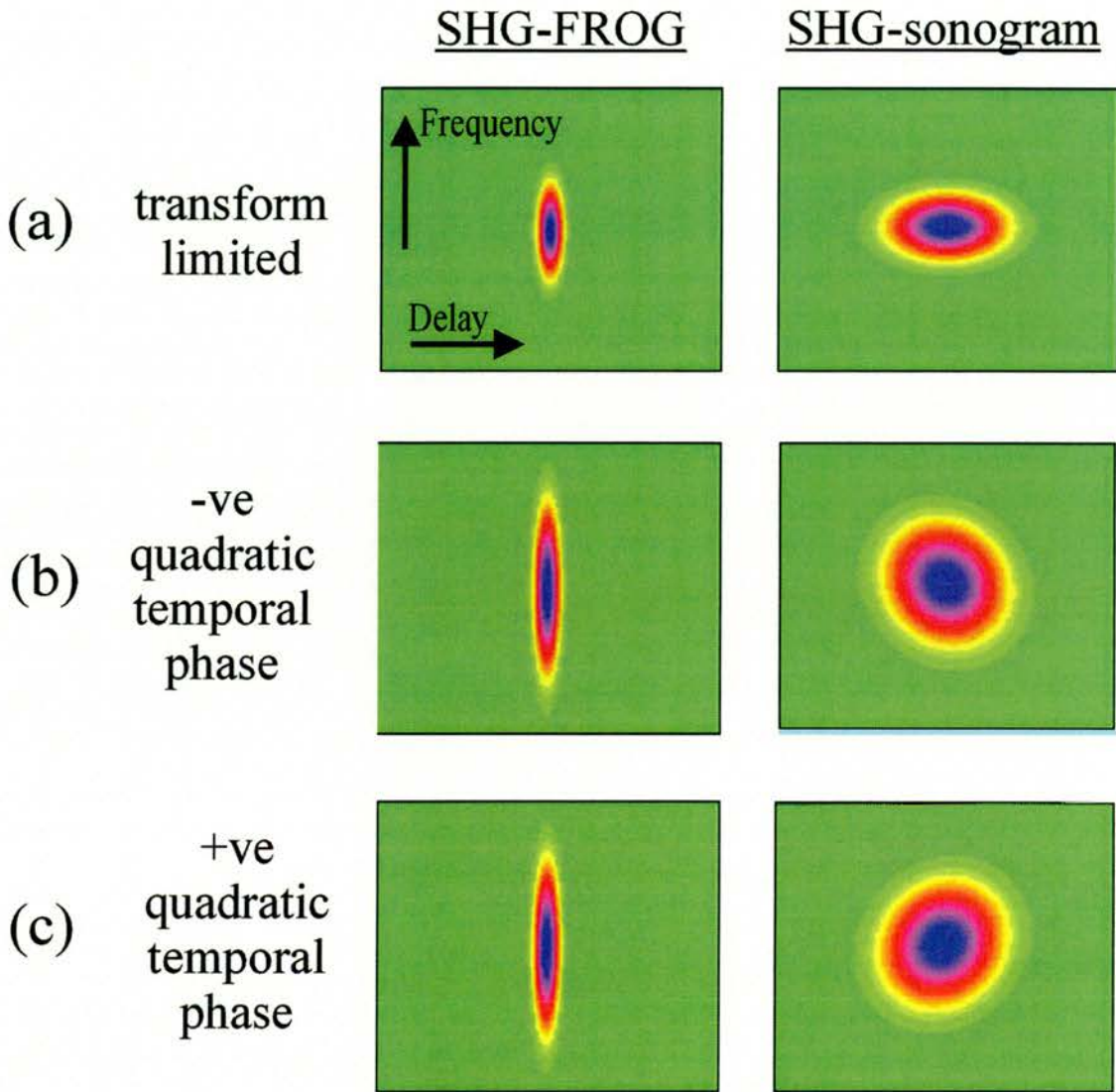


**Figure 4.2** Comparison between a SHG-FROG (left column) and a SHG-sonogram (right column) trace for a Gaussian pulse with (a) no chirp, (b) negative quadratic phase and (c) positive quadratic phase

When measuring a sonogram using a cross-correlation technique like that in Figure 4.1(b) the actual measurement being taken is

$$I(t) * I_{\text{sonogram}}(t, \Omega) \quad (4.2)$$

where \* indicates convolution. To ensure this experimental quantity is equal to the sonogram trace of the pulse, the spectral filter must be sufficiently narrow for the filtered pulse to be much longer than the original pulse. When this occurs the pulse intensity  $I(t)$  approximates to

a delta function relative to the temporal width of the sonogram. A filter bandwidth of around one third of the pulse spectrum works well, although narrower filters can be used [17, 18]. If the filter bandwidth is too small the trace becomes broad in time and large grid sizes are required.

As with FROG, the sonogram technique can also use the frequency and time marginals of the trace to confirm the integrity to the acquired data [18]. The time marginal of the experimentally measured sonogram trace is the integral along the frequency axis and is given as,

$$M_{\tau}(\tau) = A^{(2)}(\tau) * |F\{G(\omega)\}|^2 \quad (4.3)$$

where  $A^{(2)}(\tau)$  is the second-order background-free intensity autocorrelation, \* indicates convolution and  $F$  represents the Fourier transform operation. Similarly the frequency marginal of the sonogram trace is given as,

$$M_{\omega}(\omega) = I(\omega) * |G(\omega)|^2 \quad (4.4)$$

The frequency marginal is equivalent to the convolution of the independently measured pulse spectrum and the retrieved filter transmission intensity. The delay marginal is equivalent to the convolution of the pulse autocorrelation and the intensity of the Fourier transformed filter amplitude. Equations (4.3) and (4.4) will be used later on in this chapter to verify that the measured sonograms are void of any systematic errors.

Using sonograms to characterise pulses in real time has, until recently, not been considered viable. There are two main reasons for this, firstly the computationally intensive retrieval algorithm required to extract pulse information from the sonogram trace and secondly the large amount of data that must be acquired and processed to obtain a sonogram trace. However, the recent advancements in retrieval algorithms [9, 18-21] combined with the availability of high-speed personal computers has meant the overall speed of the procedure is

now limited not by the pulse retrieval routine, but solely by the acquisition time of the sonogram trace.

The acquisition of a sonogram involves the collection of many data points, all of which have to be calibrated and analysed correctly. Whereas in FROG, it is possible to utilise multi-channel detectors (eg CCD arrays) the absence of nonlinear line or area detectors means sonograms must generally be recorded using point detectors.

To develop a fast sonogram characterisation setup, many separate practical problems need to be solved simultaneously within a single system. Firstly, an accurate sonogram needs to be recorded quickly. A sonogram optical setup is made up from two major parts, the spectral bandpass filter and the delay line. For rapid acquisition, both the delay line and the spectral bandpass filter have to be carefully synchronised to enable fast and accurate recording of cross-correlations at each different filter position. To avoid systematic errors, the method by which this is achieved must be carefully implemented. Secondly, the many cross-correlation traces which are combined to create a sonogram trace must be acquired by a personal computer so that the trace can be calibrated, retrieved and displayed on the computer screen.

Described within this chapter are two systems that have been used successfully to rapidly acquire and retrieve a sonogram trace. The main difference between these two arrangements is how the spectral bandpass filtering is implemented. The first technique uses the traditional optical arrangement, first used by Chilla and Martinez [12], that consists of a grating and slit to spatially separate and filter out the different spectral components. The second system is faster and uses a scanning Fabry-Perot filter as the bandpass filter.

## 4.2 Using the ‘traditional’ sonogram optical arrangement

In 1992 Chilla and Martinez were the first researchers to demonstrate a practical pulse phase characterisation technique [12]. This section describes how a similar optical arrangement constitutes a sonogram-based system.

### 4.2.1 Design of the frequency bandpass filter

The design of the frequency bandpass filter used in this section originated from early pulse shaping experiments [22, 23] (Figure 4.3). This system used a pair of diffraction gratings and a pair of lenses in a  $4f$  arrangement. By placing a mask within the Fourier plane, the spectral intensity and phase of the pulse can be altered. Recently, this optical arrangement has been used to correct the spectral phase of a pulse so that it becomes near transform limited [24].

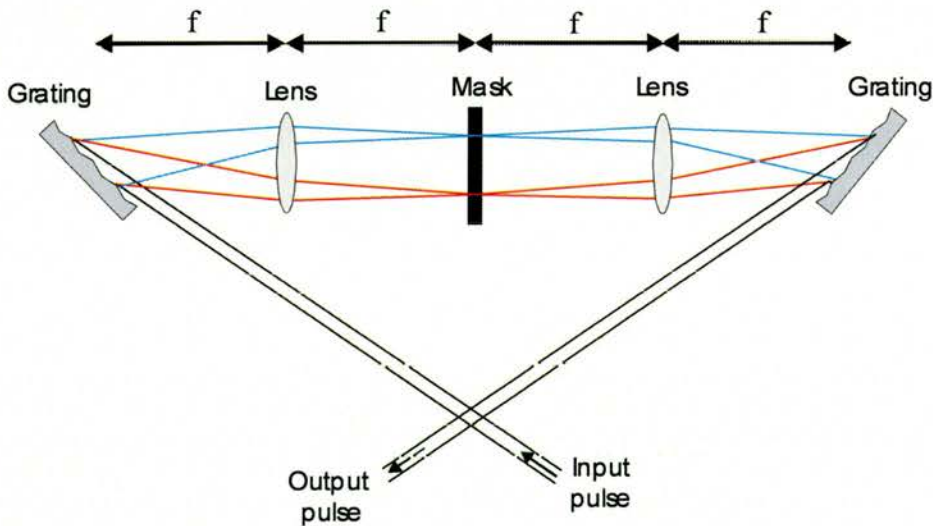


**Figure 4.3** Optical filtering arrangement used in a pulse shaping experiment

In the experiments described here we used a folded filter and replaced the mask with a mirror, allowing a single diffraction grating and lens to be used. By placing a narrow slit at the surface of this mirror, the bandwidth and frequency of the light returned by the filter was able to be selected. In my arrangement (Figure 4.4) I used a grating with 1200 lines/mm, a lens with a focal length of 125mm and a silver coated mirror to ensure a constant reflectivity and phase across the spectral bandwidth of the pulse.

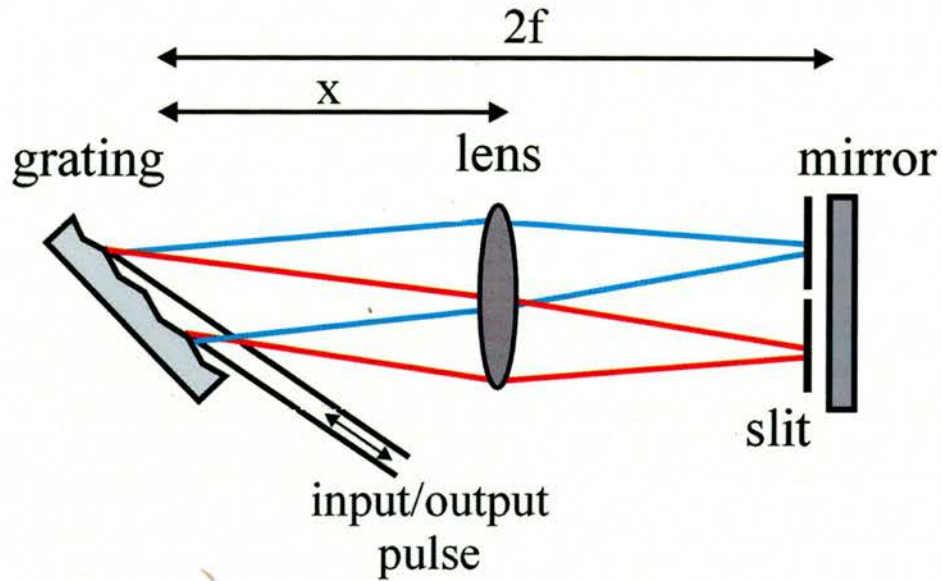


**Figure 4.4** Schematic of the frequency bandpass filter consisting of a grating, lens and mirror within a  $2f$  arrangement, enabling a slit to be placed at the Fourier plane to selectively filter the outgoing pulse

To enable the returning, filtered pulse to be readily collected, a vertical offset within the lens was made so that the filtered pulse returned back at a different height to the incoming pulse. It was important to ensure that both the incoming and outgoing pulses passed through the same amount of glass within the lens and the arrangement used is shown in Figure 4.5.

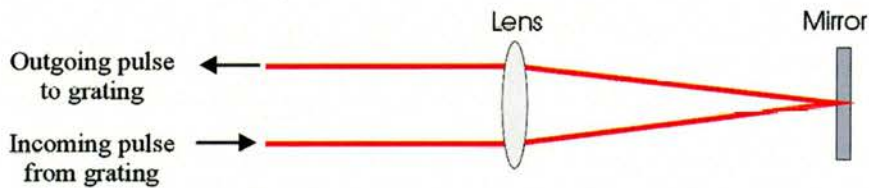


**Figure 4.5** Side view of the lens-mirror configuration

To verify that a linear movement of the slit corresponded to a linear change in filtered wavelength, the spectrum of the outgoing pulse was measured with respect to the position of the slit. The slit was mounted on a translation stage and the movement of this stage was computer controlled by using a stepper motor. Using a screwthread of 80 turns per inch and a stepper motor that rotated  $1.8^\circ$  every time a TTL pulse was applied to it, we obtained a resolution of  $1.58\mu\text{m}$  per TTL pulse. Figure 4.6 shows a graph of outgoing pulse spectra against number of TTL pulses applied to the stepper motor. Four measurements were taken,

each separated by 500 steps of the stepper motor and shows a clear linear relationship between slit position and peak wavelength of the filtered spectra. All spectra were normalised to enable comparison of their peak wavelengths.

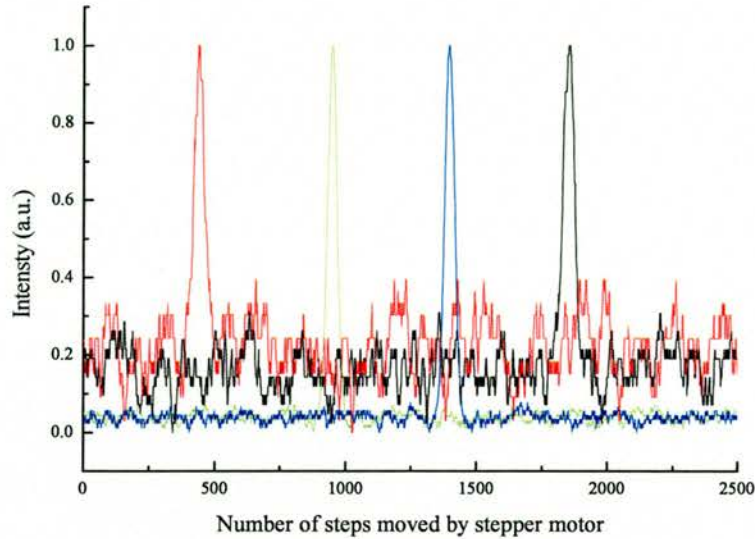


**Figure 4.6** *The filtered spectra at 4 equally spaced slit positions*

An important consideration when designing the bandpass filter was its dispersion related response. Ideally the bandpass filter should be dispersionless so that the spectral phase of the pulse is unaltered when it returns from the filter. It is important to define two separate forms of dispersion that are associated with a spectral bandpass filter. Firstly there is spectral-independent phase that can occur in a number of filters such as a Fabry-Perot filter described in Section 4.3.1. This type of phase has a characteristic form which remains centred on the filter transmission wavelength. Consequently, the phase response is intrinsically associated with the filter or gate function and can therefore be fully retrieved when the sonogram trace is passed through the retrieval algorithm. The spectral bandpass filter used in the experiments described within this section consisted only of a slit so it was safe to assume that there was no spectral-independent phase associated with it. As a result, the phase of the gate function was set to zero and used as a constraint to reduce the number of iterations required for convergence. The second type of dispersion is wavelength dependent phase in the form of group velocity dispersion. This type of dispersion distorts the pulse measurement and must

either be minimised or fully characterised and removed from the retrieved pulse spectral phase

The group-velocity dispersion that is introduced by the filter in Figure 4.4 varies from negative to positive when the position of the lens is moved with respect to the grating and mirror (varying distance  $X$  in Figure 4.4). The dispersion was carefully characterised to ensure the filter provided zero-group-velocity dispersion across the bandwidth of the pulse and this was implemented using white light interferometry. Described in more detail in Chapter 3 the technique was specifically chosen because it was well suited to measuring the dispersion of the filter *in situ* by recording two interferograms from a Michelson interferometer into one arm of which the filter can be inserted. The first interferogram is a bias signal and is measured without the filter and contains information on the intrinsic dispersion differences between two arms of the interferometer. The second interferogram was recorded when the frequency filter (without a slit) was introduced in one arm of the interferometer. The Fourier transform of both interferograms contains information on the intensity and phase of the spectrum of the white light signal. By subtracting the phase of the bias spectrum from that of the filter spectrum, the phase dispersion of the filter was obtained which was then differentiated numerically to provide the filter group-delay dispersion. For the purpose of this experiment the incoherent light source used was the fluorescence produced from the Ti:Sapphire laser when the pump power was reduced below threshold. A lock in amplifier was also used in order to measure the interferograms more accurately. Results shown in Figure 4.7 illustrate dispersion measurements at different lens positions (varying position  $X$  within Fig. 2). These results are compared to theoretical ray-tracing calculations (dashed lines). The results show that a lens position exists where there is near zero-dispersion across a 50nm bandwidth which is sufficient for measuring the  $\sim 80$ fs pulses from the test laser used.

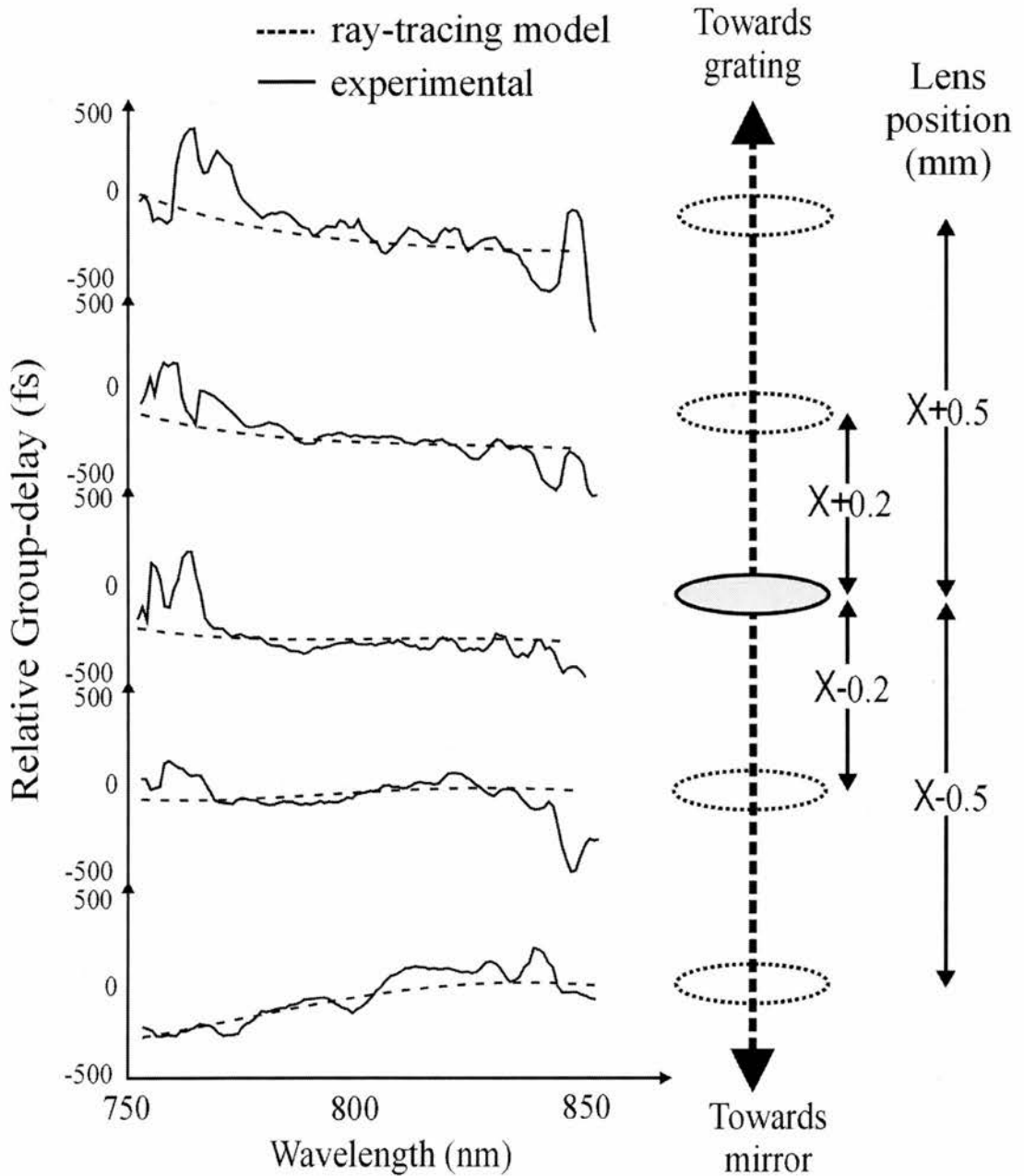


**Figure 4.7** Group-delay dispersion measurements recorded using white light interferometry at various lens positions (solid lines) and comparison with theoretically calculated results (dashed lines)

Because it would be impractical to make these dispersion measurements every time the optical arrangement was altered we compared the intensity autocorrelation of the pulse entering the filter to the cross-correlation between the input and output pulses from the filter. The lens position was moved so that the cross-correlation shape and duration closely matched that of the autocorrelation (Figure 4.8). I found that this position was identical to the zero-

dispersion position determined by using white-light interferometry, and this observation allowed us to move the lens to the correct position without having to accurately measure the filter dispersion every time.

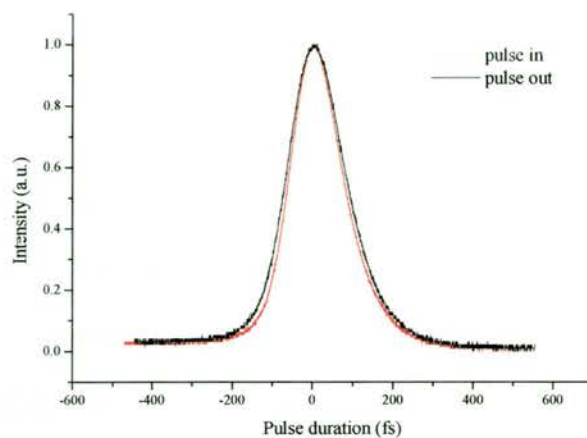


**Figure 4.8** Comparison between the intensity autocorrelation of the incident pulses (black solid line) and the cross-correlation between the incident pulses and the pulses returning from the filter adjusted for zero dispersion

#### 4.2.2 Experimental configuration and procedure

For all of the experiments described in this chapter, a stable, chirped mirror Ti:Sapphire laser system was used which produced 80fs near transform-limited pulses at a centre wavelength of 790nm. The sonogram cross-correlator (Figure 4.9) comprised a standard near-IR broad-band dielectric beamsplitter with a 50:50 splitting ratio and silver-coated end mirrors in each of the two interferometer arms. One arm of the interferometer incorporated the filter design discussed in section 4.2.4 with the static end mirror mounted on a precision translation stage for calibration purposes. A motorized slit was positioned directly in front of this mirror to allow the center frequency of the filter to be accurately controlled by the computer. The width of the slit was altered until it allowed the required one third of the pulse bandwidth to pass. The second arm comprised a silver mirror that was mounted on a piezo-electric translation (PZT) stage that was capable of traveling a distance of 400 $\mu$ m that corresponded to a total optical delay of 2.7 ps. The PZT stage allowed accurate and precise control of the optical delay within the interferometric arm and was capable of oscillating at frequencies up to

~60Hz. The pulses from the delay arm and the frequency filtered arm were recombined noncollinearly with a small crossing angle in the vertical plane on a GaAsP photodiode which acted as the TPA detector. A cross-correlation signal free of interference fringes was then obtained by scanning the PZT-stage through the zero delay position and a sonogram trace was constructed from many cross-correlation profiles, each recorded for a different filter centre-frequency (different slit position).

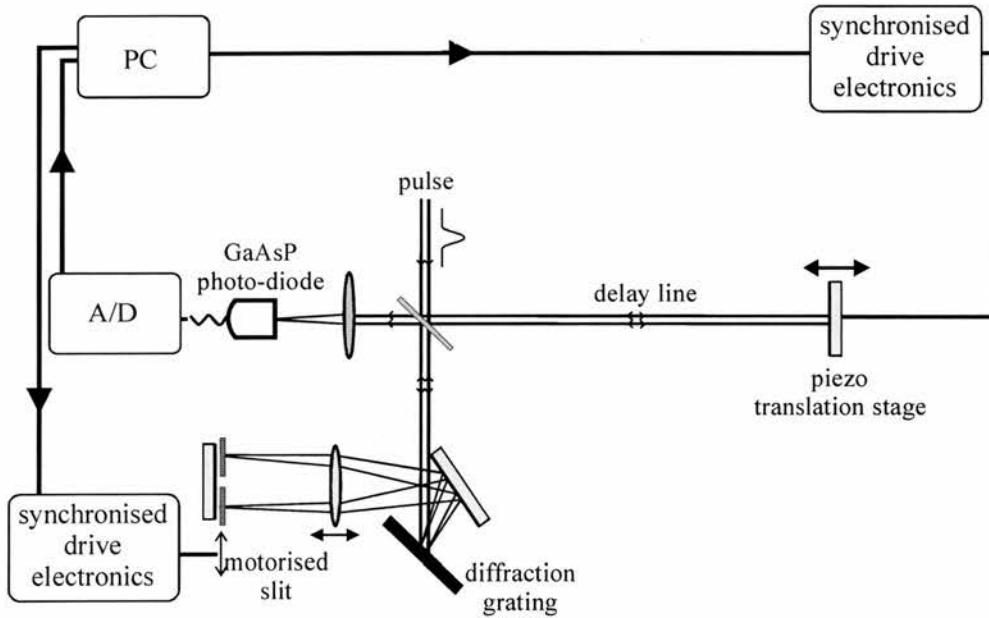


**Figure 4.9** Schematic of the optical system used to rapidly acquire the sonogram. The pulses returning from the zero-dispersion filter and delay line are combined at the GaAsP photodiode, having a small crossing angle in the vertical plane, to avoid interference fringes

### 4.2.3 Synchronisation and acquisition of the sonogram trace

Precise control of the slit and PZT stage, as well as the acquisition of the two-photon signal, was achieved using a combination of an analogue-digital / digital-analogue expansion card (Eagle Technology, part no. PC30G) within a personal computer and a specially designed digital signal generator (Figure 4.10).

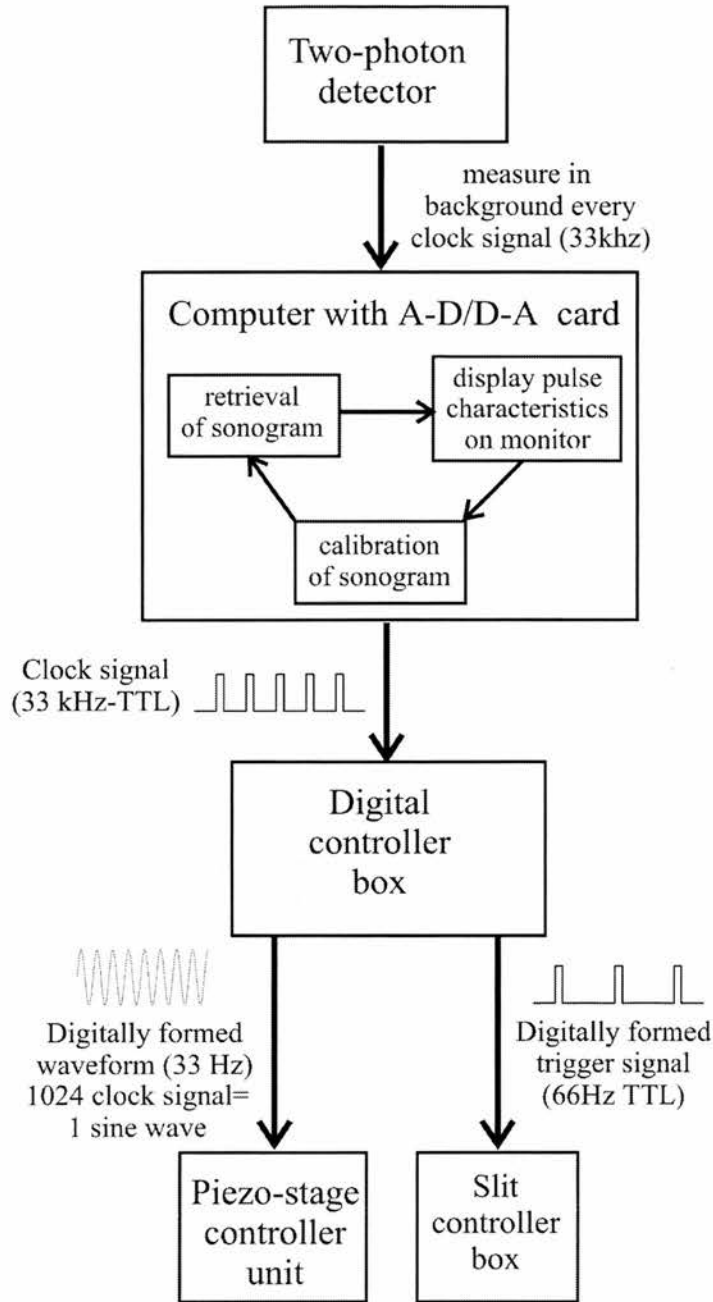


**Figure 4.10** Schematic representation of the electronic acquisition and retrieval system

This digital control box used a clock signal from the expansion card to produce two different waveforms. The first waveform controlled the PZT stage and consisted of a digitally constructed sine-wave (0 to 10V) with a period equal to 1024 clock signals. The frequency of the clock signal corresponded to the frequency at which the signal from the two-photon detector was being recorded, thus for every periodic movement of the PZT stage 1024 cross-correlation points were recorded. For every period of the PZT stage, two separate cross-

correlations were recorded, the first while the delay was increasing and the other while the delay was decreasing. The second waveform provided a TTL trigger every 512 clock signals and was used to advance the slit every time the PZT reached the end of its travel. This enabled two cross-correlations with differing filter positions to be recorded every period of the PZT stage. The translation stage was designed so the whole bandwidth of the pulse was scanned across 120 stepper motor steps, enabling a sonogram consisting of 512x120 points to be recorded every 2 seconds (0.5Hz) when a 33kHz trigger signal was being used. Once all 120 slit positions were scanned, the movement of the slit direction was reversed and the procedure was immediately repeated. The whole acquisition process was carried out in on the A-D card and utilized none of the processor power of the computer so, once sonogram trace had been recorded, acquisition of the next sonogram began immediately while the processor was used to calibrate, filter and retrieve existing the sonogram data.

#### **4.2.4 Calibration and filtering of acquired sonogram trace**

The acquired sonogram trace was comprised of 61440 data points. The data had to be carefully manipulated to form a single 64x64 sonogram that could be fed into the retrieval algorithm. All data handling and retrieval was handled using the FORTRAN computer language due to its fast numerical capability.

The calibration of the time and frequency axis was done prior to the sonogram measurement and was then added as a variable within the FORTRAN program. The wavelength axis was calibrated by scanning the slit across the pulse spectrum while measuring the wavelength. By building up a graph similar to that in Figure 4.6 a direct relation was obtained which described the change in filter frequency per unit slit movement. The time axis calibration was achieved by modifying the path length in the unfiltered arm by a known distance. By measuring the corresponding temporal movement of the cross-correlation trace, a value for the delay per pixel was determined. Background subtraction and a small amount of Fourier filtering (where necessary) [25] was applied to eliminate high frequency noise. Background

subtraction simply consisted of averaging intensities of a number of points that were distant from any regions containing pulse information (eg. a corner of the sonogram trace) and the resulting value was subtracted from the whole array. Any points that became negative during this procedure were set to have a value of zero.

The filtered sonogram trace was then interpolated [26] into a 64x64 Fourier array so that the sampling periods in time and frequency were related by

$$\Delta t = \frac{1}{N\Delta f} \quad (4.5)$$

where  $\Delta t$  and  $\Delta f$  were the sampling periods in time and frequency respectively and  $N$  was the number of samples across the array. An appropriate sampling period for the Fourier array was selected and a 64 x 64 Fourier array was obtained. It was important to carefully select the sampling period to ensure that both the time and frequency were efficiently sampled on the trace so that no data were lost from the edges or squeezed within an insufficiently small number of pixels. This trace was then processed by the retrieval algorithm.

#### 4.2.5 Retrieval of the sonogram trace

The retrieval algorithm used in this work was based upon principal-component generalised projections (PCGP)[9, 18, 20]. PCGP has already been described in more detail in section 2.3.1.3 for the retrieval of frequency resolved optical gating (FROG) traces, and when applied to sonogram retrieval uses a matrix approach based on the idea that a sonogram can be generated from the outer product of the pulse complex spectral amplitude and the frequency filter amplitude response. The sonogram generation procedure is outlined schematically in Figure 4.11.

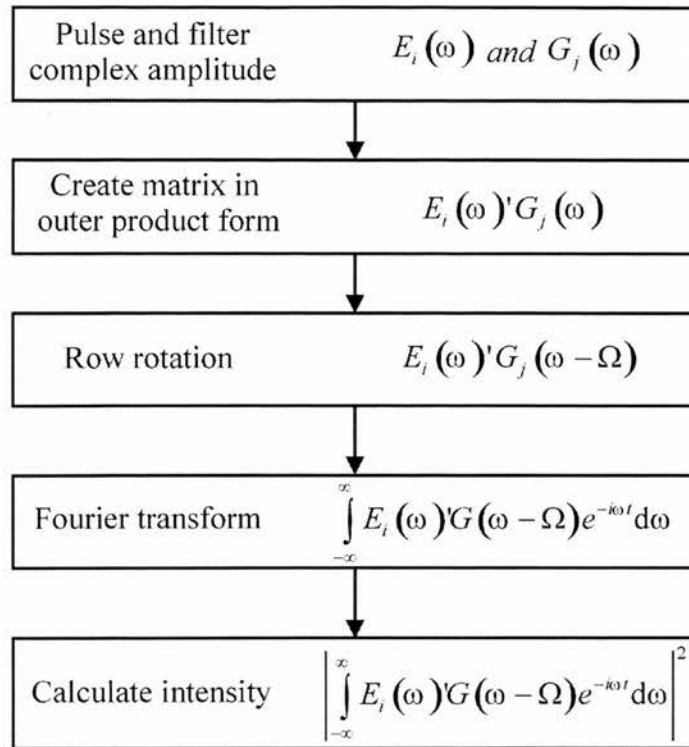


**Figure 4.11** The procedure for generating a sonogram from the outer product form

Prior to the retrieval of the first sonogram, trial solutions of the filter ( $G$ ) and the pulse ( $E$ ) are prepared using a Gaussian envelope with random phase. These trial solutions are then used to calculate the sonogram complex amplitude and its intensity is replaced by the intensity of the first acquired sonogram. The resultant pseudosonogram is then manipulated to produce a new guess of the pulse spectral amplitude and the filter transmission. In our implementation this was initially repeated 50 times to retrieve the pulse characteristics of the first sonogram trace and these were plotted on the computer screen. Further retrieval used results from the previous retrieval as trial solutions. Rapid acquisition meant that it was unlikely the next pulse would have changed significantly from the previous one, thus the number of iterations required for subsequent retrievals was dramatically reduced to only 20. The use of FORTRAN (Salford FTN77) computer language to achieve fast data processing allowed the sonogram algorithm to complete 100 iterations every second on a personal computer (Pentium II 450 MHz) using a 64 by 64 array. Figure 4.12 outlines the processes involved within the retrieval algorithm.

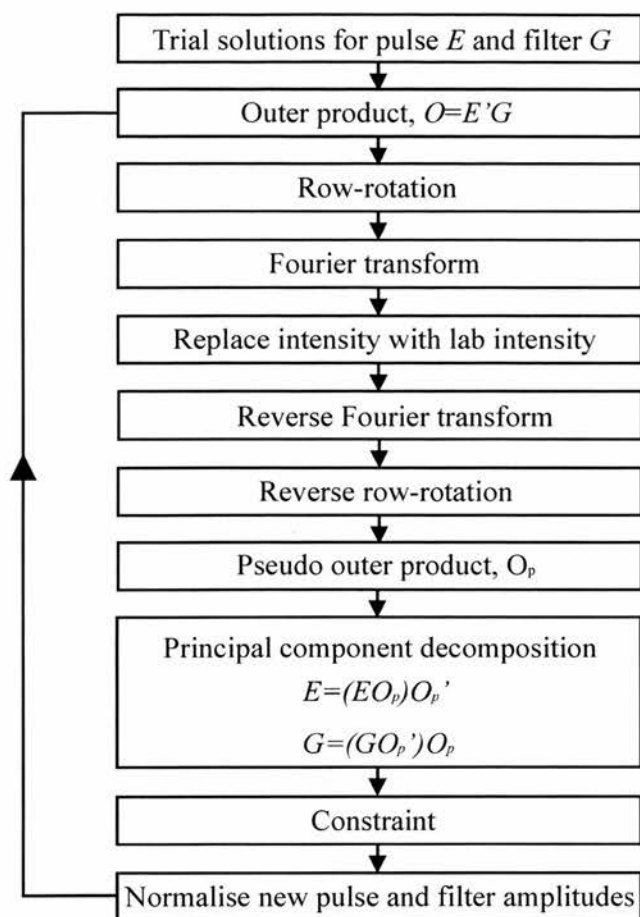


**Figure 4.12** Schematic representation of the sonogram retrieval algorithm

Once the required number of iterations were completed, all retrieved pulse information including temporal and spectral intensity and phase were plotted on the screen. The calibration, filtering and retrieval process was then repeated for the next acquired sonogram. This whole process could be carried out at a repetition rate of 0.5Hz.

#### 4.2.6 Results

All results shown within this section were acquired rapidly, calibrated, retrieved and displayed on screen using the method described in the previous sections. For clarity of reproduction these results were recorded to disk and re-plotted using MATLAB. Figure 4.13 shows an experimentally acquired sonogram. The graphs above and to the side of the sonogram trace show a comparison between the trace marginal and those quantities described in equations (4.3) and (4.4).

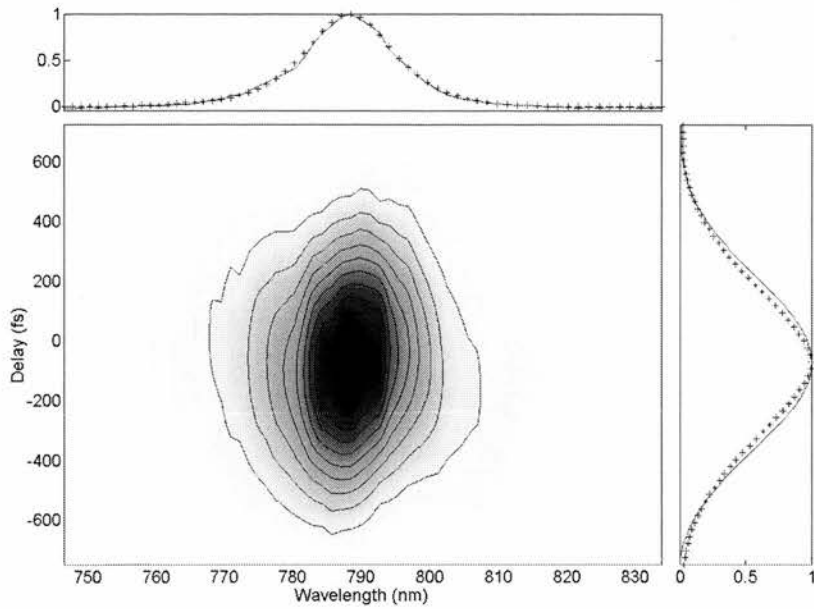


**Figure 4.13** Experimental sonogram trace with corresponding time and frequency marginals (solid lines) compared respectively with quantities described in equations (4.3) and (4.4)

Excellent agreement can be seen between the marginals thus demonstrating that there is negligible systematic error. The slight difference in the delay marginal can be attributed to some noise within the trace. This is confirmed when the trace is retrieved and a similar comparison is made between the marginals.

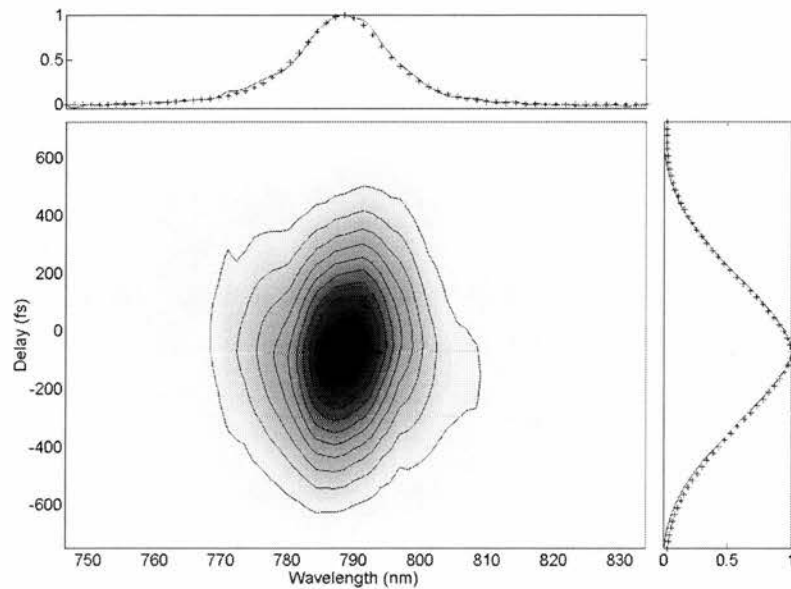


**Figure 4.14** Retrieved sonogram trace with corresponding time and frequency marginals (solid lines) compared with quantities described in equations (4.3) and (4.4)

Even better agreement is shown on the retrieved pulse showing that the slight difference in the marginals was in fact due to noise within the trace. That these marginals compare so well implies a confidence that the retrieved pulse information is correct. Figure 4.15 shows the temporal intensity and phase of the retrieved pulse.

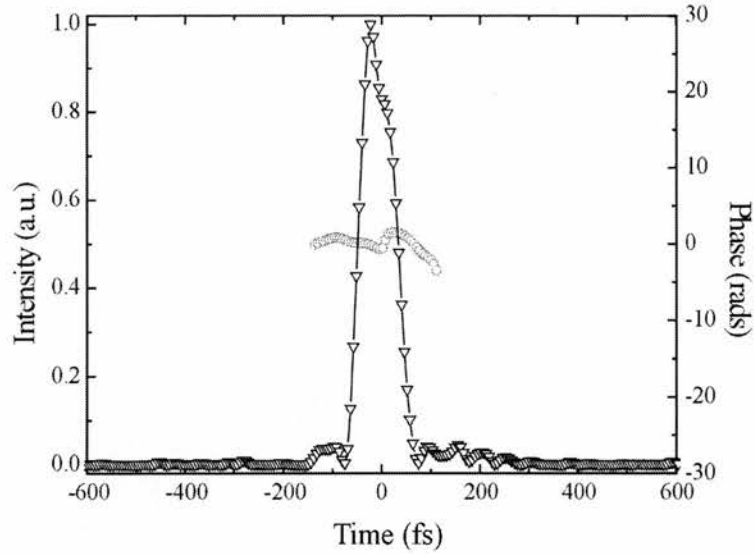


**Figure 4.15** Temporal intensity (triangles) and phase (circles) of the retrieved pulse

In Figure 4.16, the retrieved pulse spectrum is shown together with the spectral phase. For comparison the experimentally measured spectrum is also plotted, again showing excellent agreement.

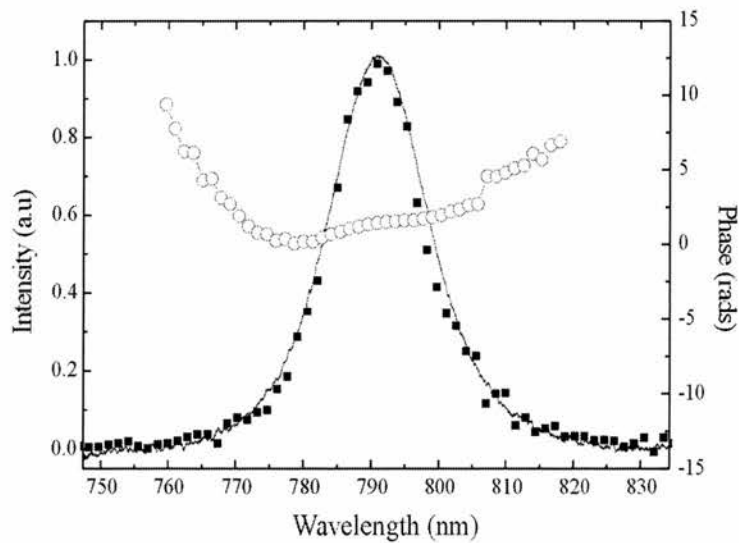


**Figure 4.16** Comparison between the experimental (solid line) and retrieved (squares) spectra along with the retrieved spectral phase (circles)

Finally, by convolving together the retrieved temporal intensity (in Figure 4.15) and its inverse, a simulation of the pulse autocorrelation can be carried out. Figure 4.17 shows a comparison between the retrieved and experimentally acquired autocorrelation.

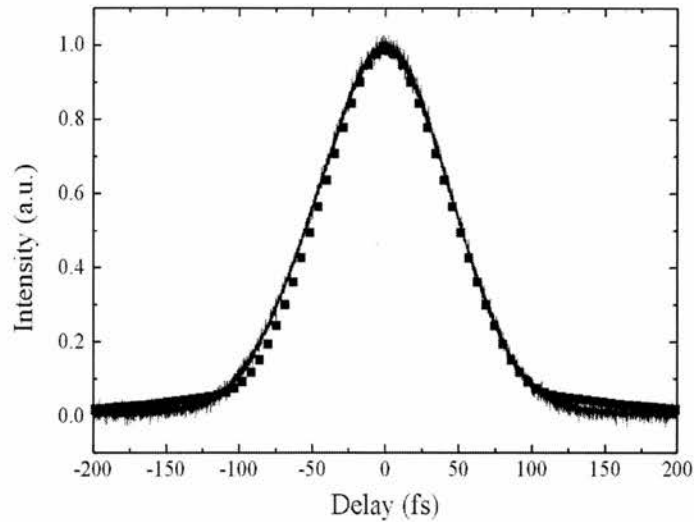


**Figure 4.17** Comparison between the experimental (solid line) and retrieved (squares) intensity autocorrelation

The results given within this section demonstrate that the sonogram characterisation technique is very robust and is able to give complete characterisation with the reassurance that there are no ambiguities within the experimental data. Before obtaining these results there was often a false preconception when dealing with time-frequency characterisation techniques, like sonograms, that the retrieval of the trace was the limiting factor when it comes to the development of a real time system. Improved pulse retrieval algorithms, combined with ever increasing speeds of personal computers have now made the speed of retrieval small compared to the time taken to acquire the trace. Consequently, techniques to enable faster acquisition of a sonogram trace are required.

### 4.3 Fast acquisition of a sonogram using a scanning Fabry-Perot etalon

The optical scheme described in section 4.2 was very simple and easy to calibrate and gave excellent results. For real-time measurements, however, the technique is solely restricted by how fast the slit can accurately travel back and forward across the Fourier plane. Ideally, for rapid acquisition, a method is required that allows the scanning of the pulse spectrum to be achieved more rapidly, but with the same accuracy as the slit technique. Recently an alternative bandpass filter was used to measure very low energy picosecond pulses [16]. Here, a Fabry-Perot filter was used to selectively filter the narrow bandwidth of a picosecond pulse. Even for the considerably broader spectral bandwidths associated with femtosecond pulses, a Fabry-Perot filter presents an extremely attractive means of implementing a rapidly scanning frequency filter due to the very small changes in mirror position that are required to scan across a bandwidth of tens of nanometres.

#### 4.3.1 Design of the frequency bandpass filter

The maximum frequency-scanning range which a Fabry-Perot filter can achieve is determined by the size of its free spectral range (FSR). The value of the FSR is directly related to the separation of the two mirrors

$$FSR = \frac{c}{2d} \quad (4.6)$$

where  $FSR$  is in frequency,  $c$  is the speed of light and  $d$  is the mirror separation. Equation (4.6) states that the larger the FSR, the smaller the mirror separation must be. This factor becomes important when the large bandwidths that are associated with ultrashort pulses are taken into consideration. For example, a 100fs pulse centred at 800nm has a spectral bandwidth of  $\sim 7$ nm. To scan across the whole pulse spectrum, including the wings, a FSR of around 40nm is needed and this is equivalent to a mirror separation of  $8\mu\text{m}$ . The mirror separation must also be accurately scanned through a distance of  $\frac{1}{2} \lambda$ , the distance corresponding to one full FSR. For a pulse centred at 800nm, this implies that the mirrors

must accurately scan a distance of at least  $0.4\mu\text{m}$ . Figure 4.18 shows the design of the filter that was used.

Top view

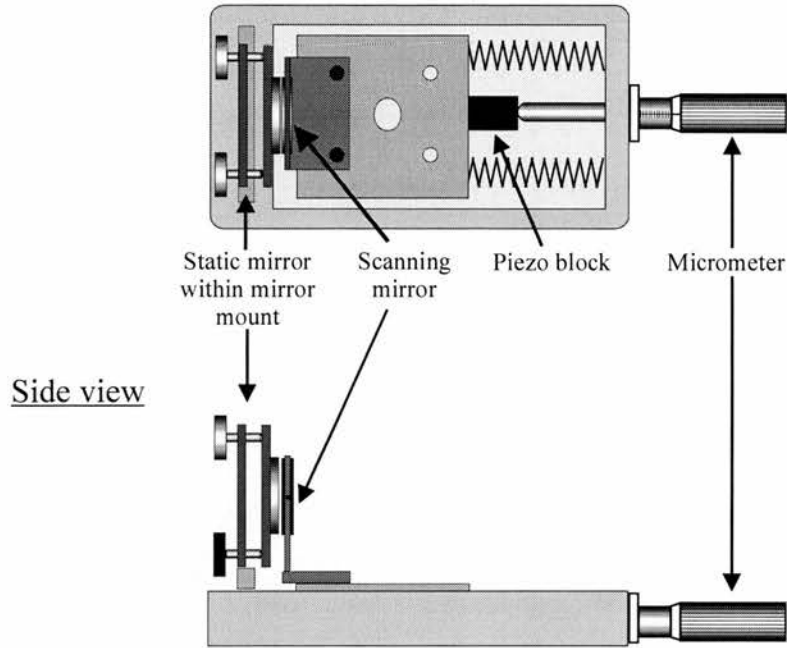


**Figure 4.18** Mechanical design used for the scanning Fabry-Perot frequency filter

Having such a small mirror separation meant that the two mirrors had to be perfectly parallel with one another and to achieve this the static mirror was placed within a mirror mount to allow angular adjustment relative to the scanning mirror. The scanning of the mirror separation was achieved by placing a small piezo-electric stack within a translation stage between the micrometer and the side of the translation block. This attractively simple technique allowed coarse translations to be made using the micrometer screw gauge and final small translations to be made using the piezo-electric stack. The piezo transducer used (Thorlabs, Inc., Part no. AE050D08) provided a translation of  $\sim 6\mu\text{m}$  across the 0-150V output available from the controller box (Linos Photonics, part number 40 6050) and therefore allowed scanning across 15 FSR's.

The second critical parameter to be considered when designing the filter is the FWHM of its passband. This characteristic is solely dependent upon the reflectivity of the mirrors within a Fabry-Perot filter and is described by:

$$\Delta\nu_{FWHM} = \frac{\Delta\nu_{FSR}}{\frac{\pi\sqrt{r_1 r_2}}{1-r_1 r_2}} \quad (4.7)$$

where  $\Delta\nu_{FWHM}$  is the frequency FWHM of the filtered spectrum frequency,  $\Delta\nu_{FSR}$  is the FSR and  $r_1$  and  $r_2$  are the reflectivities of the two mirrors. As mentioned earlier within this chapter, when measuring a sonogram, filter bandwidths of around one third of the pulse spectrum work well. In this experiment two mirrors with reflectivities  $r_1=r_2=0.95$  at 800nm were used, corresponding to  $\Delta\lambda_{FWHM} = 1.3\text{nm}$  (assuming a FSR of 40nm). In practice, the actual value was usually larger due to the combination of scattering / absorption loss, small misalignments and imperfect mirror flatness.

The complete filter response of an air-spaced Fabry-Perot etalon is a complex quantity which can be represented as [27]

$$G(\omega) = \frac{T}{1 - R \exp\left(\frac{i2\pi l \omega \cos\theta}{c}\right)} \quad (4.8)$$

This filter has a wavelength-independent phase profile in the form of a slowly-varying ramp which passes through zero at the centre of the passband. Unlike dispersive filters (eg. grating spectrometer designs) which can be optimised to have zero phase across their full tuning bandwidth, the phase of the Fabry-Perot filter is never flat, but can be minimised across the passband by a suitable choice of mirror reflectivity and separation.

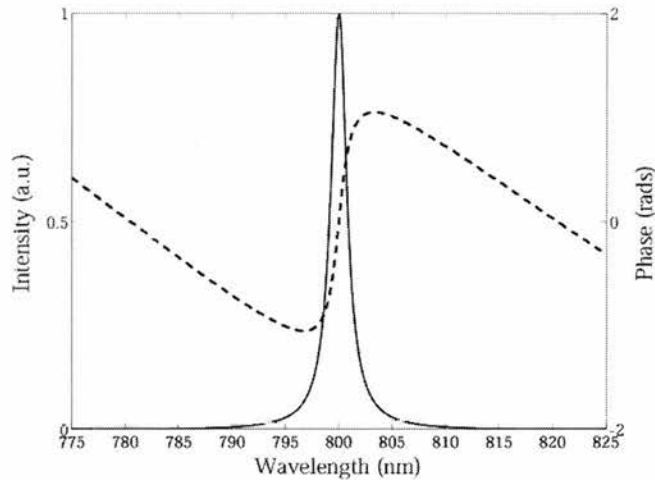


**Figure 4.19** Representative Fabry-Perot filter function (straight line) and its phase (dashed)

For illustrative purposes, there is a depiction in Figure 4.19 of the Fabry-Perot filter function calculated using values of the FSR and the mirror reflectivities given above. As will be shown later, the algorithm retrieves the complete profiles of both the pulse and the filter, and when the Fabry-Perot filter is configured to have high finesse the phase change across the filter bandwidth is obtained and retrieved.

### 4.3.2 Design of the delay line

Compared to characterisation techniques such as autocorrelation and FROG, the measurement of the sonogram requires an increased length in scan due to the increased pulse duration caused by bandpass filtering the pulse. Typically the filtered pulse is broader than the unfiltered one by a factor of  $\sim 3$ -4 and therefore the pulse broadening caused by the filter is not a problem provided techniques exist that allow rapid and accurate delay scanning with sufficient range. The previous rapid sonogram arrangements in section 4.2 used a piezoelectric translation (PZT) stage to provide the required delay. PZT stages have the advantage of being able to give direct control over the exact position of the delay line. Unfortunately at high frequencies (ie  $>100$ Hz) these devices were found to be driven into resonance causing violent vibrations and resulting in severe distortion of the cross correlation signal. Instead of a PZT stage, a loudspeaker (Farnell, part number 562-336) was used within this sonogram

arrangement to provide the scanning delay. The use of speakers is commonplace within devices such as autocorrelators and provides a cheap and simple way of implementing a delay arm with the advantage of being able to work at high frequencies without risk of distortion. A hollow corner-cube retroreflector was fixed within the centre of the speaker cone and three translation stages were used to provide X, Y and Z movement. These three adjustments allowed control over the position of the reflected beam as well as coarse control over the length of the delay arm.

### 4.3.3 Design of the optical setup

The optical setup, shown in Figure 4.20, used a Mach-Zehnder interferometer arrangement. This was preferred over the Michelson arrangement as it allowed the pulses to pass only once through the filter before being recombined with the reference pulses. The loudspeaker was placed directly after the Fabry-Perot filter, allowing the second arm of the interferometer to be much simplified, requiring only two mirrors for path length matching and to steer the beam onto the output beamsplitter. For ease of alignment, an optical isolator (Optics For Research, part number IO-5-TiS1) was placed before the optical setup to prevent reflections from the Fabry-Perot returning back into the laser and thus stopping it from mode-locking. To avoid pulse distortion associated with the isolator it could have been removed after slightly angling the Fabry-Perot etalon mirrors so that they were not perfectly perpendicular with the incident beam. The beams from the two interferometer arms were recombined at the second beamsplitter with a small vertical offset. When focused ( $f \sim 25\text{mm}$ ), this offset allowed the pulses to be recombined noncollinearly with a small crossing angle in the vertical plane on the GaAsP photodiode which acted as the TPA detector. As the speaker scanned through the zero delay position a cross-correlation signal free of interference fringes could be observed. A kinematic mirror mount was placed at the output of the Fabry-Perot filter so that the filtered spectrum could be observed using a scanning spectrometer (Rees LSA). Accurate alignment of the two mirrors within the Fabry-Perot filter was achieved by bringing the mirrors visibly

close to one another using the coarse control of the micrometer. By changing the alignment of the static mirror, the peak intensity of the modes monitored on the spectrometer was maximised so that their FWHM narrowed. The micrometer could then be carefully adjusted so that the FSR gradually increased. Final, small adjustments that were required to obtain the full FSR were made using the bias control on the piezo controller box.

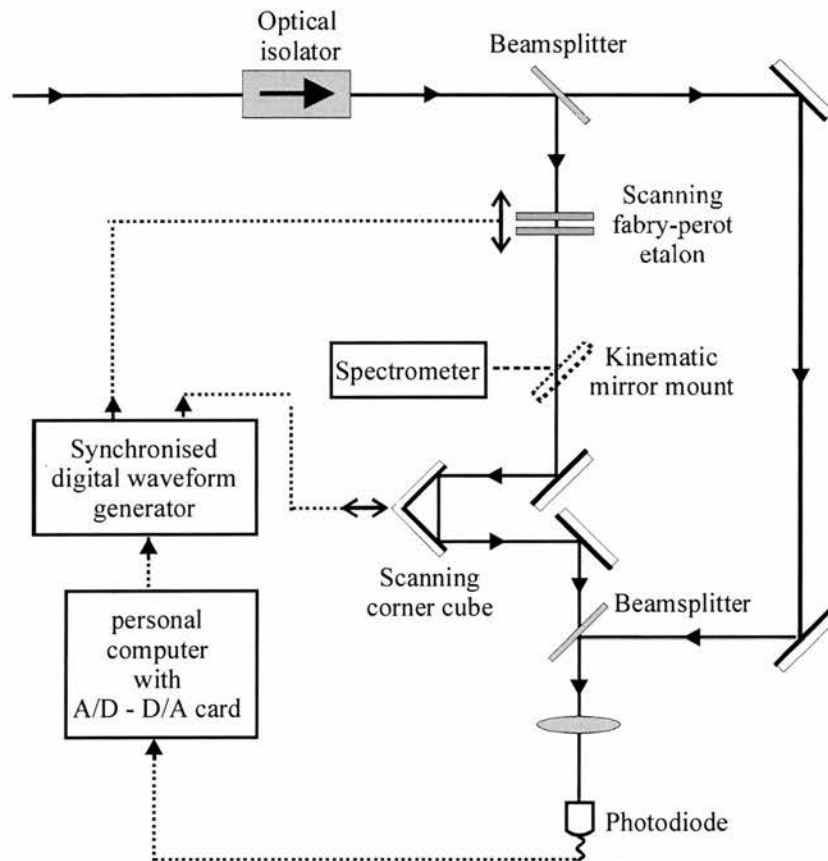


*Figure 4.20* A schematic diagram of the optical system used to rapidly acquire the sonogram

#### 4.3.4 Acquisition and synchronisation of the frequency filter and delay-line

The synchronisation between the frequency filter and the delay-line was one of the most crucial parts of the experimental setup. The presence of even small errors in the synchronisation would potentially make the acquired data meaningless. As acquisition speeds were increased so too was the difficulty of synchronisation.

Synchronisation was achieved using a combination of an analogue to digital data acquisition card (Eagle Technology, part number PC30G) and a specially designed digital signal generator. Our data acquisition card was able to digitise 100000 data points per second, and each time a sample was recorded a TTL pulse was produced. These pulses were vital for calibration purposes because they enabled the computer to have control over the movement of the loudspeaker and the filter, whose positions could be directly related to the number of data points that had been recorded by the computer. The control was achieved by using the TTL sample pulses as a clock signal for a digital signal generator, the circuit diagram of which is shown in Figure 4.21.

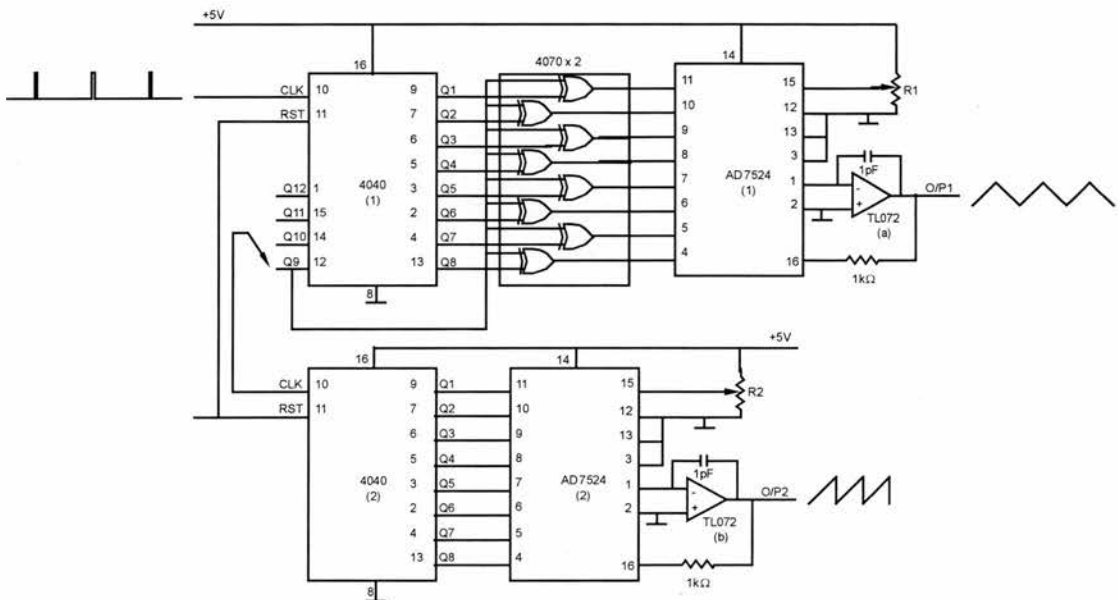


**Figure 4.21** The circuit diagram of the digital signal generator used to produce the two separate waveforms that synchronise the spectral filter and the delay line.

The electronic circuit provided two separate waveforms, one which controlled the speaker and another that controlled the Fabry-Perot filter. The waveform controlling the speaker was a triangular waveform that had a period comprised from 512 clock pulses (Figure 4.22) meaning that a clock signal having a maximum frequency of 100kHz would produce a triangular waveform with a frequency of 195.3Hz. This signal was then amplified using an audio power-amplifier which was used to enable accurate control over the amount of delay that was provided by the speaker. Although a triangular waveform was being generated, the

rapid change in direction at the extremes of the signal was dampened by the speaker resulting in a loss of scan linearity in these regions. This had no effect on the pulse measurement as long as the amplitude of the speaker was large enough so that the cross-correlation was completely measured within the linear region of travel at the centre of the speaker's movement. The second waveform used to control the Fabry-Perot filter produced a voltage ramp made up from 256 levels, each of which corresponded to 128 clock pulses (see Figure 4.22).

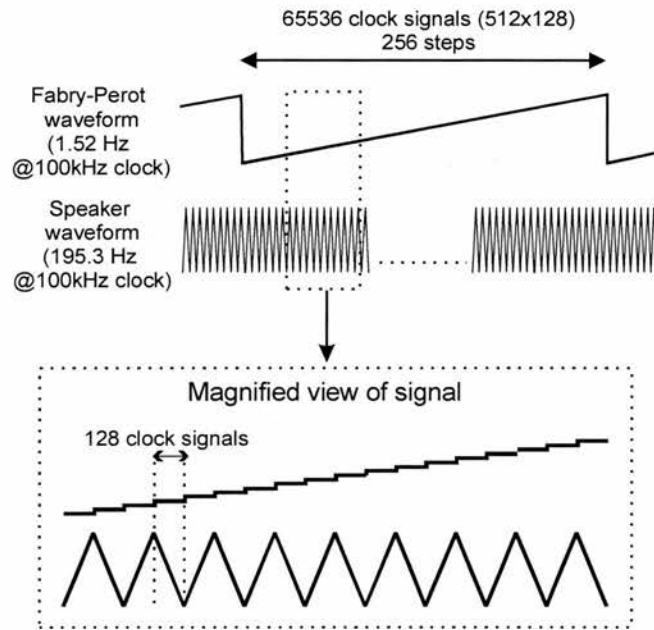


**Figure 4.22** A representation of the two waveforms created from the signal generator for movement of the Fabry-Perot etalon and the delay line

When the clock signal had frequency of 100 kHz the ramp waveform had a frequency of 1.52Hz. This signal was fed into a piezo controller box (high-voltage amplifier), which in turn was connected to the piezo block within the translation stage of the Fabry-Perot filter. The filter was setup by initially scanning the piezo slowly and monitoring the spectrum of the filtered pulses using our spectrometer. The voltage of the ramp was then adjusted (using variable resistor R2 in Figure 4.21) so that the whole FSR was scanned over a range greater than the pulse spectral bandwidth. By modifying the DC offset voltage on the piezo controller the filter scan was adjusted to start at the short-wavelength edge of the pulse spectrum.

When the clock signal was generated at 100kHz, the two control waveforms allowed the acquisition of 256 cross-correlation signals at a frequency of 1.52Hz, each having a separate filter position and thus providing a sonogram consisting of a 256 by 256 array. It should be pointed out that cross-correlation signals were acquired during both the outward and return excursions of the speaker and subsequently it was necessary to reverse half of these data before the formation of the sonogram.

### 4.3.5 The calibration and retrieval program

Figure 4.23 shows a block diagram outlining the different stages which the acquisition and retrieval program followed.

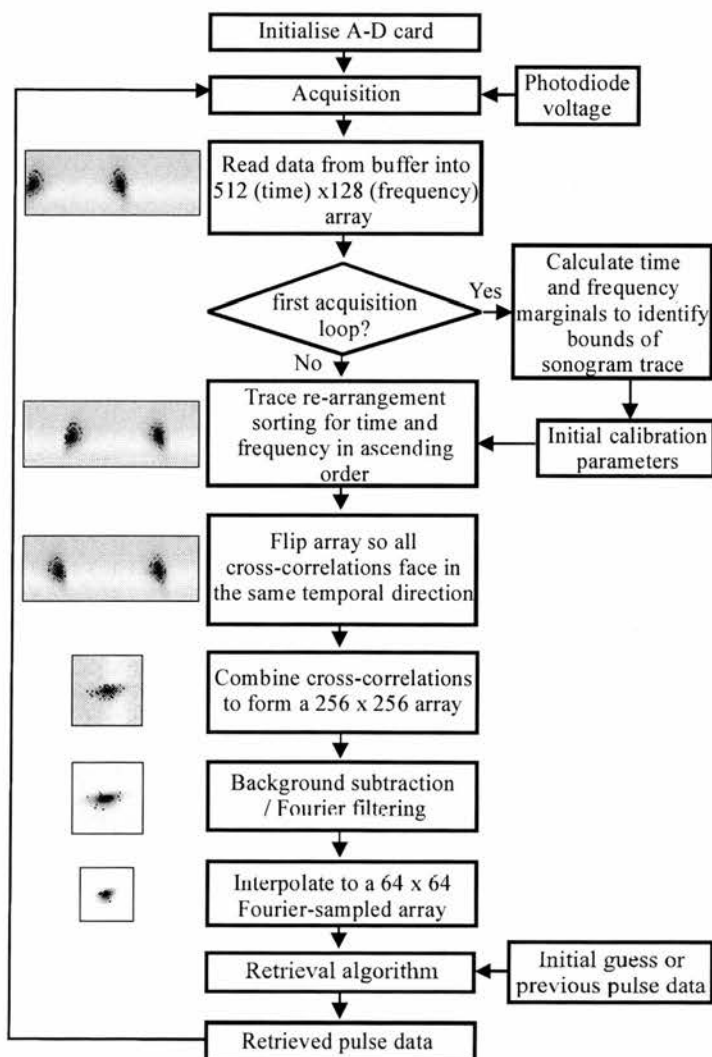


**Figure 4.23** Schematic representation outlining the processes that were carried out by the acquisition and retrieval program

The acquisition card was configured so that it continuously acquired data within a circular buffer consisting of 65536 points (512 by 128 array). Once the end of the buffer was reached, new data points were loaded into the start of the buffer. The combination of the acquisition and synchronisation techniques allowed all 65536 data points, once initially calibrated, to be assigned a specific frequency and delay value, and data at these positions were capable of being continuously updated at a frequency of 1.52 Hz. It should also be noted that, as in the previous technique, because all data acquisition was achieved using background processing on the A-D card all the calibration and pulse retrieval procedures were able to make full use of the computer's processing power.

Once the first sonogram was acquired, the buffer was initially read into a 512 x 128 array. These data consisted of two sets of cross-correlations that were obtained with the speaker moving either forward or backwards. As part of the initial calibration procedure, the start of the scan was first deduced from the array and this was achieved by measuring the time and frequency marginals. The time marginal (made up from 512 data points) consisted of two main maxima that corresponded to the two cross-correlation signals from the outward and return speaker movements. By detecting the two peaks of these cross-correlations, the start of each scan was easily deduced by understanding that a single cross-correlation comprised of 256 data points. The 512 rows of the array were then either shifted up or down in delay to set the start of one set of cross-correlation data at the beginning of the array. The same procedure was carried out for the frequency marginal (128 points) with the maximum peak this time referring to the peak wavelength of the laser and this point was centred within the array. The array now consisted of two mirror-image sonogram traces that were combined and then interlaced together to produce a 256 x 256 sonogram trace. Again, as in the previous technique described in section 2.2 background subtractions was applied as well as a small amount of Fourier filtering. The filtered sonogram trace was then interpolated into a Fourier array so that the sampling periods in time and frequency were related by equation (4.5)

Calibration information about the acquired sonogram trace was now required. The calibration of the frequency axis was achieved with the use of a separate spectrometer to measure the FSR of the Fabry-Perot filter. Once the value of the FSR was obtained, the trace was easily calibrated by knowing there were exactly 256 samples across this range. The time axis was calibrated by moving the delay a known distance and, by measuring the subsequent displacement of the cross-correlation, an accurate value of the experimental delay step could be inferred. All calibration data were entered into the program before acquisition was started. An appropriate sampling period for the Fourier array was selected and a 64 x 64 Fourier array was obtained. The retrieval process used was identical to that detailed in section 4.2.5 except for the removal of the constraint that forced the gate to have zero phase. This was because the Fabry-Perot filter has a non-zero phase profile (Figure 4.19). The whole calibration, retrieval and plotting of data onto the computer screen was achieved at a frequency of 1 Hz on a Pentium II 450 MHz processor. Update rates of 1.52Hz (the acquisition rate) could be achieved by simply using a faster computer.

#### **4.3.6 Results**

The results presented within this section have all been acquired and retrieved at an overall frequency of 1Hz, though it should be highlighted that the sonogram was in fact acquired at a frequency of 1.52Hz. The sonogram trace that was analysed was the 10<sup>th</sup> sonogram trace to be acquired within a 10 second period. The results were saved to disk and plotted using Matlab for clarity. Figure 4.24 shows a comparison between the experimentally acquired and retrieved sonogram trace.

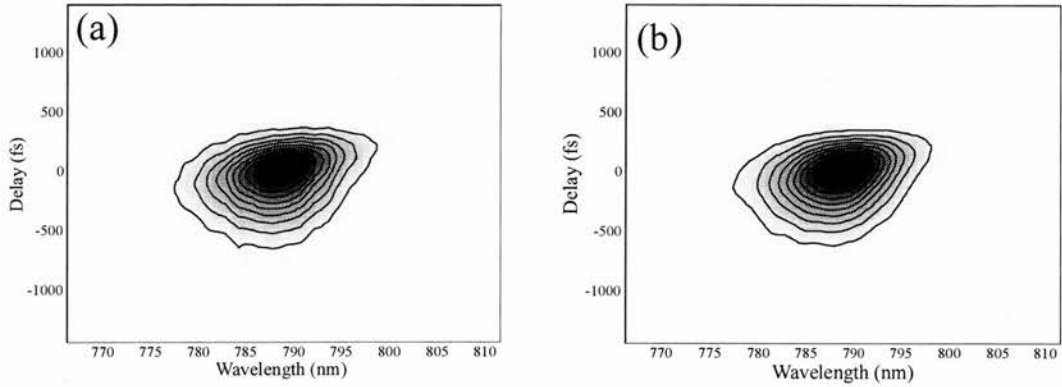


**Figure 4.24** Comparison between the experimentally acquired sonogram trace (a) and the retrieved sonogram trace (b)

The comparison between the two traces show excellent agreement giving the first indication that the retrieval process was a success. Figure 4.25 shows the retrieved pulse intensity and phase.

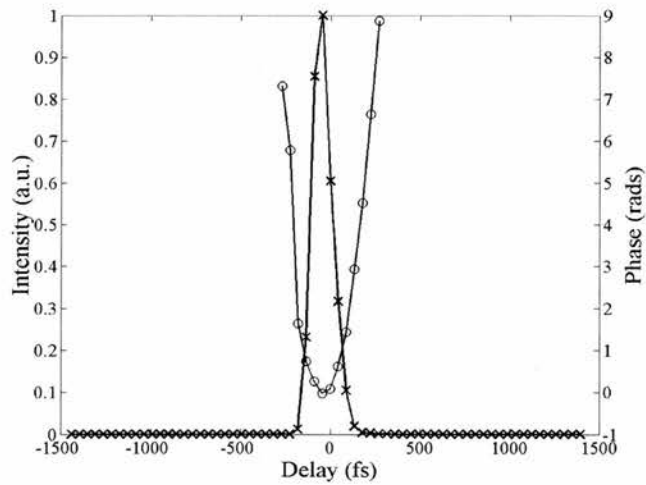


**Figure 4.25** The temporal intensity (crosses) and phase (circles) of the retrieved pulse

The quadratic phase profile is what was expected due the chirped pulse passing through the optical isolator. Figure 4.26 compares the independently measured pulse spectrum and autocorrelation with the retrieved spectrum (Figure 4.26a) and autocorrelation (Figure 4.26b).

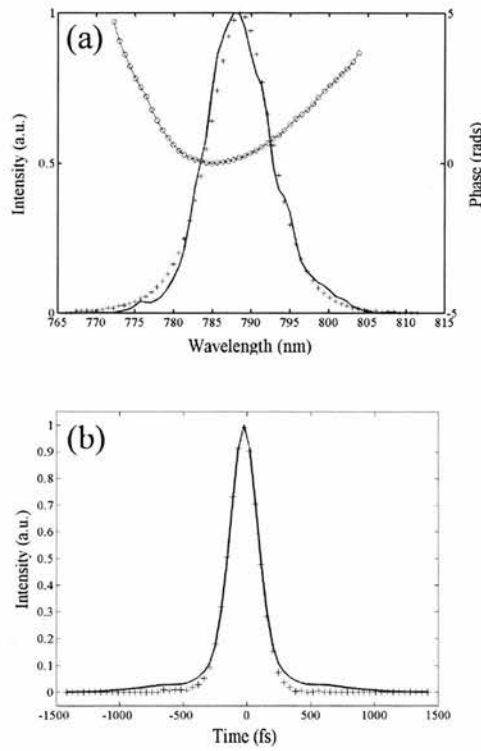


**Figure 4.26** (a) Comparison between the experimental (solid line) and retrieved (crosses) spectra along with the retrieved spectral phase (circles). (b) Comparison between the experimental (solid line) and retrieved (crosses) intensity autocorrelation

Although the experimental data compare very well with those of the retrieved data, for completeness Figure 4.27 shows the marginals of the retrieved sonogram trace compared with the quantities given in equations (4.3) and (4.4).

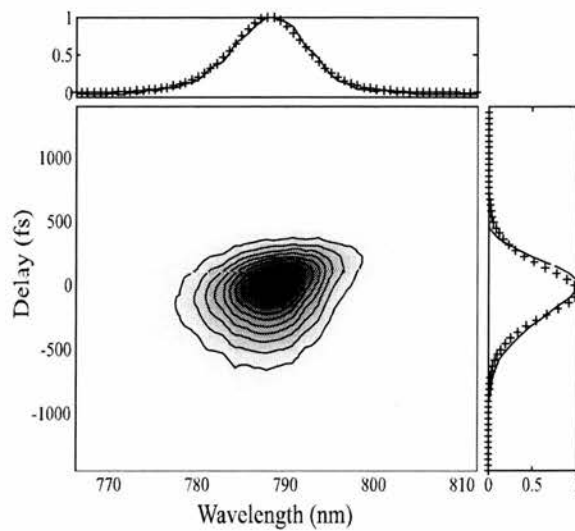


**Figure 4.27** The retrieved sonogram trace with corresponding time and frequency marginals (solid lines) compared with quantities described in equations (4.3) and (4.4)

Figure 4.28 compares the experimentally measured filter against the retrieved filter. Although a good fit is observed it should be noted that as a 64x64 array was used, the sampling period was large compared to the size of the filter, so for a more accurate comparison a larger grid size would be preferred. The same comments apply to the phase of the filter, which is also displayed in Figure 4.28 and, as predicted in Figure 4.19, a definite ramp was retrieved by the algorithm.

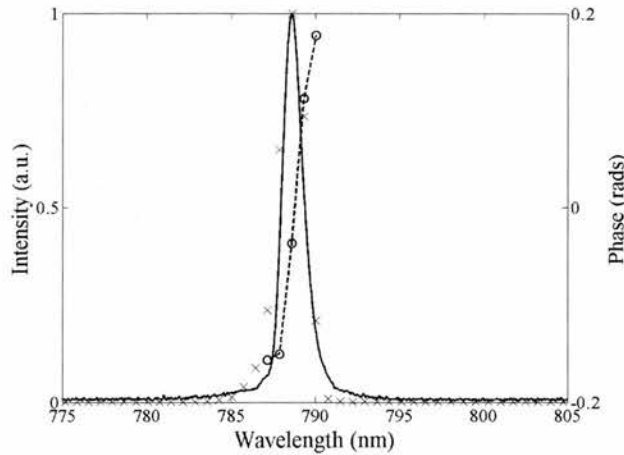


**Figure 4.28** The retrieved filter function (crosses) and phase (circles) compared with the experimentally measured filter (solid line)

From the results outlined in the previous pages it is clear that using a Fabry-Perot filter was successful in rapidly characterising ultrashort pulses by measuring their sonogram. However it should be realised that by making a number of small alterations to the experimental configuration the speed of acquisition and retrieval could be dramatically increased. Firstly, by acquiring a 128 by 128 array instead of the 256 by 256 array the acquisition speed could be quadrupled. This could be simply implemented by switching the position of the clock signal originating from the first 4040 counter integrated circuit (see Figure 4.21). A Fabry-Perot etalon has the potential to oscillate at much higher frequencies than the speaker, so if a specifically designed filter was manufactured, the roles of the speaker and the filter could be reversed so that the filter oscillated at the higher frequency. This again would have the potential to acquire a sonogram at much higher frequencies, although increasing the acquisition rate would require a faster acquisition card. The acquisition card used in this

experiment could acquire at 100kHz which is relatively slow compared to more modern acquisition cards that can acquire at many times this rate. The speed of the computer program which calibrates, retrieves and visualises the sonogram trace can also be increased. Perhaps the simplest (though not necessarily the cheapest) method is to upgrade the computer with a faster processor. A Pentium II 450 MHz processor was used in all experiments outlined in this chapter but at the time of writing more modern computers have the potential to run at three times this speed. Further optimisation of the code would also help increase the overall speed of the program, especially by using more sophisticated means for visually displaying the data.

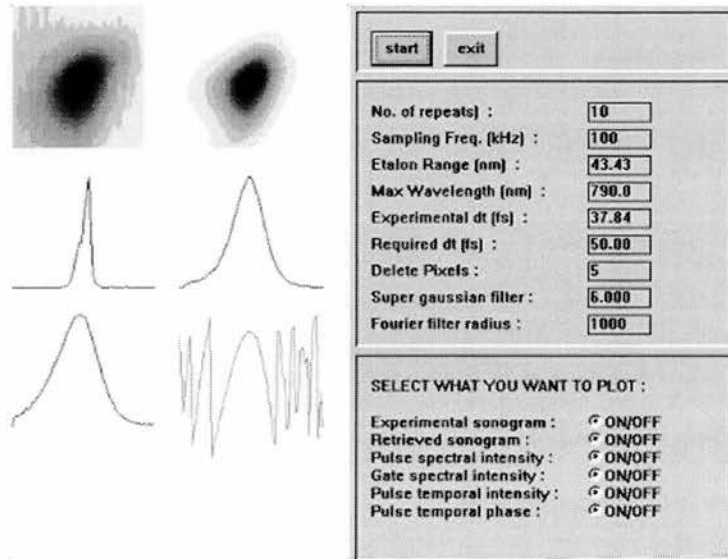


**Figure 4.29** A typical screenshot of the computer rapidly displaying the pulse characteristics

The program used in this experiment visually displayed all the pulse characteristics as depicted in Figure 4.29 but for certain applications only display of the sonogram trace or the phase measurement would be required, again resulting in an increase in the update frequency. It should be noted that for this work we programmed the visual display routine only as a demonstration and further work could easily be done to enhance its usability. Figure 4.29 also shows that super-gaussian filtering was also implemented within the program, although it was found that this type of filtering was not generally required.

#### **4.4 Conclusion**

Within this chapter descriptions are given for two separate rapid characterisation systems that have demonstrated how the measurement of a sonogram is a viable technique for rapid pulse characterisation. The sonogram technique is very robust, easy to implement and extremely flexible. The use of two-photon absorption detectors also makes this technique very sensitive, broadband and polarisation insensitive thus making it ideally suited for ultrashort pulse characterisation. The sonogram approach can be implemented in the blue and mid-IR with minimum modifications, making it an attractive alternative to FROG at these wavelengths. The use of marginals for error checking also gives it an advantage over the SPIDER technique making it a real alternative for rapid pulse characterisation.

## 4.5 References

- [1] B. Kohler, V. V. Yakovlev, J. W. Che, J. L. Krause, M. Messina, K. R. Wilson, N. Schwentner, R. M. Whitnell, and Y. J. Yan, "Quantum Control of Wave-Packet Evolution With Tailored Femtosecond Pulses," *Physical Review Letters*, vol. 74, pp. 3360-3363, 1995.
- [2] J. C. M. Diels, J. J. Fontaine, I. C. McMichael, and F. Simoni, "Control and Measurement of Ultrashort Pulse Shapes (in Amplitude and Phase) With Femtosecond Accuracy," *Applied Optics*, vol. 24, pp. 1270-1282, 1985.
- [3] R. Trebino, K. W. DeLong, D. N. Fittinghoff, J. N. Sweetser, M. A. Krumbugel, B. A. Richman, and D. J. Kane, "Measuring ultrashort laser pulses in the time-frequency domain using frequency-resolved optical gating," *Review of Scientific Instruments*, vol. 68, pp. 3277-3295, 1997.
- [4] R. Trebino and D. J. Kane, "Using Phase Retrieval to Measure the Intensity and Phase of Ultrashort Pulses - Frequency-Resolved Optical Gating," *Journal of the Optical Society of America a-Optics Image Science and Vision*, vol. 10, pp. 1101-1111, 1993.
- [5] D. J. Kane and R. Trebino, "Characterization of Arbitrary Femtosecond Pulses Using Frequency-Resolved Optical Gating," *IEEE Journal of Quantum Electronics*, vol. 29, pp. 571-579, 1993.
- [6] C. Iaconis and I. A. Walmsley, "Self-referencing spectral interferometry for measuring ultrashort optical pulses," *IEEE Journal of Quantum Electronics*, vol. 35, pp. 501-509, 1999.
- [7] C. Iaconis, V. Wong, and I. A. Walmsley, "Direct interferometric techniques for characterizing ultrashort optical pulses," *IEEE Journal of Selected Topics in Quantum Electronics*, vol. 4, pp. 285-294, 1998.
- [8] C. Iaconis and I. A. Walmsley, "Spectral phase interferometry for direct electric-field reconstruction of ultrashort optical pulses," *Optics Letters*, vol. 23, pp. 792-794, 1998.
- [9] D. J. Kane, "Recent progress toward real-time measurement of ultrashort laser pulses," *IEEE Journal of Quantum Electronics*, vol. 35, pp. 421-431, 1999.
- [10] T. M. Shuman, M. E. Anderson, J. Bromage, C. Iaconis, L. Waxer, and I. A. Walmsley, "Real-time SPIDER: ultrashort pulse characterization at 20 Hz," *Optics Express*, vol. 5, pp. 134-143, 1999.
- [11] K. W. DeLong, R. Trebino, and D. J. Kane, "Comparison of Ultrashort-Pulse Frequency-Resolved-Optical-Gating Traces For 3 Common Beam Geometries," *Journal of the Optical Society of America B-Optical Physics*, vol. 11, pp. 1595-1608, 1994.
- [12] J. L. A. Chilla and O. E. Martinez, "Direct Determination of the Amplitude and the Phase of Femtosecond Light-Pulses," *Optics Letters*, vol. 16, pp. 39-41, 1991.
- [13] D. T. Reid, M. Padgett, C. McGowan, W. E. Sleat, and W. Sibbett, "Light-emitting diodes as measurement devices for femtosecond laser pulses," *Optics Letters*, vol. 22, pp. 233-235, 1997.
- [14] D. T. Reid, W. Sibbett, J. M. Dudley, L. P. Barry, B. Thomsen, and J. D. Harvey, "Commercial semiconductor devices for two photon absorption autocorrelation of ultrashort light pulses," *Applied Optics*, vol. 37, pp. 8142-8144, 1998.
- [15] J. K. Ranka, A. L. Gaeta, A. Baltuska, M. S. Pshenichnikov, and D. A. Wiersma, "Autocorrelation measurement of 6-fs pulses based on the two-photon-induced photocurrent in a GaAsP photodiode," *Optics Letters*, vol. 22, pp. 1344-1346, 1997.
- [16] D. T. Reid, B. C. Thomsen, J. M. Dudley, and J. D. Harvey, "Sonogram characterisation of picosecond pulses at 1.5  $\mu\text{m}$  using waveguide two photon absorption," *Electronics Letters*, vol. 36, pp. 1141-1142, 2000.
- [17] V. Wong and I. A. Walmsley, "Ultrashort-pulse characterization from dynamic spectrograms by iterative phase retrieval," *Journal of the Optical Society of America B-Optical Physics*, vol. 14, pp. 944-949, 1997.
- [18] D. T. Reid, "Algorithm for complete and rapid retrieval of ultrashort pulse amplitude and phase from a sonogram," *IEEE Journal of Quantum Electronics*, vol. 35, pp. 1584-1589, 1999.
- [19] K. W. DeLong, D. N. Fittinghoff, R. Trebino, B. Kohler, and K. Wilson, "Pulse Retrieval in Frequency-Resolved Optical Gating Based On the Method of Generalized Projections," *Optics Letters*, vol. 19, pp. 2152-2154, 1994.
- [20] D. J. Kane, "Real-time measurement of ultrashort laser pulses using principal component generalized projections," *IEEE Journal of Selected Topics in Quantum Electronics*, vol. 4, pp. 278-284, 1998.

- [21] D. J. Kane, W. Wood, and K. Peterson, "Real-time ultrashort pulse shaping diagnostics using Frequency-Resolved Optical Gating," presented at Conference on Lasers and Electro-Optics (CLEO), Baltimore, 2001.
- [22] C. Froehly, B. Colombeau, and M. Vampouille, "Shaping and Analysis of Picosecond Light-Pulses," *Progress in Optics*, vol. 20, pp. 65-153, 1983.
- [23] A. M. Weiner, J. P. Heritage, and E. M. Kirschner, "High-Resolution Femtosecond Pulse Shaping," *Journal of the Optical Society of America B-Optical Physics*, vol. 5, pp. 1563-1572, 1988.
- [24] L. Xu, N. Nakagawa, R. Morita, H. Shigekawa, and M. Yamashita, "Programmable chirp compensation for 6-fs pulse generation with a prism-pair-formed pulse shaper," *IEEE Journal of Quantum Electronics*, vol. 36, pp. 893-899, 2000.
- [25] "FFT in two or more dimensions," in *Numerical recipes in Fortran 77: The art of scientific computing*: Cambridge University press, 1992, pp. 515-524.
- [26] "Interpolation in two or more dimensions," in *Numerical recipes in Fortran 77: The art of scientific computing*: Cambridge University press, pp. 116-117.
- [27] A. Siegman, *Lasers*: University Science publishing, 1986.

## CHAPTER 5

# Dispersive propagation time-resolved optical gating (DP-TROG)

---

### 5.1 Introduction

In stark contrast to frequency-resolved optical gating (FROG) which has various geometries (section 2.3.1.1), the measurement of a sonogram, often referred to as time-resolved optical gating (TROG), has until recently consisted only of a single geometry. Frequency-domain phase measurement (FDPM) [1-3], devised by Chilla and Martinez cross-correlates a pulse with its frequency filtered replica to form a smoothed map of the bandpass-filter centre frequency against delay from which the pulse data can be extracted using an iterative retrieval algorithm [2, 4]. For the retrieval to be accurate the duration of the unfiltered pulse must be significantly shorter [2] than the filtered pulse and the dispersion of the spectral bandpass filter must be zero or well-characterised [4]. Chapter 4 provides a description of how this geometry has been used to rapidly acquire and retrieve a sonogram trace to fully characterise a pulse.

Recently, Koumans and Yariv have reported an alternative to the FDPM sonogram (or TROG) geometry called dispersive-propagation time resolved optical gating (DP-TROG) [5]. The DP-TROG measurement yields an auto-sonogram of the pulse by recording a series of second-order autocorrelation profiles of the pulse after it has passed through a system of variable group-velocity dispersion. A direct mapping from dispersion  $\rightarrow$  time is used to generate the TROG trace from the Fourier-transformed autocorrelation data. This technique has been used to characterise pulses at 1.5 $\mu\text{m}$  using a dual grating disperser [6] to vary the dispersion [7].

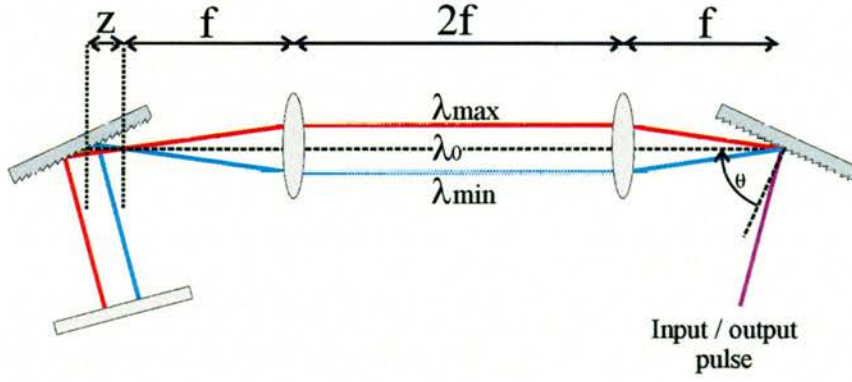


**Figure 5.1** The dual grating disperser used by Koumans to vary the dispersion of a pulse [7]

The amount of dispersion added to the pulse is varied by adjusting the distance  $z$  between the grating and the focal point of the telescope and this can be described mathematically as:

$$D(z) = -2\pi\beta_2 z \quad (5.1)$$

where the dispersion parameter  $\beta_2$  is given as

$$\beta_2 = \frac{-\lambda_0^3}{\pi c^2 d^2 \cos^2 \theta} \quad (5.2)$$

$\lambda$  is the centre wavelength,  $c$  is the speed of light,  $1/d$  is the grating line density and  $\theta$  is the angle between the normal to the grating and the telescope axis. By taking a number of autocorrelation traces around a dispersion point  $D_0$  that corresponds to where the maximum pulse compression occurs (ie. minimum autocorrelation width), the resulting set of autocorrelation traces is given as:

$$R(D, T) = \left| \int A'(t, D) A'(t - T) dt \right|^2 \quad (5.3)$$

where  $A'(t, D)$  is the pulse envelope. The Fourier transform of this trace is then taken to produce

$$\tilde{R}(D, F) = \left| \int A'(t, D) \exp(-i2\pi Ft) dt \right|^2 \quad (5.4)$$

Equation (5.4) can then be expanded using the convolution theorem to give

$$\tilde{R}(D, F) = \left| \int \tilde{A}(f) \tilde{A}^*(f - F) \exp(i2\pi fFD) df \right|^2 \quad (5.5)$$

The signal given by the normal sonogram geometry (ie. FDPM-TROG) can be expressed as

$$I_{FDPM-TROG}(T, F) = \left| \int \tilde{A}(f) \tilde{G}(f, F) \exp(i2\pi fT) df \right|^2 \quad (5.6)$$

where the gate function  $\tilde{G}(f, F)$  is small enough to be assumed as a delta function. By making a direct comparison between equations (5.5) and (5.6) it can be seen that there is a direct scaling between the two equations so that

$$T = FD \quad (5.7)$$

such that

$$I_{DP-TROG}(T, F) = \tilde{R}\left(\frac{T}{F}, F\right) \quad (5.8)$$

Equations (5.3) through to (5.8) show how a DP-TROG trace can be constructed from a measured set of autocorrelation traces  $R(D, T)$ . By Fourier transforming the autocorrelation with respect to T and interpolating at points  $(T/F, F)$  so that a Fourier array is formed where  $\Delta T$  and  $\Delta F$  are related by equation (5.9), a DP-TROG trace is formed.

$$\Delta T = \frac{1}{N\Delta F} \quad (5.9)$$

The DP-TROG is then processed by a retrieval algorithm to obtain the pulse information.

Although the DP-TROG technique has been shown to be successful [7], there are some experimental issues associated with implementing the DP-TROG method that need to be addressed before DP-TROG can be used as a viable alternative to other characterisation techniques. The initial dispersion calibration is crucial to the whole success of the DP-TROG technique given that it is this calibration which is used to construct the DP-TROG trace using equation (5.7). If the measurement of dispersion is incorrect, all data originating from this trace will also be incorrect. In the Koumans publication [7], Equation (5.1) was used to calculate the dispersion originating from the dual grating disperser. Basing the DP-TROG dispersion calibration entirely on a calculation, although in principle correct, is unreliable because it is prone to experimental uncertainties in the disperser alignment and in all of the

variables that are associated with the dispersion parameter  $\beta_2$  in equation (5.2). Within this chapter there is a description of how the marginals of the DP-TROG trace can be utilised to automatically calibrate the dispersion axis. Also there is the first demonstration of a sub 100fs pulses measurement using DP-TROG and discussion of the limitations of DP-TROG when measuring even shorter pulses.

## 5.2 Experimental configuration

The optical setup used to experimentally acquire a TROG trace (Figure 5.2) is made up of two main parts, a dispersive filter and an autocorrelator.

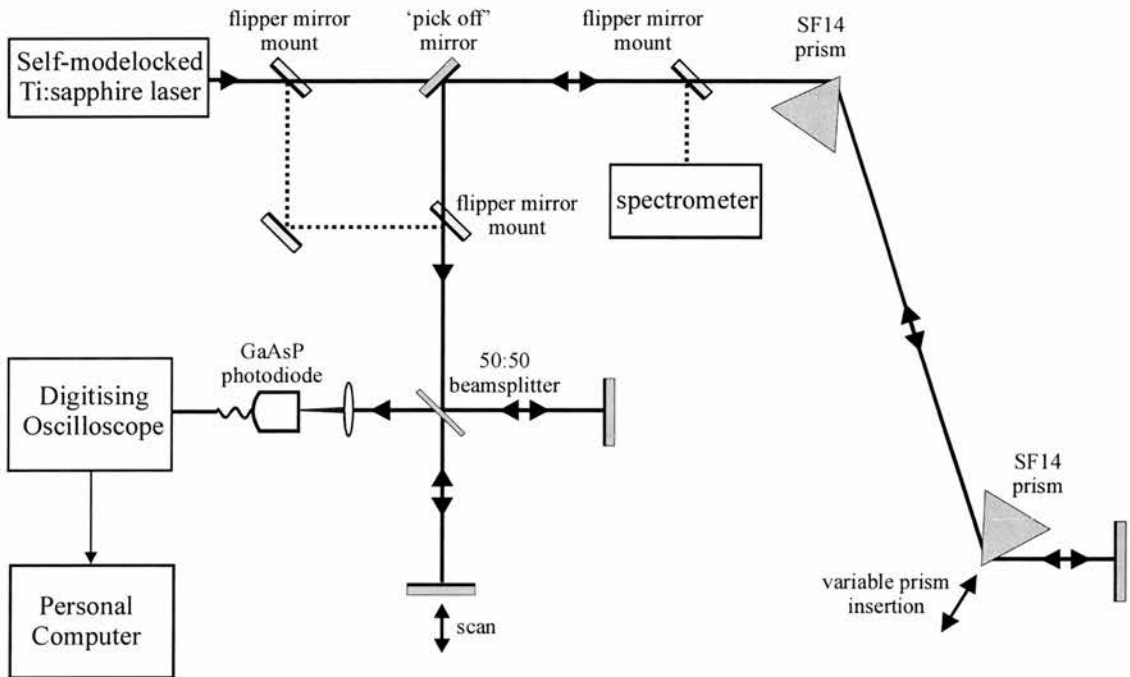


**Figure 5.2** The optical arrangement used to acquire the experimental TROG trace

Instead of the dual grating disperser previously used to acquire a DP-TROG trace [7], a prism-pair arrangement was used as the dispersive element. Using the retrieval algorithm (Section 5.3) it was found that in order to successfully characterise a pulse using DP-TROG, the dispersion introduced must cover a sufficient range to cause the autocorrelations at the minimum and maximum GVD values to have intensities below 30% of the maximum autocorrelation intensity. When the dispersion range is too small, Equation (5.8) illustrates

that regions of the DP-TROG trace where  $(T/F)$  is large will lack any data. For the pulses measured in this work, a sufficient dispersion range was achieved by using a pair of SF14 prisms with an apex separation of 275 mm. Alternative arrangements could easily be substituted to measure pulses at other wavelengths or with durations significantly different from those studied here. In a prism pair arrangement, suitable configurations could be realised by choosing a different prism material or apex separation. In my configuration, by introducing a slight vertical displacement of the returning beam through the prism pair, the dispersed light was collected by a mirror situated above the input beam and directed into the autocorrelator. The autocorrelator was a standard collinear Michelson design and used a mirror attached to a loudspeaker to provide the required movement of one of the arms. Appropriate capacitive filtering was used to obtain the intensity autocorrelation signal using a digitising oscilloscope. Strong autocorrelation signals were measured for the full range of dispersion, and signal averaging was used to eliminate residual noise. A two-photon detector (GaAsP photodiode) was used to provide a sensitive, cheap and simple nonlinear element with which to measure the autocorrelation trace.

A total of 70 autocorrelation traces were measured at different prism insertions, a process taking around 20 minutes to complete manually. It should be noted that this acquisition procedure could easily be automated to reduce this time dramatically. Starting initially at minimum prism insertion, the second prism was stepped at constant intervals of 0.2 mm until maximum insertion was reached. After each step, the autocorrelation trace was recorded using a digitising oscilloscope (Tektronix TDS3032) capable of sampling 10000 data points per channel. The results obtained are shown in Figure 5.3

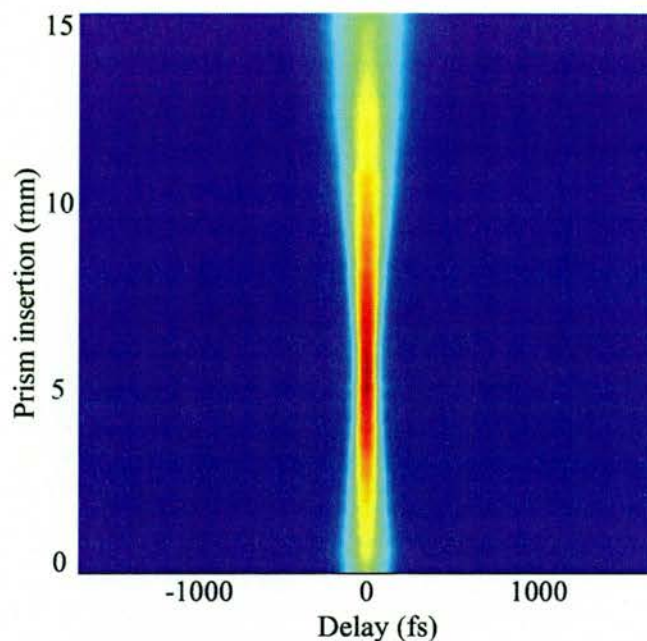


*Figure 5.3* Pulse intensity autocorrelation traces at various prism insertions

It was important to confirm that the pulses from the laser did not change while acquiring the set of autocorrelation traces. To ensure that this was the case, the spectrum and autocorrelation of the pulses were measured at the beginning and the end of the data acquisition. By verifying that both measurements remained unchanged it was reasonable to assume that the pulses had not varied during the course of the acquisition procedure. As discussed later, in section 5.3, an accurate measurement of the autocorrelation of the pulse was critical to the entire calibration procedure and so, to ensure consistency, a direct autocorrelation of the pulse was measured with the same autocorrelator used in the series of dispersed pulse measurements. This was achieved by using a sequence of kinematic mirror mounts to redirect the incoming beam directly into the autocorrelator.

As part of the measurement calibration procedure, the prism insertion corresponding to zero dispersion had to be established. This was achieved in practice by finding the two prism insertions that produced autocorrelations with FWHM durations equal to the FWHM autocorrelation duration produced by the original pulse. Except in the case of a transform-limited pulse, there will always be two prism insertions that have identical autocorrelation FWHM's (although not with necessarily with identical pulse shapes, eg. in the case of

uncompensated third-order group-velocity dispersion). For our system, it was known that positively chirped pulses were being generated, and this information ensured that the correct prism insertion was chosen ie. the one corresponding to the greater prism insertion. When the sign of the chirp is unknown it should be noted that an incorrect choice of the zero-GVD prism insertion will become evident when attempting to calibrate the DP-TROG measurement using the trace marginals as described later in this chapter. In this case, a switching of the zero-GVD prism insertion value to the other position is all that is required. Alternatively, *a priori* knowledge of the dispersive filter can be used to determine the zero-GVD position.

Once a suitable set of experimental autocorrelation profiles was assembled, the data were resampled in time onto a 128 element array (Figure 5.3) then Fourier-transformed to give a frequency-domain representation of each autocorrelation (Figure 5.4).

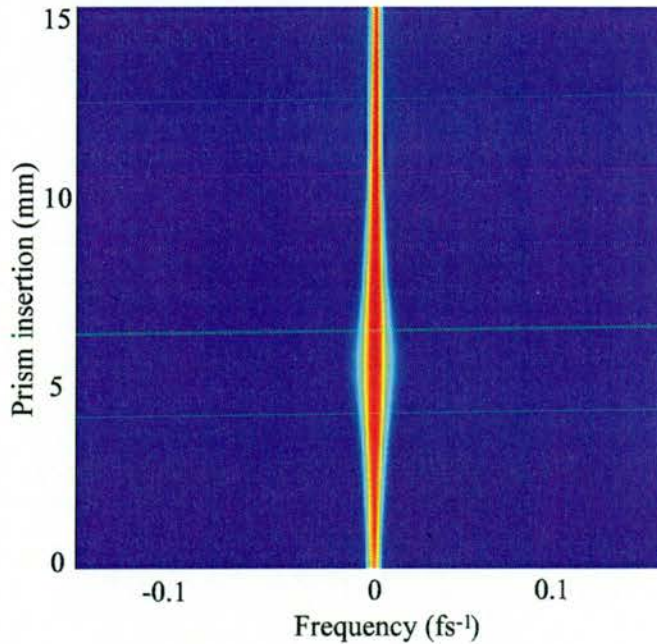


**Figure 5.4** Fourier transform of the pulse intensity autocorrelation at various prism insertions

Creation of the DP-TROG trace simply requires a mapping from this dispersion-frequency domain to a time-frequency representation. By assuming that only second-order group velocity dispersion is added to the pulse by the prism-pair arrangement, the mapping function given in equation (5.7) can be represented as

$$t \leftrightarrow -2\pi \frac{d^2\phi}{d\omega^2} f \quad (5.10)$$

Before this mapping function can be applied to the trace in Figure 5.4 it is necessary to re-calibrate the dispersion axis so that it replaces the prism insertion axis in terms of dispersion.

### 5.3 Calibration, analysis and retrieval of experimental results

One of the most attractive attributes of the DP-TROG implementation described within this chapter is the absence of any complex dispersion calibration procedures, the only requirement being that an accurate measurement is made of the delay axis of the autocorrelation data. Interestingly, as long as the GVD introduced by the dispersive filter varies linearly, no measurement of the absolute filter dispersion is required. By exploiting the properties of the TROG trace marginals, complete calibration can be achieved if the pulse autocorrelation and spectrum are known.

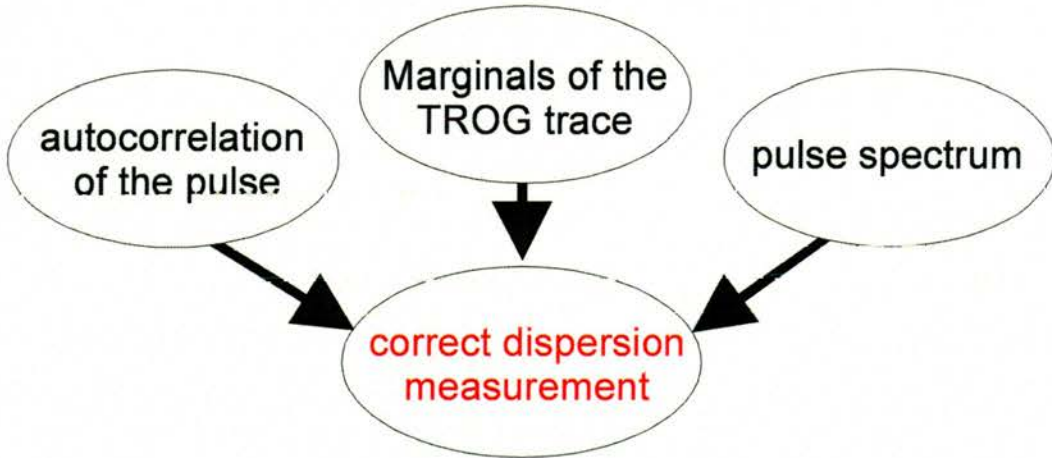


**Figure 5.5** Block diagram, emphasising the simplicity of calibration when utilising the DP-TROG trace marginals

To start, an estimate of the filter GVD is made using knowledge of the change in the material thickness with prism insertion, the Sellmeier data for SF14 glass and the known zero-GVD position. As explained in reference [8] this simple approach does not accurately predict the exact GVD introduced in the measurement. Next, a preliminary TROG trace is generated using Equation (5.10) and its marginals calculated. From equation (5.10) it is possible to see that as frequencies become small and tend towards zero, larger values of dispersion are

required. Experimentally it is not always possible to measure these values of dispersion with the result that no experimental data are available for points close to zero frequency. Data at zero frequency offset ( $f = 0$ ) which are not accessible at all from equation (5.10) are obtained by Fourier-transforming the pulse spectrum and squaring it in magnitude [5].

The DP-TROG trace is the spectral analogue to the SHG-FROG trace and consequently the time marginal of the DP-TROG trace is equal to the pulse temporal intensity autocorrelation and the frequency marginal is identical to the pulse spectral intensity autocorrelation. By comparing the trace marginals with the experimental temporal and spectral autocorrelations, the estimated GVD was linearly scaled until a precise match was found. An agreement could only be found when the value of GVD was set correctly. If this could not be achieved it would suggest that either the incorrect zero dispersion position had been selected or that the calibration of the spectrometer or the delay arm was incorrect. To check the validity of this approach, test retrievals were carried out on traces generated with a range of dispersion calibrations and these showed that the minimum RMS retrieval error

$$error_{rms} = \sqrt{\frac{1}{N} \sum_1^N \{(x_N - y_N)^2\}} \quad (5.11)$$

was obtained when the marginals were in exact agreement as described where  $x$  and  $y$  are the data points from the trace marginal and its equivalent spectral or temporal pulse autocorrelation. This procedure highlights one of the major advantages of our technique in that if there is any error in the calibration it will be apparent immediately in analysing the trace marginals. Figure 5.6 shows a comparison between the temporal and spectral autocorrelations and the marginals of the DP-TROG trace generated from experimental data using the procedure above.

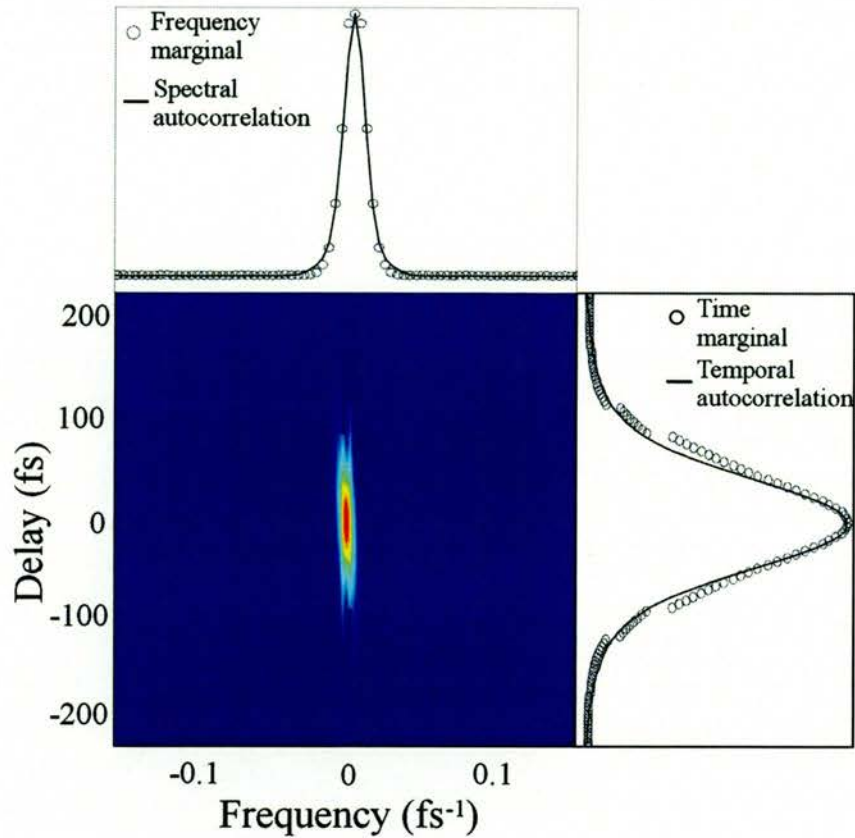


**Figure 5.6** The experimental DP-TROG trace with comparison of its time and frequency marginals with the temporal and spectral intensity autocorrelations of the pulses respectively

The marginals show good agreement, implying that the correct values of GVD have been identified. It should be highlighted that there are a number of points on the time marginal plot which do not coincide with the autocorrelation of the pulse. This discrepancy is due solely to a few missing data points around  $f=0$  which are not mapped to because of the limited experimental dispersion range. The effect can be eliminated by using a smaller sampling step in time or by applying an interpolation procedure [5].

Using an algorithm based on principal-component generalised projections (PCGP) [4, 9, 10], the DP-TROG trace can be quickly retrieved (assuming, as is common with all spectrogram / sonogram methods, that a given pulse is uniquely represented by its DP-TROG trace). PCGP, described already in detail earlier in this thesis, uses a matrix approach based on the idea that a sonogram can be generated from the outer product of the pulse complex spectral amplitude

and the frequency filter amplitude response. In DP-TROG, the pulse and filter are identical, and applying the outer product idea in reverse and exploiting certain properties of matrix singular value decomposition forms the basis of the retrieval algorithm. Figure 5.7 shows a schematic of the retrieval algorithm used for DP-TROG sonograms.

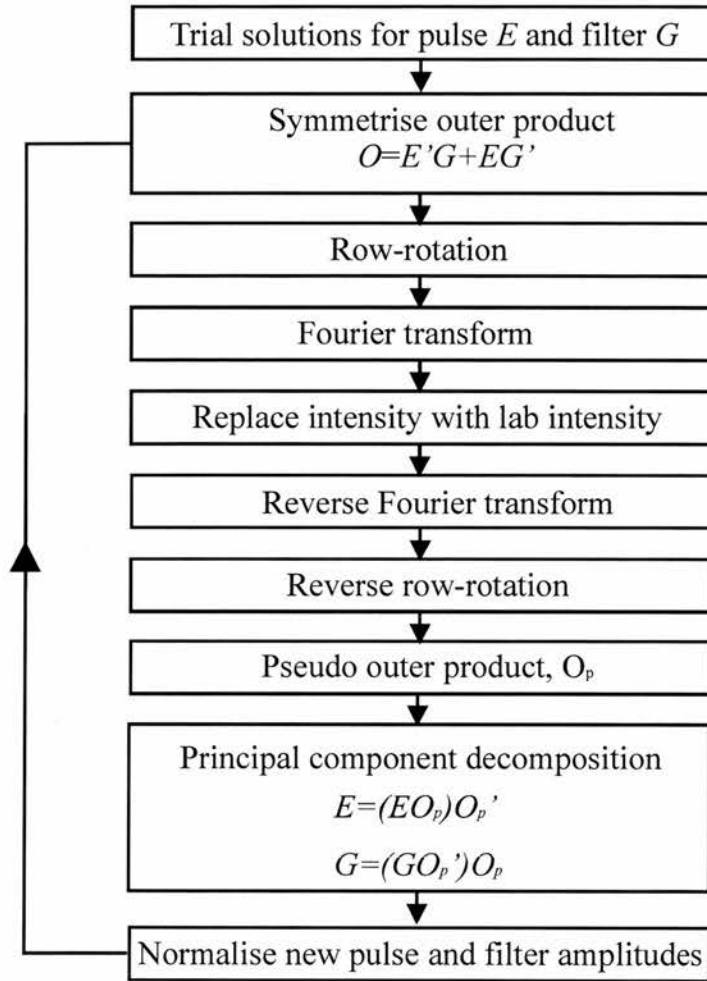


**Figure 5.7** Schematic representation of the DP-TROG retrieval algorithm. The symbol ' represents the complex conjugate and transpose operation

An initial trial solution for the gate ( $G$ ) and the pulse ( $E$ ) spectral amplitude is constructed using an arbitrary Gaussian envelope with random phase. In the DP-TROG geometry, the gate and pulse spectral amplitudes are identical. The trial solutions are used to calculate the TROG-sonogram complex amplitude and its intensity is replaced by the intensity of the laboratory-measured sonogram. This resulting pseudosonogram is manipulated using the PCGP procedure to obtain an improved estimate of the pulse and gate spectral amplitudes. As

pointed out in reference [5], the DP-TROG trace is insensitive to the transformation  $E(\omega) \rightarrow E(-\omega)$  and this is analogous to the temporal ambiguity of SHG-FROG [11] which is unable to discriminate between  $E(t)$  and  $E^*(-t)$ . This ambiguity means the outer product should always be symmetrical, and consequently this fact is utilised within the algorithm so that the outer-product is automatically symmetrised, enabling the number of iterations before convergence to be reduced.

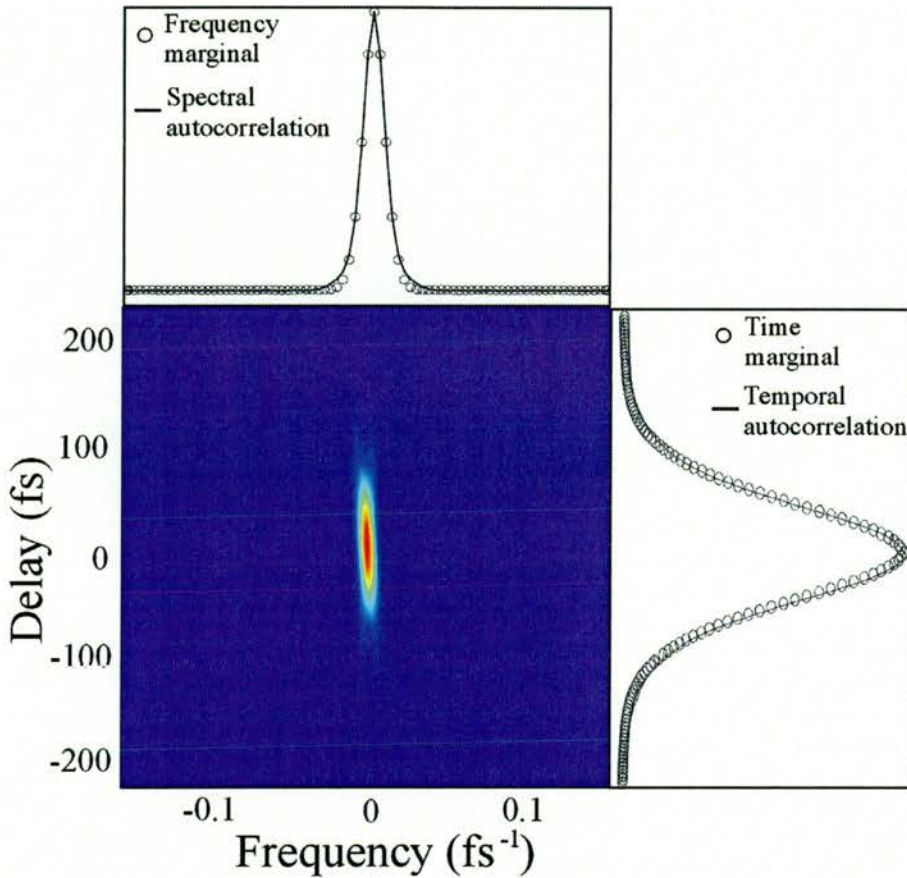


**Figure 5.8** The retrieved DP-TROG trace with comparison of its time and frequency marginals with the temporal and spectral intensity autocorrelations of the pulses respectively

Figure 5.8 shows the retrieved DP-TROG trace after 50 iteration, corresponding to a total retrieval time (MATLAB / Pentium II 450 computer) of  $\sim 7$  seconds. Again, the marginals of the retrieved trace are compared with the spectral and temporal pulse autocorrelations, showing excellent agreement. It should be highlighted that unlike previous techniques [7], no interpolation routine was carried out to fill in missing data points before retrieval. It is evident that provided a suitable sampling period is selected, interpolation is found to be unnecessary

when using the PCGP retrieval algorithm. Figure 5.9 shows comparisons between the retrieved data and the independently measured autocorrelation (Figure 5.9a) and pulse spectrum (Figure 5.9b)

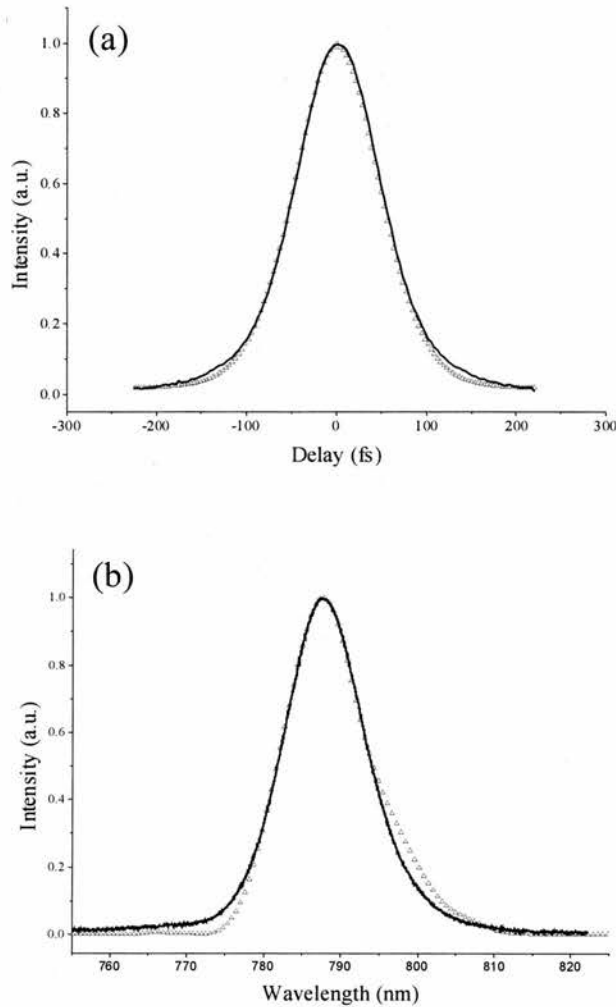


**Figure 5.9** A comparison between the independently measured (solid-line) and retrieved (triangles) autocorrelation (a) and independently measured (solid-line) and retrieved (triangles) pulse spectrum (b)

Figure 5.10 shows the retrieved temporal intensity and phase. It is believed that the fluctuations on the temporal pulse intensity are genuinely present, particularly because the autocorrelation, spectral and marginal data inferred from the retrieved pulse match independent measurements well. Alternatively, the fluctuations may be an artefact associated with missing data on the DP-TROG trace resulting from the dispersion  $\rightarrow$  time mapping

procedure when no interpolation is used. Although the algorithm used is different from the one used from previous work [5, 7] retrieval of theoretical data indicated no tendency of the algorithm to introduce temporal fluctuations.

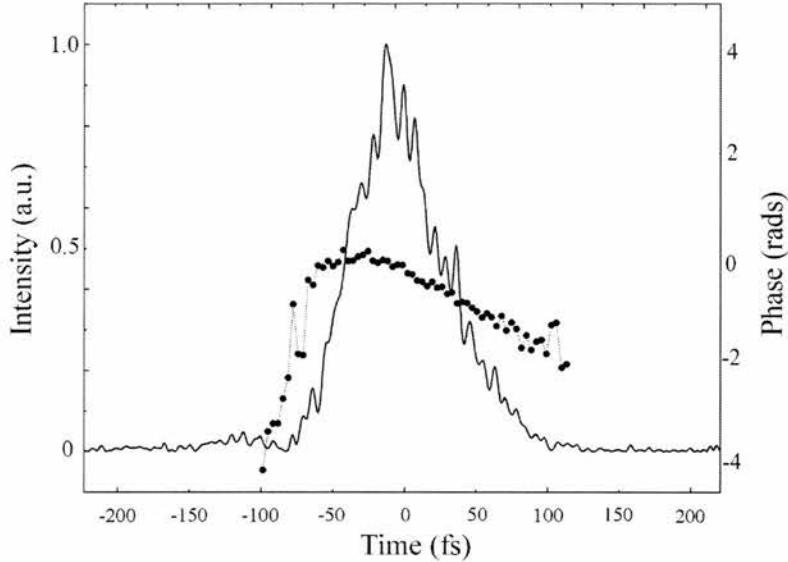


**Figure 5.10** The retrieved temporal intensity (solid-line) and phase (circles)

#### 5.4 Limitations of the DP-TROG technique

The DP-TROG method is attractive because it is simple to implement experimentally and involves a series of straightforward autocorrelation measurements to construct the final dataset. The sensitivity of the technique is only limited by the detectivity of the autocorrelator, and autocorrelation experiments combining two-photon autocorrelation with lock-in amplification have implied that pulses with tens of fJ energies can be readily recorded [12]. Compared with SHG-FROG, DP-TROG has a possible advantage in that it is able (when an external spectral measurement is available) to determine the sign of the pulse chirp. As pointed out in Ref. [5], the TROG trace is insensitive to the transformation  $E(\omega) \rightarrow E(-\omega)$  and this is analogous to the temporal ambiguity of SHG-FROG [11] which is unable to discriminate between  $E(t)$  and  $E^*(-t)$ . Of greater concern are several practical issues which ultimately limit the versatility and reliability of the DP-TROG method. The first of these is the problem that regions in the TROG trace which correspond to large  $|t/f|$  values require autocorrelation data to be recorded at very large positive and negative filter dispersions.

Generally there is an experimental limit to the range of dispersion that can be conveniently introduced which is associated with the material dispersion of the optics or the geometry of the dispersive filter. The result is that narrow regions of the final TROG trace contain no data, but interpolation has been shown to be effective in correcting this effect in some cases [5]. Careful re-sampling of the experimental data can also be used to minimise the amount of missing data and using a larger grid with a smaller  $\Delta t$  value maintains precision in frequency while reducing the dispersion range required to construct the DP-TROG trace. By using numerical simulations, interpolation has been found to be partially successful even when large areas of the DP-TROG trace have been corrupted by missing data. To illustrate the performance of the retrieval algorithm, a test pulse with substantial temporal and spectral structure was used to form a DP-TROG trace with and without trace correction. The test pulse is a transform-limited 100 fs pulse which has been spectrally filtered by a waveplate-like element with a sinusoidal transmission function. This test pulse is a difficult one for the DP-TROG technique because it exhibits considerable structure in regions of the trace with large time-frequency products and is therefore corrupted by missing data in areas where  $|t/f|$  exceeds the maximum filter dispersion applied in the DP-TROG measurement. Figure 5.11 shows the comparison between the exact TROG trace (a) with the DP-TROG trace constructed with (b) and without (c) interpolation. The dashed region in Figure 5.11(c) indicates the missing data points in the non-interpolated DP-TROG trace.

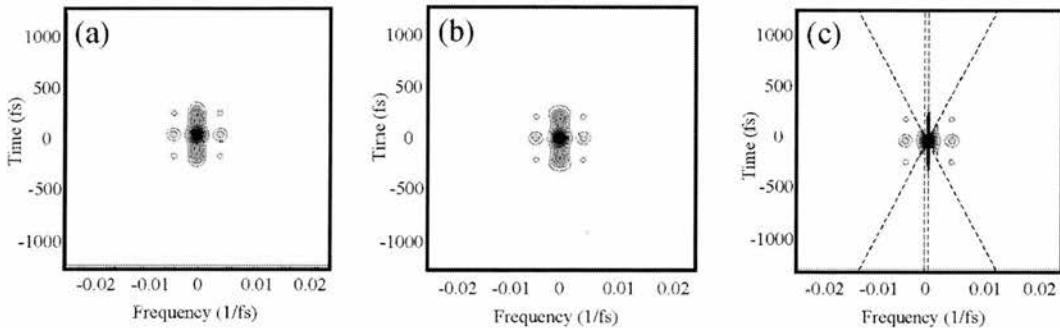


**Figure 5.11** The exact TROG sonogram calculated using Equation (5.5) (a) and DP-TROG traces constructed with (b) and without (c) interpolation

The constructed DP-TROG traces given in Figure 5.11(b-c) were then processed by the retrieval algorithm to extract the pulse information. Figure 5.12 compares the retrieved results of the interpolated DP-TROG trace with the original pulse characteristics.

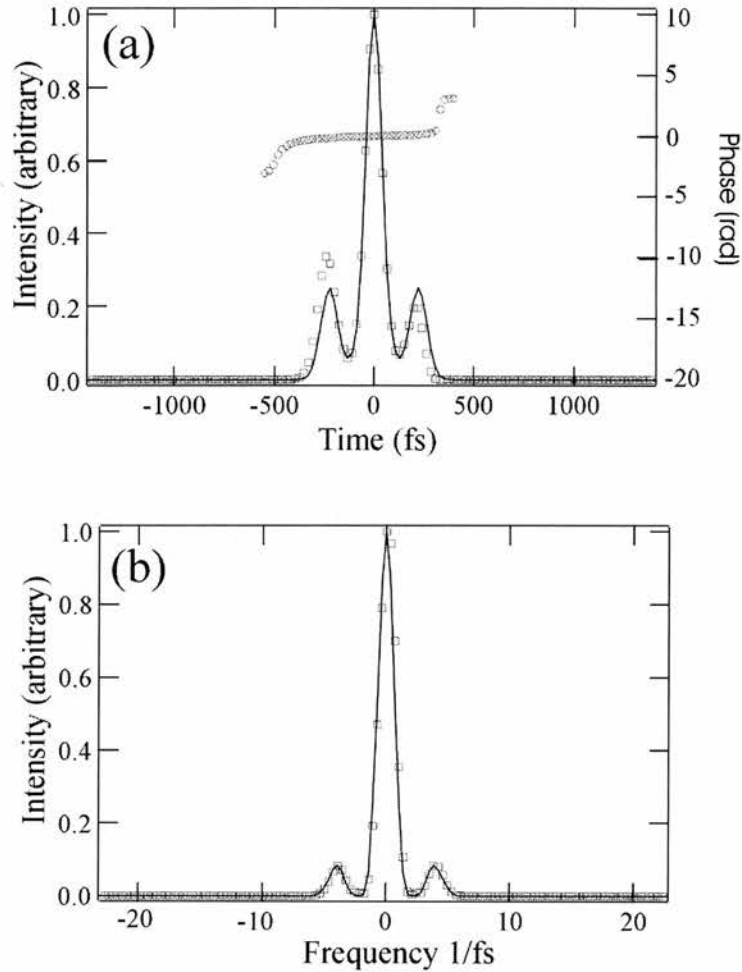


**Figure 5.12** Comparison of the original (solid) line and retrieved (symbols) temporal (a) and spectral (b) pulse data with trace interpolation applied

The results in Figure 5.12 with interpolation applied shows satisfactory agreement with the original pulse with the majority of the pulse structure being successfully retrieved. When no interpolation was applied the agreement was found to become much worse with much of the pulse structure not being retrieved successfully. Figure 5.13 shows the retrieved results of the DP-TROG trace with no interpolation applied to it (Figure 5.11(c))

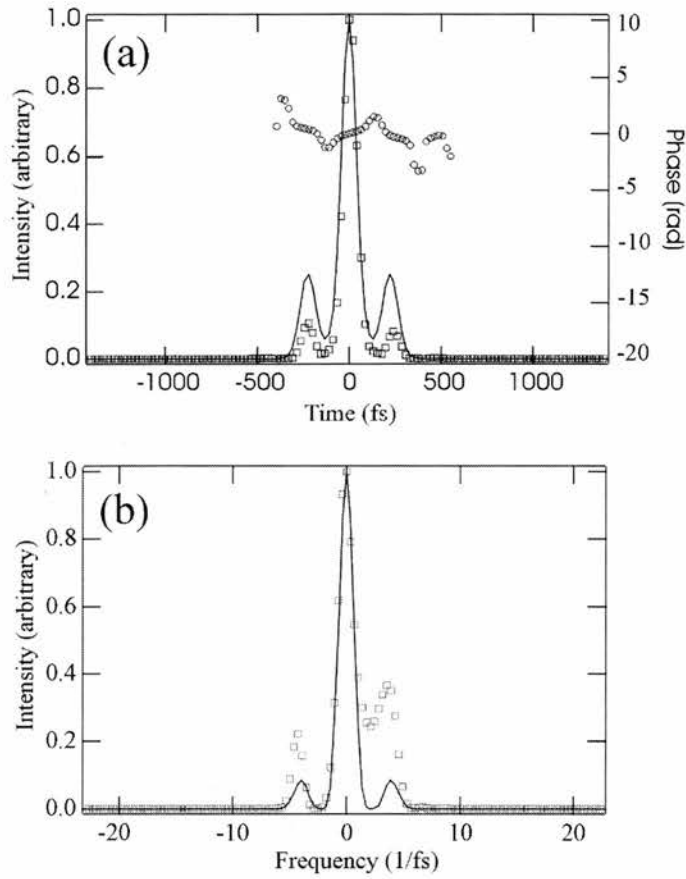


**Figure 5.13** Comparison of the original (solid) line and retrieved (symbols) temporal (a) and spectral (b) pulse data without trace interpolation applied

From these results it was concluded that to reduce the error resulting from the missing regions within the DP-TROG trace great care should first be taken when choosing the time and frequency re-sampling interval. If the sampling interval is not sufficient to minimise the effect of missing data on the DP-TROG trace, interpolation should then be applied to improve the retrieval process.

The next important limitation of the DP-TROG method concerns the requirement that the dispersive filter only introduce second-order group-velocity dispersion to the pulse. This condition is easily met for narrow-bandwidth picosecond pulses but calls for careful selection of the experimental filter arrangement when shorter pulses are used. By simulating a DP-TROG measurement made using a double-pass prism-pair it is shown here that, under certain conditions, pulses as short as 10 fs can be measured reliably using the DP-TROG method.

Using the expressions for the second and third order group-velocity dispersion of a prism pair given in [13], a comparison has been made of the measurement of transform-limited 10 fs Gaussian pulses using DP-TROG at two centre wavelengths, 800 nm and 850 nm. The prism-pair was modelled in a double-pass configuration with an apex separation of 850 mm, and the DP-TROG dispersion was varied by changing the inserted prism glass thickness from 0-50 mm

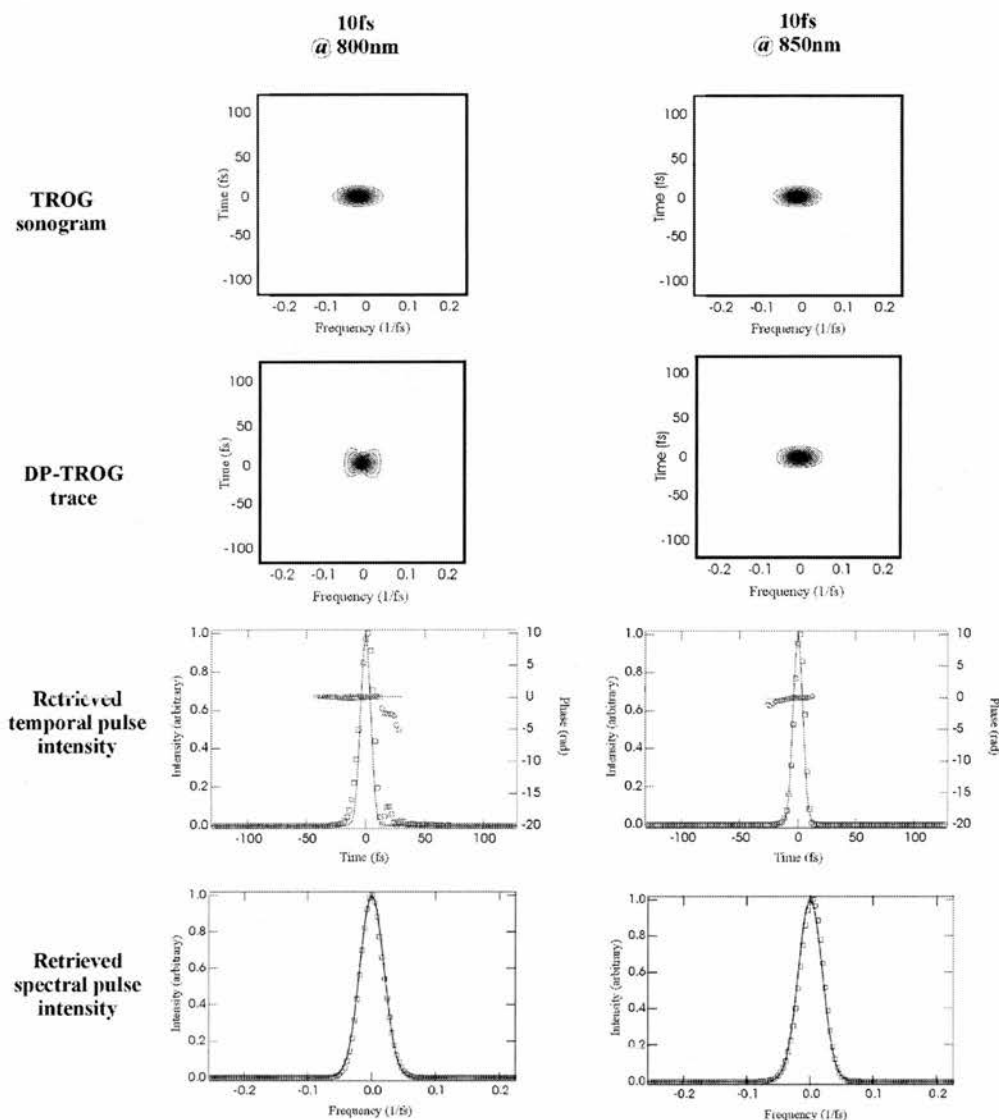


**Figure 5.14** Columns (1-2): Simulation of DP-TROG measurements of pulses with durations of 10fs at centre wavelengths of 800 nm and 850 nm; Rows (1-4): TROG-sonogram calculated from original pulse data; DP-TROG trace derived from dispersive propagation using a fused-silica prism (see main text); original (solid lines) and retrieved temporal pulse intensity (squares) and phase (circles); and original (solid line) and retrieved spectral pulse intensity (symbols).

At 800 nm, corruption of the DP-TROG data by third-order dispersion introduced by the prism-pair is evident in the generated DP-TROG trace which does not match the TROG sonogram calculated for a 10 fs pulse (Figure 5.14 column 1) and the retrieved temporal pulse profile clearly shows an asymmetry associated with third-order dispersion. Simulating the same measurement at 850 nm (Fig. 5.14, column 2), where the residual third-order dispersion of the prism-pair is small, shows that an accurate DP-TROG measurement can be made which agrees well with the calculated TROG-sonogram and produces retrieved pulse data which exactly match the actual pulses.

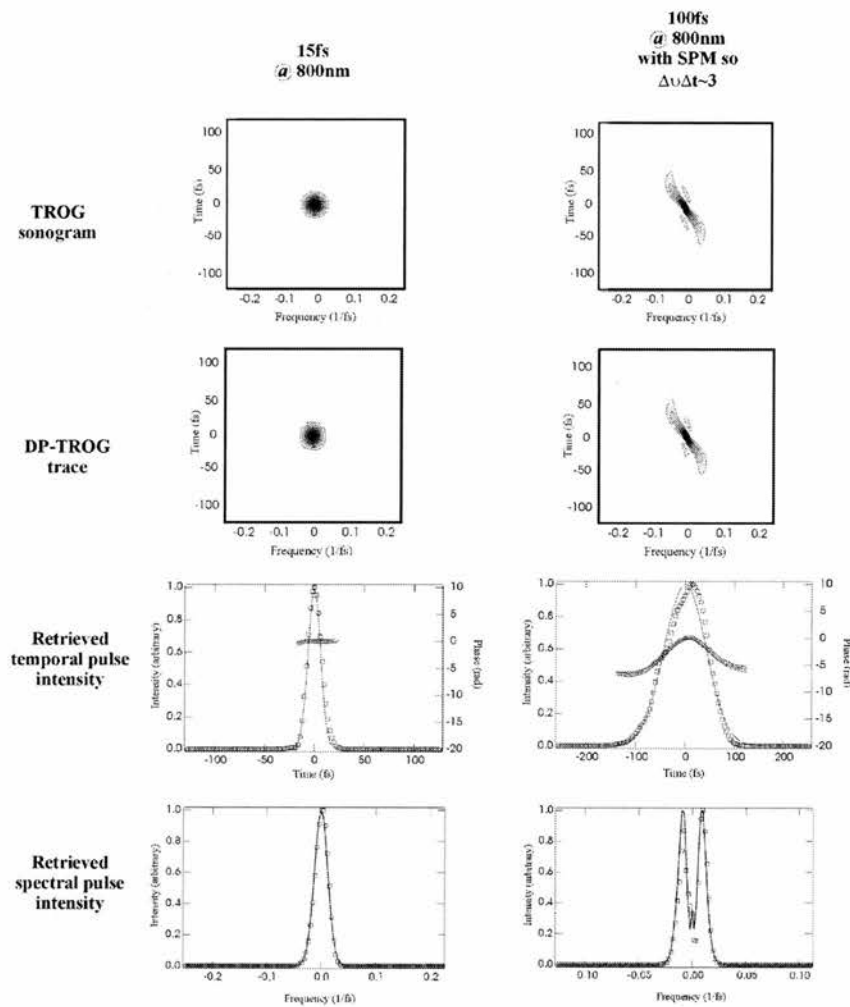


**Figure 5.15** Columns (1-2): Simulation of DP-TROG measurements of pulses with durations of 15 fs and 100 fs at centre wavelengths of 800 nm; Rows (1-4): TROG-sonogram calculated from original pulse data; DP-TROG trace derived from dispersive propagation using a fused-silica prism (see main text); original (solid lines) and retrieved temporal pulse intensity (squares) and phase (circles); and original (solid line) and retrieved spectral pulse intensity (symbols).

Modelling a DP-TROG measurement of 15 fs pulses at 800 nm using the same prism configuration (Fig. 5.15, column 1) also shows good agreement between the DP-TROG trace and the TROG-sonogram and indicates accurate pulse retrieval. Finally, a DP-TROG measurement of a 100 fs pulse was studied at 800 nm which had been spectrally broadened by self-phase modulation to yield a duration-bandwidth product  $\Delta\nu\Delta\tau \sim 3$ , (Fig. 5.15, column 2) and results show the retrieved pulses and generated DP-TROG trace match the exact data well.

By calculating the RMS error between the exact TROG sonogram and the trace generated by DP-TROG based on the fused-silica prism-pair already described, the accuracy of the DP-TROG method has been quantified for measurements involving transform-limited Gaussian pulses with different durations and centre wavelengths.

Durations (fs)	Wavelength (nm)			
	790	810	830	850
10	.0212	.0149	.0068	0.0024
15	.0054	.0030	.0011	.0005
20	.0014	.0007	.0003	.0002

**Table 5.1** RMS error between the exact TROG sonogram trace for transform-limited 10, 15 and 20 fs pulses and the DP-TROG trace measured using a fused-silica prism pair of separation 850 mm and variable material path length of  $\pm 25$  mm. RMS differences of approximately 0.005 or less imply sufficiently close agreement to ensure accurate retrieval of the pulse data. Values refer to a grid size of  $128 \times 128$ .

The results summarised in Table 5.1 indicate that DP-TROG is capable of accurately measuring transform-limited pulses longer than 15 fs at typical Ti:sapphire laser wavelengths. Although the analysis of a Gaussian profile pulse has been carried out it should be noted that the results apply equally to  $\text{sech}^2(t)$  profiles and, in fact, DP-TROG may be capable of

measuring  $\text{sech}^2(t)$  pulses shorter than 15 fs because the FWHM duration-bandwidth product of  $\text{sech}^2(t)$  pulses is less than that of Gaussian pulses.

Based on the results of our simulations it can be concluded that DP-TROG can be usefully applied to the measurement of femtosecond pulses with the proviso that third-order filter dispersion is minimised and that re-sampling and interpolation are applied judiciously to the DP-TROG trace to minimise data lost in the dispersion-to-time mapping process.

## 5.5 Conclusion

The DP-TROG measurement is attractive because of its simplicity. Using two-photon absorption in readily available devices such as photodiodes and laser-diodes has made sensitive autocorrelation of modelocked ultrashort pulses a straightforward procedure at wavelengths from the blue to the mid-infrared [14-16], and the broad spectral response of TPA detectors is well-suited to measuring very short optical pulses [17]. The straightforward calibration procedure using the frequency and time marginals of the DP-TROG trace ensures any systematic errors can be quickly identified. A further attractive feature of DP-TROG is its ability to make pulse measurements at any wavelength for which an autocorrelator is available. This means that direct measurements of modelocked blue or mid-infrared pulses -- both difficult regimes for FROG because of restrictions associated with phasematching bandwidth and / or second-harmonic detection -- are possible using two-photon absorption techniques. While the implementation described here relies on mechanical scanning in delay and dispersion, a single-shot DP-TROG could be realisable using a single-shot autocorrelator and a dispersive-filter with spatially varying dispersion. In conclusion, the DP-TROG represents a versatile and easily implemented method of femtosecond modelocked pulse measurement which will find application at a variety of wavelengths and pulse durations.

## 5.6 References

- [1] J. L. A. Chilla and O. E. Martinez, "Direct Determination of the Amplitude and the Phase of Femtosecond Light-Pulses," *Optics Letters*, vol. 16, pp. 39-41, 1991.
- [2] V. Wong and I. A. Walmsley, "Ultrashort-pulse characterization from dynamic spectrograms by iterative phase retrieval," *Journal of the Optical Society of America B-Optical Physics*, vol. 14, pp. 944-949, 1997.
- [3] T. Beddard, W. Sibbett, D. T. Reid, J. Garduno-Mejia, N. Jamasbi, and M. Mohebi, "High-average-power, 1-MW peak-power self-mode-locked Ti : sapphire oscillator," *Optics Letters*, vol. 24, pp. 163-165, 1999.
- [4] D. T. Reid, "Algorithm for complete and rapid retrieval of ultrashort pulse amplitude and phase from a sonogram," *IEEE Journal of Quantum Electronics*, vol. 35, pp. 1584-1589, 1999.
- [5] R. Koumans and A. Yariv, "Time-resolved optical gating based on dispersive propagation: A new method to characterize optical pulses," *IEEE Journal of Quantum Electronics*, vol. 36, pp. 137-144, 2000.
- [6] O. Martinez, "3000 times grating compressor with positive group-velocity dispersion - Application to fiber compensation in 1.3 - 1.6 micrometer region," *IEEE Journal of Quantum Electronics*, vol. 23, pp. 59-64, 1987.
- [7] R. Koumans and A. Yariv, "Pulse characterization at 1.5  $\mu\text{m}$  using time-resolved optical gating based on dispersive propagation," *IEEE Photonics Technology Letters*, vol. 12, pp. 666-668, 2000.
- [8] C. G. Durfee, S. Backus, M. M. Murnane, and H. C. Kapteyn, "Design and implementation of a TW-class high-average power laser system," *IEEE Journal of Selected Topics in Quantum Electronics*, vol. 4, pp. 395-406, 1998.
- [9] D. J. Kane, "Real-time measurement of ultrashort laser pulses using principal component generalized projections," *IEEE Journal of Selected Topics in Quantum Electronics*, vol. 4, pp. 278-284, 1998.
- [10] D. J. Kane, "Recent progress toward real-time measurement of ultrashort laser pulses," *IEEE Journal of Quantum Electronics*, vol. 35, pp. 421-431, 1999.
- [11] K. W. DeLong, R. Trebino, J. Hunter, and W. E. White, "Frequency-Resolved Optical Gating With the Use of 2nd-Harmonic Generation," *Journal of the Optical Society of America B-Optical Physics*, vol. 11, pp. 2206-2215, 1994.
- [12] D. T. Reid, W. Sibbett, J. M. Dudley, L. P. Barry, B. Thomsen, and J. D. Harvey, "Commercial semiconductor devices for two photon absorption autocorrelation of ultrashort light pulses," *Applied Optics*, vol. 37, pp. 8142-8144, 1998.
- [13] R. L. Fork, C. H. B. Cruz, P. C. Becker, and C. V. Shank, "Compression of Optical Pulses to 6 Femtoseconds By Using Cubic Phase Compensation," *Optics Letters*, vol. 12, pp. 483-485, 1987.
- [14] P. Loza-Alvarez, W. Sibbett, and D. T. Reid, "Autocorrelation of femtosecond pulses from 415-630nm using GaN laser diode," *Electronics Letters*, vol. 36, pp. 631-633, 2000.
- [15] D. T. Reid, C. McGowan, M. Ebrahimzadeh, and W. Sibbett, "Characterization and modeling of a noncollinearly phase-matched femtosecond optical parametric oscillator based on KTA and operating to beyond 4  $\mu\text{m}$ ," *IEEE Journal of Quantum Electronics*, vol. 33, pp. 1-9, 1997.
- [16] D. T. Reid, M. Padgett, C. McGowan, W. E. Sleat, and W. Sibbett, "Light-emitting diodes as measurement devices for femtosecond laser pulses," *Optics Letters*, vol. 22, pp. 233-235, 1997.
- [17] J. K. Ranka, A. L. Gaeta, A. Baltuska, M. S. Pshenichnikov, and D. A. Wiersma, "Autocorrelation measurement of 6-fs pulses based on the two-photon-induced photocurrent in a GaAsP photodiode," *Optics Letters*, vol. 22, pp. 1344-1346, 1997.

# CHAPTER 6

## Single-shot acquisition of a sonogram trace

---

### 6.1 Introduction

The acquisition of a sonogram trace, described in Chapter 4, consists normally of two separately scanning mechanical components – the spectral bandpass filter and the delay line. By scanning the filter across the pulse spectrum and recording the arrival time of each spectral component, a sonogram trace is built up [1]. The arrival time is recorded by measuring the cross-correlation of the pulse with its frequency filtered replica. The resulting signal can be described mathematically as

$$I(\tau) = \int_{-\infty}^{\infty} I_{filtered}(t) I_{original}(t - \tau) dt \quad (6.1)$$

Provided the original pulse ( $I_{original}$ ) is significantly shorter than the filtered pulse ( $I_{filtered}$ ), the unfiltered pulse will act as a delta function. Consequently, using a detector with a quadratic response to intensity, the filtered pulse intensity as a function of delay is recorded.

$$I(\tau) = I_{filtered}(t) \quad (6.2)$$

The detection of the cross-correlation signal is normally carried out using a two-photon detector [2, 3] or a combination of a mixing crystal and a photomultiplier tube [1]. Both of these devices are point detectors and consequently the speed at which the sonogram trace can be recorded depends solely on how fast the scanning components can be moved accurately in synchronism and how fast the data can be collected from the point detector using a data acquisition card. Because of this, the fastest acquisition of a sonogram to date has been at a frequency of 1.52Hz [4] and the resulting sonogram trace is necessarily constructed from millions of pulses.

The measurement of a SHG-FROG trace [5-8] has proved to be much simpler to acquire at high frequencies[9-11]. The reason for this lies in the ability to gate first in time and then in frequency. This allows a multi-point detector such as a CCD camera to be used to image in a single shot the spectrum of the mixing signal with respect to time. An optical arrangement called GRENOUILLE [12-14] has recently been developed by the Trebino group that is capable of acquiring an SHG-FROG trace without any moving parts. The optical arrangement (Figure 6.1) consists of only 6 optical elements - three cylindrical lenses, a Fresnel biprism, a SHG crystal and a CCD camera.

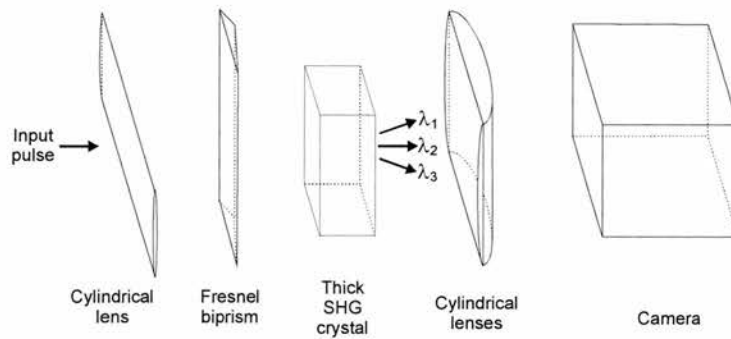


**Figure 6.1** The GRENOUILLE optical arrangement consisting of a few cylindrical lenses, CCD camera, fresnel biprism and a thick SHG crystal[12-14]

The scanning delay line has been replaced by a Fresnel biprism. This simple optical component separates the beam into two separate parts and recombines them at an angle within the crystal, resulting in the delay of the pulse being mapped horizontally across the crystal. This in turn can then be imaged across the horizontal axis of the camera. The spectrometer has in fact been replaced by the SHG crystal by utilising phase mismatch within a mixing crystal. GRENOUILLE uses the limited phasematching bandwidth of a crystal to its advantage, making it act as a wavelength filter so that the wavelength achieving the phase-matching criteria varies linearly with crystal incidence angle. By focussing in the vertical plane, a large divergence is achieved, so that when a couple of Fourier transforming lenses are aligned with the SHG crystal being placed within the Fourier plane, a map of wavelength can be imaged in the vertical plane of the CCD camera. (see section 2.3.1.2 for further detail of the GRENOUILLE optical setup)

In this chapter a description is given of a sonogram equivalent of GRENOUILLE which possesses crucial advantages over GRENOUILLE and allows for the first time, video rate acquisition of a sonogram trace as well as being the first ever technique capable of taking a single-shot sonogram measurement.

## 6.2 Design of the mixing crystal

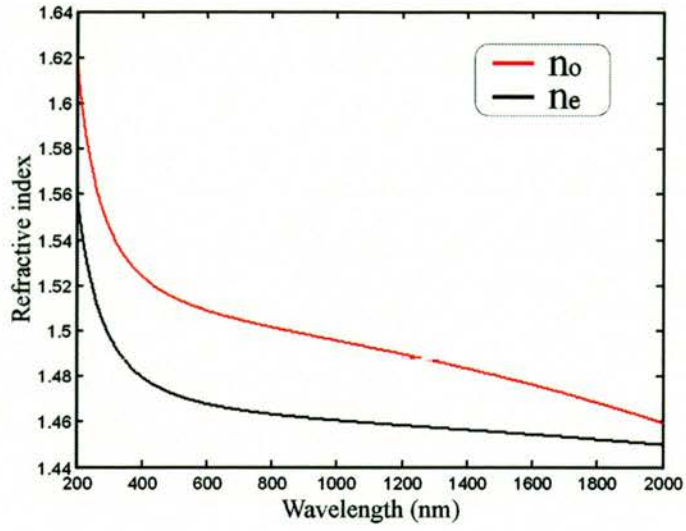
The frequency-mixing crystal is the crucial component within the single-shot sonogram optical arrangement. In GRENOUILLE a thick SHG crystal is used so that two identically polarised beams can interact to create the second harmonic signal. By using a thick crystal the finite phase-matching bandwidth is exploited and the angular variation of the crystal phase-matching wavelength serves as a spectral filter. For the single-shot sonogram optical arrangement, a Type II crystal was used so that two pulses with orthogonal polarisation states could be used to create the mixing signal. By carefully selecting a suitable material and crystal orientation it was possible to frequency mix a pulse with its frequency filtered replica (having an opposite polarisation). By varying the crystal angle, the centre frequency of the filter changed. A description is included here of how this crystal was designed.

A Type II Potassium Dihydrogen Phosphate (KDP) crystal was used as the mixing crystal. The Sellmeier equations used to calculate the refractive indices of the ordinary and extraordinary axis of the KDP crystal are given in equations (6.3) and (6.4) respectively [15].

$$n_o^2 = 2.259276 + \frac{0.01008956}{\lambda^2 - 0.012942625} + \frac{13.00522\lambda^2}{\lambda^2 - 400} \quad (6.3)$$

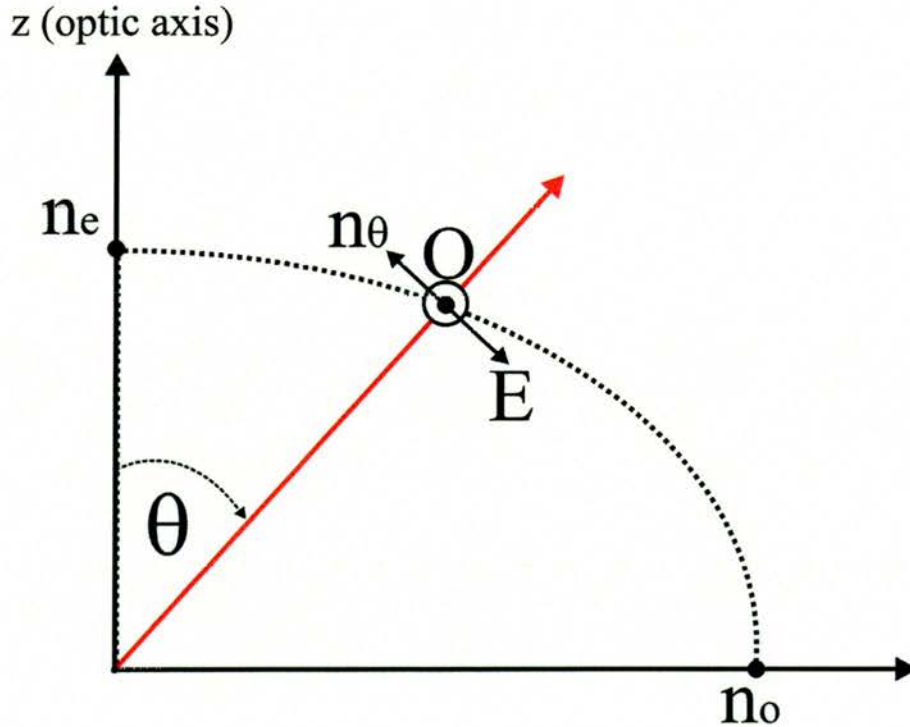
$$n_e^2 = 2.132668 + \frac{0.008637494}{\lambda^2 - 0.012281043} + \frac{3.2279924 \cdot \lambda^2}{\lambda^2 - 400} \quad (6.4)$$

Figure 6.2 uses equations (6.3) and (6.4) to plot the refractive indices of both crystal axis at a range of wavelengths.



**Figure 6.2** The variation of refractive index with wavelength of the ordinary (red line) and extraordinary (black line) axis of a KDP crystal

A KDP crystal is a negative uniaxial so that the refractive index of its ordinary axis has a larger value than the extraordinary axis ( $n_o > n_e$ ) [16]



**Figure 6.3** The index ellipsoid of a negative uniaxial crystal, showing the polarisation directions of E- and O-waves

The refractive index which is found when light propagates at an angle  $\theta$  away from the optical axis ( $n_\theta$ ) (see figure 6.3) can be calculated using equation (6.5)

$$\frac{1}{n_{\theta}^2} = \frac{\cos^2 \theta}{n_o^2} + \frac{\sin^2 \theta}{n_e^2} \quad (6.5)$$

For sum frequency mixing within a nonlinear crystal the phasematching criterion must be met

$$k_{\omega_3} = k_{\omega_1} + k_{\omega_2} \quad (6.6)$$

where  $k_{\omega_{1,2,3}}$  are the propagation constants for their specific wavelengths. In the case of imperfect phasematching, Equation (6.6) can be modified to give the wavevector mismatch as

$$\Delta k = k_3 - k_1 - k_2 \quad (6.7)$$

where the propagation constant  $k$  can be expressed as

$$k_i = \frac{2\pi n(\lambda_i)}{\lambda_i} \quad (6.8)$$

KDP is a negative uniaxial crystal, therefore Type II phasematching is achieved according to

$$E + O \rightarrow E \quad (6.9)$$

where the E-polarisation lies in the plane parallel to the optic axis and the O-polarisation in the plane normal to the optic axis (see Figure 6.3). From this knowledge, Equation (6.7) can be modified to the specific form:

$$\Delta k = \frac{2\pi n_{\theta}(sfm)}{\lambda_{sfm}} - \frac{2\pi n_{\theta}(fund1)}{\lambda_{fund1}} - \frac{2\pi n_o(fund2)}{\lambda_{fund2}} \quad (6.10)$$

The efficiency,  $\eta$ , of the nonlinear mixing has a dependence on  $\Delta k$  which is mathematically described in equation (6.11) [17]

$$\eta = \frac{\sin^2(\Delta k L / 2)}{(\Delta k L / 2)^2} = \text{sinc}^2(\Delta k L / 2) \quad (6.11)$$

Figure 6.4 uses Equation (6.11) to demonstrate how, if the thickness,  $L$ , of the nonlinear crystal increases, the efficiency at higher values of  $\Delta k$  decreases. This is the reason why extremely thin crystals are required to allow the successful frequency mixing of the large bandwidths associated with ultrashort pulses.

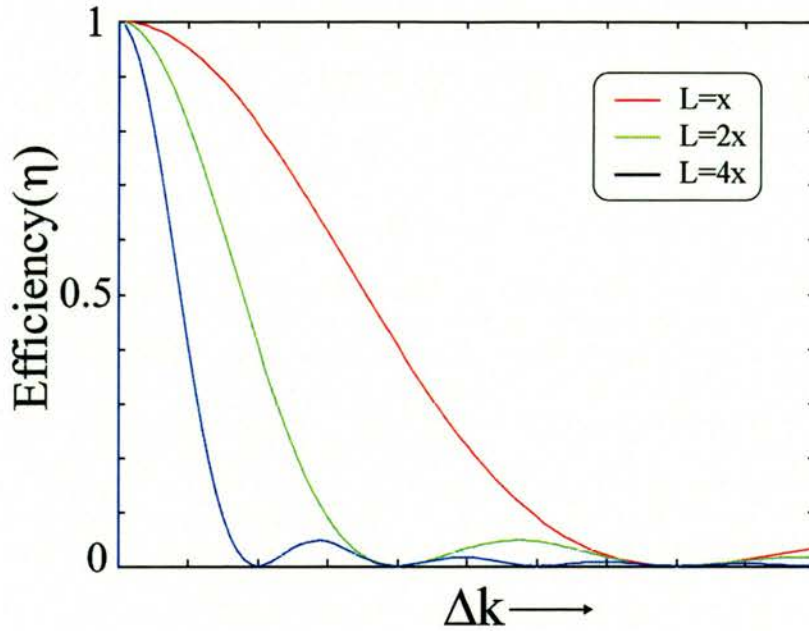


Figure 6.4 The efficiency of sum frequency mixing at various values of crystal thickness,  $L$

If the waves begin in perfect phase so that

$$\frac{\Delta k L}{2} = 0 \quad (6.12)$$

then, they are totally out of phase with one another when

$$\frac{\Delta k L}{2} = \frac{\pi}{2} \quad (6.13)$$

and the efficiency will have fallen to zero. The distance into the crystal at which this happens is known as the coherence length ( $L_c$ )

$$L_c = \frac{\pi}{\Delta k} \quad (6.14)$$

By combining equations (6.10) and (6.11) a plot can be made of all possible mixing signals through a range of fundamental wavelengths. Figure 6.5 shows five such graphs, each with different crystal orientations

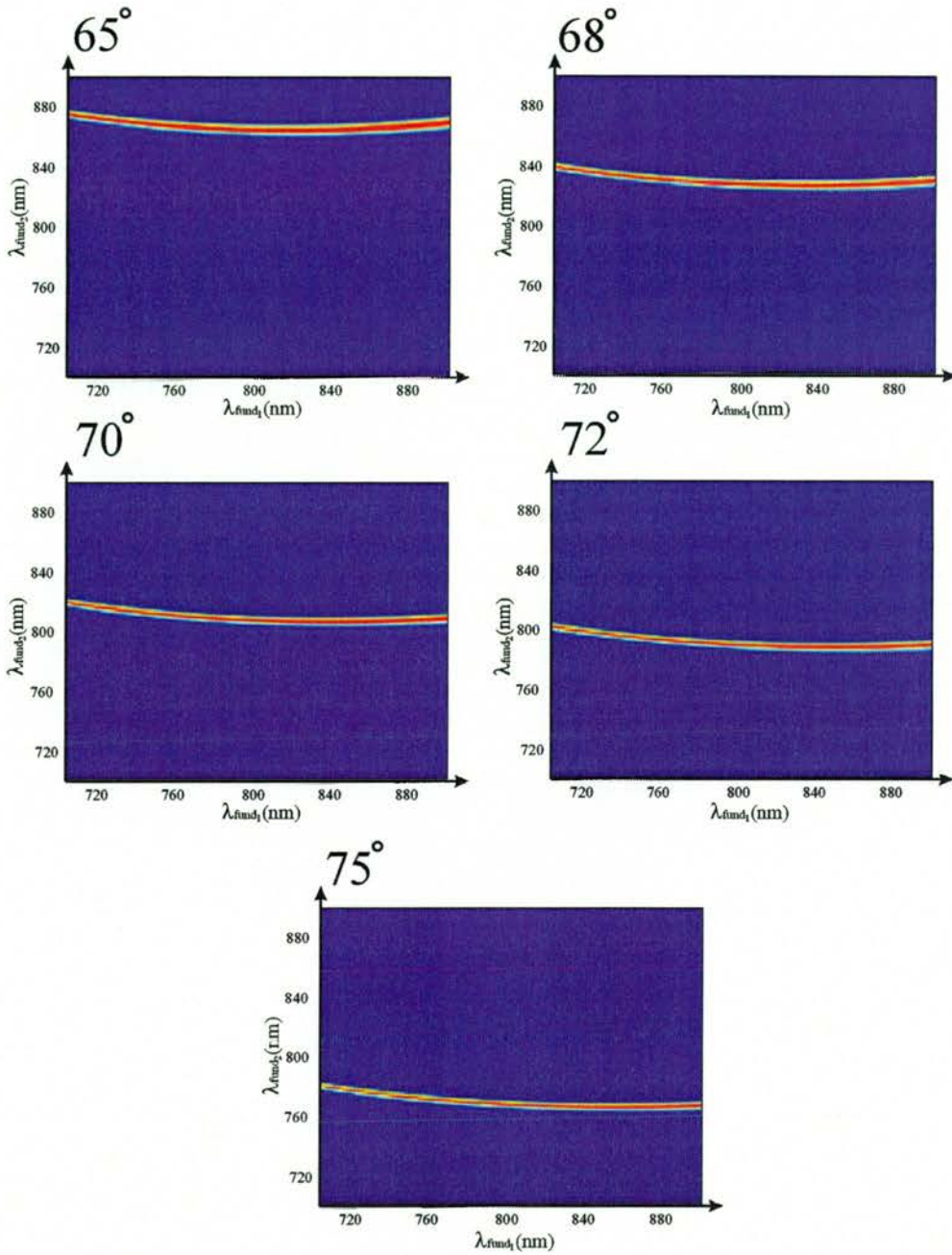


**Figure 6.5** The mixing efficiency of a Type II KDP crystal at various crystal angles

The results in Figure 6.5 show how the bandwidth of a pulse, polarised in one direction will be fully phase matched while an identical pulse with an orthogonal polarisation will be only phasematched for a discrete range of wavelengths. Figure 6.6 tries to conceptualise this idea further.

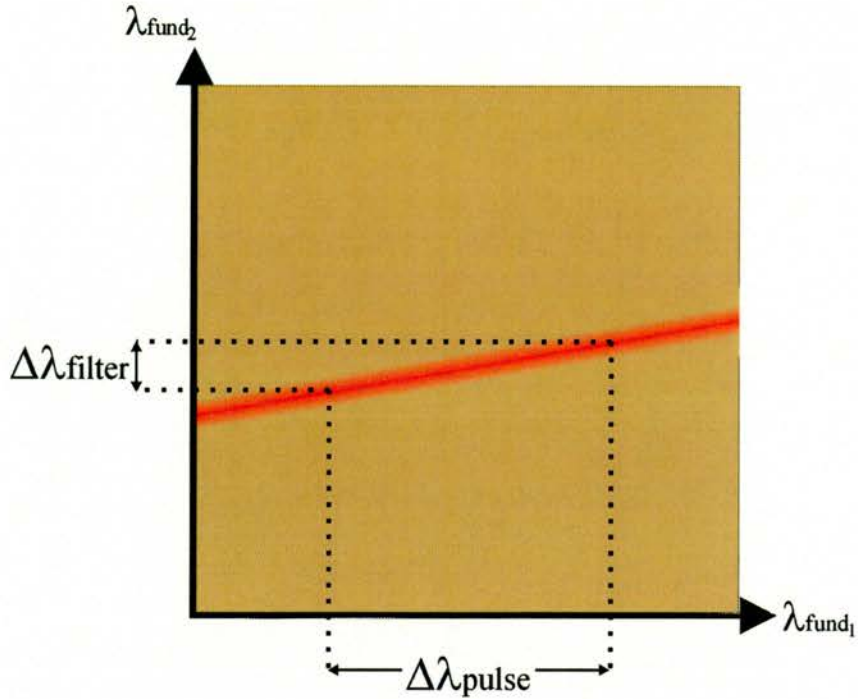


**Figure 6.6** Visualisation of how a pulse at one polarisation can be mixed with a filtered pulse that has an orthogonal polarisation

As the crystal angle is changed, the phasematching band moves up and down so that the  $\Delta\lambda_{filter}$  varies. By ensuring that  $\Delta\lambda_{pulse}$  is large enough to cover the spectral bandwidth of the pulse the resulting frequency mixing signal is, in essence, the cross-correlation of a pulse with its filtered replica, where the centre frequency of the filter is dependent upon the angle of the crystal. This means the scanning of the frequency filter is achieved by rotating the crystal (see figure (6.7))

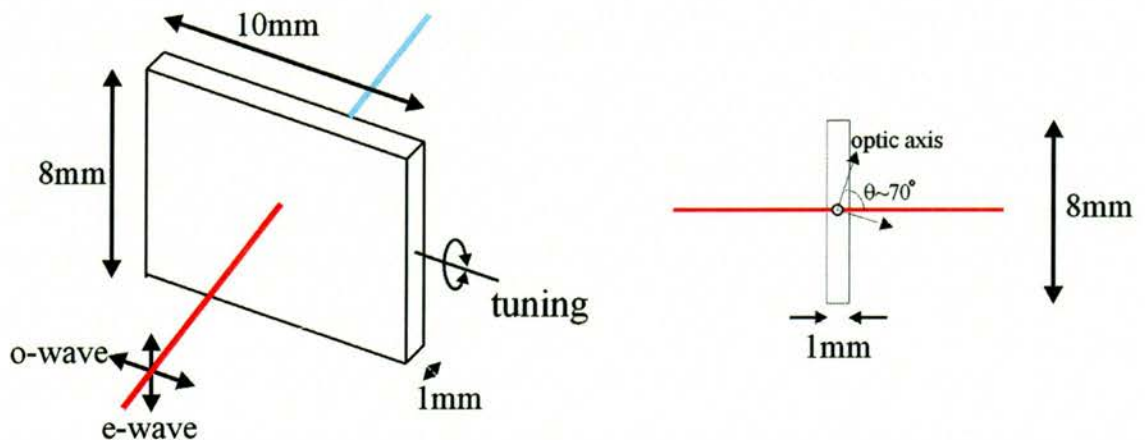


**Figure 6.7** Design of the Type II KDP crystal

The laser used during the experimental procedure had a centre wavelength of  $\sim 815\text{nm}$ . By analysing Figure 6.5 it was possible to see at a crystal orientation of  $70^\circ$  that  $\Delta\lambda_{\text{filter}}$  has a centre wavelength of around  $815\text{nm}$ . Consequently, by having the crystal cut  $70^\circ$  off axis, the effective filter bandwidth will be seen when the crystal is perpendicular with the crystal. A small change in crystal angle ( $\sim \pm 5^\circ$ ) allows  $\Delta\lambda_{\text{filter}}$  to scan across the whole bandwidth of a  $50\text{ fs}$  pulse. The size of the filter is dependent upon the phase matching criterion and as a result, the thickness of the crystal was carefully chosen so that FWHM of  $\Delta\lambda_{\text{filter}}$  was less than one third of the FWHM of the measured pulse [1] - a suitable thickness was found to be  $1\text{ mm}$ . By focussing tightly into the crystal, a bundle of rays can converge within the crystal that covers a large range of incident angles thus angularly mapping out the variation in the filter centre frequency. If the pulse incident on the crystal is polarised at  $45^\circ$  to the optic axis, 50% of the beam will be passed down the o-axis of the crystal and 50% will be passed down the e-axis. The resulting mixing signal will be an angularly resolved cross-correlation signal (at  $\Delta t=0$ ) between the pulse and its frequency filtered replica that has a centre frequency which varies with angle.

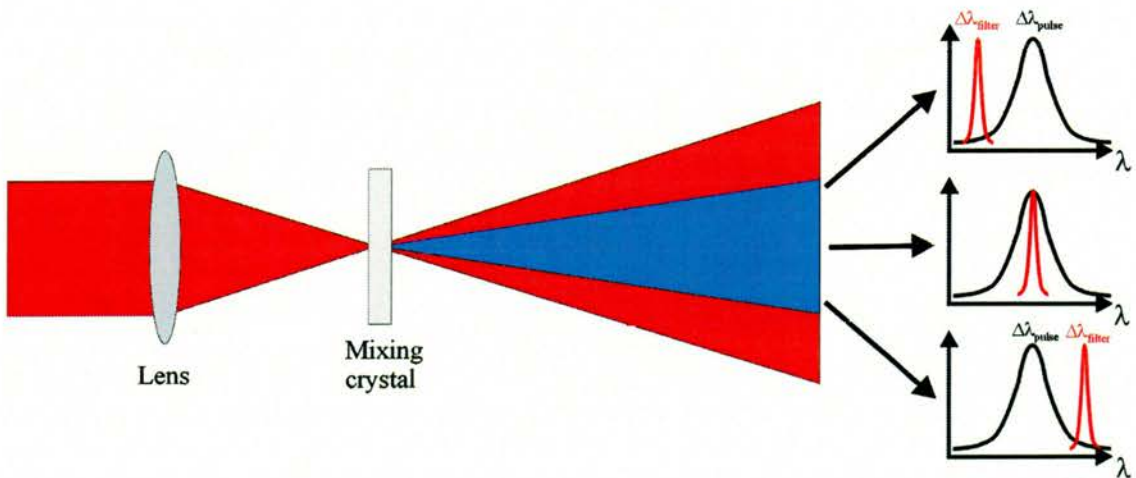


**Figure 6.8** Visualisation of how a mixing crystal can angularly map out a cross-correlation signal at different filter centre frequencies

### 6.3 Creating a variable delay

The crystal design described in Section 6.2 outlines how it is possible to angularly map out the cross correlation at varying filter position when the delay is equal to zero. To enable a sonogram to be acquired, a varying delay needs to be created between the two differing polarisation states that are incident upon the crystal. In the GRENOUILLE optical setup, the varying delay is achieved using a Fresnel biprism. This separates the beam into two separate parts and recombines them at an angle within the crystal. This results in the delay of the pulse being mapped horizontally across the crystal. For the single-shot sonogram, a Type II crystal is used so that there is a requirement to have the incident beam polarised at  $45^\circ$  to the tuning axis of the crystal. This fact meant that, instead of a Fresnel biprism, a polarising Wollaston prism should be used.

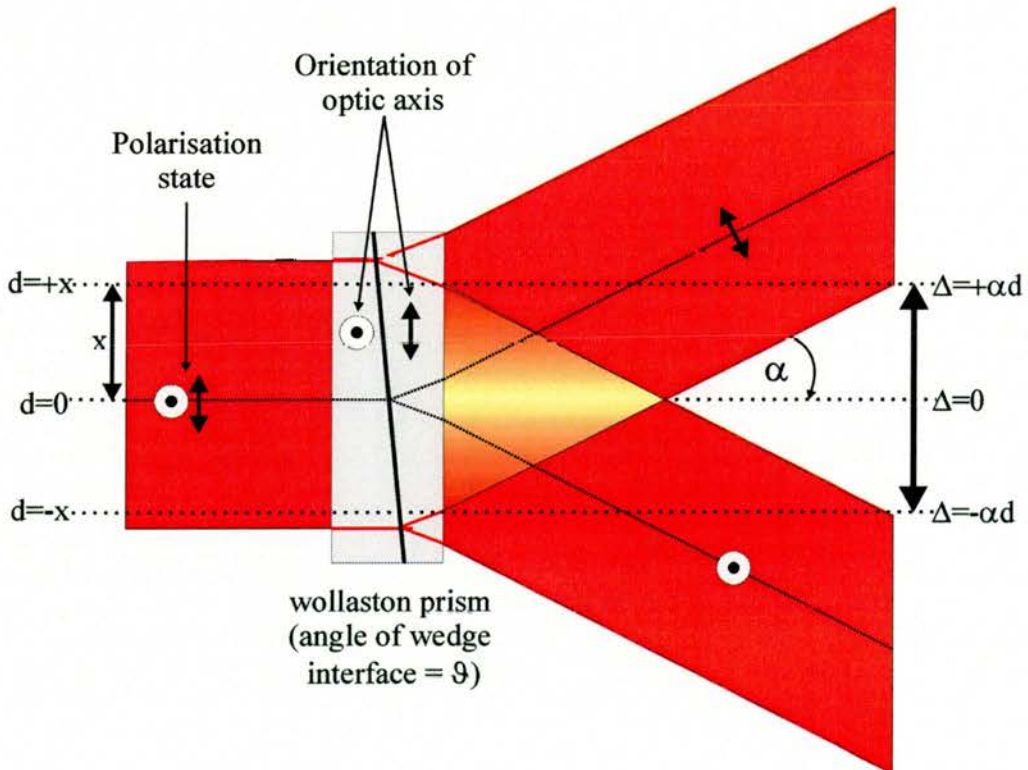


**Figure 6.9** Schematic of what happens when light is passed through a Wollaston prism

Light which is passed through a Wollaston prism is split into two orthogonal polarisations that diverge from one another with a half angle,  $\alpha$ , given by [18].

$$\alpha \approx 2(n_e - n_o) \tan \vartheta \tag{6.15}$$

where  $n_e$  and  $n_o$  are the extraordinary and ordinary refractive indices of the prism and  $\vartheta$  is the angle of the prism wedge interface. By having the two separate polarisation states within the prism, a path difference  $\Delta$  is created upon transmission out of the prism which is given as[18]

$$\Delta \cong \alpha d \tag{6.16}$$

where  $d$  is the lateral displacement from the centre of the prism. By having the incident beam at  $45^\circ$  to the horizontal axis, 50% will diverge in one direction while the other 50% will diverge in the opposite direction. The Wollaston prism used for the purposes of this experiment was made from calcite and had a separation angle of  $\sim 5^\circ$  (dimensions 10mmx10mmx5mm). Using equation (6.16), this corresponds to having a spatial temporal delay of  $\sim 290$  fs/mm.

### 6.4 The optical arrangement

The complete optical arrangement of the single-shot sonogram is outlined in Figure 6.10

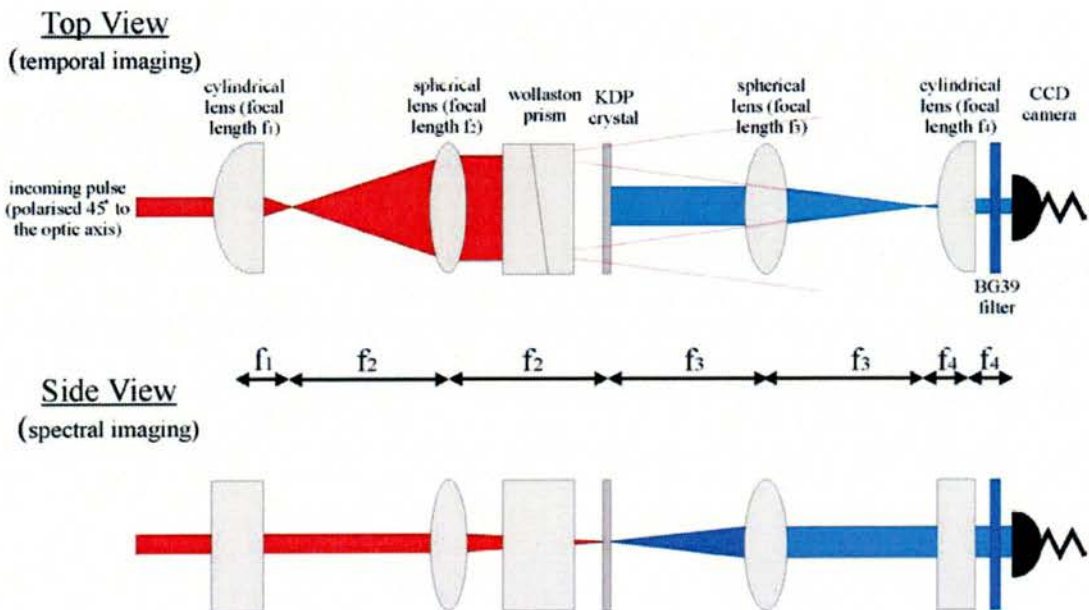


Figure 6.10 Optical arrangement to enable the single-shot acquisition of a sonogram trace

As with GRENOUILLE, the single-shot sonogram arrangement is much easier to visualise when it is explained in two separate planes. Starting with the horizontal plane (top view in Figure 6.10), which images the pulse temporally, it can be seen that the first two lenses form a telescope arrangement. This allows the incoming beam to be expanded within the horizontal plane so that the whole aperture of the Wollaston prism is utilised thus allowing the maximum delay of the prism to be realised. The mixing crystal is placed directly after the Wollaston so that it sees a varying delay across the length of the crystal between the two oppositely polarised beams (see Figure 6.9). The two lenses after the crystal are used to image the focal point within the crystal onto the CCD array. The horizontal axis of the camera will become the delay axis. The vertical plane (side view in Figure 6.10) is used to spectrally image the sonogram trace. Only two lenses are of importance in this plane given that the two vertically oriented cylindrical lenses do not affect the path of the beam. The first spherical lens causes the beam to be tightly focussed within the crystal, the tight focussing (as described in section 6.2) causes the centre frequency of the filter to be angularly dependent. The spherical lens after the crystal collimates the mixing signal and is then imaged directly onto the CCD array so that the vertical axis of the CCD camera becomes the frequency axis. Table 6.1 outlines the actual lenses used to acquire results that are described in Section 6.5

Lens type	Focal length
$f_1$ (Cylindrical lens)	12mm
$f_2$ (Spherical lens)	25mm
$f_3$ (Spherical lens)	14.5mm
$f_4$ (Cylindrical lens)	25mm

**Table 6.1** *The focal length of lenses used for acquiring experimental data*

The values of  $f_3$  and  $f_4$  were suitably chosen so to fully image the spectral and temporal trace respectively across the CCD array. A BG39 bandpass filter was used to block out all of the fundamental wavelength reaching the CCD camera. An 8-bit digital CCD array (ST Microelectronics 5410 sensor evaluation kit) was used to capture an image onto a computer

screen allowing the direct capture of the image to file. Figure 6.11 outlines the optical arrangement used to acquire all results.

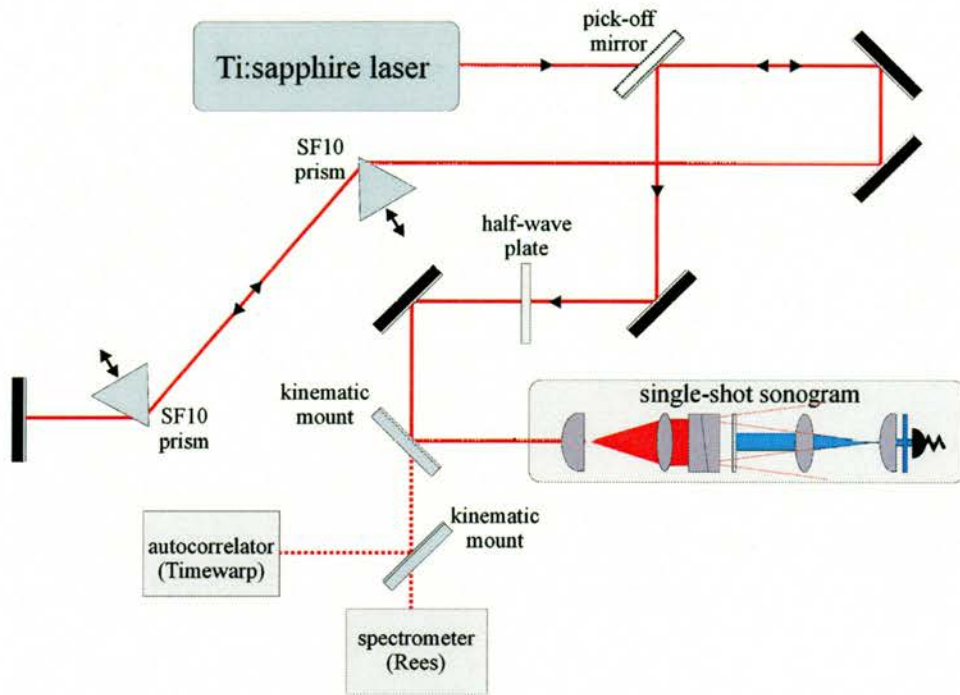


**Figure 6.11** The experimental arrangement to provide a variable dispersion of the pulse

The output of the Ti:Sapphire laser was passed through a pair of SF10 prisms and returned back with a slight vertical offset allowing the returning beam to be picked off. Both prisms were orientated so that they were at Brewster's angle to ensure there would be no deviation in the beam when more prism glass was inserted. The prism separation was  $\sim 750\text{mm}$  and provided sufficient dispersion to modify the pulses from positive to negative chirp across the full insertion range of a single prism. A half-wave plate was used to rotate the polarisation of the input beam so that it was  $45^\circ$  to horizontal. The correct orientation was achieved by rotating the half-wave plate until the two oppositely diverging beams from the Wollaston prism had identical powers. Two kinematic mirror mounts were used to allow simple and quick measurements of the spectrum and autocorrelation of the pulse before it entered the single-shot sonogram apparatus.

The alignment of the optical components within the single-shot arrangement was critical to the overall success of the technique. Each component was placed in the beam one at a time and carefully aligned. A critical parameter was to ensure all lenses were exactly centred on the beam axis. This was achieved by adjusting the input beam so that if it emerged from each lens with an identical vertical and horizontal position. The exact distance between each lens was achieved by having knowledge of which axis should be collimated. For example, the position of the second lens ( $f_2$ ) was achieved by moving the lens until the horizontal component of the beam was collimated whereas the third lens ( $f_3$ ) was positioned so that the vertical axis was collimated.

## 6.5 Calibration of the sonogram trace

The procedure for the calibration of the sonogram trace is normally very straightforward. To calibrate the frequency axis, the spectrum of the filtered pulse is measured while it is being scanned so that a direct correlation between filter position and its centre frequency is obtained. The calibration of the time axis is normally achieved by moving the delay arm a known set distance and measuring the temporal change seen by autocorrelation trace thus providing a direct correlation between temporal and spatial delay. With the single-shot sonogram however, the use of such calibration procedures are not possible given there are no moving parts. Consequently, two separate calibration procedure were needed to successfully and accurately obtain values for the frequency and time axis of the sonogram trace.

### 6.5.1 Calibration of the time axis

For the time axis to be accurately calibrated, a known fixed delay between the two polarisations of the incident pulse was required. This was achieved by placing a quartz waveplate of known thickness into the beam. A waveplate has two separate values of refractive index for each axis ( $n_e$  and  $n_o$ ). The group velocity dispersion seen by each axis is given by:

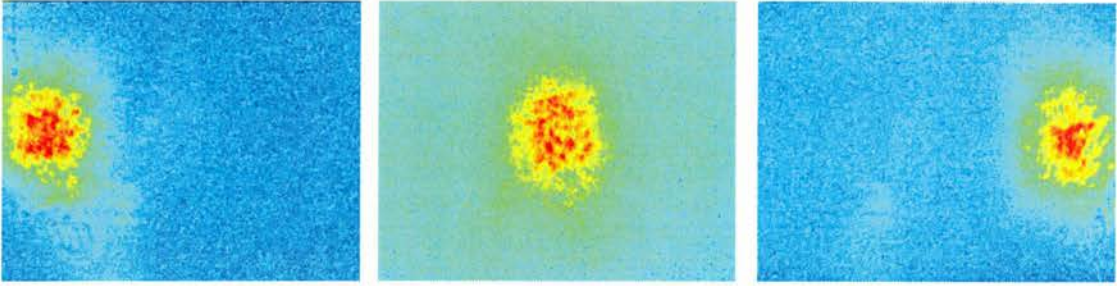
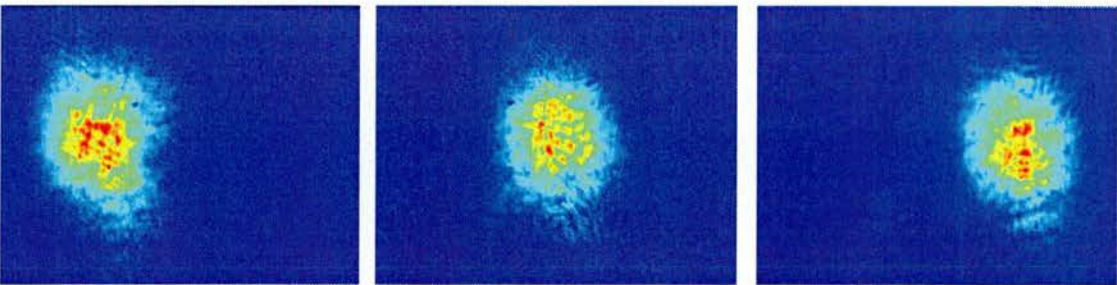
$$v_{g_o} = \frac{c}{n_o - \lambda_o \frac{dn_o}{d\lambda}} \quad (6.17)$$

$$v_{g_e} = \frac{c}{n_e - \lambda_o \frac{dn_e}{d\lambda}} \quad (6.18)$$

By positioning the waveplate so that its e and o axes lie at 45° to the polarisation of the beam, the vertically polarised part of the beam will see a different optical path to that of the horizontally polarised beam. By rotating the waveplate exactly 90°, the delay between the two polarisation will be reversed. The overall delay between the e and o polarisation states is added can be mathematically expressed as:

$$\Delta t = 2 \left( \frac{d_{\text{waveplate}}}{v_{g_o}} - \frac{d_{\text{waveplate}}}{v_{g_e}} \right) \quad (6.19)$$

where  $d_{\text{waveplate}}$  is the thickness of the waveplate. Two separate quartz waveplates with thicknesses, 4500µm and 7500µm were used to calibrate the time axis. Using Equation (6.19) it was calculated that the 4500µm and 7500µm waveplates corresponded to an overall delay ( $\Delta\tau$ ) of 281fs and 469 fs respectively ( $\lambda_o=824\text{nm}$ ). For each waveplate, three separate sonograms were recorded. Two of these traces corresponded to the extreme delays created when the ordinary and extraordinary axis of the waveplate were horizontally or vertically aligned with polarisation of the beam. The third sonogram trace was taken when the ordinary and extraordinary axis was aligned was at 45° to the polarisation of the beam. This caused both the horizontal and vertically polarised light to see the same refractive index and hence corresponded to zero delay. Figure 6.12 outlines the results obtained.

7500 $\mu\text{m}$  waveplate4500 $\mu\text{m}$  waveplate

*Figure 6.12* Six sonogram traces showing various temporal delays (horizontal shifts) caused by various orientations of half wave plates

Each sonogram trace was integrated across the time axis to obtain the temporal marginal. By measuring the peak of each marginal trace it was possible to calculate how many pixels across the CCD array corresponded the maximum delay. Using the delay values calculated from equation (6.19) it was then possible to infer the delay that corresponded to each camera pixel. In the experimental data shown in Figure 6.12, results from both waveplates implied a delay of  $\sim 1.73\text{fs/pixel}$ . The CCD array used had 356 pixels across its horizontal axis, corresponding therefore to a total delay of  $\sim 620\text{fs}$  across its horizontal aperture.

A less accurate technique to calibrate the time axis would have been to use the value of the delay calculated using the construction details of the Wollaston prism. By traversing the Wollaston prism a known distance across the beam, one could measure how many pixels the sonogram trace had been shifted across the CCD array. The calculated delay across the aperture of the Wollaston prism was  $291\text{ fs/mm}$  and it was found that a movement of  $\sim 2\text{mm}$

caused the sonogram trace to move across the whole width of the CCD array. This result, although relying on assumptions about the Wollaston prism geometry, compared well with the more accurate calibration measurements using the waveplates.

### 6.5.2 Calibration of the frequency axis

To calibrate the frequency axis, ideally one would want to scan the centre frequency of the filter while measuring its output spectrum. This is not possible with the single-shot geometry so instead it was decided to scan the centre frequency of the pulse itself. This was achieved by slightly altering the laser cavity alignment. A number of sonogram traces were recorded with their respective pulse spectrum.

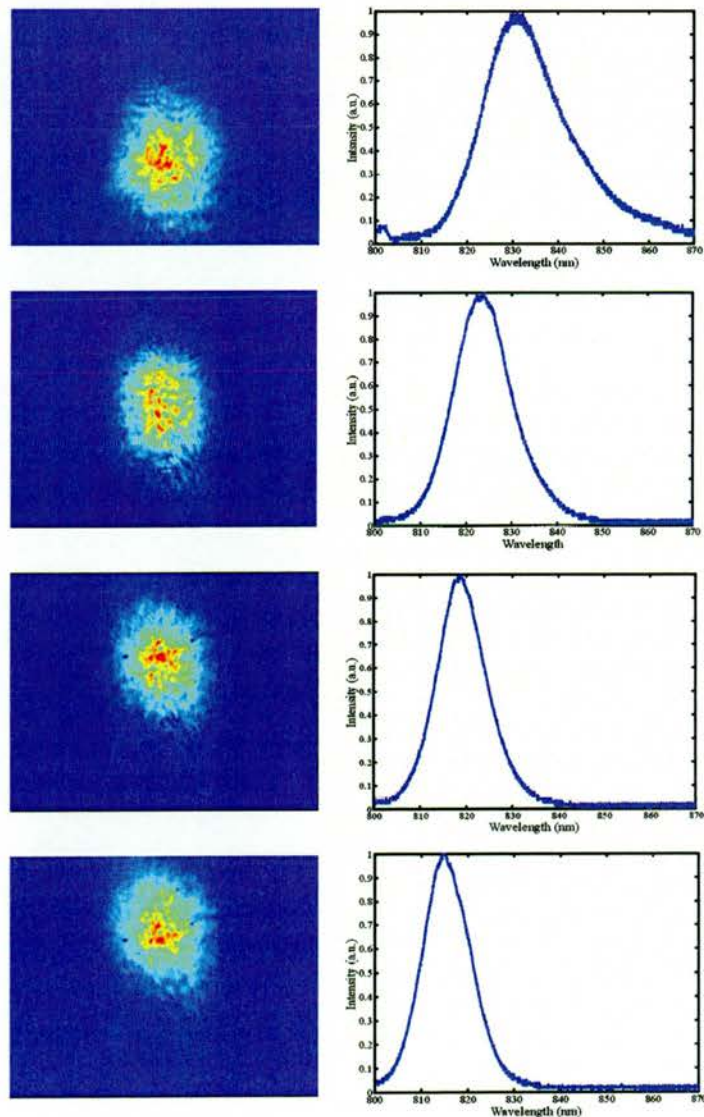


*Figure 6.13 Four sonogram traces along with their respective pulse spectra.*

The results in Figure 6.13 show four separate sonogram traces recorded for different laser centre wavelengths. The spectrum of each pulse is shown alongside each sonogram. It can be seen that as the centre wavelength of the laser pulses was reduced, the sonogram trace moved up the vertical axis of the CCD array. This initially tells us that longer wavelengths correspond to lower positions on the CCD array. Using a similar technique as in the time calibration, the frequency marginal of the sonogram trace was used to find the pixel number that corresponded to the peak intensity value. By repeating this with all four sonogram traces and correlating them with their respective pulse centre wavelength a calibration of the frequency axis was achieved.

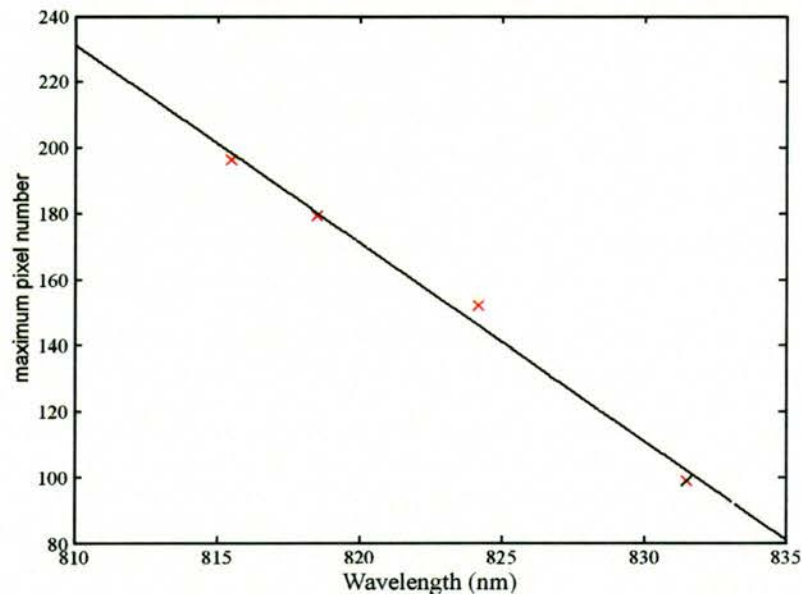


**Figure 6.14** Results obtained from measuring the maximum pixel position of the frequency marginal of each sonogram with the pulse centre wavelength (red crosses) plotted with a linear fitting function (black line)

Figure 6.14 shows the clear linear relationship between the maximum pixel position obtained from each frequency marginal with the centre wavelength of the pulse. By making a linear fit, the calibration of the frequency axis was obtained.

### 6.5.3 Normalisation of the sonogram trace due to spatially varying intensity profile

The temporal varying component of the single-shot sonogram (Wollaston prism) relies on cross-correlating across the spatial profile of a pulse. To produce a linear response across the length of the Wollaston prism a pulse profile with a top hat profile would need to be used. In practice this is not possible experimentally and as a consequence to avoid any systematic errors being produced in the sonogram trace, the varying intensity profile across the temporal delay needs to be considered.

The intensity of the cross-correlation signal produced by the nonlinear signal is dependent upon the product of the two oppositely polarised beams that emerge from the Wollaston prism. Assuming that the most intense part of the beam profile is in the centre, a larger mixing signal will be produced at the centre of the Wollaston than at the edges. By measuring the beam profile at the focus (ie. the crystal position) this discrepancy can be compensated for.

The beam profile at the crystal position was measured by placing a knife edge at the focal position. By scanning the knife edge across the beam and measuring the power passing the slit, the integral of the beam profile was obtained. The beam profiles of both polarisations were required. This was done by rotating the half-wave plate until all of the light passed down either the ordinary or extraordinary axis. Figure 6.15 shows the results of one of these measurements

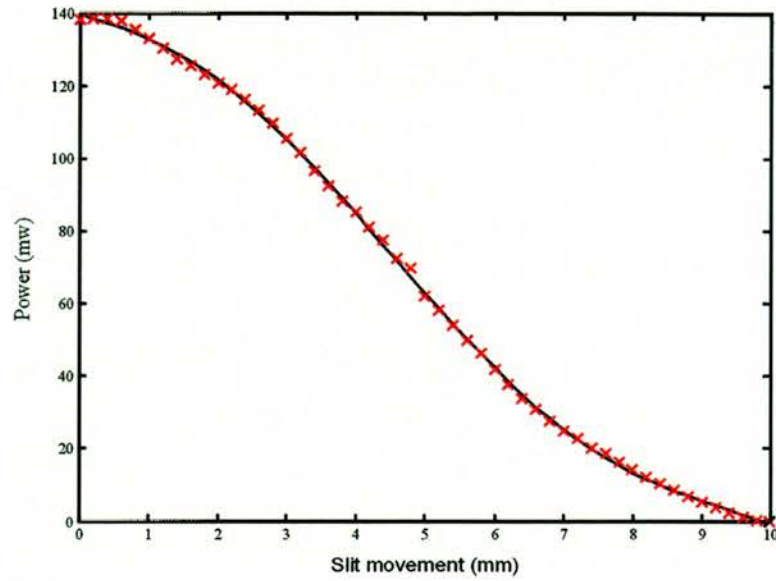


**Figure 6.15** Results obtained by scanning a knife edge across a beam and measuring the power of light passing it (red crosses). A 7<sup>th</sup> order polynomial fit is also plotted with the results (black line)

To avoid a jagged pulse profile when the results were differentiated, a 7<sup>th</sup> order polynomial fit was applied to find a smooth and accurate mathematical interpretation of the results. This equation was then differentiated to obtain the pulse profile of each of the two diverging beams. The product between the two pulse profiles was then obtained and normalised and the results of which are shown in Figure 6.16

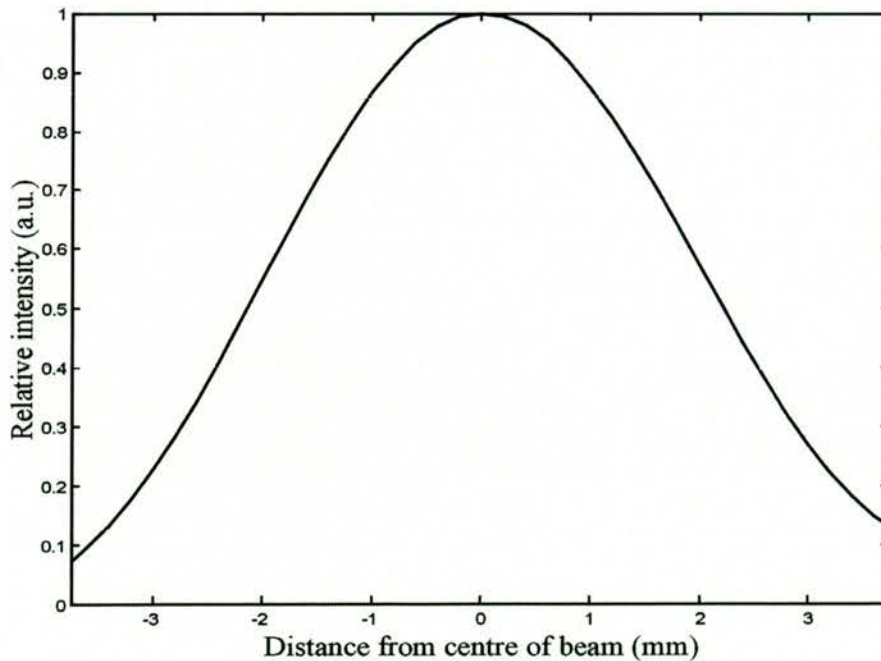


**Figure 6.16** The spatial intensity profile seen within the mixing crystal

Having already calibrated the temporal axis, the spatial distance seen across the CCD array was calculated to  $\sim\pm 1$ mm from the centre of the beam. By looking at figure 6.16, a variation of  $\pm 1$ mm corresponds to a maximum reduction of intensity  $\sim 20\%$ . An array defining the intensity profile across the CCD array was created and used as a dividing factor across the temporal profile of the sonogram trace.

## 6.6 Results

All of the acquired results reported in this section were obtained using the optical arrangement shown in Figure 6.11. By measuring a pulse directly from the Ti:sapphire laser, the acquired sonogram trace was averaged over millions of pulses. It should be noted that this optical arrangement could just as easily be used in a single-shot geometry to measure the output of single pulse from an optical amplifier.

By varying the prism insertion, the chirp on the pulses was modified from positive to negative. Figure 6.17 shows three separate sonogram traces acquired at three different prism insertions. Each time a measurement was taken, a second trace was acquired with the beam blocked. By subtracting the two traces, the majority the background noise entering the CCD array was removed providing a much cleaner sonogram trace.

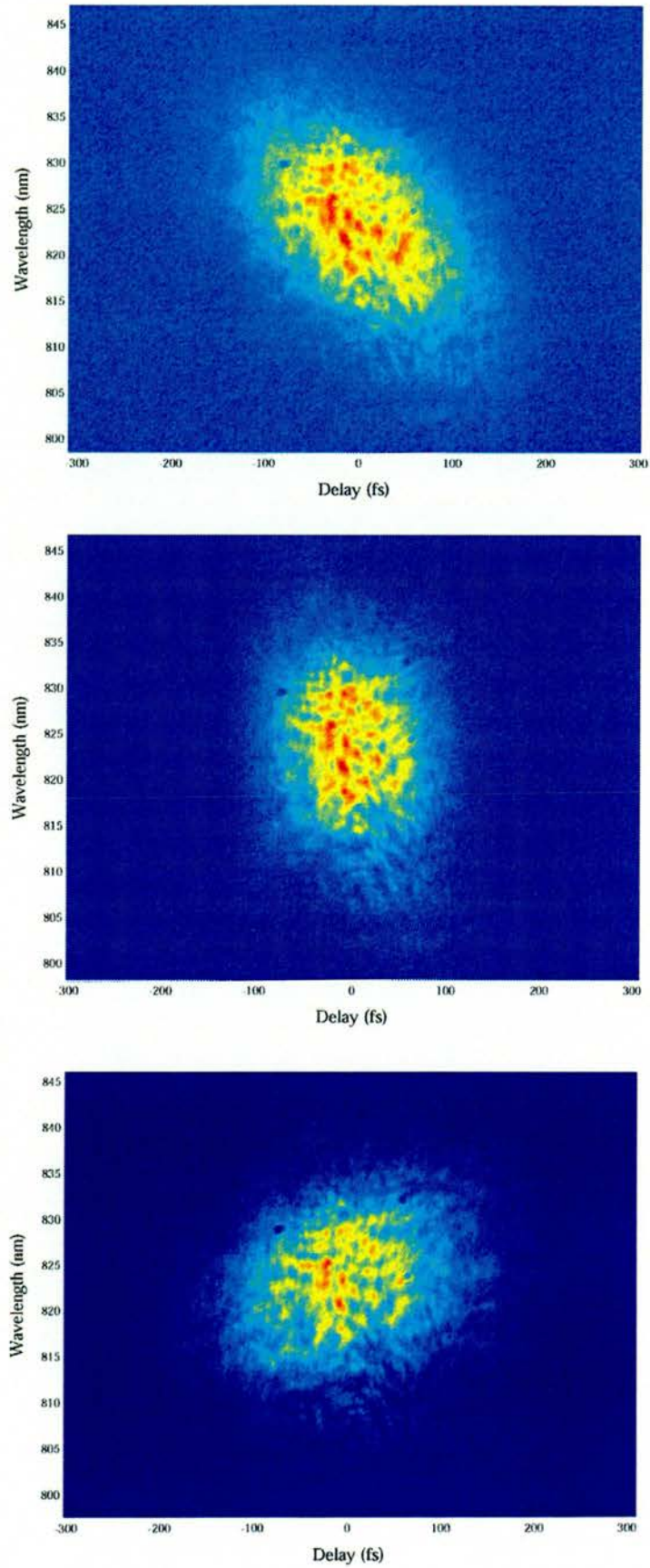


**Figure 6.17** Three sonogram traces with various amounts of positive and negative dispersion

The results in Figure 6.17 show clearly that the pulse goes from being negatively chirped to being positively chirped. This highlights a major advantage which this technique has over GRENOUILLE, in that even before any type of retrieval algorithm is used, it is possible to visually estimate both the sign and magnitude of the chirp that is present on the pulse by measuring the angle of the trace. This is not possible with GRENOUILLE due to the temporal ambiguity that is associated with SHG-FROG. By using the same procedure outlined in Section 4.2.4, the near-transform limited pulse in Figure 6.17 (middle trace) was retrieved. Figure 6.18 compares the acquired and retrieved sonogram traces.

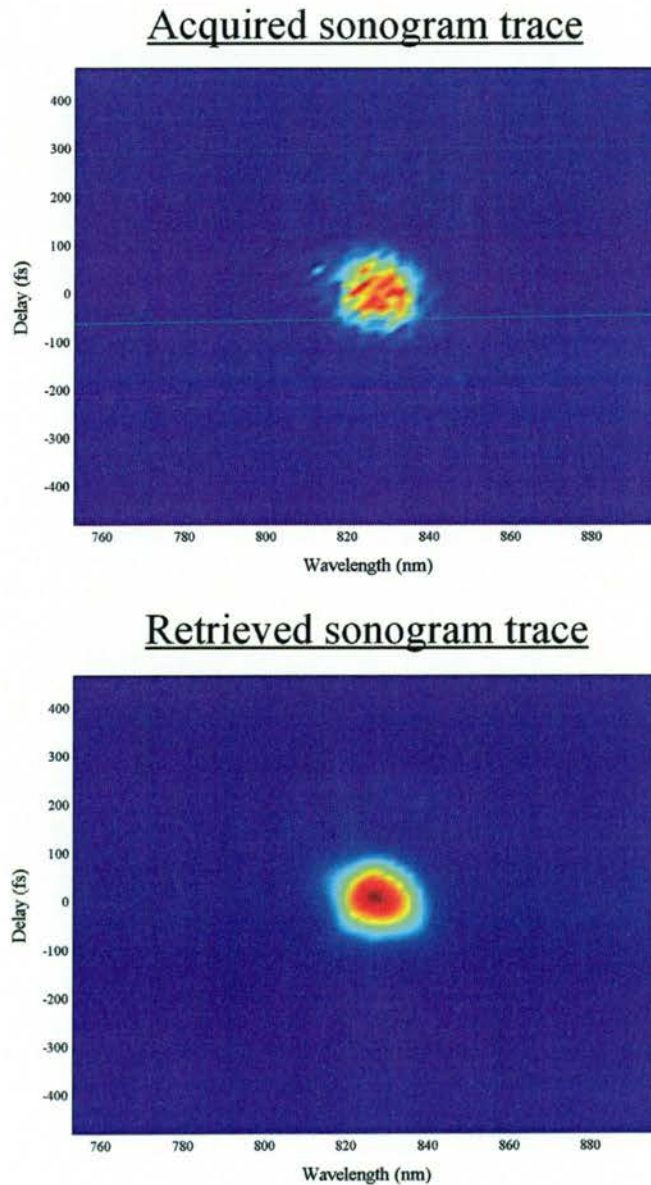


**Figure 6.18** Comparison between the experimentally acquired and retrieved sonogram trace

A small amount of Fourier filtering was applied to the sonogram as well Gaussian filtering to help remove some of the background noise. Figure 6.19 show the retrieved temporal intensity and phase.

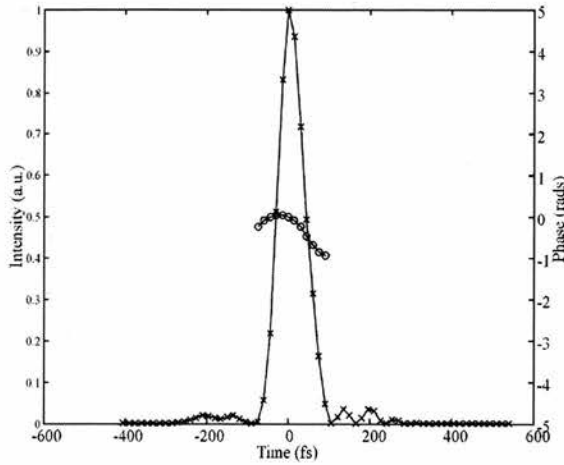


Figure 6.19 The retrieved temporal intensity (crosses) and phase (circles)

To verify that the retrieval was successful, the retrieved data were also compared with the experimentally measured spectrum and intensity autocorrelation

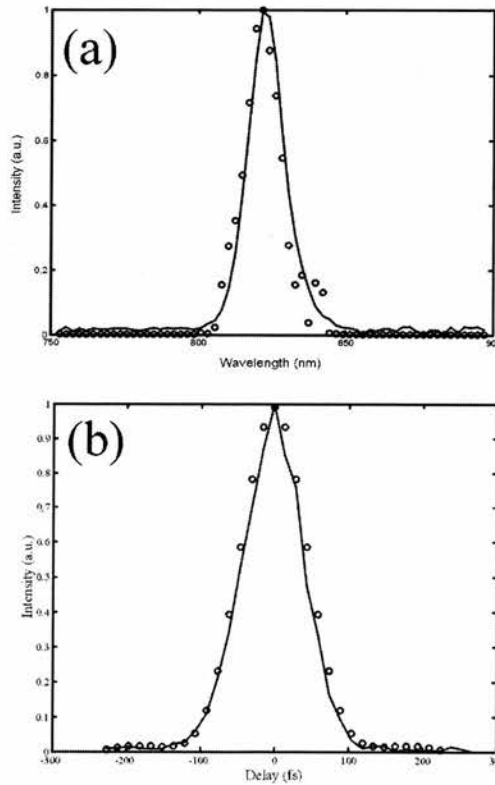


Figure 6.20 Comparison between the experimental (solid line) and retrieved (circles) (a) spectral intensity and (b) intensity autocorrelation

The results outlined in Figure 6.20 show that the retrieved data compare extremely well with those measured experimentally. Since the filter function cannot be directly measured with this sonogram technique a comparison with the trace marginals cannot be undertaken. Consequently, the comparisons made in Figure 6.19 are vital to show that the calibration routines have been successful.

It should be noted as the pulse increased in chirp, and the pulse spread across the whole area of the CCD array, the retrieved autocorrelation trace started to become shorter than the measured autocorrelation. This indicated that mixing signal was not being fully detected by the camera at low intensities. This problem could have easily been solved by either using a more sensitive CCD array at the mixing signal wavelength ( $\sim 400\text{nm}$ ). Care must also be taken to ensure that the whole sonogram is projected on the CCD array, which may be achieved by using a larger camera aperture or reducing the focal length of the final lens ( $f_4$ ) so that the temporal delay was spread across a narrower region. It should also be highlighted that although beam profile correction was carried out on results discussed in this chapter, the results obtained when beam profile correction was not considered were not significantly different.

## 6.7 Conclusion and discussion

Based upon ideas gained from the previously reported GRENOUILLE optical arrangement [12-14] this chapter provides a description of the first ever technique that is capable of the real-time acquisition of a sonogram trace. The new sonogram arrangement also allows for the first time the possibility of taking a single-shot measurement. This technique possesses a major advantage over the GRENOUILLE in that it produces a more intuitive trace. Because the optical setup is compact it would be a simple task to configure the whole instrument within a single unit. It could then be used as a convenient diagnostic tool to place in a beam to determine the sign of the pulse frequency chirp. Also, by calculating the angle of the slope of the sonogram trace, a rough estimate of this chirp can be deduced.

There are several improvements that could be made to this technique, some of which are discussed in Chapter 7. As already mentioned, there was the need for a sensitive camera to ensure that all of the mixing signal was detected. Secondly, since the optical arrangement has no moving parts, the whole trace is recorded spatially. This means the cleanliness and quality of the optics must be excellent because any dust particles or grease on any of the optical surfaces causes distortion in the final sonogram trace.

Results have also shown that provided the camera is sufficiently sensitive to collect all of the mixing signal, the retrieved data are very accurate and can be used to provide a comprehensive characterisation of ultrashort pulses. By combining the sonogram retrieval algorithm used in Chapter 4 with this optical arrangement there is true potential of creating the first technique that is capable of fully characterising a pulse using sonogram trace at video-rate repetition rates. This constitutes a powerful optical femtosecond oscilloscope.

## 6.8 References

- [1] J. L. A. Chilla and O. E. Martinez, "Direct Determination of the Amplitude and the Phase of Femtosecond Light-Pulses," *Optics Letters*, vol. 16, pp. 39-41, 1991.
- [2] D. T. Reid, M. Padgett, C. McGowan, W. E. Sleat, and W. Sibbett, "Light-emitting diodes as measurement devices for femtosecond laser pulses," *Optics Letters*, vol. 22, pp. 233-235, 1997.
- [3] D. T. Reid, W. Sibbett, J. M. Dudley, L. P. Barry, B. Thomsen, and J. D. Harvey, "Commercial semiconductor devices for two photon absorption autocorrelation of ultrashort light pulses," *Applied Optics*, vol. 37, pp. 8142-8144, 1998.
- [4] I. Cormack, W. Sibbett, and D. T. Reid, "Measurement of femtosecond optical pulses using time-resolved optical gating," presented at Conference on Lasers and Electro Optics (CLEO2001), Baltimore, 2001.
- [5] D. J. Kane and R. Trebino, "Characterization of Arbitrary Femtosecond Pulses Using Frequency-Resolved Optical Gating," *IEEE Journal of Quantum Electronics*, vol. 29, pp. 571-579, 1993.
- [6] D. J. Kane and R. Trebino, "Single-Shot Measurement of the Intensity and Phase of an Arbitrary Ultrashort Pulse By Using Frequency-Resolved Optical Gating," *Optics Letters*, vol. 18, pp. 823-825, 1993.
- [7] R. Trebino and D. J. Kane, "Using Phase Retrieval to Measure the Intensity and Phase of Ultrashort Pulses - Frequency-Resolved Optical Gating," *Journal of the Optical Society of America a-Optics Image Science and Vision*, vol. 10, pp. 1101-1111, 1993.
- [8] R. Trebino, K. W. DeLong, D. N. Fittinghoff, J. N. Sweetser, M. A. Krumbugel, B. A. Richman, and D. J. Kane, "Measuring ultrashort laser pulses in the time-frequency domain using frequency-resolved optical gating," *Review of Scientific Instruments*, vol. 68, pp. 3277-3295, 1997.
- [9] D. J. Kane, W. Wood, and K. Peterson, "Real-time ultrashort pulse shaping diagnostics using Frequency-Resolved Optical Gating," presented at Conference on Lasers and Electro-Optics (CLEO2001), Baltimore, 2001.
- [10] D. J. Kane, "Real-time measurement of ultrashort laser pulses using principal component generalized projections," *IEEE Journal of Selected Topics in Quantum Electronics*, vol. 4, pp. 278-284, 1998.
- [11] D. J. Kane, "Recent progress toward real-time measurement of ultrashort laser pulses," *IEEE Journal of Quantum Electronics*, vol. 35, pp. 421-431, 1999.
- [12] P. O'Shea and R. Trebino, "Extremely simple Intensity-and-phase ultrashort-pulse measurement device with no spectrometer, thin crystal, or delay line," presented at Conference on Lasers and Electro-Optics, San Francisco, 2000.
- [13] P. O'Shea and R. Trebino, "Highly simplified ultrashort-pulse measurement," presented at XII International Conference on Ultrafast Phenomena, Charleston, SC, 2000.
- [14] P. O'Shea, M. Kimmel, and R. Trebino, "Increased phase-matching bandwidth in GRENOUILLE measurements," presented at Conference on Lasers and Electro-Optics (CLEO2001), Baltimore, 2001.
- [15] V. Dmitriev, G. Gurzadyan, and D. Nikogosyan, *Handbook of Nonlinear Optical Crystals*: Springer-Verlag, 1990.
- [16] A. Yariv, "Chapter 5, Electromagnetic Fields and their Quantization," in *Quantum Electronics*, third ed: Wiley, 1988.
- [17] A. Yariv, "Chapter 16, Introduction to Nonlinear Optics - Second-Harmonic Generation," in *Quantum Electronics*: Wiley, 1988.
- [18] M. Francon and S. Mallick, "Chapter 2," in *Polarization interferometers*: Wiley Interscience, 1971.

# CHAPTER 7

## Conclusions and future work

---

### 7.1 Summary and conclusions

The work carried out in this research project has mainly concerned itself with the measurement of sonograms to rapidly characterise ultrashort laser pulses. A sonogram trace is intrinsically much more intuitive than a SHG-FROG trace and provides immediate knowledge of some characteristics that are associated with the pulse. Many novel and exciting techniques have been developed during the course of this project that allow the acquisition and retrieval of a sonogram to occur in a short period of time. In this chapter the work carried out within this thesis is reviewed and particular highlights are emphasised. Examples of how this work can be extended in the future will also be discussed.

In Chapter 3, I developed a procedure based on white light interferometry that provided a quick and accurate way to measure the dispersion of optical components. Both the sensitivity and accuracy of the technique were demonstrated. This technique was immediately used to explain why a Cr:LiSAF laser was modelocking within a femtosecond pulse regime. The simplicity and ease with which dispersion characteristics are obtainable using this technique has made it a valuable tool within the ultrafast-science laboratory and has been used many times by colleagues who have been interested in finding out the dispersion of optical components. The main goal of this work was to develop a technique that could determine the dispersion of a frequency filter. This was an important part of Chapter 4 in which the dispersion from the filter had to be minimised. As well as a useful diagnostic tool, the procedure could easily be utilised for a teaching laboratory experiment, enabling students to be

introduced to key concepts such as optical phase, group delay and dispersion in a physical and meaningful way together with ideas of birefringence and Sellmeier relations.

In Chapter 4, two separate, rapid pulse characterisation schemes were developed to provide a fast and accurate way of acquiring and retrieving information from a sonogram trace. Both techniques share some fundamental advantages. Firstly, the use of two-photon detection provides a sensitive, broadband and polarisation insensitive way of detecting the trace, making it ideally suited to ultrashort pulse characterisation. The use of two-photon detectors is not possible with SHG-FROG in which a mixing crystal must be used, the design of which must be carefully chosen to ensure it has a sufficient bandwidth. Secondly, exhaustive comparisons between the trace marginals and experimental data were carried out for both techniques to ensure all results were free from systematic errors. Such exhaustive checks are not possible with interferometric pulse characterisation schemes such as SPIDER.

The first sonogram acquisition arrangement used a traditional frequency filter comprising a grating, lens and mirror within a  $4f$  arrangement. A scanning slit was placed in the Fourier plane to select which frequencies passed through the filter. The dispersion characterisation technique developed in Chapter 3 was used to ensure the filter was near-dispersionless across the bandwidth of the pulse. These dispersion data obtained from the filter agreed very well with theoretical ray-tracing calculations, thereby further demonstrating the effectiveness of this measurement technique. The use of the FORTRAN computer language for all calibration and retrieval calculations enabled very fast calibration and retrieval of sonogram traces. The computational speed was so impressive that unexpectedly it was the speed of the sonogram acquisition that became the limiting factor for increasing the update rate. With this system, a sonogram trace could be acquired and retrieved every two seconds. The overall simplicity of the resulting optical setup therefore makes it very attractive. The technique developed to align the spectral filter to give a near-dispersionless response across the spectral bandwidth of the pulse helped overcome the major difficulty that was initially thought to be the limiting factor

associated with this optical setup. A key future application of this system could be the implementation of phase control at the Fourier plane of the filter. This arrangement has already been used to compensate dispersion. By combining the sonogram characterisation arrangement described here with a pulse shaping experiment, a real-time pulse phase control system could be developed, not only to minimise dispersion but also to tailor the phase to a desired profile.

The second sonogram characterisation system described in chapter 4 used a scanning Fabry-Perot filter. The use of this filter served to address the requirement for a faster scanning frequency filter. The full capabilities of the A-D card were utilised so that a single sonogram trace (256 by 256) was acquired at a frequency of 1.52Hz. In this system, the speed of calibration and retrieval procedure was a limiting factor so that the acquisition and retrieval process was reduced to a frequency of  $\sim 1$ Hz. The overall update rate could therefore have been increased with the use of a faster computer. Modifications to the overall setup could also be implemented in the future to increase the overall acquisition speed. Firstly a faster data acquisition card would be needed to enable data to be acquired at a faster rate. The acquisition speed could have been quadrupled by using a 128 by 128 array instead of the 256 by 256 trace used here. A specifically designed Fabry-Perot filter has the capability of scanning at much higher frequencies than demonstrated here. Using such a filter as the faster scanning component would enable the acquisition speed of a sonogram trace to be dramatically increased. Finally, the use of a Fabry-Perot filter allows the overall optical setup to be miniaturised to provide a very compact, real-time pulse characterisation arrangement that could be placed in the optical beam to obtain pulse characteristics.

During the course of this project, a second geometry was devised for the production of a sonogram trace. Dispersion-propagation time-resolved optical gating (DP-TROG) provides a way to determining the sonogram of a pulse by measuring a number of second-order autocorrelation traces after the pulse has passed through a system of variable dispersion.

Although this technique was novel it was not very practical because it relied on precise knowledge of the added dispersion. In Chapter 5 the first practical demonstration of the DP-TROG was outlined. The experimental procedure had the fundamental advantage of not having to rely on error-prone dispersion measurements. Instead, marginals of the sonogram trace were fully utilised to provide self-calibration and immediate identification of systematic errors. Only the measurement of the pulse spectrum and autocorrelation were required to provide calibration. A further attractive feature of DP-TROG was its ability to make pulse measurements of any wavelength for which an autocorrelator is available. The straightforward optical arrangement also allows quick and accurate measurements to be taken without the need to acquire additional equipment. The limitations of the DP-TROG were investigated to show that the smallest pulse duration, before third-order nonlinear effect had to be considered was a 15fs pulse centred at 800nm. Future work to develop the DP-TROG technique further would involve taking into consideration higher orders of dispersion so that distortion of the DP-TROG trace would not occur and smaller pulses could be measured.

Some of the most exciting results outlined within this thesis were described in Chapter 6 where the first ever technique capable of taking a single-shot sonogram measurement of a pulse was outlined. The use of a Wollaston prism and a carefully designed mixing nonlinear crystal allowed a sonogram trace to be projected onto a CCD camera. In a multi-pulse configuration this provided, for the first time, a video-rate acquisition of a sonogram trace. Using an identical optical arrangement an amplified laser system could be used in the future to provide single-shot sonogram measurements. The optical arrangement consisted of only 6 optical elements, making alignment extremely fast and straightforward. The lack of any scanning components or synchronisation electronics highlights further the overall attractiveness of this technique. An acquired sonogram trace was retrieved, the results of which were compared with experimentally measured results. All results compared very well with one another. Firstly, this showed the practicality of this technique and secondly it proved that the new calibration procedures that were devised for this technique were successful. The

scope for future work for this new characterisation technique is immense. The optical arrangement is so compact, the next logical step would be to mount the whole optical arrangement within a single highly compact unit. This unit could simply be placed in front of a laser system to provide an invaluable pulse diagnostic tool. Mentioned throughout this thesis is the fact that a sonogram trace is much more intuitive than a SHG-FROG trace. With a sonogram trace it is possible to estimate promptly the size and sign of chirp on a pulse even before it is passed through a retrieval algorithm. This is much more difficult to do with a SHG-FROG trace and consequently gives my real-time sonogram arrangement a fundamental advantage over techniques such as GRENOUILLE. Once the initial calibration procedure is carried out with the aid of a tunable laser system (required for frequency calibration), as long as none of the optical components are moved there is no need to re-calibrate the system. This allows laser systems that are not tunable to be used with this optical setup. Another logical progression for this technique is to combine the retrieval algorithm that was developed within the work described in Chapter 4 to provide a real-time pulse acquisition and retrieval system. The use of a faster computer will allow this system to have a dramatically increased update rate to provide a real-time femtosecond oscilloscope.

## Publications

### *Journal publications*

- 1) I. G. Cormack, W. Sibbett, D. T. Reid, “*Rapid measurement of ultrashort pulse amplitude and phase from a two-photon absorption sonogram trace*”, JOSA B, **18**(9), pg. 1377-1382, 2001
- 2) I. G. Cormack, W. Sibbett, D. T. Reid, “*Ultrashort pulse characterisation using a scanning Fabry-Perot etalon enabling rapid acquisition and retrieval of a sonogram at rates up to 1.52Hz*” Review of Scientific Instruments, **72**(11), 2001
- 3) I. G. Cormack, W. Sibbett, D. T. Reid, “*Practical measurement of femtosecond pulses using time-resolved optical gating*”, Optics Communications, **194**, pg. 415-423, 2001
- 4) I. G. Cormack, W. Sibbett, D. T. Reid, “*Measurement of group velocity dispersion using white light interferometry – a teaching laboratory*”, American Journal of Physics., **68**(12), pg. 1146-1150, 2000
- 5) I. G. Cormack, W. Sibbett, D. T. Reid, “*Rapid retrieval of ultrashort pulse amplitude and phase from a sonogram trace*”, Ultrafast Phenomenon XII, Springer, pg. 135-137
- 6) I. G. Cormack, D. T. Reid, “*Observation of the soliton self-frequency shift in photonic crystal fibre*” submitted to Electronic letters
- 7) D. T. Reid, I. G. Cormack, “*Soliton self-frequency shift effects in photonic crystal fibre*”, accepted to Journal of Modern Optics

- 8) D. T. Reid, I. G. Cormack, "*Single-shot sonogram: a real-time chirp monitor for ultrafast oscillators*", submitted to Optics Letters

### ***Conference publications***

- 1) I. G. Cormack, W. Sibbett, D. T. Reid, "*Practical measurement of femtosecond optical pulses using time-resolved optical gating*" in Technical digest of the 15<sup>th</sup> Quantum Electronics and Photonics conference, Glasgow, 2001, poster P2-21, pg. 126
- 2) I. G. Cormack, W. Sibbett, D. T. Reid, R. Ortega-Martinez "*Ultrashort pulse characterisation using a scanning etalon to rapidly acquire and retrieve a sonogram*" in Technical digest of the 15<sup>th</sup> Quantum Electronics and Photonics conference, Glasgow, 2001, oral presentation, pg. 43
- 3) I. G. Cormack, D. T. Reid "*Observations of self-frequency shift in photonic crystal fibre*", " in Technical digest of the 15<sup>th</sup> Quantum Electronics and Photonics conference, Glasgow, 2001, oral presentation, pg. 41
- 4) I. G. Cormack, W. Sibbett, D. T. Reid, "*Measurement of femtosecond optical pulses using time-resolved optical gating*" in Technical Digest of Conference on Lasers and Electro-Optics, Optical Society of America, Baltimore, 2001, paper CTuN3
- 5) I. G. Cormack, W. Sibbett, D. T. Reid, "*Ultrashort pulse characterisation using a scanning fabry-perot etalon to rapidly acquire and retrieve a sonogram*", in Technical Digest of Conference on Lasers and Electro-Optics, Optical Society of America, Baltimore, 2001, paper CWA10

- 6) I. G. Cormack, W. Sibbett, D. T. Reid, "*Measurement of ultrashort pulse amplitude and phase by rapidly acquiring and retrieving a sonogram*", in Technical Digest of Conference on Lasers and Electro-Optics -Europe, Optical Society of America, Nice, 2000, paper CTuH3
  
- 7) I. G. Cormack, W. Sibbett, D. T. Reid, "*Rapid retrieval of ultrashort pulse amplitude and phase from a sonogram trace*", The Twelfth International Conference on Ultrafast Phenomena, Optical Society of America, Charleston, 2000, paper MB1
  
- 8) I. G. Cormack, W. Sibbett, D. T. Reid, "*Measurement of femtosecond optical pulses using time-resolved optical gating*" LEOS Scottish chapter, University of St. Andrews, 2000, poster presentation
  
- 9) I. G. Cormack, W. Sibbett, D. T. Reid, "*Ultrashort pulse characterisation using a sonogram*", in Technical digest of the Fourteenth Quantum Electronics conference, Manchester, 1999, oral presentation